Universitat Politècnica de València
Departamento de Máquinas y Motores Térmicos

Optimal Control for Automotive Powertrain Applications

PhD Dissertation

Presented by

Alberto Reig

Advised by

Dr. Benjamín Pla

Valencia, September 2017

PhD Dissertation

Optimal Control for Automotive Powertrain Applications

Presented by	Alberto Reig
Advised by	Dr. Benjamín Pla

Examining committee

President:	Dr. José Galindo Lucas
Secretary:	Dr. Octavio Armas Vergel
Vocal:	Dr. Marcello Canova

Valencia, September 2017

To the geniuses of the past, who built our future;
to those names in the shades, bringing our knowledge.
They not only supported this work but also the world we live in.

If you can solve it, it is an exercise; otherwise it's a research problem.

— Richard Bellman

Resumen

El Control Óptimo (CO) es esencialmente un problema matemático de búsqueda de extremos, consistente en la definición de un criterio a minimizar (o maximizar), restricciones que deben satisfacerse y condiciones de contorno que afectan al sistema. La teoría de CO ofrece métodos para derivar una trayectoria de control que minimiza (o maximiza) ese criterio.

Esta Tesis trata la aplicación del CO en automoción, y especialmente en el motor de combustión interna. Las herramientas necesarias son un método de optimización y una representación matemática de la planta motriz. Para ello, se realiza un análisis cuantitativo de las ventajas e inconvenientes de los tres métodos de optimización existentes en la literatura: programación dinámica, principio mínimo de Pontryagin y métodos directos. Se desarrollan y describen los algoritmos para implementar estos métodos así como un modelo de planta motriz, validado experimentalmente, que incluye la dinámica longitudinal del vehículo, modelos para el motor eléctrico y las baterías, y un modelo de motor de combustión de valores medios.

El CO puede utilizarse para tres objetivos distintos:

1. Control aplicado, en caso de que las condiciones de contorno estén definidas. Puede aplicarse al control del motor de combustión para un ciclo de conducción dado, traduciéndose en un problema matemático de grandes dimensiones. Se estudian dos casos particulares: la gestión de un sistema de EGR de doble lazo, y el control completo del motor, en particular de las consignas de inyección, SOI, EGR y VGT.

2. Obtención de reglas de control cuasi-óptimas, aplicables en casos en los que no todas las perturbaciones se conocen. A este respecto, se analizan el cálculo de calibraciones de motor específicas para un ciclo, y la gestión energética de un vehículo híbrido mediante un control estocástico en bucle cerrado.

3. Empleo de trayectorias de CO como comparativa o referencia para tareas de diseño y mejora, ofreciendo un criterio objetivo. La ley de combustión así como el dimensionado de una planta motriz híbrida se optimizan mediante el uso de CO.

Las estrategias de CO han sido aplicadas experimentalmente en los trabajos referentes al motor de combustión, poniendo de manifiesto sus ventajas sustanciales, pero también analizando dificultades y líneas de actuación para superarlas. Los métodos desarrollados en esta Tesis Doctoral son generales y aplicables a otros criterios si se dispone de los modelos adecuados.

Resum

El Control Òptim (CO) és essencialment un problema matemàtic de cerca d'extrems, que consisteix en la definició d'un criteri a minimitzar (o maximitzar), restriccions que es deuen satisfer i condicions de contorn que afecten el sistema. La teoria de CO ofereix mètodes per a derivar una trajectòria de control que minimitza (o maximitza) aquest criteri.

Aquesta Tesi tracta l'aplicació del CO en automoció i especialment al motor de combustió interna. Les ferramentes necessàries són un mètode d'optimització i una representació matemàtica de la planta motriu. Per a això, es realitza una anàlisi quantitatiu dels avantatges i inconvenients dels tres mètodes d'optimització existents a la literatura: programació dinàmica, principi mínim de Pontryagin i mètodes directes. Es desenvolupen i descriuen els algoritmes per a implementar aquests mètodes així com un model de planta motriu, validat experimentalment, que inclou la dinàmica longitudinal del vehicle, models per al motor elèctric i les bateries, i un model de motor de combustió de valors mitjans.

El CO es pot utilitzar per a tres objectius diferents:

1. Control aplicat, en cas que les condicions de contorn estiguen definides. Es pot aplicar al control del motor de combustió per a un cicle de conducció particular, traduint-se en un problema matemàtic de grans dimensions. S'estudien dos casos particulars: la gestió d'un sistema d'EGR de doble llaç, i el control complet del motor, particularment de les consignes d'injecció, SOI, EGR i VGT.

2. Obtenció de regles de control quasi-òptimes, aplicables als casos on no totes les pertorbacions són conegudes. A aquest respecte, s'analitzen el càlcul de calibratges específics de motor per a un cicle, i la gestió energètica d'un vehicle híbrid mitjançant un control estocàstic en bucle tancat.

3. Utilització de trajectòries de CO com comparativa o referència per a tasques de disseny i millora, oferint un criteri objectiu. La llei de combustió així com el dimensionament d'una planta motriu híbrida s'optimitzen mitjançant l'ús de CO.

Les estratègies de CO han sigut aplicades experimentalment als treballs referents al motor de combustió, manifestant els seus substancials avantatges, però també analitzant dificultats i línies d'actuació per superar-les. Els mètodes desenvolupats a aquesta Tesi Doctoral són generals i aplicables a uns altres criteris si es disposen dels models adequats.

Abstract

Optimal Control (OC) is essentially a mathematical extremal problem. The procedure consists on the definition of a criterion to minimize (or maximize), some constraints that must be fulfilled and boundary conditions or disturbances affecting to the system behavior. The OC theory supplies methods to derive a control trajectory that minimizes (or maximizes) that criterion.

This dissertation addresses the application of OC to automotive control problems at the powertrain level, with emphasis on the internal combustion engine. The necessary tools are an optimization method and a mathematical representation of the powertrain. Thus, the OC theory is reviewed with a quantitative analysis of the advantages and drawbacks of the three optimization methods available in literature: dynamic programming, Pontryagin minimum principle and direct methods. Implementation algorithms for these three methods are developed and described in detail. In addition to that, an experimentally validated dynamic powertrain model is developed, comprising longitudinal vehicle dynamics, electrical motor and battery models, and a mean value engine model.

OC can be utilized for three different purposes:

1. Applied control, when all boundaries can be accurately defined. The engine control is addressed with this approach assuming that a the driving cycle is known in advance, translating into a large mathematical problem. Two specific cases are studied: the management of a dual-loop EGR system, and the full control of engine actuators, namely fueling rate, SOI, EGR and VGT settings.

2. Derivation of near-optimal control rules, to be used if some disturbances are unknown. In this context, cycle-specific engine calibrations calculation, and a stochastic feedback control for power-split management in hybrid vehicles are analyzed.

3. Use of OC trajectories as a benchmark or base line to improve the system design and efficiency with an objective criterion. OC is used to optimize the heat release law of a diesel engine and to size a hybrid powertrain with a further cost analysis.

OC strategies have been applied experimentally in the works related to the internal combustion engine, showing significant improvements but non-negligible difficulties, which are analyzed and discussed. The methods developed in this dissertation are general and can be extended to other criteria if appropriate models are available.

h

Agradecimientos

El director de tesis es como una bujía: lo necesitas en tiempos de compresión, debes darle la mezcla adecuada y su chispa hace que todo funcione. De estar bien dirigido depende que una tesis doctoral sufra o evite el *knock*. Y creo que he sido enormemente afortunado de haber contado con Benjamín Pla durante este largo camino. No solo me ha transmitido su pasión por todo lo que hace, desde la primera idea, hasta el último experimento, pasando por todas y cada una de las líneas de código, sino que más que un director ha sido un compañero y amigo que ha soportado todas mis dudas y errores, que no han sido pocos. Ya hace tiempo convirtió lo que pretendía ser un simple proyecto académico en todo un reto científico, descubriéndome lo que era el mundo de la investigación, algo que por aquel entonces me era totalmente ajeno. De él he aprendido a apreciar la belleza que reside en los problemas: son una elegante excusa para recorrer el camino hasta la solución. Sin su contagiosa pasión jamás me habría embarcado en este viaje y no habría conseguido algo de lo que hoy me siento realmente satisfecho. Es por ello que todo lo que he aprendido, todo lo que hay en esta tesis y toda mi experiencia, se la debo a él.

Otro pilar fundamental ha sido Carlos Guardiola que, sin perder ese aire informal, cercano y desenfadado que le caracteriza, siempre ha estado dispuesto a ofrecer una visión crítica e incluso disruptiva de mis ideas. Su capacidad de asimilar en pocos minutos un problema completamente desconocido para él y ofrecer otro punto de vista ha sido, a parte de envidiable, fundamental para darme cuenta que muchas veces los árboles no me dejaban ver el bosque.

Por supuesto, merece una mención especial mi querido compañero de doctorado, Pau Bares. Aunque me hagas rabiar y me queje constantemente de ti, lo cierto es que ha sido muy divertido tenerte al lado todo este tiempo. Que seas mi antítesis es precisamente el motivo por el cual he podido aprender, profesional y personalmente, tantas cosas buenas de ti. Tampoco puedo olvidarme de Javier Mora, compañero de despacho, de risas y de deportes. Cuánto me alegro de que al fin alguien aprecie lo absurdo de mis profundas reflexiones. No todos los héroes llevan capa.

Y qué sería de nosotros, estudiantes de doctorado, sin todos nuestros compañeros de batalla que viven nuestros mismos quebraderos de cabeza en el desarrollo de sus propias tesis. Ellos te comprenden mejor que nadie, te animan a superarte en los momentos más complicados y, con los pequeños detalles, hacen que este viaje sea mucho más amable. Marcelo Real, Alvin Barbier, Varun Pandey, David Blanco, Diana Graciano, Pedro Cabrera, Javier Pérez, ha sido un placer navegar junto a ustedes, camaradas.

Todas las personas que, por distintos motivos (proyecto fin de carrera,

trabajo fin de grado, máster, ...), han pasado una porción de su vida en este departamento, merecen también un verdadero reconocimiento. Trabajando en unos proyectos u otros, han estado siempre compartiendo buenos momentos y haciendo del despacho una verdadera segunda casa. Iván, José, Vicent, Josep, Juanfran, Nando, Vero I, Vero II, Isa, Rubén, Loïc, Marco, Thierry, Keyao, Jaime, Chema, Abhinav, Abhishek, Jorge, Vishnu, Chris, José María, . . . , a todos vosotros: GRACIAS.

I would like to shift to English to show my sincere gratitude to Professors Sciarretta and del Re. They both gave me the opportunity to be part of their great research teams during my internships. My time in Paris and Linz was intense and full of challenges that taught me more than I ever expected. I really enjoyed the experience and learned so much from my truly exceptional supervisors that I do not have enough words to express my gratitude. I can just say: merci, dankeschön and, of course, grazie. And for those who spent some of their time with me (Zeijang, Thomas, Harald, . . .), thanks for making me feel like I was in my hometown.

Esta tesis no habría sido posible, tampoco, sin la ayuda de los integrantes de este departamento: técnicos, que han visto de cerca la copa pistón con mis numerosos ensayos, profesores e investigadores, que han sido una verdadera ayuda ante diversos problemas, la dirección, que ha mostrado todo su apoyo en mis proyectos, y todas las personas que conforman la administración, que siempre con una sonrisa me han evitado más de un problema burocrático.

No puedo concluir estos agradecimientos sin mencionar a las personas que más me conocen, que más me han sufrido, y gracias a los que soy quien soy: mi familia y mis amigos. Gracias por soportar mis extraños horarios, mis reiterativas ausencias, mi falta de humor, mi estrés y la aparente carencia de orden de mi vida. Sin esa sonrisa incondicional y ese verdadero apoyo no sé qué sería de mí ahora. Mil gracias.

Valencia, septiembre de 2017

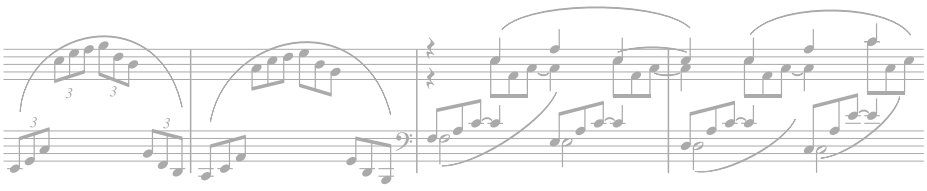

Contents

Glossary

A	Vehicle frontal area
A_{egr}	EGR valve effective opening area
A_{ex}	Engine heat exchange surface
$\widetilde{A}_{ex}$	Reference engine heat exchange surface
AFR	Air-fuel ratio
α	Crank angle
α_e	Engine crank angle at EVO
α_i	Engine crank angle at IVC
α_{soc}	Engine crank angle at start of combustion
A_{wall}	Cylinder walls heat exchange area
b	Piston bore
β	Track gradient
$\mathbf{C}$	Constraint vector of the Nonlinear Programming (NLP) problem
C	Constant
c	Path constraint function
C_b	Battery price
$C_{b,man}$	Battery cost for the manufacturer
C_{cha}	Vehicle chassis price
C_d	Aerodynamic drag coefficient
$C_{d,egr}$	EGR valve discharge coefficient
c_f	Fuel price per mass unit
c_i	Generic coefficient
C_{ice}	Engine price
$\mathbf{c}_i$	Gas velocity
C_{km}	Total cost of operation per kilometer, including fuel and vehicle costs
C_m	Motor price

$\mathbf{c}_m$	Mean piston speed
$C_{m,man}$	Motor cost for the manufacturer
c_p	Specific heat capacity at constant pressure
c_r	Rolling friction coefficient
$\mathbf{c}_u$	Tangential flow velocity
C_v	Vehicle price
c_v	Specific heat capacity at constant volume
$\widehat{\delta p}_{ic}$	In-cylinder pressure gradient limit
Δt	Discrete time interval
d_{oc}	Pondered performance of fuel consumption and NO_x emissions used to compute η_{oc}
E_b	Battery stored energy
$E_{b,0}$	Battery nominal energy
e_{chem}	Specific energy of battery chemicals
E_{ice}	Engine delivered mechanical energy
$\widetilde{E}_{ice}$	Reference engine delivered mechanical energy
η_c	Compressor efficiency
η_{gb}	Gearbox efficiency
η_{ic}	Intercooler efficiency
η_{ice}	Engine fuel-to-torque efficiency
η_{ind}	Engine indicated efficiency
η_m	Motor efficiency
$\widetilde{\eta}_m$	Reference motor efficiency
η_{oc}	Efficiency of control strategy compared to Optimal Control performance
η_{ps}	Power-split device efficiency
η_t	Turbine efficiency
η_v	Engine volumetric efficiency
f	State dynamics function
F_a	Aerodynamic drag force
F_b	Braking force
$\widehat{F}_b$	Maximum braking force
F_g	Gravitational component of the drag force
F_i	Intertial force
F_n	Normal force of the vehicle
F_ω	Force induced by the moment of inertia of rotating masses

F_R	Force in the ring
F_r	Rolling friction force
F_S	Force in the sun
F_t	Traction force
$\mathbf{G}$	Gradient of the cost index of the NLP problem
g	Gravity acceleration
γ	Adiabatic index
Γ_f	Forwards control horizon
Γ_r	Receding control horizon
H	Hamiltonian
H_f	Fuel heat of combustion
H_i	Gas enthalpy at point i
h_{wall}	Cylinder walls heat transfer coefficient
$\mathcal{I}$	Constraint penalization quantity for DP
i_b	Battery current
$i_{b,cont}$	Maximum battery continuous discharge current
$i_{b,pulse}$	Maximum battery pulse discharge current
I_C	Moment of inertia of the carrier
$I_{clt,ds}$	Clutch moment of inertia at downstream disc
$I_{clt,us}$	Clutch moment of inertia at upstream disc
i_m	Motor current
I_ω	Moment of inertia of rotating masses
I_P	Moment of inertia of the planet
I_R	Moment of inertia of the ring
I_S	Moment of inertia of the sun
I_{tc}	Turbocharger moment of inertia
$\mathcal{J}$	Cost-to-go
$\mathbf{J}$	Jacobian of the NLP problem
J	Cost index
$\widetilde{\mathcal{J}}$	Approximate cost-to-go
k_i	Generic parameter
κ	Polytropic index
$\varkappa$	Powertrain size parameters to optimize

$\mathbf{L}$	Cost index of the NLP problem
L	Cost function
Λ	Interval of λ_0 candidates for λ_0^* calculation
λ	Lagrangian multiplier function
λ_e	Exhaust gas λ value
$\widehat{\lambda}_e$	Engine λ limit
$\bar{\lambda}_0$	Upper value of λ_0 for λ_0^* calculation
$\underline{\lambda}_0$	Lower value of λ_0 for λ_0^* calculation
λ_0	Costates initial value
m	Mass
m_b	Battery mass
$m_{b,1}$	Battery chemicals mass
$m_{b,2}$	Battery thermal management system mass
$m_{b,3}$	Battery tray mass
$m_{b,4}$	Battery buses, harnesses and terminals mass
m_{cha}	Vehicle chassis mass
$\dot{m}$	Variation of mass
$\dot{m}_c$	Compressor gas mass flow
$\dot{m}_{c,sp}$	Compressor gas mass flow setpoint
$\dot{m}_{egr}$	EGR valve gas mass flow
$\dot{m}_{ep}$	Exhaust port gas mass flow
$\dot{m}_f$	Fuel mass flow
$\dot{m}_{f,hp}$	Fuel mass flow from a test using HP-EGR only
$\dot{m}_{f,lp}$	Fuel mass flow from a test using LP-EGR only
$\dot{m}_{hpegr}$	HP-EGR gas mass flow
$\dot{m}_i$	Gas mass flow at point i
$\dot{m}_{ip}$	Intake port gas mass flow
$\dot{m}_{nox}$	NO_x mass flow
$\dot{m}_{nox,hp}$	NO_x mass flow from a test using HP-EGR only
$\dot{m}_{nox,lp}$	NO_x mass flow from a test using LP-EGR only
$\dot{m}_{O_2}$	Oxygen mass flow
$\dot{m}_{soot}$	Soot mass flow
$\dot{m}_t$	Turbine gas mass flow
$\dot{m}_{t,cor}$	Corrected turbine gas mass flow
m_f	Fuel mass
$\widetilde{m}_f$	Reference control strategy fuel consumption
m_i	Gas mass stored at reservoir i
m_{ice}	Engine mass

m_m	Motor mass
$m_{m,1}$	Motor electronics mass
$m_{m,2}$	Motor mechanicals mass
m_{nox}	Mass of generated NO_x
$\widehat{m}_{nox}$	NO_x generation mass limit
$\widetilde{m}_{nox}$	Reference control strategy NO_x emissions
m_{pm}	Mass of particulate matter
m_{soot}	Total generated soot mass
μ	Lagrangian multiplier scalar
μ_{clt}	Clutch friction coefficient
m_v	Mass of the vehicle
$\tilde{m}_v$	Corrected vehicle mass, including rotating masses moment of inertia
$\nabla\zeta$	State of Charge (SoC) gradient to correct deviation from target level
$N_{\mathbf{C}}$	Number of elements in constraint vector
n_c	Number of engine revolutions per cycle
n_{cyl}	Number of cylinders
$n_{\mathbf{DP}}$	Number of elements to store a generic DP problem
$N_{\mathbf{G}}$	Number of elements in gradient vector of the cost index
N_{gb}	Selected gear number
N_{ic}	Number of integral constraints
N_{ice}	Engine rotational speed
n_{inj}	Number of fuel injections
$N_{\mathbf{J}}$	Number of elements in Jacobian matrix
$n_{\mathcal{J}}$	Number of elements of the complete cost-to-go matrix
$N_{\mathbf{L}}$	Number of elements in cost index
N_λ	Number of costates or adjoined states to the cost function
n_{lc}	Life cycle of the vehicle
N_m	Motor rotational speed
$\widehat{N}_m$	Motor speed for switch from maximum torque to maximum power
N_{nz}	Total number of non-zero elements
N_{pc}	Number of path constraints

N_t	Number of time intervals the problem time span is divided into
n_t	Number of elements of discretized time span
N_u	Number of controls
$n_{\mathcal{U}}$	Number of elements to store the optimal control matrix
n_u	Number of elements of discretized control
$N_{\breve{u}}$	Number of integer controls
N_x	Number of states
n_x	Number of elements of discretized state
$N_{\breve{x}}$	Number of integer states
ω_C	Rotational speed of the carrier
$\omega_{clt,ds}$	Clutch rotational speed at downstream shaft
$\omega_{clt,us}$	Clutch rotational speed at upstream shaft
$\dot{\omega}_{clt,ds}$	Clutch rotational acceleration at downstream shaft
$\dot{\omega}_{clt,us}$	Clutch rotational acceleration at upstream shaft
$\omega_{gb,ds}$	Gearbox rotational speed at downstream shaft
$\omega_{gb,us}$	Gearbox rotational speed at upstream shaft
ω_{ice}	Engine rotational speed
ω_m	Motor rotational speed
ω_P	Rotational speed of the planet
$\omega_{ps,i}$	Power-split device rotational speed at the i shaft
ω_R	Rotational speed of the ring
ω_S	Rotational speed of the sun
ω_{tc}	Turbocharger rotational speed
$\widetilde{\omega}_{tc}$	Turbocharger corrected rotational speed
$\widehat{\omega}_{tc}$	Turbocharger rotational speed limit
σ	Exhaust gas opacity
p	Pressure
p_1	Atmospheric pressure
p_2	Intake manifold pressure
$p_{2,sp}$	Intake manifold pressure setpoint
p_3	Exhaust manifold pressure
$p_{3,0}$	Turbine inlet pressure at testing conditions
p_4	Turbine outlet pressure

P_b	Battery internal power supply
P_c	Compressor power
p_{clt}	Clutch contact pressure
P_e	Motor electrical power supply
$\widehat{P}_e$	Maximum battery power output
P_f	Fuel power
P_g	Electrical generator power
ϕ	Final value function
φ	Generic function
p_i	Pressure at point i
Π_c	Compressor pressure ratio
p_{ic}	In-cylinder pressure
P_{ice}	Engine power output
$\widehat{p}_{ic}$	In-cylinder pressure limit
$\widetilde{\Pi}_c$	Normalized compressor pressure ratio
Π_{cr}	Critical pressure ratio
Π_{egr}	EGR valve pressure ratio
Π_{srg}	Compressor surge limit pressure ratio
Π_t	Turbine pressure ratio
p_{ivc}	In-cylinder pressure at the intake valve closing
P_m	Mechanical motor power
$P_{m,n}$	Nominal motor mechanical power output
$\widetilde{P}_{m,n}$	Reference motor nominal power output
p_{mo}	In-cylinder pressure in motoring conditions
$\widetilde{P}_m$	Mechanical motor power reference trajectory
$P_{ps,i}$	Power-split device power i
$\mathbf{Pr}(\cdot)$	Probability distribution function
p_{rail}	Fuel rail pressure
$p_{rail,sp}$	Fuel rail pressure setpoint
Ψ_{egr}	EGR valve expansion factor
$\widetilde{\Psi}_{egr}$	Empirical approximation to EGR valve expansion factor
P_t	Turbine power
q	Integral constraint function
Q_b	Battery charge
q_b	Heat released during the combustion process
$Q_{b,0}$	Battery nominal charge
$\dot{Q}$	Heat flow
q_{wall}	Heat transfer to the cylinder walls

R	Ideal gas constant
$\mathbb{R}$	Subset of real numbers
r	Radius
R_b	Battery internal resistance
R_c	Engine compression ratio
$r_{clt,i}$	Clutch inner radius
$r_{clt,o}$	Clutch outer radius
R_{gb}	Gear ratio
ρ	Density
ρ_i	Gas density
$\lfloor \cdot \rceil$	Nearest integer function
r_P	Radius of the planet
$R_{ps,i}$	Power-split device ratio i
r_R	Radius of the ring
r_S	Radius of the sun
r_w	Wheel radius
$\mathcal{S}$	Total distance of the problem
s	Distance
ς	Engine pedal position
S_{year}	Distance covered with the vehicle per year
$\mathcal{T}$	Time duration of the problem
t	Time
τ_{egr}	Pure delay of EGR gas measurements
τ_{exh}	Pure delay of exhaust gas measurements
τ_{σ}	Pure delay of opacimeter measurements
T_C	Torque at the carrier
$T_{clt,ds}$	Clutch torque at downstream shaft
$T_{clt,us}$	Clutch torque at upstream shaft
$T_{gb,ds}$	Gearbox torque at downstream shaft
$T_{gb,us}$	Gearbox torque at upstream shaft
θ	Temperature
θ_{ad}	Adiabatic temperature of combustion
θ_{atm}	Atmospheric temperature
θ_{cf}	Cooling fluid temperature
θ_{ci}	Compressor inlet temperature
$\theta_{ci,0}$	Compressor inlet temperature at testing conditions

θ_{co}	Compressor outlet temperature
$\dot{\theta}_{em}$	Variation of exhaust manifold temperature
$\dot{\theta}_{im}$	Variation of intake manifold temperature
θ_{em}	Exhaust manifold temperature
$\theta_{em,0}$	Turbine inlet temperature at testing conditions
θ_{ep}	Exhaust port temperature
θ_{hpegr}	HP-EGR outlet temperature
θ_i	Temperature at point i
θ_{ic}	In-cylinder gas temperature
θ_{ico}	Intercooler outlet temperature
θ_{im}	Intake manifold temperature
θ_{ivc}	In-cylinder temperature at the intake valve closing
θ_{to}	Turbine outlet temperature
θ_{wall}	Cylinder walls temperature
t_i	Discrete time instant i
T_{ice}	Engine effective torque output
$\widetilde{T}_{ice}$	Prescribed engine torque trajectory
T_{ind}	Engine indicated torque
$\widehat{\mathcal{T}}$	Total time limit
T_{loss}	Engine torque losses
$\widetilde{T}_{loss}$	Torque losses of the reference engine
T_m	Motor shaft torque
$T_{m,max}$	Maximum motor shaft torque
$T_{ps,i}$	Power-split device torque i
T_R	Torque at the ring
T_S	Torque at the sun
T_w	Torque at the wheels
$\mathcal{U}$	Space of optimal controls in DP
$\boldsymbol{U}$	Space of permitted control candidates
U	Internal energy of a gas
$\mathbf{u}$	Vector of discretized control variables
$\mathbf{u}$	Discretized control variable
$\boldsymbol{u}$	Vector of control variables
u	Control variable
u_b	Brakes control
u_{bp}	Backpressure valve control

$\check{\mathbf{u}}$	Vector of discrete controls containing integer values
$\check{u}_{gb}$	Integer gear number trajectory
u_{clt}	Clutch control variable
$u_{\delta f}$	Fueling rate gradient control
$u_{\delta p}$	Fuel burning rate control that follows the maximum in-cylinder pressure derivative $\widehat{\delta p}_{ic}$
$u_{\delta soi}$	SOI difference with respect to factory SOI
$u_{\delta vgt}$	VGT gradient control
u_{egr}	EGR opening control
u_f	Fueling rate control
u_{fbr}	Fuel burning rate control
$u_{f,main}$	Fuel amount injected in main injection
$u_{f,piN}$	Fuel amount injected in pilot injection number N
$u_{f,poN}$	Fuel amount injected in post injection number N
u_{gb}	Gear number control
$\bar{u}$	Upper boundary for control
u_i	Specific internal energy of gas
u_{it}	Ignition timing control
$\underline{u}$	Lower boundary for control
u_{lphp}	EGR switching strategy control
u_p	Fuel burning rate control that follows the maximum in-cylinder pressure $\widehat{p}_{ic}$
u_{ps}	Power-split control
Υ	Motor scaling factor
u_{soi}	SOI control
$u_{soi,main}$	Main injection timing
$u_{soi,piN}$	Pilot injection number N timing
$u_{soi,poN}$	Post injection number N timing
u_{thr}	Throttle position demand
$u_{thr,egr}$	EGR bypass throttle position demand
$u_{thr,ic}$	Intercooler bypass throttle position demand
u_{vgt}	Turbine geometry control
u_{wg}	Waste gate control
V	Volume
v	Vehicle speed
v_0	Initial vehicle speed

ϱ	Heat transfer coefficient multiplier factor
V_b	Battery terminals voltage
V_d	Engine displacement
$\dot{v}$	Acceleration
V_{em}	Exhaust manifold volume
v_f	Final vehicle speed
v_i	Specific volume of gas
V_{ic}	In-cylinder volume
v_{ic}	In-cylinder specific volume
V_{im}	Intake manifold volume
V_{ivc}	In-cylinder volume at the intake valve closing
$\widehat{v}$	Vehicle speed limit
V_{oc}	Open circuit voltage
$V_{oc,0}$	Battery nominal open circuit voltage
W	Work
w_b	Boundary constraint weight
$\dot{\omega}_{tc}$	Turbocharger rotational acceleration
W_i	Indicated engine work
$\boldsymbol{x}$	Vector of state variables
$\mathbf{x}$	Vector of discretized state variables
$\mathbf{x}$	Discretized state variable
x	State variable
$\boldsymbol{x}_0$	Vector of initial state values
$\check{\mathbf{x}}$	Vector of discrete states containing integer values
$\dot{X}_{O_2}$	Variation of the oxygen mass fraction
$\dot{X}_{O_2,em}$	Variation of exhaust manifold oxygen mass fraction
$\dot{X}_{O_2,im}$	Variation of intake manifold oxygen mass fraction
x_f	Fueling rate control u_f expressed as an auxiliary state to the Optimal Control Problem (OCP)
ξ	State of Energy
X_{nox}	NO_x emissions fraction
X_{O_2}	Oxygen mass fraction
$X_{O_2,atm}$	Atmospheric oxygen mass fraction
$X_{O_2,c}$	Compressor oxygen mass fraction

$X_{O_2,em}$	Exhaust manifold oxygen mass fraction
$X_{O_2,ep}$	Exhaust port oxygen mass fraction
$X_{O_2,hpegr}$	HP-EGR oxygen mass fraction
$X_{O_2,im}$	Intake manifold oxygen mass fraction
x_{vgt}	Variable Geometry Turbine (VGT) position control u_{vgt} expressed as an auxiliary state to the OCP
y	Generic function
$\mathbb{Z}$	Subset of natural numbers
z	Height
ζ	State of Charge

Acronyms

ABS	Anti-lock Braking System
ADAS	Advanced Driver-Assistance Systems
ADP	Approximate Dynamic Programming
AFR	Air to Fuel Ratio
BFC	Before Factory Calibration
BFGS	Broyden-Fletcher-Goldfarb-Shanno
BPO	Bellman's Principle of Optimality
BVP	Boundary Value Problem
CAN	Controller Area Network
CI	Compression Ignition
CO	Carbon Monoxide
DC	Direct Collocation
DI	Direct Injection
DM	Direct Method
DMS	Direct Multiple Shooting
DOC	Diesel Oxidation Catalyst
DoE	Design of Experiments
DP	Dynamic Programming
DPF	Diesel Particulate Filter
DSS	Direct Single Shooting
ECMS	Equivalent Consumption Minimization Strategy
ECU	Engine Control Unit
ED	Eco-Driving
EGR	Exhaust Gas Recirculation
EM	Energy Management

EMP	Energy Management Problem
ESP	Electronic Stability Program
EU	European Union
EV	Electric Vehicle
EVO	Exhaust Valve Opening
FSN	Filter Smoke Number
GB	Gigabyte
GPS	Global Positioning System
HC	Hydrocarbon
HCCI	Homogeneous Charge Compression Ignition
HCLD	Heated Chemiluminescent Detector
HEV	Hybrid Electric Vehicle
HFID	Heated Flame Ionization Detector
HJB	Hamilton-Jacobi-Bellman
HP	High Pressure
HRL	Heat Release Law
ICE	Internal Combustion Engine
IM	Indirect Method
ISFC	Indicated Specific Fuel Consumption
IVC	Intake Valve Closing
IVP	Initial Value Problem
L-BFGS	Limited-memory Broyden-Fletcher-Goldfarb-Shanno
LP	Low Pressure
LTC	Low Temperature Combustion
MB	Megabyte
MEP	Mean Effective Pressure
MINLP	Mixed Integer Nonlinear Programming
MPC	Model Predictive Control
MVEM	Mean Value Engine Model
NDIR	Non-Dispersive Infrared
NEDC	New European Driving Cycle
NLP	Nonlinear Programming

NTC	Negative Temperature Coefficient thermistor
NVH	Noise, Vibration, and Harshness
OBD	On-Board Diagnostics
OC	Optimal Control
OCP	Optimal Control Problem
ODE	Ordinary Differential Equation
PDE	Partial Differential Equation
PEMS	Portable Emissions Measurement System
PHEV	Plug-in Hybrid Electric Vehicle
PID	Proportional-Integral-Derivative
PM	Particulate Matter
PMP	Pontryagin Minimum Principle
PMSM	Permanent Magnet Synchronous Machine
PWM	Pulse-Width Modulation
RAM	Random-Access Memory
RDE	Real Driving Emissions
RE	Range Extender
SCR	Selective Catalytic Reduction
SDP	Stochastic Dynamic Programming
SFC	Specific Fuel Consumption
SI	Spark Ignition
SoC	State of Charge
SoE	State of Energy
SOI	Start of Injection
SQP	Sequential Quadratic Programming
TB	Terabyte
TDC	Top Dead Center
VGT	Variable Geometry Turbine
VVT	Variable Valve Timing
WLTC	Worldwide harmonized Light vehicles Test Cycle

Operators

*	Optimal trajectory
Δ	Increment
δ	Finite difference
d	Differential
∇	Gradient
∂_y	Partial derivative with respect to variable y
^{T}	Transpose

Part I

Thesis overview

Chapter 1

Introduction

If you don't know where you are going, any road will get you there.

— Lewis Carroll

Contents

1.1 Background

There is a general rule in engineering: first, things must work; afterwards, things must work better; and then, things must work in the best way. This is the common timeline of the evolution of any technology, and the history of the automobile is a particularly good example. In 1886, Karl Benz patented the world first production vehicle: the Benz Patent-Motorwagen. Benz's goal was to make a working self-moving vehicle, but outperforming any existing transportation mean was, of course, out of his expectations. It just worked and that was fine at that time. Later, many technological advances were progressively introduced. Porsche gave birth to the first Hybrid Electric Vehicle (HEV) in 1898, the Lohner-Porsche Mixte Hybrid; drum brakes were introduced by Renault in 1902; gasoline direct injection was devised by Leon

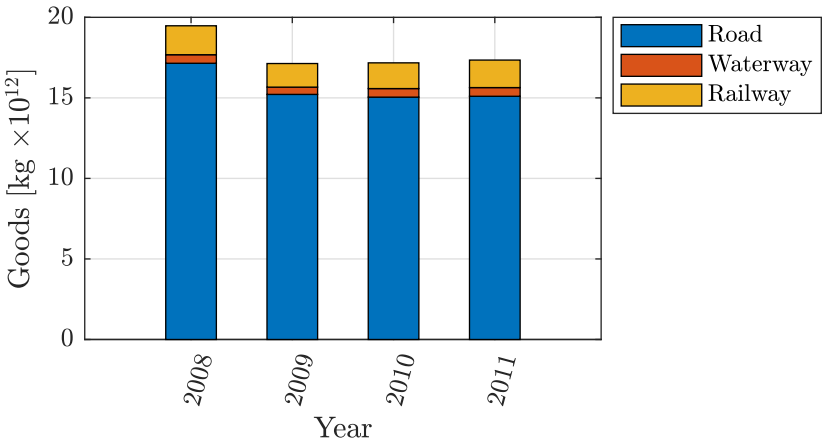

Figure 1.1: Gross amount of goods transported in the EU by road, waterway and railway. Source: [3].

Levavasseur also in 1902; hydraulic brakes were invented by Malcolm Loughead in 1919; first automatic transmission was conceived by Hermann Rieseler in 1924; the Mercedes-Benz 380 embodied independent suspension in 1933; self-leveled suspension was introduced by Citroën in 1954; and first turbocharged car, the Oldsmobile Jetfire, came into production in 1962, among other inventions. That was a time of making better engines and vehicles [1, 2]. The modern era is characterized for cutting-edge advances, pushing current technologies to their limits. Electronics, computer-aided design and a much better understanding of internal engine processes has brought a technology that approaches to the best way vehicles can be conceived. However, it is not over and Internal Combustion Engine (ICE) technology has still quite more room for improvement. Novel and promising advances are yet to come. In the current scenario, automotive industry is moving not only towards a higher standardization for reduced development time an improved economy, but also to higher efficiency, better performance and lower pollutant emissions, which unavoidably carries a significant increase in technology complexity.

Transportation is key for the world economy since it gives opportunities for economic development, social benefits, health and safety. It is the cornerstone of globalization and markets share in a world where everything is connected. Transportation and logistics entail a significant part of the final price of goods, affecting to economy in every single aspect. Road vehicles play a major role as 87% of goods were carried by road in the European Union (EU) in the 2008–2011 period, as shown in figure 1.1.

Vehicles are also responsible of a significant portion of the energy share.

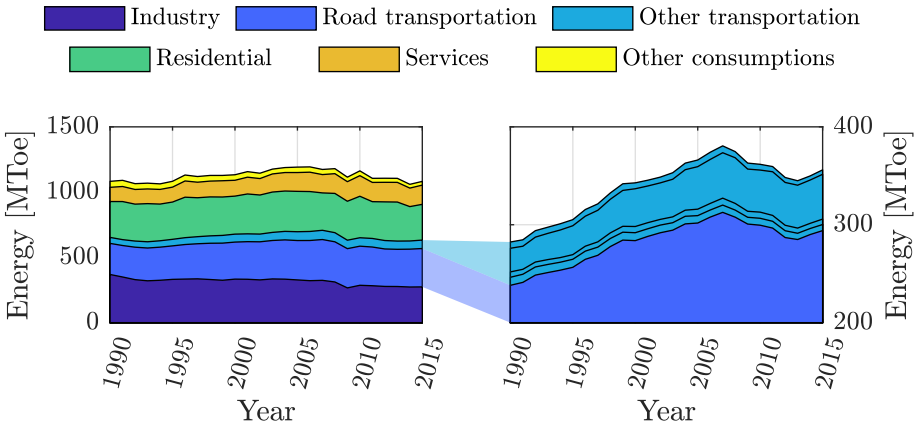

Figure 1.2: Energy consumption share (in mega tonnes of oil equivalent) in the EU during the 1990–2015 period. The left plot shows, from bottom to top, the contribution of industry, road transportation, other transportation means, residential, services and other types of energy consumption. The right plot shows a disaggregation of transport sector with, from bottom to top, road, rail, domestic aviation, international aviation and waterways energy consumption. Source: [3].

According to Eurostat data [3]–shown in figure 1.2–transportation takes around 30% of the total energy consumption in the EU, with industry and residential consumption at similar levels. Road transportation is responsible of 83% of the total transport energy consumption [3].

The penetration of vehicles in society is a sign of economical and social development. Motorization indices–vehicles per inhabitant–are rapidly growing in developing economies and the expectations are that those numbers will keep on rising. Countries such as China are experiencing a significant increase in vehicle registration as a consequence of the expanding economy, showing motorization rates of 20–40%/year, as shown in figure 1.3.

Due to the expansion of vehicle market, environmental issues are a major drawback. During the last decade the pollution in highly populated cities has been a critical issue that have forced local governments to take immediate actions such as banning diesel vehicles in inner cities, restricting traffic entrance by license plate, or limiting the number of yearly vehicle registrations. This scenario has brought some interesting solutions such as the use of Electric Vehicles (EVs) and HEVs in urban areas [6] or car sharing [7].

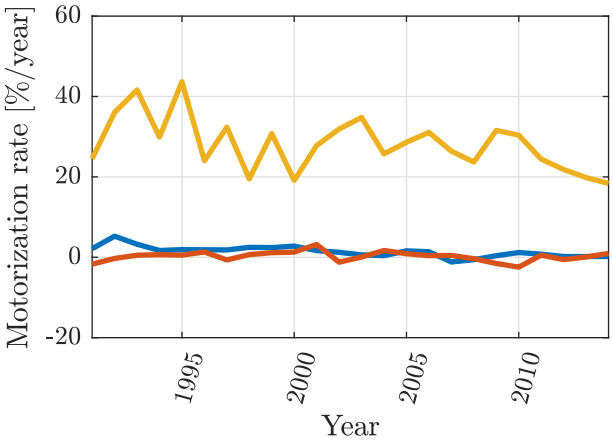

Figure 1.3: Motorization rates (growth rate of passenger vehicles) for the euro area (blue), USA (red) and China (yellow). Note that despite the high motorization rate, China is still far from western countries indices. In 2014 the euro area, USA and China showed 520, 816 and 80 vehicles per 1000 inhabitants respectively. Sources: [3–5].

1.2 Emissions regulation in automotive industry

The combustion of fossil fuels for road transportation entailed 21% of total CO_2 emissions in 2014. Passenger vehicles are responsible of a 61% of total road transportation CO_2 generation [3]. Greenhouse gas emissions effects on climate change and human health are well known, and their reduction are on the agenda of many governments and on the roadmap of the Kyoto Protocol. During the last decades the EU took actions in order to limit the generation of pollutants emissions, achieving a significant decrease as it may be appreciated during the 1990–2014 period in figure 1.4, and the target is to lessen these figures in the near future with more stringent regulations. Pollution in major cities have become a critical issue for local governments and, despite a reduction is visible between 2008 and 2014 (see right plot in figure 1.4), numbers are still alarming as respiratory diseases are becoming more frequent in highly populated and congested cities.

The fact is that road transportation and, especially passenger vehicles, contribute to a significant part of pollutant emissions–13% in the EU in 2014. These current environmental issues require an emissions regulation framework to promote cleaner vehicles. This is the target of emission standards that have been adopted during the last decades in many countries, becoming more stringent along the years in an attempt to tackle the global environmental

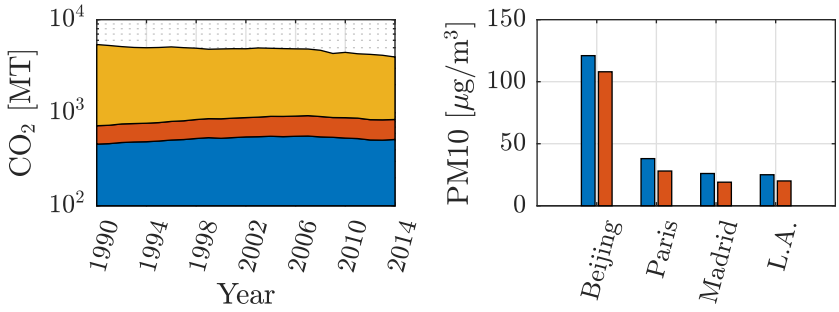

Figure 1.4: Pollutant trend during last years. On the left, passenger vehicles (blue) are responsible of 61% of gross road transportation CO_2 emissions (red) and 13% of total EU emissions (yellow) in 2014. On the right, 10 microns particulate matter measurements in major cities are shown for 2008 (blue) and 2014 (red). Sources: [3, 8, 9].

issues. These standards impose limits on several pollution agents for a vehicle to be approved and entails a big challenge for the automotive industry. For example, NO_x emission standards in the EU have fallen from 500 mg/km with Euro 3 standard–Euro 1 and Euro 2 did not impose any limit–to 80 mg/km for Compression Ignition (CI) vehicles with Euro 6. Past and current limits of Euro standards are shown in figure 1.5, illustrating the swift movement to cleaner technologies. Other current standards are EPA Tier 3 (US), CARB LEV III (California) or Japanese regulations; many countries stick to current or past EPA or Euro standards [10].

The approval procedure for the Euro standards has been criticized because it is not representative of actual driving conditions [11]. The procedure consists of a prescribed driving cycle, the New European Driving Cycle (NEDC), which is simulated in a rolling test bench under a number of different conditions. This cycle, last updated in 1997, shows smooth accelerations and a poor diversity of operating conditions. Due to the predictability of this procedure, engine control and vehicles can be calibrated to best perform in this cycle and not in the road, which is not the goal of emission regulations. These drawbacks lead to dirtier vehicles on the road with higher fuel and emission levels [12]. In fact, during the last years real pollutant emissions shows no significant improvements on real driving despite the stricter standards [13]. To this effect, the EU has adopted a new driving cycle, the Worldwide harmonized Light vehicles Test Cycle (WLTC) [14], expecting to reduce discrepancy between approval and real emissions. However, some weakness have already been pointed out [15] and probably many other will be discovered and exploited by manufacturers. For this reason, Real Driving Emissions (RDE) with Portable

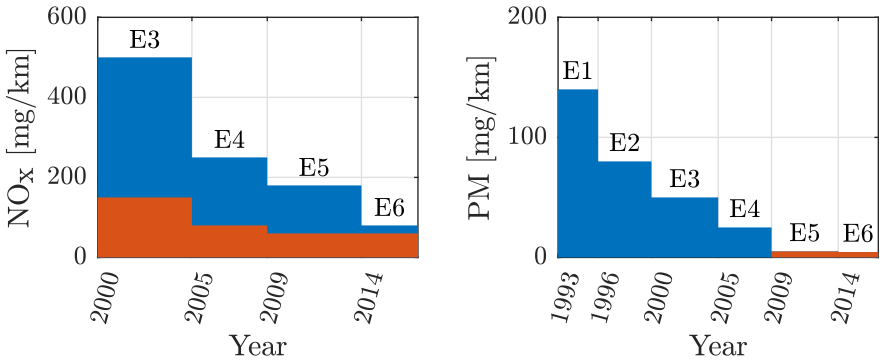

Figure 1.5: Pollutant limits of past and current Euro standards for CI (blue) and SI (red) vehicles. Note that NO_x limits were introduced with Euro 3–former standards set a limit of combined NO_x+HC emissions–and PM are only regulated since Euro 5 for SI engines.

Emissions Measurement System (PEMS) [16] is to be adopted as an alternative to assess a real evaluation of emissions performance. These tests are scheduled to be introduced with Euro 6d and consist of a trip that lasts between 90 and 120 minutes, composed of urban (34%), rural (33%) and highway (33%) roads with several speed constraints [17]. These tests entail an important challenge for manufacturers as vehicle design and control strategies become more complex.

Emission standards have a strong impact on engine and control design. In order to assess the stricter regulations, engine technology has become much more complex with sophisticated controls and numerous peripherals improving emissions performance. These new challenges can be faced with two main approaches: limiting the tail pipe emission of the generated pollutants or reducing the level of pollutants formation during the combustion. The first is generally achieved with efficient–but expensive–after-treatment systems such as Diesel Oxidation Catalyst (DOC), Diesel Particulate Filter (DPF) or Selective Catalytic Reduction (SCR), that promotes chemical reactions reducing the amount of pollutants or impose physical barriers to the emission of harmful gases. The latter is addressed in several ways:

- Introducing new engine technologies, such as downsizing, new combustion modes, sophisticated forced induction systems, dual-loop Exhaust Gas Recirculation (EGR), improved injection systems, or Variable Valve Timing (VVT) among many others. These are aimed to find a better balance between the improvement of the engine thermodynamic efficiency–less fuel means less CO_2–and the reduction of the combustion

temperature, reducing NO_x emissions at the expense of penalizing the combustion efficiency.

- Alternative powertrain schemes, mainly HEV, EV and fuel cell vehicles. These exploit alternative energy sources reducing–or eliminating–the impact of the ICE in emissions performance.

- Sophisticated control strategies, making use of additional sensors–in-cylinder pressure measurements–, or different control schemes, such as Model Predictive Controls (MPCs) or Optimal Control (OC), maximizing the benefits of a given engine technology.

1.3 Control role in vehicular systems

Engines are intrinsically connected to control. Without it, an engine would be a quiet piece of engineering. It has been like that since Nicolaus Otto made his first prototype. As long as there are decisions to take or things to regulate in a system, control is unavoidably necessary. Although control is always somehow involved, its importance is up to the level of perfection to be achieved, *i.e.* how good is the system performing compared to the best it can perform–this is a pretty good definition of OC. Generally, the more exhaustive the control task is, the better the performance results.

Traditionally, control has not been always the priority. During the early years of the automobile the main concern was to make things work. Later, fuel was so cheap that control was just a question of making comfortable vehicles with good performance. Efficiency was not critical and efforts in that direction were limited.

In 1970s the energy crisis changed the scenario. Not only efficiency but also pollutant emissions became the main concerns in engine development. The growth of electronics that came across at the beginning of the 1980s and the new demanding scenario were the critical factors that brought control to its current importance. Control has experienced an enormous growth in complexity during the last decades, and nowadays it is a main concern for manufacturers and object of numerous studies and new approaches [18].

Engine control requirements are increasingly demanding. Like it shows in figure 1.6, the necessary calculation resources to compute the engine control has grow rapidly in the last decades and the expectation is to raise much faster in the next years. The typical approach in today's engines is mainly based on calibrated maps that contain control setpoints as a function of volatile variables. These setpoints are interpolated according to current sensor readings and estimations, and corrected for dynamic transients. This type of

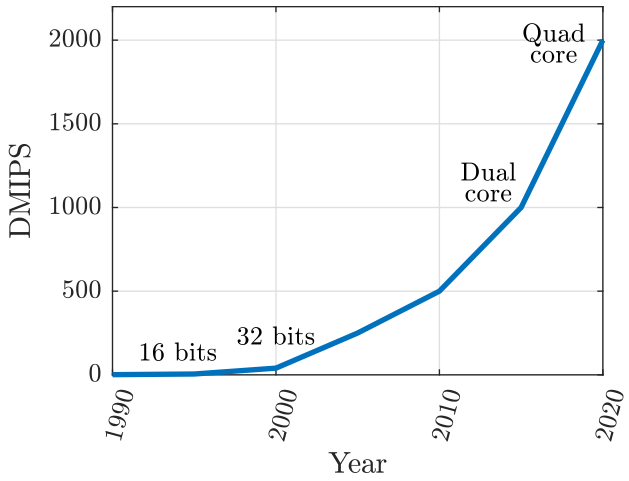

Figure 1.6: Past, current and expected engine control requirements for processor architectures performance in Dhrystone million of instructions per second. Source: [22].

control is predictable and robust thanks to the extensive heuristic knowledge in this field. However, it requires lots of experiments for a single calibration to be done. Automated calibration frameworks [19], model-based [20] and self-tuning calibrations [21] have been proposed to address this costly and time demanding solution.

Not only engines are the target for control applications. It plays an important role in many automotive devices such as automatic transmission, cruise control, automatic parking, battery management, HEV energy management, and the–yet to come–autonomous vehicle.

OC is a branch of control theory that is raising interest. Briefly, it consists of mathematical methods that guarantee optimality–for a specific target–of the behavior of the controlled system. It has important contributions in other fields of engineering such as aviation [23], aerospace [24] and automated trains [25]. However, its acceptance in the automotive industry is moderate for several reasons: in first place, the proper definition of the problem to address and the required boundary conditions for a practical use of OC theory is difficult; second, the computational burden that OC requires was out of the hardware capabilities in the past; and third, there have been no special needs for OC as long as traditional approaches perform sufficiently good for the current requirements–but that might change in the future.

OC is promising for novel and recent technologies such as autonomous vehicles [26]. It outperforms traditional control approaches in many fields and

it might be a question of time that the automotive industry–reticent to big changes but subject to great challenges–starts adopting OC concepts.

1.4 Objectives

This dissertation aims to extend the current development of applied OC in the automotive field, particularly on the powertrain side. Applications are analyzed for three different scenarios: onboard control application, OC for benchmarking and analysis of powertrains, and OC for designing purposes. Current state-of-the-art mathematical methods and algorithms are exploited for engine and powertrain control, providing experimental measurements and validation in cases where testing facilities are available. The analyzed applications comprise the control of engine acutators–replacing the Engine Control Unit (ECU) role–, vehicle and speed control, energy management of HEVs, dual-loop EGR control, fuel injection system design and powertrain sizing, all addressed with an OC approach.

The specific objectives that this dissertation attempts to cover are:

- Exploration of the OC potential in automotive applications, especially in engine and powertrain control, analyzing current state-of-the-art advances (chapter 2).
- Identification of OC advantages in engine control in order to assess both fuel and emissions savings for a given engine technology (chapter 6).
- Examination of energy inefficiencies in a vehicle at different levels in order to identify potential room for improvement from a control point of view, with the ultimate target of covering a distance in a specified time (chapter 7).
- Proposal of a technique for a practical implementation of OC in HEVs energy management with no look-ahead information and near-optimal performance (chapter 8).
- Providing of tools and methods to benefit from OC in benchmarking and designing tasks such as fuel injection scheduling and powertrain components sizing (chapter 9).

1.5 Methodology

This dissertation is structured in four main parts: (i) an overview of current OC, (ii) tools that have been used and developed for the works presented

here, (iii) practical cases and their results, and (iv) main conclusions. The philosophy is quite straightforward. First, a powertrain model is developed and the corresponding testing facility is provided. Then, an OCP is stated, describing the control objective–generally the minimization of fuel consumption subject to emission constraints. Finally, the formulation and implementation of this OCP is detailed, and simulation or experimental results are shown. This methodology is followed in chapters 6 to 9. For the ease of clarity, the dissertation organization is given below.

1.5.1 Dissertation organization

Chapter 1 has introduced the current scenario for the automotive industry. A brief journey on the social awareness in fuel economy and pollutant emissions reduction across the last decades has presented the root of current and future emission standards. The control role for automotive applications and, more particularly, in powertrain management has been reviewed emphasizing the importance of new control schemes and methodologies to assess future stringent regulations, bringing OC to the stage as a promising solution that motivates this dissertation.

Chapter 2 analyzes the current state-of-the-art advances in OC. First, the OC mathematical background is introduced with a basic definition of the OCP, which is a recurrent concept throughout this work. Second, past and current studies focused to the vehicle control and Advanced Driver-Assistance Systems (ADAS) are reviewed. Traditional cruise control approaches are compared to the most recent works that propose optimal and model-based predictive controls. The novel concept of eco-driving is introduced pointing out the most interesting advances in vehicle speed control and driver advising systems. Third, a comprehensive review of OC in powertraing management is issued. Optimal engine calibration, self-tuning controls, variable calibrations and the direct application of OC theory in engine control are under review. A historical journey through the prolific field of energy management in HEVs shows the most relevant works and the evolution of the OC application in this topic. Finally, the current scenario in OC applied to powertrain design is analyzed.

Then, the necessary tools to apply OC are presented and developed in chapters 3, 4 and 5.

Chapter 3 introduces to the OC theory with some mathematical formalisms. The mathematical theory and its properties are described from a practical point of view. The main three families of OC methods–according to [27]–are introduced and their performance and advantages are analyzed. These methods are: (i) the Hamilton-Jacobi-Bellman (HJB) equation and its numerical

implementation, the Dynamic Programming (DP), (ii) indirect methods, which are derived from the HJB equation, and the well known Pontryagin Minimum Principle (PMP), and (iii) direct methods, with a brief review of the different approaches in literature, emphasizing in the direct collocation methodology. These methods are applied to the works presented in this dissertation and their corresponding algorithm implementations are also detailed in this chapter.

Chapter 4 describes the mathematical models used in this work. Due to the diverse objectives of this dissertation, models describing the powertrain components are supplied. Vehicle dynamics are addressed with a longitudinal dynamic model. The transmission model includes a quasi-steady gearbox, a dynamic clutch coupling, and several models of power-split devices. Electrical path models are included for HEVs, comprising the electric motor and the batteries. Finally, the ICE is modeled with an airpath Mean Value Engine Model (MVEM) and a quasi-steady cylinder model experimentally validated. A quasi-steady version of the engine model is also described in this section.

Chapter 5 pictures the four experimental facilities that have been used for the works in this dissertation. These setups are: (i) a 4-cylinder Direct Injection (DI) CI turbocharged engine, (ii) an in-house developed single cylinder engine, (iii) a conventional passenger vehicle, and (iv) a hybrid powertrain with a Range Extender (RE). Specifications and instrumentation for these setups are also provided. In the second part of this chapter, the test campaigns that have been issued to validate both models and proposed control approaches are detailed.

From chapter 6 to 9, several OC case studies are applied and discussed. According to the target of the OC approach, these works can be divided in: (i) ideal cases with known problem boundaries–where rigorous OC can be applied–in chapter 6, (ii) applied cases without certain problem boundaries–near-optimal strategies are derived from OC–in chapters 7 and 8, and (iii) laboratory cases where OC is used as a benchmark or assessment tool, in chapter 9.

Chapter 6 presents two control approaches to apply OC in engine management for given engine speed and torque trajectories. The first work addresses the optimal split between High Pressure (HP)- and Low Pressure (LP)-EGR for a dual-loop EGR system at the NEDC cycle. A control strategy is developed from the OC framework and is experimentally validated. The second part of this chapter addresses the control of engine actuators–fueling rate, Start of Injection (SOI), EGR position and VGT opening–with an OC method, replacing the ECU control for a given driving cycle. Experimental results and the analysis of fuel efficiency and emissions performance for an actual driving

cycle are also provided. A Pareto analysis is issued to study the optimal tradeoff between fuel economy and NO_x emissions.

Chapter 7 discusses the importance of an appropriate speed control of a vehicle and its impact on the engine control. A joined vehicle speed and engine actuators control is performed with the OC techniques from the previous chapter. The performance of the control in a real route and its effect on both driving and engine efficiency are reviewed.

Chapter 8 addresses the optimal power-split of a HEV among its two energy sources: the fuel tank and the battery. The contribution of this approach is a methodology to provide an onboard-capable algorithm that does not require look-ahead information for a near-optimal performance. The methodology is based on the PMP and a stochastic analysis of past driving requirements on a receding horizon, providing the likelihood-based optimal control.

Chapter 9 extends the previous OC studies to assess the design of a powertrain. OC is used to explore the boundary efficiency of the powertrain to provide an objective criterion for two designing scenarios. On the one hand, OC is applied to analyze the fuel injection scheduling based on the optimal Heat Release Law (HRL) that can be calculated for maximum pressure, maximum pressure derivative and NO_x constraints. On the other hand, the optimal sizing of a HEV powertrain devices–engine, motor and battery–is addressed from an economical point of view, minimizing lifetime costs. This is issued for city and highway driving cycles in order to find the effect on the powertrain size of driving conditions.

Chapter 10 finalizes this dissertation with a summary of the conclusions and main findings that have been collected in previous chapters. Interesting facts and challenges are discussed for future works.

References

[1] E. H. Wakefield. *History of the electric automobile-hybrid electric vehicles.* Vol. 187. Society of Automotive Engineers, 1998.

[2] G. Constable and B. Somerville. *A century of innovation: Twenty engineering achievements that transformed our lives.* Joseph Henry Press, 2003.

[3] *Energy, transport and environment indicators, 2016 edition.* Eurostat, European Union. 2016.

[4] S. C. Davis, S. E. Williams, and R. G. Boundy. *Transportation energy data book: Edition 35.* Tech. rep. Oak Ridge National Laboratory, 2016.

[5] N. B. of Statistics of China. *China Statistical Yearbook 2015.* 2015.

[6] C. E. S. Thomas. "Transportation options in a carbon-constrained world: Hybrids, plug-in hybrids, biofuels, fuel cell electric vehicles, and battery electric vehicles". In: *International Journal of Hydrogen Energy* 34.23 (2009), pp. 9279–9296.

[7] R. Katzev. "Car sharing: A new approach to urban transportation problems". In: *Analyses of Social Issues and Public Policy* 3.1 (2003), pp. 65–86.

[8] *WHO global urban ambient air pollution database, update 2011*. World Health Organization. 2011.

[9] *WHO global urban ambient air pollution database, update 2016*. World Health Organization. 2016.

[10] T. V. Johnson. "Vehicular emissions in review". In: *SAE International Journal of Engines* 7 (2014), pp. 1207–1227.

[11] J. Demuynck et al. "Recommendations for the new WLTP cycle based on an analysis of vehicle emission measurements on NEDC and CADC". In: *Energy Policy* 49 (2012), pp. 234–242.

[12] P. Mock et al. *Discrepancies between type-approval and "real-world" fuel-consumption and CO*. Tech. rep. International Council on Clean Transportation, 2012.

[13] P. Mock et al. *From laboratory to road*. Tech. rep. 30. International Council on Clean Transportation, 2013.

[14] M. Tutuianu et al. *Development of a world-wide worldwide harmonized light duty driving test cycle (WLTC)*. Tech. rep. WLTP DHC Chair, 2013.

[15] L. Sileghem et al. "Analysis of vehicle emission measurements on the new WLTC, the NEDC and the CADC". In: *Transportation Research Part D: Transport and Environment* 32 (2014), pp. 70–85.

[16] M. Weiss et al. "Will euro 6 reduce the NOx emissions of new diesel cars?–insights from on-road tests with portable emissions measurement systems (PEMS)". In: *Atmospheric Environment* 62 (2012), pp. 657–665.

[17] The European Comission. *Comission regulation (EU) 2016/427 of 10 March 2016 amending regulation (EC) No 692/2008 as regards emissions from light passenger and commercial vehicles (Euro 6)*. 2016.

[18] F. Payri et al. "A challenging future for the IC engine: New technologies and the control role". In: *Oil & Gas Science and Technology – Revue d'IFP Energies nouvelles* 70.1 (2015), pp. 15–30.

[19] H. Stuhler et al. "Automated model-based GDI engine calibration adaptive online DoE approach". In: *SAE Technical Paper*. 2002.

[20] S. Jiang, D. Nutter, and A. Gullitti. "Implementation of model-based calibration for a gasoline engine". In: *SAE Technical Paper*. 2012.

[21] E. Hellström et al. "On-board calibration of spark timing by extremum seeking for flex-fuel engines". In: *IEEE Transactions on Control Systems Technology* 21.6 (2013), pp. 2273–2279.

[22] H. Xie et al. "Future engine control enabling environment friendly vehicle". In: *SAE Technical Paper*. 2011.

[23] P. Hagelauer and F. Mora-Camino. "A soft dynamic programming approach for on-line aircraft 4D-trajectory optimization". In: *European Journal of Operational Research* 107.1 (1998), pp. 87–95.

[24] P. J. Enright and B. A. Conway. "Optimal finite-thrust spacecraft trajectories using collocation and nonlinear programming". In: *Journal of Guidance, Control and Dynamics* 14.5 (1991), pp. 981–985.

[25] X. Yang et al. "A survey on energy-efficient train operation for urban rail transit". In: *IEEE Transactions on Intelligent Transportation Systems* 17.1 (2016), pp. 2–13.

[26] P. Falcone et al. "Predictive active steering control for autonomous vehicle systems". In: *IEEE Transactions on Control Systems Technology* 15.3 (2007), pp. 566–580.

[27] M. Diehl et al. "Fast direct multiple shooting algorithms for optimal robot control". In: *Fast motions in biomechanics and robotics*. Springer, 2006, pp. 65–93.

Chapter 2

State of the art in automotive optimal control

If I have seen further than others, it is by standing upon the shoulders of giants.

— Isaac Newton

Contents

2.1 General overview

When managing a dynamic system to deliver a given task, it seems very convenient to do it in the very *best* way among all the possible ways it can be done. The term *best*–which might seem vague in this context–could resemble

to *cheapest*, not only in the economic sense but also in a general way. Of course the ability to guarantee that a system acts in such an optimal way is not a trivial nor an easy problem. The OC approach is to transform this wish into a mathematical problem where the concept *best* is translated into a quantity–the cost index–to be minimized, constrained to the dynamic response of the system and the particular limitations of the job to be done [1]. This mathematical problem is known as an OCP.

OC theory originated in the 1950s with the advances of Lev Pontryagin [2] and Richard Bellman [3]. It brings together the mathematical methods, properties, conditions and algorithms that allow to–at least–approach an OCP. The goal of this theory is to serve as a tool to find the time trajectories of the system controls such that the operation cost is minimum. The drawback is that the fundamental OC theory is a set of mathematical properties and not a bundle of optimization methodologies. In [4], Vinter wrote about this fact,

> The truth is, solving optimal control problems of scientific or engineering interest is often extremely difficult. Analytical tools of Optimal Control, such as the Maximum Principle, provide equations satisfied by minimizers. They do not tell us how to solve them or, if we do succeed in solving them, that the "solutions" are the right ones.

Fortunately, there exist many methodologies in literature that make use of OC theory to solve OCPs with numerical methods [5] or benefiting from some particular properties of the problem [1, 6] (see section 3).

OC has been a field of interest in engineering for many decades, but the reduced calculation resources from the early years limited the chances of applying such demanding methods to simple approaches. However, the advances in computational capabilities from the last decades and the existence of sophisticated state-of-the-art numerical solvers made possible the successful application of OC to many engineering fields. Some examples are: aerospace orbit transfers [7], aviation trajectory planning [8], railway control [9] or robotics applications [10].

The automotive field is not an exception. The increase of engine and powertrain complexity, the growth of electronic controls and devices, and autonomous vehicles, among others, made OC especially interesting to address the technological challenges that are to be faced.

In this chapter, the reader may find a brief introduction to the mathematical apparatus that founds the basics of OC (section 2.2), followed by the main works and trends of OC that have been developed in the automotive field

literature, divided by topics: cruise control and eco-driving (section 2.3), powertrain management (section 2.4) and design applications (section 2.5).

2.2 Mathematical introduction to optimal control

Formally, an OCP is a mathematical problem that consists in finding the trajectories of the control variables (quantities to be directly controlled) of a dynamic system such that a cost index is minimized [6]. The cost index is an scalar value that quantifies the magnitude to be optimized, such as energy consumption, economic cost of operation, traveled distance or time spent during a process, to give some examples. Accordingly, the trajectories are optimal when the cost is minimum. A general cost index can be written in terms of states $\boldsymbol{x}$ (variables that determine the condition of the system in a particular time) and control variables $\boldsymbol{u}$ as the integral of a cost function L, known as Lagrangian, over the time:

$$J = \int_0^{\mathcal{T}} L(\boldsymbol{x}, \boldsymbol{u}, t)\,\mathrm{d}t \tag{2.1}$$

where $0 \leq t \leq \mathcal{T}$ is the span of the problem. The cost function L represents the instantaneous cost of operation of the system. An additional term including a penalization on the terminal state of the problem may be also included. The aim of the OCP is to minimize this optimality criterion:

$$J(\boldsymbol{x}^*, \boldsymbol{u}^*, t) = \min_{\boldsymbol{u}}\{J\} \tag{2.2}$$

Note that an asterisk denotes an optimal trajectory.

The states of the dynamic system are driven by Ordinary Differential Equations (ODEs):

$$\dot{\boldsymbol{x}} = f(\boldsymbol{x}, \boldsymbol{u}, t) \tag{2.3}$$

The system generally starts with a set of prescribed states at $t = 0$. Thus, we arise with an Initial Value Problem (IVP):

$$\boldsymbol{x}(0) = \boldsymbol{x}_0 \tag{2.4}$$

Usually the system is also constrained to reach a particular set of states–or a function of the states–at $t = \mathcal{T}$, resulting in a Boundary Value Problem (BVP):

$$\phi(\boldsymbol{x}(\mathcal{T})) \leq 0 \tag{2.5}$$

In addition to the above boundary constraints, the system may be completed with two more kind of constraints: the path constraint, which defines a time varying quantity c that the system must not exceed:

$$c(\boldsymbol{x}, \boldsymbol{u}, t) \leq 0 \tag{2.6}$$

and the integral constraint, which specifies a limit to the accumulation of the quantity q:

$$\int_0^{\mathcal{T}} q(\boldsymbol{x}, \boldsymbol{u}, t)\, \mathrm{d}t \leq 0 \tag{2.7}$$

Note that the inequality from any of the above constraints can be replaced by the corresponding equality constraint if required with no loss of generality.

Therefore, eqs. (2.1)–(2.7) define a general OCP [6]. The next task to state an OCP is to model the system to particularize the above equations (see chapter 4).

2.2.1 Considerations on constraints treatment

The constraints stated in eqs. (2.3)–(2.7) are also known as *hard* constraints since a solution must fulfill all of them to be accepted as a feasible solution to the problem. Alternatively, some of them can be interchanged with *soft* constraints–adjoining the constraints to the cost index with a weighting factor as a penalization. The term *soft* refers to the slackness of these constraints since a solution would be feasible even not fulfilling the former *hard* constraints. However, the trick remains on the fact that there is a value for the weighting factor such that the problem fulfills the *hard* constraint and, then, the problem is equivalent to the original one. It is basically a tradeoff between *hard* constraints and additional unknowns–weighting factors–, which can reduce problem complexity in some situations. Of course, there is an extensive mathematical artifact behind this idea, but for the sake of practicality it will be partially simplified in the following sections. A comprehensive development of this formulation may be found in [6, 11].

The terminal constraint (2.5) can be adjoined to the cost index with a weighting parameter w_b:

$$J = w_b \phi(\boldsymbol{x}(\mathcal{T})) + \int_0^{\mathcal{T}} L(\boldsymbol{x}, \boldsymbol{u}, t)\, \mathrm{d}t \tag{2.8}$$

Given that $\phi(\boldsymbol{x}(\mathcal{T})) \leq 0$, the minimization of this term is more relevant to the optimal solution as the weight w_b is more negative. On the limit, $J^* = \min_{\boldsymbol{u}} \{\phi(\boldsymbol{x}(\mathcal{T}))\}$ for a sufficiently negative w_b, and for $w_b = 0$ $J^* =$

$\min_{\boldsymbol{u}} \left\{ \int_0^{\mathcal{T}} L(\boldsymbol{x}, \boldsymbol{u}, t)\, \mathrm{d}t \right\}$, regardless of $\phi(\boldsymbol{x}(\mathcal{T}))$ value. For continuity reasons there is a value ${w_b}^* \in (-\infty, 0]$ such that $\phi(\boldsymbol{x}(\mathcal{T})) = 0$ for the optimal solution– $\phi(\boldsymbol{x}(\mathcal{T})) < 0$ is not interesting as this constraint would not be active at the problem. Given the appropriate ${w_b}^*$, the set of $\boldsymbol{x}$ and $\boldsymbol{u}$ trajectories that minimize this augmented cost index J also minimize the integral term and, therefore, they are the optimal solution of the original OCP [6].

Path constraints (2.6), integral constraints (2.7) and system dynamics (2.3) may be adjoined to the cost index with an augmented cost function of the problem H, also known as Hamiltonian:

$$H(\lambda, \boldsymbol{x}, \boldsymbol{u}, t) = L(\boldsymbol{x}, \boldsymbol{u}, t) + \lambda^T(t) y(\boldsymbol{x}, \boldsymbol{u}, t) \tag{2.9}$$

with $y = \{f, c, q\}$ and λ a vector of Lagrangian multipliers also known as costates. The above statement is a direct result of the *calculus of variations* [2, 4]. Unfortunately, costates are generally driven by ODEs and their trajectories are hard to calculate [1]. However, this approach may help to find the optimal control trajectories in some particular cases. A detailed discussion on this formulation is carried out in section 3.3.2, and comprehensive dissertations are available at [6, 12].

2.3 ADAS: cruise control and eco-driving

Many researching efforts are addressed to the development of engine and powertrain technologies to improve fuel efficiency of transportation vehicles. However, the vehicle operating conditions play a major role in global efficiency and, hence, they must be taken into consideration as well. ADAS are onboard systems that provide additional information or assistance to the driver in order to improve comfort, efficiency and safety. ADAS are a growing technology with a great variety of devices aimed to different tasks: adaptive light control, blind spot monitor and automatic parking among others [13–15]. Cruise controllers, which are part of the ADAS systems, are of special interest to vehicle efficiency optimization.

Several cruise control approaches have been presented in literature so far such as MPCs [16] using look-ahead information [17, 18], fuzzy logic controllers [19–21] or even Stochastic Dynamic Programming (SDP) approaches [22]. Despite these systems have been proven to perform much better than the traditional constant speed Proportional-Integral-Derivative (PID)-based cruise control, from an OC point of view it is interesting to address this topic as an OCP. The application of OC, also known as Eco-Driving (ED), provides optimal trajectories with a significant improvement in fuel efficiency compared

to other control approaches [23, 24]. Generally, this OCP consists in the minimization of a cost index:

$$\min_{u} \left\{ \int_0^{\mathcal{T}} L(u, v, t)\, \mathrm{d}t \right\} \tag{2.10}$$

with L the fueling rate, electrical consumption, or any other energy resource, u the vehicle controls and v the vehicle speed, which follows a dynamic equation:

$$\dot{v} = f(u, v, t) \tag{2.11}$$

This problem is generally constrained in both speed and distance since the driver usually wants to cover a prescribed distance $\mathcal{S}$ in a given time $\mathcal{T}$:

$$\begin{aligned} v(0) &= v_0 \\ v(\mathcal{T}) &= v_f \\ s(0) &= 0 \\ s(\mathcal{T}) &= \mathcal{S} \end{aligned} \tag{2.12}$$

Therefore, the ultimate goal is to find the speed trajectory $v(t)$ that minimizes the cost index. It is important to remark that the above OCP is not only affected by the powertrain model uncertainty, but also involves a road grade and vehicle mass identification problem [25]. Note that the above generic problem is formulated in time to be consistent with the common definition of an OCP, however it may be more convenient to reformulate it in distance if disturbances are specified in that domain–which is the typical case–by following the notes in appendix A. Examples showing these two approaches can be found in literature, both in time domain [26–28] and in distance domain [29–31].

Schwarzkopf and Leipnik addressed the ED problem for the first time in literature in 1977 [32]. They used the recently developed PMP–Lev Pontryagin published his work in 1962–to study the optimal speed profiles of a vehicle at several road grades. The results showed a typical trend that can be found in later works: for a given time constraint–*i.e.* a specific average speed–the vehicle should keep constant speed, decelerate on top of a hill and accelerate downhill. It might be a quite intuitive policy but since that moment it was mathematically demonstrated.

Some years later, Hooker et al. addressed the same problem but focusing on the speed trajectory between two stops [33]. They found that all examples that they calculated followed a common strategy: first, the vehicle performs a strong acceleration, then it cruises for some time, coasts to reduce speed and, eventually, brakes when reaching the destination. This is another well known trend for speed optimization of dissipative systems [34]. Unfortunately, the use of DP and the reduced computational resources at that time only

allowed to calculate short distance cases. Based on these promising results, Hooker et al. repeated their study performing a detailed analysis on different vehicles and road grades [35]. Pointing the importance of ED, up to 30% of fuel saving–in simulation–was possible thanks to the optimization of vehicle speed. Addressing the limited computational power, [36] adjoined the time constraint to the cost index in order to reduce the DP problem dimensions.

During the next decade there was little interest on this topic and few works exists on literature. Nevertheless, in 2000s ED came to the optimal control community attention and many comprehensive works analyzed and extended the previous knowledge on this topic. First, in 2006, [26] analyzed the ED problem with an analytical PMP approach that allowed to extract some common conclusions for several road grade situations:

1. Flat road: constant speed is the optimal solution for a long distance cruise.

2. Uphill: if achievable, constant speed is also the choice; if not, the optimal control is full throttle.

3. Downhill: if possible, keep speed constant without using the brakes; if not, the optimal solution is to cut off fuel injection–introducing more kinetic energy into the vehicle when overspeeding is inefficient due to the increased losses.

4. On top of a hill: decrease speed such that, considering the downhill overspeeding that is yet to come, the required average speed is satisfied.

Hellström et al. reached similar conclusions with DP [29]. Following, [37] addressed the ED problem with Direct Method (DM) and Mixed Integer Nonlinear Programming (MINLP) to deal with discrete gear shifts. In 2009, [27] analyzed the optimal speed profile reaching a 4.6% improvement on fuel efficiency compared to a constant speed PID cruise control. Despite this result seems to contradict [26], the key point is that the road grade was continuously varying in [27]. For a case like this, the optimal solution is a question of the balance between kinetic and potential energy, which is not trivial. Therefore, [27] remarks the importance of look-ahead road information.

In this sense, [30] used look-ahead road elevation information to implement ED onboard a truck to minimize fuel consumption on an actual road. However, for computational reasons, the DP algorithm was applied to a short horizon. In order to address this issue, the authors proposed in [31] an approximation of the cost-to-go value at a given horizon in order to virtually apply DP to the complete route. This approximation is based on a tradeoff between fuel

consumption and kinetic energy. A similar experiment, using an advisor to the driver, was carried out in [38]. Authors opted to download a cloud-based DP solution instead of addressing the ED problem onboard.

A quite different approach to the ED question was followed in [39]. The authors, after addressing the optimal speed profile calculation with PMP in [40] and with DP in [41] for an EV, applied the PMP theory explicitly. With a sufficiently simple model, and neglecting drag forces, a *singular control* was obtained (see section 3.3.3 for details on *singular control*). This enabled to derive six different phases that the optimal speed profile is made of: (i) positive torque, (ii) linear decrease of torque, (iii) zero torque, (iv) linear decrease of torque, (v) negative torque, and (vi) maximum braking force. Therefore, the speed optimization problem is reduced to the selection of the torque levels and switching times between phases, such that both the time and distance constraints are fulfilled. The authors followed the same philosophy for conventional vehicles and HEV at [28].

2.4 Powertrain management

OC is extensive in powertrain applications with works in the fields of automatic transmissions, fuel cells, EV batteries or hybrid powertrains. Nevertheless, and according to the scope of this dissertation, two main topics of interest are focused below: engine control and hybrid powertrain energy management.

2.4.1 Engine control

ICEs are complex systems with many control actuators, coupled devices and an extreme nonlinear behavior. Hence, the control of the numerous subsystems is a challenging task that the control field community has faced during many decades. The introduction of electronic controls in the 1980s made possible the use of comprehensive control algorithms that have grown in complexity to thousands of tunable parameters in modern ECUs. This looks like the perfect scenario for optimal control: a complex system with a non trivial control. Surprisingly, it has not been the case until recent years.

So far, engine control has been mostly performed with a set of PID controller that track setpoints factory calibrated to perform adequately. These setpoints are mapped by measurable quantities–many times by engine speed and torque output or fueling rate–and interpolated during operation. Several corrections are performed to adapt those steady state setpoints to dynamic transients.

Engine control optimization has not been a topic of interest for the community and few works are available at literature. There are many reasons for

this, but mainly it is because of two important questions: first, an engine is a highly nonlinear dynamic system whose complexity exceeds the capabilities of both optimization methods and computational resources that were available during most of the history and, second, there are lots of heuristic knowledge in engine control with modern ECUs performing really well, making optimal approaches too difficult for the little gain that can be achieved, even in the last years. Looking for more historical reasons, in 1978 Athans discussed the applicability of OC theory to the engine control field [42]. He stated that dynamic optimization of engine controls may be desirable, but the necessary models to describe engine processes were not available at that time. Athans reasoned that "if the adequate nonlinear dynamic models of the automotive engine system were available, a wealth of tools from optimal control theory could be employed". This was, with the lack of the necessary computational resources and current state-of-the-art optimization algorithms, the main drawbacks of OC in this field.

Fortunately, computational power has grown exponentially and nowadays specialized optimization algorithms are available. Engine dynamics and physical processes are generally well known, and model-based controls are a frequent topic in literature. This is, now, the perfect scenario for optimal control.

One of the first works that may be found in engine control optimization is [43]. Scotson and Wellstead presented in 1990 an algorithm to self-tune optimized ignition timing parameters. The conventional ECU control scheme was still used but the ignition timing map was recalibrated with the extremum seeking method. This was a first approach to engine optimal control.

A similar methodology was followed by several authors. Many works are based on the same concept: keeping the conventional control scheme, including an online parameter optimization. They are not optimal control applications in the rigorous sense, but some kind of optimality is stated while constraining to the PID-based control. Most of these works are based on extremum seeking as well, such as [44] where ignition, intake and exhaust timings are tuned, or [45] that proposed an online calibration for ignition timing that faced the use of different fuels. Learning algorithms that tune engine control calibration accounting for driving behavior were also developed in [46, 47]. Not only a better performance was achieved in those works but also a methodology to address engine aging effects and offsets. In line with those works, [48] presented a methodology to optimize the PID parameters of the VGT and EGR controllers. Guardiola et al. introduced a control strategy based on the switching among a set of different engine calibrations [49, 50], formulating a discrete OCP, concluding that there is a potential benefit on the ability to switch along the pollutants emissions and fuel consumption tradeoff.

Model-based control has also been a common approach in automotive purposes. MPCs have been successfully applied to airpath [51, 52], Homogeneous Charge Compression Ignition (HCCI) combustion [53], or fuel injection [54] among others. A detailed review of MPC applications in the automotive industry may be found in [55].

One of the first dynamic OC works was presented by Sun et al. in 2000 [56]. This work studies the optimal ignition timing and throttle trajectories for an idle speed controller. To do so, they used a variant of DMs with a Broyden-Fletcher-Goldfarb-Shanno (BFGS) algorithm that enabled to address the unconstrained nonlinear problem. The resulting control performed much faster and smoother than conventional PID controllers, even allowing a lower idle speed.

Following this philosophy, in 2009, [57] found the optimal throttle trajectory for an engine speed transient with multiple shooting DM, and [58] calculated the optimal VGT trajectory for a transient minimizing opacity and maximizing power output, using BFGS to address the DM. Two years later, [59] included EGR, VGT, rail pressure, SOI and throttle controls to minimize a weighted combination of PM and NO_x, using a single shooting DM. Following, [60] addressed the fuel minimization problem during short power transients using DP and PMP, while [61] applied multiple shooting DM in combination of Sequential Quadratic Programming (SQP) to minimize time and fuel, with waste gate, fueling rate and generator power controls in a diesel-electric powertrain. These studies, whose main characteristics are summarized in table 2.1, calculate the optimal trajectories for the engine controls but limiting to short transients that last 30 seconds in the best cases. It was in 2014 when Asprion et al. addressed the complete control of an engine for longer driving cycles by calculating the optimal trajectories for fueling rate, VGT opening, SOI and rail pressure, minimizing fuel consumption [62]. This work focused on the capabilities of different DM approaches to address this OCP, as well as the potential of the solution to derive dynamic controls. This was the first and, so far, the only trial to deliver a full optimal control along a driving cycle.

It is remarkable that DM is generally the optimization method of choice in any of its forms. Despite DP and PMP have been used in some specific works, DM is, by far, the only method capable of dealing with such a complex OCP as the one concerning the engine control [63].

The choice of the optimization horizons shown in the above works might be influenced by computational reasons. A long problem such as the one addressed in [62] is computationally expensive, and in many situations they can be avoided. For example, it is pointless to extend the OCP beyond a couple of seconds for a VGT control to perform a load transient where

Authors	Objective	Controls	Method	Horizon
Sun et al. [56]	$\lvert\Delta N_{ice}\rvert$, $\lvert\Delta u_{it}\rvert$, $\dot{u}_{thr}$	u_{it}, u_{thr}	DM	1.5–2 s
Saerens et al. [57]	m_f	u_{thr}	DM	25–30 s
Omran et al. [58]	$-P_{ice}$, σ	u_{vgt}	DM	3 s
Benz et al. [59]	m_{nox}, m_{pm}	$p_{rail,sp}$, u_{soi}, u_{vgt}, u_{egr}, u_{thr}	DM	4 s
Nilsson et al. [60]	m_f	u_f	DP, PMP	10 s
Sivertsson et al. [61]	m_f, $\mathcal{T}$	u_f, u_{wg}, P_g	DM	0.4 s
Asprion et al. [62]	m_f	u_f, u_{vgt}, u_{soi}, $p_{rail,sp}$	DM	6–295 s

Table 2.1: Main characteristics of engine control related works that can be found in literature, namely the minimization objective, the controls whose trajectories are optimized, the optimization method and the control horizon. Note that when several objectives are present, they are weighted into a single cost index. The denoted variables are: deviation from target engine speed $\lvert\Delta N_{ice}\rvert$, deviation from ignition timing setpoint $\lvert\Delta u_{it}\rvert$, throttle position u_{thr}, ignition timing u_{it}, total fuel consumption m_f, engine output power P_{ice}, exhaust gases opacity σ, VGT opening u_{vgt}, NO_x generation m_{nox}, PM generation m_{pm}, rail pressure setpoint $p_{rail,sp}$, SOI u_{soi}, EGR position u_{egr}, fueling rate u_f, total time $\mathcal{T}$, waste gate position u_{wg}, and generator power output P_g.

terminal states are constrained (such as target manifold pressure from ECU calibration) since the problem is fully defined for that time window. However, if the optimization target goes farther, such as a driving cycle optimization, decisions on a given window may jeopardize the performance in the following phases of the cycle. A compromise solution might be performing sequential optimizations for a short horizon, but there is no guarantee that this approach will deliver the optimal solution since estimations or fictitious state constraints have to be imposed at the end of the control window. Whether that suboptimal solution is close enough to the rigorous full optimization of a driving cycle to be acceptable is something that seems unanswered in literature as far as the author's information is concerned. Nevertheless, this question will be addressed again in section 6.3 with optimization results.

Additional few works addressed the engine OCP attending to some other objectives and control actuators. Some of these works are: [64] calculated

the optimal gear shift for a 1st to 2nd transition during a transient with DP; [65] estimated the optimal piston speed during a cycle with PMP in order to minimize entropy losses and found out that the ideal mechanism must perform a fast compression, keep minimum volume until pressure reaches its maximum value, and then expand at maximum rate; [66] applied genetic algorithms to calculate the optimal set of controls that minimize fuel consumption, NO_x emissions and noise during a cycle for a given steady condition; [60] addressed the optimal transition between two operating points throughout the engine operating map. An interesting journey through many more OC examples applied to different automotive aspects, including engine control, may be found in [67].

An especially interesting field of application of OC in engine control is the management of dual EGR systems. This specific topic is reviewed below.

Optimal dual EGR control

A cost-effective approach to NO_x control is to consider a dual EGR system with both LP- and HP-EGR loops. These systems consist of two EGR valves, one installed between intake and exhaust manifolds (high pressure loop), and the other mounted between intake and exhaust lines (low pressure loop) as shown in figure 2.1. Both systems show several drawbacks when used alone. HP-EGR introduces the exhaust gases into the cylinders at high temperature, despite using coolers, due to the high temperatures at the turbine inlet. In addition, the introduction of the EGR close to the cylinders usually leads to a poor homogeneity in the EGR distribution among cylinders [68]. Both effects impact negatively the engine efficiency and emissions, especially if Low Temperature Combustion (LTC) concepts are applied [69]. LP-EGR has been traditionally avoided because of compressor wheel reliability, but the widespread use of DPF in current engines allows the use of this configuration [70]. Therefore, LP-EGR becomes a suitable alternative to HP-EGR since it can provide high EGR rates without a significant increase in intake temperature and minimizing cylinder-to-cylinder charge dispersion [71], among other benefits related to the turbocharger operation [72–74]. In general, due to the better EGR distribution [75] and lower temperature [72, 76], the use of LP-EGR involves a reduction in NO_x and PM. Nevertheless, the HP-EGR route has a faster settling time than LP-EGR due to the length of the EGR path [77, 78], produces lower HC emissions and shows a higher efficiency, especially at cold conditions, due to the increase in the intake temperature [79].

Different authors propose the dual-loop EGR system as a possible method to combine the advantages of both routes [80–82]. This control problem can be addressed with two different approaches. On the one hand, some

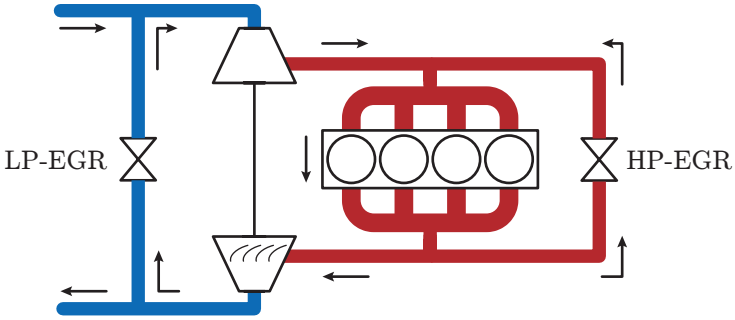

Figure 2.1: Schematic layout of an engine with LP- and HP-EGR systems. Coolers, after-treatment and other devices are obviated for the sake of clarity. The red airpath represents the high pressure loop while the blue is the low pressure section. The arrows denote the direction of the flow.

manufacturers prefer a sequential EGR control, where only one recirculating loop can be active, switching from one configuration to another according to the requirements. On the other hand, another possibility is to perform a simultaneous control of both systems working together to reach the desired inlet conditions. The sequential approach entails a significant advantage in EGR fraction estimation as long as exhaust gases are recirculated through a single path. On the contrary, the simultaneous control approach requires the estimation of the EGR fraction at two different loops, not only to guess the total recirculated amount but also to find out the actual rate between LP- and HP-EGR, which is critical to reach the required thermodynamic conditions at the intake manifold [83, 84]. In addition to that, both loops are coupled together with the VGT control, which increases the complexity of the whole system. However, this last approach may carry benefits on engine performance as nearly any desired temperature and oxygen fraction setpoints are affordable, and higher amounts of EGR are possible with this configuration [81].

Due to the performance advantages of the simultaneous control of LP- and HP-EGR, several works address this control problem in literature [80–82]. The main idea is to decouple the controls so individual EGR loops can be controlled separately. To this effect, [80] decomposed the dual-loop system into two subsystems, each of them with their own control laws and PID controllers, assuming knowledge of the mass flow through the valves. This allowed to accurately track oxygen fraction, temperature and pressure setpoints at the intake manifold. The authors in [81] proposed a model-based approach to build EGR fraction estimators. The model also allows to calculate the total EGR fraction and the split between both loops that bring the desired intake

conditions. Once these decisions are taken, the control of the two valves can be done separately in order to achieve their individual targets according to their mass flow estimations.

All the above works focus on the developing of a control able to track a set of desired intake conditions with an acceptable accuracy and dynamic response. However, despite the interest on this topic, little research has been carried out in the field of the OC in order to explore the full potential of this airpath architecture without constraining to predefined setpoints. Some works such as [85] already introduced OC strategies to this topic, by linearizing a MVEM and applying a linear-quadratic regulator. The results of this optimization show a better response during transient operation but the problem is still constrained to the tracking of some setpoints.

2.4.2 Hybrid powertrains: power-split control

The availability of two different energy sources in a hybrid vehicle opens the possibility to operate the powertrain in many different ways, with numerous advantages in both fuel economy and emission terms [86, 87]. Nevertheless, the increased architecture complexity comes at the expense of a more sophisticated control. In a HEV, the control role has several layers. On the one hand, engine, battery and motor are controlled to deliver the required setpoints according to a set of individual operational requisites (temperatures, smoothness, safeness, etc.). This layer is also common to conventional and electric vehicles and already discussed in 2.4.1. On the other hand, a supervisory layer manages the interaction between those devices with a global energy management. This last control layer, also known as power-split, is in charge of dividing the driver requirements among the available energy sources. This is HEV-specific as long as the driver plays this role in a vehicle with a single energy source. The question that arises is how to perform this power-split in order to minimize fuel consumption–and eventually pollutant emissions. This introduces the Energy Management Problem (EMP).

The EMP consists in finding the power-split control strategy that best fits a given criterion [88, 89], usually the fuel consumption. Given that the driver–or the driving cycle–is requesting a specific amount of torque, both the electric motor and the engine should fulfill this demand together. The control has the ability to somehow modulate this driving cycle request on the engine by splitting the demand, so the benefits of the appropriate power-split on the powertrain, and especially on the engine efficiency, are comparable to that from an adequate speed management. In fact, the engine can be run at nearly whichever operating condition regardless of the driver demand, as long as the electric motor supplies–or absorbs–the torque difference.

The history of the EMP gets back to 1980 when Mosbech published the first work in literature that approached the control of a hybrid vehicle [90]. It carries out a comprehensive analysis of different hybrid architectures (briefly described in section 4.3.3; further discussion available at [88]) and introduces a set of criteria for minimum fuel consumption control strategy: (i) the engine and other devices must be operated maximizing their efficiency, (ii) as much kinetic energy as possible must be recovered, and (iii) the stored energy must be used for maximum benefit. These criteria give a very good idea of the main three ways a HEV improves global efficiency compared to a conventional vehicle:

1. The engine is operated mostly on high efficiency regions.
2. Idling is avoided, electric mode is used for very low speed maneuvers.
3. Braking and coasting are replaced by kinetic energy recovering whenever possible.

In addition to the above, [90] addressed the EMP as an OCP, which is the approach that was followed by most of the subsequents works on this topic. Mosbech chose DP (see section 3.2.1 for a detailed description of this optimization method) to solve this OCP but, unfortunately, this is a heavy algorithm and computational resources were not enough at that time for such a complex problem. Mosbech also faced a major drawback of power-split control with OC: the OCP offers an optimal control trajectory but not a control strategy–which would be desirable. Due to this, the trajectory is constrained to the particular driving cycle that is analyzed and, therefore, the cycle must be known in advance, limiting this methodology to offline purposes. This issue would be addressed several years later.

The next reference in literature happened in 1987, when Bumby and Forster addressed the EMP with further analysis on the optimal control [91]. Intuitively they stated that fuel minimization may be achieved by minimizing a weighted sum of the fuel and battery contributions to the total torque:

$$L = \lambda_1 E_1 + \lambda_2 E_2 \tag{2.13}$$

where E_1 and E_2 are, respectively, the fuel and battery energy contribution, and λ_1/λ_2 the weighting factors (note that the nomenclature from [91] is preserved in the above expression). According to this equation, the power-split optimization is just a question of selecting the control that minimizes L at each calculation step. Note that, this time, the proposed control can be issued on real time–no cycle knowledge is assumed–with a minor drawback: λ_1/λ_2 is

unknown in advance. The results of the presented simulations in [91] are quite representative of the typical optimal sequence on a short acceleration-cruising-coasting-braking cycle: (i) the engine runs at high loads–high efficiency–at the very beginning of the acceleration phase, (ii) the load is reduced during cruising but still at a high efficiency region, (iii) the engine is switched off whenever the total amount that has deliver is enough to keep a similar level of battery charge between the beginning and the end of the cycle, and (iv) the vehicle runs in pure electrical mode to the end, recovering as much kinetic energy as possible.

During the following decade several studies focused on the minimum fuel EMP with diverse methodologies. In 1993, Farrall and Jones applied fuzzy-logic techniques to achieve an efficient solution to the EMP [92]. They used the same driving cycle than the former study from Bumby and Forster [91], and results were similar, confirming the effectiveness of the inferred control sequence. Also several works provided heuristic controllers whose rules were partially based on previous OC results such as [93–96].

Paganelli et al. carried out an interesting study in 2000 [97], with an extended discussion in [98], which served as the basis of many forthcoming works on this topic. They proposed that the fuel minimization may be addressed as the instantaneous minimization of an equivalent fuel consumption. This equivalent quantity must account for both the actual fuel burnt in the engine and the necessary fuel to restore the spent electrical energy. This intuitive idea, which they called Equivalent Consumption Minimization Strategy (ECMS), is synthesized in the minimization of the following index:

$$L = P_f + \mu P_b \tag{2.14}$$

with P_f and P_b the current fuel and battery power supply, and μ a weighting factor. Note that fuel and battery power values refer to the expenditure of raw internal energy–from the fuel tank and the battery chemicals respectively–since the idea is to find a balance between the contribution of different energy sources. In this study, Paganelli et al. also used an heuristics-based minimization method to approach the EMP. The comparison between both approaches showed that results were quite the same. It looked like ECMS method offered some kind of near optimal control. But it remained just an intuitive idea without a mathematical background.

It was in 2001 when a more rigorous study was carried out by Delprat et al. to address the EMP with OC theory [99]. The proposed methodology was based on the theory of PMP, developed by Lev Pontryagin in his work *The mathematical theory of optimal processes* [2] (for an extended review of this optimization method see section 3.3.1). According to this, the EMP may be

transcribed into a sequence of two point BVPs. These problems consist in the instantaneous minimization of the following cost index:

$$H(t) = \dot{m}_f(t) + \lambda(t)\dot{\zeta}(t) \tag{2.15}$$

where $\dot{m}_f$ is the fueling rate and $\dot{\zeta}$ the variation of battery SoC. The costate–Lagrangian multiplier–$\lambda(t)$ follows the ODE:

$$\dot{\lambda}(t) = -\frac{\partial H}{\partial \zeta} \tag{2.16}$$

Note that the nomenclature of the above equations is different to that from [99] to be consistent with this dissertation.

The work from Delprat et al. concluded that the PMP can be successfully applied to find the optimal power-split in a HEV. Only one question remains, which is the fact that the initial costate value $\lambda(0)$ needs to be specified in order to solve (2.16). According to PMP, the optimal $\lambda(0)$ value is such that fulfills the terminal SoC level. Therefore, this study followed an iterative methodology to correct $\lambda(0)$ until terminal constraint is satisfied within a tolerance.

The resemblance between (2.15) and (2.14) cost indices is more than obvious. For a constant λ, the PMP approach converges to the ECMS minimization objective. Therefore, ECMS is just a particular case of PMP, where the dynamics of the battery are neglected (see section 3.3.2 for a discussion on the cases where the costate is a constant value). This fact was demonstrated and discussed in 2009 by Serrao et al. [100]. In addition to that, and although it has not been discussed in the literature so far, the ECMS cost index (2.14) and the Bumby and Forster approach in (2.13) from 1987 are identical, with $\mu = \lambda_2/\lambda_1$, which is nothing but a curious fact. All these similarities mean that [91] and [97] were actually applying OC in their studies, intuitively, without knowing it; they were just lacking the formal OC background.

From this point, the EMP rapidly became a common topic in control literature for several reasons: in first place, HEVs rose as an effective and promising answer to the increasingly stringent emission limits; second, there are lots of room for improvement for an adequate power-split; and third, it is a relatively cheap and easy to solve OC problem with the ECMS simplification. Since that time, it has been an attractive topic and many authors have been filling an extensive list of works addressing the EMP with a number of different approaches. Mainly, DP [101–108] and PMP (including the ECMS approach) [109–121] are the two usual optimization methods of choice in literature, being the last the most common. Performance benchmarks of these two methods

are issued in [122–124], with an detailed discussion in [125]. Other approaches such as DM [126], fuzzy logic [127], neural networks [128], genetic algorithms [129, 130], or linear optimization [131] have also been already investigated in literature with limited acceptance. Heuristics are the topic for some works as well [132–134], which is the solution usually adopted by the industry, but since it is an arbitrary question these works fall out of the interest of this thesis. [89] carried out an interesting review of the main approaches in literature to address the EMP.

During the years, the topic has transitioned from the basic power-split EMP to many complex approaches that minimize fuel consumption in HEVs considering the effect of the thermal state of the engine [135], battery aging during long-term operation [136], pollutant emissions [108, 120, 137], emissions in combination of coolant temperature [137], variable composition fuels [138], additional Noise, Vibration, and Harshness (NVH) constraints [139] and catalyst temperature [140]. Many of those approaches are reviewed and analyzed in [141].

Generally, DP and PMP approaches face the EMP assuming perfect driving cycle knowledge and hence the result is an offline solution. Also, a simple vehicle model is used because in DP increasing the number of states is computationally expensive (see section 3.2.1 for a discussion on DP's *curse of dimensionality*) and in PMP it may prevent a numerically stable solution (see section 3.3.4 for further information about PMP ill-conditioning). Therefore, a quasi-steady model is used with a simple battery representation which, in the case of ECMS, has no dynamics.

The main drawback that face the OC approach of the EMP is that all solutions are inherently cycle-dependent, which may limit the applicability of OC to offline purposes. Nevertheless, OC is still a valuable tool to benchmark, analyze and find the optimal boundary of control strategies. Anyhow, since an online controller is also desirable, several authors have addressed this drawback with a variety of approaches, which are discussed below.

Addressing cycle-dependency issue

OC in its rigorous form can only be applied with a complete knowledge of the problem, including the driving cycle, no matter the optimization method: DP explores backwards the whole cycle, PMP–or ECMS–requires the cycle to calculate $\lambda(0)$, and other algorithms assume that the cycle is known in advance. Due to this, the result of OC application to the power-split is, as Mosbech stated in [90], "an optimal sequence of control actions for a given driving schedule, and not an optimal control strategy, which is the ultimate goal", limiting the applicability to online purposes.

This cycle-dependency issue is addressed in literature mainly with three different approaches: (i) inferring an heuristic controller from optimal trajectories, (ii) including a feedback control, and (iii) estimating future driving requirements.

Heuristic–*i.e.* rule-based–controllers can be somehow deducted based on observations of optimal control trajectories [102, 142]. For example, common policies that may be found in the optimal control are to recharge the battery during coasting, to switch off the engine at low loads or to assist with the motor at launch. These heuristic controllers are no longer optimal, but they have been constructed around some kind of optimality concerns. Hence, a set of driving cycles are addressed with DP [102], PMP [142], or any other optimization algorithm, and the solution is analyzed looking for trends and relations between variables. The resulting controller is robust and predictable, but it may perform inefficiently.

Other authors opted to include an additional feedback control to the OC method [123, 143, 144]. These approaches are based on the ECMS strategy since it reduces the necessary future knowledge to just the constant multiplier μ in (2.14). Generally, a PID-like controller is in charge of guessing the appropriate μ value based on the current deviation of the SoC, with a proportional response [143], or nonlinear configurations [123, 144].

The estimation of future driving conditions is, by far, the preferred approach in power-split OC. An adequate prediction of road conditions is quite important for an efficient control [145]. Nearly all works are based in ECMS to simplify the cycle prediction into a single parameter guessing. Given that, the approaches are numerous. Some authors proposed to sample a driving cycle based on past observations and predictions. ECMS is used to calculate the optimal trajectory for this cycle and it μ value is applied to the actual driving cycle on real time [146–149]. Some of these approaches base their predictions on driving pattern recognition [148], while others characterize driving conditions as a Markov process [149, 150]. An extensive discussion on driving conditions prediction may be found in [151]. Another approach is to calculate the optimal trajectory for a receding horizon and apply its corresponding μ value to the current driving conditions [152, 153]. In order to speed up calculations in an online application, [152] used Approximate Dynamic Programming (ADP) (see [154] for a description of ADP) and an interesting methodology to extract the optimal μ value from DP results, which is thoroughly discussed in [155, 156]. A third approach in literature is to perform an stochastic analysis within a receding horizon and use a likelihood estimation to calculate the appropriate μ value under some optimality concerns [157], or including geographical information [158, 159]. Some other works base their methodologies in the estimation of

potential energy regeneration segments [160], in the relation between average power requirements and μ value [161, 162], or in the use of an MPC to estimate the most efficient μ value.

A minor stream is to use the stochastic information to solve directly the OCP instead of guessing future requirements. This is conducted by applying SDP (see [163] for a detailed description of SDP) with a likelihood approach to the driving cycle, usually referred to the power requirements [164–168].

2.5 Design applications of optimal control

OC is generally used to control a system or to derive a control law. However, one of its main applications is also serving as a benchmark for designing purposes. Optimal trajectories give a boundary to the efficiency for a given technology.

2.5.1 Heat release law design

Energy balance [169–172] has been a traditional technique to analyze the tradeoff between fuel consumption and emissions. It aims to study the mass and energy flows into and out of the different engine systems in order to identify possible undesirable energy sinks affecting efficiency. A more refined approach consists of using both the first and second Law of Thermodynamics in order to perform an exergy–available energy–balance that takes into account irreversibility in engine processes such as combustion [173, 174]. Previous approaches allow the identification of potential efficiency improvements by recovering part of the thermal energy loss, and particularly, the second one allows to find an upper bound for efficiency given the engine characteristics and its operating conditions. However, despite dealing with the minimization of energy losses, previous methods are not well-suited to take into account other parameters that impact on engine emissions and design. Another important issue of previous methods is that the complexity of the combustion process requires the assumption of an arbitrary HRL. In this sense, traditional thermodynamic processes such as constant volume, constant pressure and limited pressure combustions are assumed [173], or more sophisticated Wiebe functions are considered [174].

In order to address the limitations of prescribed thermodynamic processes, the HRL can be approached from the OC perspective calculating the fuel injection strategy that minimizes fuel consumption and, eventually, including pressure and knock constraints [175, 176]. This enables to estimate a boundary efficiency in order to properly design and schedule the injection system, without

using arbitrary combustion laws. Constraints related to non-energy-based parameters, such as pressure and emission limits, can be also taken into account.

2.5.2 Sizing of hybrid powertrains

Not only power-split control is key to improve HEVs performance, but also the design of its powertrain. The proper selection of powertrain components size is a critical choice during the design phase. A badly sizing may spoil potential benefits in both fuel and emissions [177]. Engine specifications should meet the requirements of hybrid operation; for example, engine might work at low loads if displacement is too large, and limit the capabilities of the powertrain if it is too small. In fact, HEV efficiency is strongly affected by the engine characteristics [178]. Also, both the motor and the battery should meet the characteristics of the ICE [179, 180], which is rather intuitive.

This designing problem might be addressed with a causal analysis of powertrain specifications and performance requirements [181], but effectiveness cannot be guaranteed. However, it is possible to benefit from mathematical optimization algorithms to find the most efficient powertrain design for a given set of requirements. Hence, the choice of the powertrain components may be approached as an optimization problem whose unknowns–battery, motor and engine sizes–must minimize fuel consumption [182], pollutant emissions [183] or vehicle cost [184], such that some performance constraints [185] are fulfilled. Several numerical optimization methods have been used in literature with quite similar performance [186] such as genetic algorithms [130, 183, 187, 188], particle swarm optimization [185, 189], convex optimization [190–193] or MINLP [184] among others. Despite its designing advantages, it must be taken into account that optimal approaches to his problem are cycle-dependent, since the performance of the powertrain is intrinsically linked to the particular driving cycle. In fact, it was found that charge sustaining HEVs show significant savings on city driving but negligible advantages in highway situations, and that Plug-in Hybrid Electric Vehicle (PHEV) benefits are strongly dependent on the battery size [194].

Many works in literature have focused exclusively to the powertrain sizing problem [130, 178, 179, 182–187, 190–193, 195]. However, the performance and efficiency of a HEV is unequivocal related to the power-split control [196], and an heuristic controller might produce an unfair comparison among several powertrain schemes [197]. Moreover, a given power-split strategy may perform efficiently for a specific powertrain size and produce undesirable results for another, making the size decision specially sensitive to the energy management control [197]. In order to make the powertrain characteristics the

only difference, both the sizing problem and the power-split control must be addressed together [189, 194, 197], resulting in a mixed OC and parametric optimization problem:

$$\min_{u,\varkappa} \left\{ \int_0^{\mathcal{T}} \dot{m}_f(u, \varkappa, t)\, \mathrm{d}t \right\} \tag{2.17}$$

where u is the control law, $\varkappa$ the size parameters to optimize and $\dot{m}_f$ the fuel consumption rate. This mixed problem has been addressed in literature in [188, 198, 199]. Due to the coupling of two problems of different nature, the typical approach is to surf across a space of different powertrain sizes with a numerical algorithm and, for each candidate, address the power-split OCP. This strategy involves a nested optimization of the design and the control problem by exploring all optimum candidates–which is equivalent to a brute-force search. This fact guarantees that the solution will be the optimum among the discretization grid candidates, but may be computationally expensive. Other approaches that are proposed in the literature are sequential optimization (the design problem is first addressed and, then, the control problem is solved for a given design, repeating this scheme iteratively) which cannot guarantee optimality of the solution, or the methodology proposed in [200].

Some authors also included the vehicle price to the above cost index in order to account for the tradeoff between fuel efficiency and HEV cost at different levels of electrification [189, 201]. Accurate cost models are available at literature [202, 203]. A common conclusion is that full hybrids–with a strong electrification–offer an improved fuel efficiency but they are much more expensive; on the contrary, vehicles with a low level of hybridization usually show an acceptable fuel efficiency benefit at a low cost [189]. According to Nuesch et al., "the best topology should then be selected according to the individual preference" [189], suggesting that there is still a lack of an objective criterion that minimizes the payback and total expenses.

References

[1] F. Lewis and V. Syrmos. *Optimal control*. Wiley-Interscience, 1995.

[2] L. S. Pontryagin et al. *The mathematical theory of optimal processes*. Interscience, New York, 1962.

[3] R. Bellman. "The theory of dynamic programming". In: *Bulletin of the American Mathematical Society* 60.6 (1954), pp. 503–515.

[4] R. Vinter. *Optimal control*. Springer, 2010.

[5] J. T. Betts. *Practical methods for optimal control and estimation using nonlinear programming*. SIAM, 2010.

[6] A. E. Bryson and Y.-C. Ho. *Applied optimal control: optimization, estimation, and control*. Taylor & Francis, 1975.

[7] C. L. Darby and A. V. Rao. "Minimum-fuel low-earth orbit aeroassisted orbital transfer of small spacecraft". In: *Journal of Spacecraft and Rockets* 48.4 (2011), pp. 618–628.

[8] P. Hagelauer and F. Mora-Camino. "A soft dynamic programming approach for on-line aircraft 4D-trajectory optimization". In: *European Journal of Operational Research* 107.1 (1998), pp. 87–95.

[9] R. R. Liu and I. M. Golovitcher. "Energy-efficient operation of rail vehicles". In: *Transportation Research Part A: Policy and Practice* 37.10 (2003), pp. 917–932.

[10] J. Morimoto, G. Zeglin, and C. G. Atkeson. "Minimax differential dynamic programming: Application to a biped walking robot". In: *Proceedings of the IEEE/RSJ International Conference on Intelligent Robots and Systems*. Vol. 2. 2003, pp. 1927–1932.

[11] R. Bellman. "Dynamic programming and Lagrange multipliers". In: *Proceedings of the National Academy of Sciences* 42.10 (1956), pp. 767–769.

[12] H. P. Geering. *Optimal control with engineering applications*. Springer, 2007.

[13] A. Lindgren and F. Chen. "State of the art analysis: An overview of advanced driver assistance systems (ADAS) and possible human factors issues". In: *Human Factors and Economic Aspects on Safety* 1 (2006), pp. 38–50.

[14] A. Shaout, D. Colella, and S. Awad. "Advanced driver assistance systems - past, present and future". In: *Seventh International Computer Engineering Conference*. 2011, pp. 72–82.

[15] A. Ziebinski et al. "A survey of ADAS technologies for the future perspective of sensor fusion". In: *International Conference on Computational Collective IntelligenceInternational Conference on Computational Collective Intelligence*. 2016, pp. 135–146.

[16] S. Li et al. "Model predictive multi-objective vehicular adaptive cruise control". In: *IEEE Transactions on Control Systems Technology* 19.3 (2011), pp. 556–566.

[17] B. Asadi and A. Vahidi. "Predictive cruise control: Utilizing upcoming traffic signal information for improving fuel economy and reducing trip time". In: *IEEE Transactions on Control Systems Technology* 19.3 (2011), pp. 707–714.

[18] T. Stanger and L. del Re. "A model predictive cooperative adaptive cruise control approach". In: *American Control Conference*. 2013, pp. 1374–1379.

[19] R. Muller and G. Nocker. "Intelligent cruise control with fuzzy logic". In: *Proceedings of the Intelligent Vehicles Symposium*. 1992, pp. 173–178.

[20] S. Dermann and R. Isermann. "Nonlinear distance and cruise control for passenger cars". In: *Proceedings of the American Control Conference*. Vol. 5. 1995, pp. 3081–3085.

[21] J. E. Naranjo et al. "Adaptive fuzzy control for inter-vehicle gap keeping". In: *IEEE Transactions on Intelligent Transportation Systems* 4.3 (2003), pp. 132–142.

[22] K. McDonough et al. "Stochastic dynamic programming control policies for fuel efficient in-traffic driving". In: *American Control Conference*. 2012, pp. 3986–3991.

[23] F. Mensing, R. Trigui, and E. Bideaux. "Vehicle trajectory optimization for application in ECO-driving". In: *IEEE Vehicle Power and Propulsion Conference*. 2011, pp. 1–6.

[24] W. Dib et al. "Evaluation of the energy efficiency of a fleet of electric vehicle for eco-driving application". In: *Oil & Gas Science and Technology – Revue d'IFP Energies nouvelles* 67.4 (2012), pp. 589–599.

[25] V. Winstead and I. V. Kolmanovsky. "Estimation of road grade and vehicle mass via model predictive control". In: *Proceedings of IEEE Conference on Control Applications*. 2005, pp. 1588–1593.

[26] A. Fröberg, E. Hellström, and L. Nielsen. "Explicit fuel optimal speed profiles for heavy trucks on a set of topographic road profiles". In: *SAE Technical Paper*. 2006.

[27] B. Passenberg, P. Kock, and O. Stursberg. "Combined time and fuel optimal driving of trucks based on a hybrid model". In: *European Control Conference*. 2009, pp. 4955–4960.

[28] A. Sciarretta, G. De Nunzio, and L. L. Ojeda. "Optimal ecodriving control: energy-efficient driving of road vehicles as an optimal control problem". In: *IEEE Control Systems* 35.5 (2015), pp. 71–90.

[29] E. Hellström, A. Fröberg, and L. Nielsen. "A real-time fuel-optimal cruise controller for heavy trucks using road topography information". In: *SAE Technical Paper*. 2006.

[30] E. Hellström et al. "Look-ahead control for heavy trucks to minimize trip time and fuel consumption". In: *Control Engineering Practice* 17.2 (2009), pp. 245–254.

[31] E. Hellström, J. Åslund, and L. Nielsen. "Design of an efficient algorithm for fuel-optimal look-ahead control". In: *Control Engineering Practice* 18.11 (2010), pp. 1318–1327.

[32] A. B. Schwarzkopf and R. B. Leipnik. "Control of highway vehicles for minimum fuel consumption over varying terrain". In: *Transportation Research* 11.4 (1977), pp. 279–286.

[33] J. N. Hooker, A. B. Rose, and G. F. Roberts. "Optimal control of automobiles for fuel economy". In: *Transportation Science* 17.2 (1983), pp. 146–167.

[34] N. Wan, A. Vahidi, and A. Luckow. "Optimal speed advisory for connected vehicles in arterial roads and the impact on mixed traffic". In: *Transportation Research Part C: Emerging Technologies* 69 (2016), pp. 548–563.

[35] J. N. Hooker. "Optimal driving for single-vehicle fuel economy". In: *Transportation Research Part A: General* 22.3 (1988), pp. 183–201.

[36] V. V. Monastyrsky and I. M. Golownykh. "Rapid computation of optimal control for vehicles". In: *Transportation Research Part B: Methodological* 27.3 (1993), pp. 219–227.

[37] Y. Saboohi and H. Farzaneh. "Model for developing an eco-driving strategy of a passenger vehicle based on the least fuel consumption". In: *Applied Energy* 86.10 (2009), pp. 1925–1932.

[38] E. Ozatay et al. "Cloud-based velocity profile optimization for everyday driving: A dynamic-programming-based solution". In: *IEEE Transactions on Intelligent Transportation Systems* 15.6 (2014), pp. 2491–2505.

[39] W. Dib et al. "Optimal energy management for an electric vehicle in eco-driving applications". In: *Control Engineering Practice* 29 (2014), pp. 299–307.

[40] N. Petit, A. Sciarretta, et al. "Optimal drive of electric vehicles using an inversion-based trajectory generation approach". In: *Proceedings of the 18th IFAC World Congress*. 2011, pp. 14519–14526.

[41] W. Dib, L. Serrao, and A. Sciarretta. "Optimal control to minimize trip time and energy consumption in electric vehicles". In: *IEEE Vehicle Power and Propulsion Conference*. 2011, pp. 1–8.

[42] M. Athans. *The role of modern control theory for automotive engine control*. Tech. rep. SAE Technical Paper, 1978.

[43] P. G. Scotson and P. E. Wellstead. "Self-tuning optimization of spark ignition automotive engines". In: *IEEE Control Systems Magazine* 10.3 (1990), pp. 94–101.

[44] D. Popovic et al. "Extremum seeking methods for optimization of variable cam timing engine operation". In: *IEEE Transactions on Control Systems Technology* 14.3 (2006), pp. 398–407.

[45] E. Hellström et al. "On-board calibration of spark timing by extremum seeking for flex-fuel engines". In: *IEEE Transactions on Control Systems Technology* 21.6 (2013), pp. 2273–2279.

[46] A. A. Malikopoulos, P. Y. Papalambros, and D. N. Assanis. "A learning algorithm for optimal internal combustion engine calibration in real time". In: *ASME International Design Engineering Technical Conferences and Computers and Information in Engineering Conference*. 2007, pp. 91–100.

[47] A. A. Malikopoulos, D. N. Assanis, and P. Y. Papalambros. "Real-time self-learning optimization of diesel engine calibration". In: *Journal of Engineering for Gas Turbines and Power* 131.2 (2009), pp. 1–7.

[48] J. Wahlström, L. Eriksson, and L. Nielsen. "Controller tuning based on transient selection and optimization for a diesel engine with EGR and VGT". In: *SAE Technical Paper*. 2008.

[49] B. Pla et al. *Fuel and immission potential of context aware engine control*. Tech. rep. SAE Technical Paper, 2013.

[50] C. Guardiola et al. "Adaptive calibration for reduced fuel consumption and emissions". In: *Proceedings of the Institution of Mechanical Engineers, Part D: Journal of Automobile Engineering* 230.14 (2016), pp. 2002–2014.

[51] P. Ortner and L. del Re. "Predictive control of a diesel engine air path". In: *IEEE Transactions on Control Systems Technology* 15.3 (2007), pp. 449–456.

[52] G. Stewart and F. Borrelli. "A model predictive control framework for industrial turbodiesel engine control". In: *47th IEEE Conference on Decision and Control*. 2008, pp. 5704–5711.

[53] J. Bengtssonv et al. “Model predictive control of homogeneous charge compression ignition (HCCI) engine dynamics”. In: *Proceedings of the IEEE International Conference on Control Applications*. 2006, pp. 1675–1680.

[54] C. Manzie, W. Palaniswami, and H. Watson. “Model predictive control of a fuel injection system with a radial basis function network observer”. In: *Proceedings of the IEEE-INNS-ENNS International Joint Conference on Neural Networks*. Vol. 4. 2000, pp. 359–364.

[55] D. Hrovat et al. “The development of model predictive control in automotive industry: A survey”. In: *IEEE International Conference on Control Applications*. 2012, pp. 295–302.

[56] P. Sun, B. Powell, and D. Hrovat. “Optimal idle speed control of an automotive engine”. In: *Proceedings of the American Control Conference*. Vol. 2. 2000, pp. 1018–1026.

[57] B. Saerens et al. “Minimization of the fuel consumption of a gasoline engine using dynamic optimization”. In: *Applied Energy* 86.9 (2009), pp. 1582–1588.

[58] R. Omran, R. Younes, and J. C. Champoussin. “Optimal control of a variable geometry turbocharged diesel engine using neural networks: applications on the ETC test cycle”. In: *IEEE Transactions on Control Systems Technology* 17.2 (2009), pp. 380–393.

[59] M. Benz et al. “Model-based actuator trajectories optimization for a diesel engine using a direct method”. In: *Journal of Engineering for Gas Turbines and Power* 133.3 (2011), pp. 1–11.

[60] T. Nilsson, A. Froberg, and J. Aslund. “Optimal operation of a turbocharged diesel engine during transients”. In: *SAE International Journal of Engines* 5 (2012), pp. 571–578.

[61] M. Sivertsson and L. Eriksson. “Time and fuel optimal power response of a diesel-electric powertrain”. In: *IFAC Proceedings Volumes* 45.30 (2012), pp. 262–269.

[62] J. Asprion, O. Chinellato, and L. Guzzella. “Optimal control of diesel engines: Numerical methods, applications, and experimental validation”. In: *Mathematical Problems in Engineering* 1 (2014), pp. 1–21.

[63] B. Bachmann et al. “Parallel multiple-shooting and collocation optimization with OpenModelica”. In: *Proceedings of the 9th International Modelica Conference*. 76. 2012, pp. 659–668.

[64] A. Haj-Fraj and F. Pfeiffer. "Optimal control of gear shift operations in automatic transmissions". In: *Journal of the Franklin Institute* 338.2-3 (2001), pp. 371–390.

[65] K.-Y. Teh and C. F. Edwards. "An optimal control approach to minimizing entropy generation in an adiabatic IC engine with fixed compression ratio". In: *ASME International Mechanical Engineering Congress and Exposition*. 2006, pp. 19–27.

[66] D. Siano, F. Bozza, and M. Costa. "Reducing fuel consumption, noxious emissions and radiated noise by selection of the optimal control strategy of a diesel engine". In: *SAE Technical Paper*. 2011.

[67] H. Waschl et al. *Optimization and optimal control in automotive systems*. Springer, 2014.

[68] J. M. Luján et al. "A methodology to identify the intake charge cylinder-to-cylinder distribution in turbocharged direct injection diesel engines". In: *Measurement Science & Technology* 1 (2008), pp. 1–11.

[69] F. Payri et al. "Effects of the intake charge distribution in HSDI engines". In: *SAE World Congress and Exhibition. SAE Technical paper*. 2010.

[70] O. Vítek et al. "Comparison of different EGR solutions". In: *SAE World Congress and Exhibition. SAE Technical Paper*. 2008.

[71] J. M. Luján et al. "Effect of low pressure EGR on gas exchange processes and turbocharging of a HSDI engine". In: *Thiesel International Conference on Thermo and Fluid Dynamic processes in Direct Injection Engines*. 2008, pp. 429–442.

[72] A. Maiboom, X. Tauzia, and J.-F. Hétet. "Experimental study of various effects of exhaust gas recirculation (EGR) on combustion and emissions of an automotive direct injection diesel engine". In: *Energy* 33.1 (2008), pp. 22–34.

[73] F. Millo, P. F. Giacominetto, and M. G. Bernardi. "Analysis of different exhaust gas recirculation architectures for passenger car diesel engines". In: *Applied Energy* 98 (2012), pp. 79–91.

[74] G. Zamboni and M. Capobianco. "Influence of high and low pressure EGR and VGT control on in-cylinder pressure diagrams and rate of heat release in an automotive turbocharged diesel engine". In: *Applied Thermal Engineering* 51 (2013), pp. 586–596.

[75] A. Maiboom, X. Tauzia, and J. F. Hétet. "Influence of EGR unequal distribution from cylinder to cylinder on NOx–PM trade-off of a HSDI automotive diesel engine". In: *Energy* 29.10 (2009), pp. 2043–2050.

[76] K. Akihama et al. *Mechanism of the smokeless rich diesel combustion by reducing temperature*. Tech. rep. SAE Technical Paper, 2001.

[77] J. M. Luján et al. "Considerations on the low-pressure exhaust gas recirculation system control in turbocharged diesel engines". In: *International Journal of Engine Research* 15.2 (2014), pp. 250–260.

[78] U. Asad and M. Zheng. "Exhaust gas recirculation for advanced diesel combustion cycles". In: *Applied Energy* 123 (2014), pp. 242–252.

[79] J. M. Desantes et al. "On the combination of high-pressure and low-pressure exhaust gas recirculation loops for improved fuel economy and reduced emissions in high-speed direct-injection engines". In: *International Journal of Engine Research* 14.1 (2013), pp. 3–11.

[80] F. Yan and J. Wang. "Control of diesel engine dual-loop EGR air-path systems by a singular perturbation method". In: *Control Engineering Practice* 21.7 (2013), pp. 981–988.

[81] J. V. Shutty et al. "Air system control for advanced diesel engines". In: *SAE World Congress and Exhibition*. 2007.

[82] A. Suresh et al. "Thermodynamic systems for Tier 2 Bin 2 diesel engines". In: *SAE International Journal of Engines* 6.1 (2013), pp. 167–183.

[83] F. Castillo et al. "Simultaneous air fraction and low-pressure EGR mass flow rate estimation for diesel engines". In: *IFAC Proceedings Volumes* 46.2 (2013), pp. 731–736.

[84] O. Grondin, P. Moulin, and J. Chauvin. "Control of a turbocharged diesel engine fitted with high pressure and low pressure exhaust gas recirculation systems". In: *Joint 48th IEEE Conference on Decision and Control and 28th Chinese Control Conference*. 2009, pp. 6582–6589.

[85] F. Yan, B. Haber, and J. Wang. "Optimal control of complex air-path systems for advanced diesel engines". In: *Proceedings of the ASME Dynamic System and Control Conference*. 2009, pp. 1–7.

[86] C. C. Chan. "The state of the art of electric, hybrid, and fuel cell vehicles". In: *Proceedings of the IEEE* 95.4 (2007), pp. 704–718.

[87] C. C. Chan, Y. S. Wong, and A. Bouscayrol. "Powering sustainable mobility: Roadmaps of electric, hybrid, and fuel cell vehicles". In: *Proceedings of the IEEE* 97.4 (2009), pp. 603–607.

[88] L. Guzzella and A. Sciarretta. *Vehicle propulsion systems. Introduction to modeling and optimization.* Springer-Verlag, 2005.

[89] A. Sciarretta and L. Guzzella. "Control of hybrid electric vehicles". In: *IEEE Control System Magazine* 27.2 (2007), pp. 60–70.

[90] H. Mosbech. "Optimal control of a hybrid vehicle". In: *Proceedings of the International Symposium on Automotive Technology & Automation.* 1980, pp. 303–320.

[91] J. R. Bumby and I. Forster. "Optimisation and control of a hybrid electric car". In: *IEE Proceedings D-Control Theory and Applications.* Vol. 134. 6. 1987, pp. 373–387.

[92] S. D. Farrall and R. P. Jones. "Energy management in an automotive electric/heat engine hybrid powertrain using fuzzy decision making". In: *Proceedings of the IEEE International Symposium on Intelligent Control.* 1993, pp. 463–468.

[93] D. L. Buntin and J. W. Howze. "A switching logic controller for a hybrid electric/ICE vehicle". In: *Proceedings of the American Control Conference.* Vol. 2. 1995, pp. 1169–1175.

[94] P. Waltermann. "Modelling and control of the longitudinal and lateral dynamics of a series hybrid vehicle". In: *Proceedings of the IEEE International Conference on Control Applications.* 1996, pp. 191–198.

[95] N. Jalil, N. A. Kheir, and M. Salman. "A rule-based energy management strategy for a series hybrid vehicle". In: *Proceedings of the American Control Conference.* Vol. 1. 1997, pp. 689–693.

[96] A. Brahma et al. "Modeling, performance analysis and control design of a hybrid sport-utility vehicle". In: *Proceedings of the IEEE International Conference on Control Applications.* Vol. 1. 1999, pp. 448–453.

[97] G. Paganelli et al. "Simulation and assessment of power control strategies for a parallel hybrid car". In: *Proceedings of the Institution of Mechanical Engineers, Part D: Journal of Automobile Engineering* 214.7 (2000), pp. 705–717.

[98] G. Paganelli et al. "General supervisory control policy for the energy optimization of charge-sustaining hybrid electric vehicles". In: *JSAE Review* 22.4 (2001), pp. 511–518.

[99] S. Delprat et al. "Control strategy optimization for an hybrid parallel powertrain". In: *Proceedings of the American Control Conference.* Vol. 2. 2001, pp. 1315–1320.

[100] L. Serrao, S. Onori, and G. Rizzoni. "ECMS as realization of Pontryagin's minumum principle for HEV control". In: *American Control Conference*. 2009, pp. 3964–3969.

[101] C.-C. Lin et al. "Energy management strategy for a parallel hybrid electric truck". In: *Proceedings of the American Control Conference*. Vol. 4. 2001, pp. 2878–2883.

[102] C.-C. Lin et al. "Power management strategy for a parallel hybrid electric truck". In: *IEEE Transactions on Control Systems Technology* 11.6 (2003), pp. 839–849.

[103] I. Arsie et al. "Optimization of supervisory control strategy for parallel hybrid vehicle with provisional load estimate". In: *Proceedings of the 7th International Symposium on Advanced Vehicle Control* 1 (2004), pp. 483–488.

[104] J. Liu and H. Peng. "Control optimization for a power-split hybrid vehicle". In: *American Control Conference*. 2006, pp. 466–471.

[105] L. V. Pérez et al. "Optimization of power management in an hybrid electric vehicle using dynamic programming". In: *Mathematics and Computers in Simulation* 73.1?4 (2006), pp. 244–254.

[106] J. Liu and H. Peng. "Modeling and control of a power-split hybrid vehicle". In: *IEEE Transactions on Control Systems Technology* 16.6 (2008), pp. 1242–1251.

[107] L. Johannesson and B. Egardt. "Approximate dynamic programming applied to parallel hybrid powertrains". In: *IFAC Proceedings Volumes* 41.2 (2008), pp. 3374–3379.

[108] T. Nuesch et al. "Optimal energy management and sizing for hybrid electric vehicles considering transient emissions". In: *Engine and Powertrain Control, Simulation and Modeling*. Vol. 3. 1. 2012, pp. 278–285.

[109] S. Delprat, T. M. Guerra, and J. Rimaux. "Optimal control of a parallel powertrain: from global optimization to real time control strategy". In: *IEEE 55th Vehicular Technology Conference*. Vol. 4. 2002, pp. 2082–2088.

[110] S. Delprat et al. "Control of a parallel hybrid powertrain: optimal control". In: *IEEE Transactions on Vehicular Technology* 53.3 (2004), pp. 872–881.

[111] A. Sciarretta, M. Back, and L. Guzzella. "Optimal control of parallel hybrid electric vehicles". In: *IEEE Transactions on Control Systems Technology* 12.3 (2004), pp. 352–363.

[112] P. Rodatz et al. "Optimal power management of an experimental fuel cell / supercapacitor-powered hybrid vehicle". In: *Control Engineering Practice* 13.1 (2005), pp. 41–53.

[113] R. Cipollone and A. Sciarretta. "Analysis of the potential performance of a combined hybrid vehicle with optimal supervisory control". In: *Proceedings of the IEEE International Conference on Control Applications*. 2006, pp. 2802–2807.

[114] L. Serrao and G. Rizzoni. "Optimal control of power split for a hybrid electric refuse vehicle". In: *American Control Conference*. 2008, pp. 4498–4503.

[115] L. Xu et al. "Optimal vehicle control strategy of a fuel cell/battery hybrid city bus". In: *International Journal of Hydrogen Energy* 34.17 (2009), pp. 7323–7333.

[116] D. Ambühl et al. "Explicit optimal control policy and its practical application for hybrid electric powertrains". In: *Control Engineering Practice* 18.12 (2010), pp. 1429–1439.

[117] S. Stockar et al. "Optimal control for plug-in hybrid electric vehicle applications". In: *Proceedings of the American Control Conference*. 2010, pp. 5024–5030.

[118] J. Bernard et al. "Fuel efficient power management strategy for fuel cell hybrid powertrains". In: *Control Engineering Practice* 18.4 (2010), pp. 408–417.

[119] A. Chasse and A. Sciarretta. "Supervisory control of hybrid powertrains: An experimental benchmark of offline optimization and online energy management". In: *Control Engineering Practice* 19.11 (2011), pp. 1253–1265.

[120] O. Grondin et al. "Energy management strategy for diesel hybrid electric vehicle". In: *IEEE Vehicle Power and Propulsion Conference*. 2011, pp. 1–8.

[121] S. Stockar et al. "Energy-optimal control of plug-in hybrid electric vehicles for real-world driving cycles". In: *IEEE Transactions on Vehicular Technology* 60.7 (2011), pp. 2949–2962.

[122] N. Kim, S. Cha, and H. Peng. "Optimal control of hybrid electric vehicles based on Pontryagin's minimum principle". In: *IEEE Transactions on Control Systems Technology* 19.5 (2011), pp. 1279–1287.

[123] L. Serrao, S. Onori, and G. Rizzoni. "A comparative analysis of energy management strategies for hybrid electric vehicles". In: *Journal of Dynamic Systems, Measurement, and Control* 133 (2011), pp. 1–9.

[124] Z. Yuan et al. "Comparative study of dynamic programming and Pontryagin's minimum principle on energy management for a parallel hybrid electric vehicle". In: *Energies* 6.4 (2013), pp. 2305–2318.

[125] B. De Jager, T. Van Keulen, and J. Kessels. *Optimal control of hybrid vehicles*. Springer, 2013.

[126] L. V. Pérez and E. A. Pilotta. "Optimal power split in a hybrid electric vehicle using direct transcription of an optimal control problem". In: *Mathematics and Computers in Simulation* 79.6 (2009), pp. 1959–1970.

[127] J.-S. Won and R. Langari. "Intelligent energy management agent for a parallel hybrid vehicle-part ii: torque distribution, charge sustenance strategies, and performance results". In: *IEEE Transactions on Vehicular Technology* 54.3 (2005), pp. 935–953.

[128] J. Moreno, M. E. Ortuzar, and J. W. Dixon. "Energy-management system for a hybrid electric vehicle, using ultracapacitors and neural networks". In: *IEEE Transactions on Industrial Electronics* 53.2 (2006), pp. 614–623.

[129] M. Montazeri-Gh, A. Poursamad, and B. Ghalichi. "Application of genetic algorithm for optimization of control strategy in parallel hybrid electric vehicles". In: *Journal of the Franklin Institute* 343.4 (2006), pp. 420–435.

[130] X. Liu, Y. Wu, and J. Duan. "Optimal sizing of a series hybrid electric vehicle using a hybrid genetic algorithm". In: *IEEE International Conference on Automation and Logistics*. 2007, pp. 1125–1129.

[131] A. Reig and L. del Re. "Evaluation of impact on pollution of a linear HEV optimal control strategy by engine-in-the-loop simulation". In: *7th IFAC Symposium on Advances in Automotive Control*. Vol. 7. 1. 2013, pp. 29–34.

[132] S. Barsali, M. Ceraolo, and A. Possenti. "Techniques to control the electricity generation in a series hybrid electrical vehicle". In: *IEEE Transactions on Energy Conversion* 17.2 (2002), pp. 260–266.

[133] S. Delprat, T. M. Guerra, and J. Rimaux. "Control strategies for hybrid vehicles: synthesis and evaluation". In: *IEEE 58th Vehicular Technology Conference*. Vol. 5. 2003, pp. 3246–3250.

[134] J.-S. Won, R. Langari, and M. Ehsani. "An energy management and charge sustaining strategy for a parallel hybrid vehicle with CVT". In: *IEEE Transactions on Control Systems Technology* 13.2 (2005), pp. 313–320.

[135] J. Lescot et al. "On the integration of optimal energy management and thermal management of hybrid electric vehicles". In: *IEEE Vehicle Power and Propulsion Conference*. 2010, pp. 1–6.

[136] L. Serrao et al. "Optimal energy management of hybrid electric vehicles including battery aging". In: *American Control Conference*. 2011, pp. 2125–2130.

[137] F. Merz et al. "On the optimal thermal management of hybrid-electric vehicles with heat recovery systems". In: *Oil & Gas Science and Technology – Revue d'IFP Energies nouvelles* 67.4 (2012), pp. 601–612.

[138] C. Manzie et al. "Robustness of ECMS-based optimal control in parallel hybrid vehicles". In: *Advances in Automotive Control*. Vol. 7. 1. 2013, pp. 127–132.

[139] F. Millo et al. "Development of an optimal strategy for the energy management of a range-extended electric vehicle with additional noise, vibration and harshness constraints". In: *Proceedings of the Institution of Mechanical Engineers, Part D: Journal of Automobile Engineering* 227.1 (2013), pp. 4–16.

[140] P. Michel et al. "3WCC temperature integration in a gasoline-HEV optimal energy management strategy". In: *Advances in Mechanical Engineering* 6 (2014), pp. 281–288.

[141] L. Serrao et al. "Open issues in supervisory control of hybrid electric vehicles: a unified approach using optimal control methods". In: *Oil & Gas Science and Technology – Revue d'IFP Energies nouvelles* 68.1 (2013), pp. 23–33.

[142] L. Tribioli et al. "A real time energy management strategy for plug-in hybrid electric vehicles based on optimal control theory". In: *Energy Procedia* 45 (2014), pp. 949–958.

[143] A. Chasse, A. Sciarretta, and J. Chauvin. "Online optimal control of a parallel hybrid with costate adaptation rule". In: *Proceedings of the 6th IFAC Symposium: Advances in Automotive Control*. 2010, pp. 99–104.

[144] T. van Keulen et al. "Design, implementation, and experimental validation of optimal power split control for hybrid electric trucks". In: *Control Engineering Practice* 20.5 (2012), pp. 547–558.

[145] C. Zhang et al. "Role of terrain preview in energy management of hybrid electric vehicles". In: *IEEE Transactions on Vehicular Technology* 59.3 (2010), pp. 1139–1147.

[146] C. Musardo et al. "A-ECMS: an adaptive algorithm for hybrid electric vehicle energy management". In: *European Journal of Control, Fundamental Issues in Control, special issue* 11 (2005), pp. 1816–1823.

[147] C. Musardo et al. "Supervisory control for NOx reduction of an HEV with a mixed-mode HCCI/CIDI engine". In: *Proceedings of the American Control Conference*. Vol. 6. 2005, pp. 3877–3881.

[148] S. Onori, L. Serrao, and G. Rizzoni. "Adaptive equivalent consumption minimization strategy for hybrid electric vehicles". In: *Proceedings of the ASME Dynamic Systems and Control Conference*. Vol. 1. 2010, pp. 499–505.

[149] H. Hemi, J. Ghouili, and A. Cheriti. "Combination of Markov chain and optimal control solved by Pontryagin's minimum principle for a fuel cell/supercapacitor vehicle". In: *Energy Conversion and Management* 91 (2015), pp. 387–393.

[150] K. McDonough et al. "Modeling of vehicle driving conditions using transition probability models". In: *IEEE International Conference on Control Applications*. 2011, pp. 544–549.

[151] R. Wang and S. M. Lukic. "Review of driving conditions prediction and driving style recognition based control algorithms for hybrid electric vehicles". In: *IEEE Vehicle Power and Propulsion Conference*. 2011, pp. 1–7.

[152] L. Johannesson, S. Pettersson, and B. Egardt. "Predictive energy management of a 4QT series-parallel hybrid electric bus". In: *Control Engineering Practice* 17.12 (2009), pp. 1440–1453.

[153] C. Zhang and A. Vahid. "Real-time optimal control of plug-in hybrid vehicles with trip preview". In: *Proceedings of the American Control Conference*. June 2010, pp. 6917–6922.

[154] W. B. Powell. *Approximate dynamic programming: solving the curses of dimensionality*. Vol. 703. John Wiley & Sons, 2007.

[155] C. Guardiola et al. "A new approach to optimally tune the control strategy for hybrid vehicles applications". In: *Engine and Powertrain Control, Simulation and Modeling*. Vol. 3. 1. 2012, pp. 255–261.

[156] C. Guardiola et al. "Insight into the HEV/PHEV optimal control solution based on a new tuning method". In: *Control Engineering Practice* 29 (2014), pp. 247–256.

[157] F. Payri et al. "On a stochastic approach of the ECMS method for energy management in hybrid electric vehicles". In: *Engine and Powertrain Control, Simulation and Modeling*. Vol. 3. 1. 2012, pp. 341–348.

[158] C. Guardiola et al. "Modelling driving behaviour and its impact on the energy management problem in hybrid electric vehicles". In: *International Journal of Computer Mathematics* 91.1 (2014), pp. 147–156.

[159] F. Payri et al. "A stochastic method for the energy management in hybrid electric vehicles". In: *Control Engineering Practice* 29 (2014), pp. 257–265.

[160] D. Ambühl and L. Guzzella. "Predictive reference signal generator for hybrid electric vehicles". In: *IEEE Transactions on Vehicular Technology* 58.9 (2009), pp. 4730–4740.

[161] N. Kim et al. "Optimal control of a plug-in hybrid electric vehicle (PHEV) based on driving patterns". In: *International Battery, Hybrid and Fuel Cell Electric Vehicle Symposium*. 2009, pp. 1–9.

[162] N. Kim, S. W. Cha, and H. Peng. "Optimal equivalent fuel consumption for hybrid electric vehicles". In: *IEEE Transactions on Control Systems Technology* 20.3 (2012), pp. 817–825.

[163] S. M. Ross. *Introduction to stochastic dynamic programming*. Academic press, 1983.

[164] C.-C. Lin, H. Peng, and J. W. Grizzle. "A stochastic control strategy for hybrid electric vehicles". In: *Proceedings of the American Control Conference*. Vol. 5. 2004, pp. 4710–4715.

[165] M. J. Kim et al. "Testing, modeling, and control of a fuel cell hybrid vehicle". In: *Proceedings of the American Control Conference*. 2005, pp. 3859–3864.

[166] L. Johannesson, M. Asbogard, and B. Egardt. "Assessing the potential of predictive control for hybrid vehicle powertrains using stochastic dynamic programming". In: *IEEE Transactions on Intelligent Transportation Systems* 8.1 (2007), pp. 71–83.

[167] S. J. Moura et al. "A stochastic optimal control approach for power management in plug-in hybrid electric vehicles". In: *IEEE Transactions on Control Systems Technology* 19.3 (2011), pp. 545–555.

[168] D. F. Opila et al. "An energy management controller to optimally trade off fuel economy and drivability for hybrid vehicles". In: *IEEE Transactions on Control Systems Technology* 20.6 (2012), pp. 1490–1505.

[169] E. A. Ajav, B. Singh, and T. K. Bhattacharya. "Thermal balance of a single cylinder diesel engine operating on alternative fuels". In: *Energy Conversion and Management* 41.14 (2000), pp. 1533–1541.

[170] I. Taymaz. "An experimental study of energy balance in low heat rejection diesel engine". In: *Energy* 31.2 (2006), pp. 364–371.

[171] F. Payri et al. "A new tool to perform global energy balances in DI diesel engines". In: *SAE International Journal of Engines* 7 (2014), pp. 43–59.

[172] F. Payri et al. "Experimental and theoretical analysis of the energy balance in a DI diesel engine". In: *SAE Technical Paper*. 2015.

[173] J. A. Caton. *A review of investigations using the second law of thermodynamics to study internal-combustion engines*. Tech. rep. SAE Technical Paper, 2000.

[174] C. D. Rakopoulos and D. C. Kyritsis. "Comparative second-law analysis of internal combustion engine operation for methane, methanol, and dodecane fuels". In: *Energy* 26.7 (2001), pp. 705–722.

[175] F. Zurbriggen et al. "Optimal control of the heat release rate of an internal combustion engine with pressure gradient, maximum pressure, and knock constraints". In: *Journal of Dynamic Systems, Measurement, and Control* 136.6 (2014), pp. 1–9.

[176] L. Eriksson and M. Sivertsson. "Computing optimal heat release rates in combustion engines". In: *SAE International Journal of Engines* 8.3 (2015), pp. 1069–1079.

[177] M. Ehsani, K. M. Rahman, and H. A. Toliyat. "Propulsion system design of electric and hybrid vehicles". In: *IEEE Transactions on Industrial Electronics* 44.1 (1997), pp. 19–27.

[178] R. Fellini et al. "Optimal design of automotive hybrid powertrain systems". In: *Proceedings First International Symposium on Environmentally Conscious Design and Inverse Manufacturing*. 1999, pp. 400–405.

[179] D. Assanis et al. "Optimization approach to hybrid electric propulsion system design". In: *Mechanics of Structures and Machines* 27.4 (1999), pp. 393–421.

[180] A. Kleimaier and D. Schroder. "Optimization strategy for design and control of a hybrid vehicle". In: *Proceedings of the 6th International Workshop on Advanced Motion Control*. 2000, pp. 459–464.

[181] R. A. Weinstock, P. T. Krein, and R. A. White. "Optimal sizing and selection of hybrid electric vehicle components". In: *24th Annual IEEE Power Electronics Specialists Conference*. 1993, pp. 251–256.

[182] W. Gao and S. K. Porandla. "Design optimization of a parallel hybrid electric powertrain". In: *IEEE Vehicle Power and Propulsion Conference*. 2005, p. 6.

[183] C. Desai and S. S. Williamson. "Optimal design of a parallel hybrid electric vehicle using multi-objective genetic algorithms". In: *IEEE Vehicle Power and Propulsion Conference*. 2009, pp. 871–876.

[184] C.-S. N. Shiau et al. "Optimal plug-in hybrid electric vehicle design and allocation for minimum life cycle cost, petroleum consumption, and greenhouse gas emissions". In: *Journal of Mechanical Design* 132.9 (2010), pp. 1–11.

[185] X. Wu et al. "Application of particle swarm optimization for component sizes in parallel hybrid electric vehicles". In: *IEEE Congress on Evolutionary Computation*. 2008, pp. 2874–2878.

[186] W. Gao and C. Mi. "Hybrid vehicle design using global optimisation algorithms". In: *International Journal of Electric and Hybrid Vehicles* 1.1 (2007), pp. 57–70.

[187] M. Jain et al. "Optimal powertrain component sizing of a fuel cell plug-in hybrid electric vehicle using multi-objective genetic algorithm". In: *Proceedings of the Industrial Electronics Conference*. 2009, pp. 3741–3746.

[188] A. Ravey et al. "Combined optimal sizing and energy management of hybrid electric vehicles". In: *IEEE Transportation Electrification Conference and Expo*. 2012, pp. 1–6.

[189] T. Nuesch et al. "Cost and fuel-optimal selection of HEV topologies using particle swarm optimization and dynamic programming". In: *American Control Conference*. 2012, pp. 1302–1307.

[190] L. Johannesson et al. "Including a battery state of health model in the HEV component sizing and optimal control problem". In: *IFAC Advances in Automotive Control*. Vol. 7. 1. 2013, pp. 398–403.

[191] X. Hu et al. "Optimal dimensioning and power management of a fuel cell/battery hybrid bus via convex programming". In: *IEEE/ASME Transactions on Mechatronics* 20.1 (2015), pp. 457–468.

[192] X. Hu et al. "Comparison of three electrochemical energy buffers applied to a hybrid bus powertrain with simultaneous optimal sizing and energy management". In: *IEEE transactions on intelligent transportation systems* 15.3 (2014), pp. 1193–1205.

[193] X. Hu et al. "Longevity-conscious dimensioning and power management of the hybrid energy storage system in a fuel cell hybrid electric bus". In: *Applied Energy* 137 (2015), pp. 913–924.

[194] N. Marc et al. "Sizing and fuel consumption evaluation methodology for hybrid light duty vehicles". In: *World Electric Vehicle Journal* 4.1 (2011), pp. 249–258.

[195] X. Wu et al. "Component sizing optimization of plug-in hybrid electric vehicles". In: *Applied Energy* 88.3 (2011), pp. 799–804.

[196] D. Sinoquet, G. Rousseau, and Y. Milhau. "Design optimization and optimal control for hybrid vehicles". In: *Optimization and Engineering* 12.1 (2011), pp. 199–213.

[197] D. Karbowski, C. Haliburton, and A. Rousseau. "Impact of component size on PHEV energy consumption using global optimization". In: *The World Electric Vehicle Journal* 2.2 (2008), pp. 92–100.

[198] M.-J. Kim and H. Peng. "Power management and design optimization of fuel cell/battery hybrid vehicles". In: *Journal of Power Sources* 165.2 (2007), pp. 819–832.

[199] N. Murgovski, L. M. Johannesson, and J. Sjoberg. "Engine on/off control for dimensioning hybrid electric powertrains via convex optimization". In: *IEEE Transactions on Vehicular Technology* 62.7 (2013), pp. 2949–2962.

[200] S. F. Alyaqout, P. Y. Papalambros, and A. G. Ulsoy. "Coupling in design and robust control optimization". In: *European Control Conference (ECC)*. IEEE. 2007, pp. 1414–1421.

[201] S. Ebbesen, P. Elbert, and L. Guzzella. "Engine downsizing and electric hybridization under consideration of cost and drivability". In: *Oil & Gas Science and Technology – Revue d'IFP Energies nouvelles* 68.1 (2013), pp. 109–116.

[202] M. Delucchi et al. *Electric and gasoline vehicle lifecycle cost and energy-use model.* Tech. rep. Institute of Transportation Studies, 2000.

[203] T. E. Lipman and M. A. Delucchi. *Hybrid-electric vehicle design: Retail and life cycle cost analysis.* Institute of Transportation Studies, University of California at Davis, 2003.

Part II

Analytic and experimental tools

Chapter 3

Mathematical methods for dynamic optimization

Mathematics is the art of giving the same name to different things.

— Jules Henri Poincaré

Contents

3.1 Introduction

The OCP is essentially a minimization problem in time (see section 2.2 for a detailed description of an OCP). An immediate approach is to solve the

problem analytically. While it might be possible, interesting OCPs usually involve complex models and many constraints, which are unfeasible for an analytical approach. Typical problems can be, however, addressed with numerical approaches, which take profit of the calculation capabilities of computers at the expense of discretizing time varying trajectories.

According to [1], numerical methods can be classified in three main groups attending to the mathematical properties that they exploit to address an OCP: (i) HJB equation, (ii) Indirect Method (IM), and (iii) DM. This chapter discusses the particularities of the three previously mentioned methods.

Before describing the above numerical methods, it might be interesting to briefly introduce the concepts of state, control and disturbance with a powertrain control example: the speed control of a vehicle. States x are the variables that unequivocally define the current state of the dynamic system. In the example at hand, assuming a quasi-steady engine model, it is the vehicle speed so, the total number of states is $N_x = 1$. Mathematically, these variables relate to the ODEs of the model. Controls are the variables that can be actuated in the system, and finding their optimal trajectories is the aim of OC. Following with the speed controller example, the control is the engine fueling rate so, the number of controls is $N_u = 1$. Disturbances are time-varying quantities that cannot be controlled, directly affecting to the system behavior. In the case of the speed problem, it might be speed limits and the road grade profile. All these characteristic variables are generally discretized in order to be addressed with a numerical method. Therefore, the state (vehicle speed) may be gridded arbitrarily into $n_x = 30$ individual candidates, and the control (fueling rate) into $n_u = 20$ candidates. Similarly, time trajectories must be divided into discrete time instants (*e.g.* $n_t = 100$) such that the sample time results $\Delta t = \mathcal{T}/(n_t - 1)$.

3.2 Hamilton-Jacobi-Bellman

The Hamilton-Jacobi-Bellman (HJB) equation was named after the mathematician Richard Bellman who contributed to the development of OC theory in the 1950s and introduced the DP. This equation can be deducted from Bellman's Principle of Optimality (BPO): *An optimal policy has the property that whatever the initial state and initial decisions are, the remaining decisions must constitute an optimal policy with regard to the state resulting from the first decisions* [2]. This statement directly implies that any sub-trajectory of an optimal trajectory must be also optimal. It is a rather intuitive idea but exceptionally important for the control theory because it means that any OCP may be chopped into as many small problems as desired once initial states are

given at each portion. The BPO can be expressed with the following equation [3]:

$$\mathcal{J}(\boldsymbol{x}(t),t) = \min_{\boldsymbol{u}} \left\{ \int_t^{t+\delta t} L(\boldsymbol{x}(\tau),\boldsymbol{u}(\tau),\tau)\,\mathrm{d}\tau + \mathcal{J}(\boldsymbol{x}(t+\delta t),t+\delta t) \right\} \quad (3.1)$$

The above denotes that the *cost-to-go* $\mathcal{J}$ (the value of the cost index associated to the optimal trajectories) from any state vector $\boldsymbol{x}$ at an undetermined time $0 \leq t \leq \mathcal{T}$ can be calculated as the sum of the cost index of a differential OCP with length δt and the *cost-to-go* from time $t+\delta t$. It is possible to replace $\mathcal{J}(\boldsymbol{x}(t+\delta t),t+\delta t)$ with the first two terms of a Taylor's expansion around time t:

$$\mathcal{J}(\boldsymbol{x}(t+\delta t),t+\delta t) \approx \mathcal{J}(\boldsymbol{x}(t),t) + \dot{\mathcal{J}}(\boldsymbol{x}(t),t)\delta t + \nabla_{\boldsymbol{x}}\mathcal{J}(\boldsymbol{x}(t),t) f(\boldsymbol{x}(t),\boldsymbol{u}(t),t)\delta t \quad (3.2)$$

where f is the dynamic constraints function of the state vector. Substituting, canceling $\mathcal{J}(\boldsymbol{x}(t),t)$, dividing by δt and taking limits when $\delta t \to 0$ brings:

$$\dot{\mathcal{J}}(\boldsymbol{x}(t),t) + \min_{\boldsymbol{u}} \{ L(\boldsymbol{x}(t),\boldsymbol{u}(t),t) + \nabla_{\boldsymbol{x}}\mathcal{J}(\boldsymbol{x}(t),t) f(\boldsymbol{x}(t),\boldsymbol{u}(t),t) \} = 0 \quad (3.3)$$

which is the HJB equation [3]. Both this differential or the integral forms–the expression derived from BPO at (3.1)–are necessary conditions of optimality for the OCP when evaluated locally at a particular t [3, 4]. If the OCP is evaluated globally throughout its time span, the HJB equation is a sufficient condition [3].

3.2.1 Dynamic Programming

The DP is a numerical method built around the HJB equation and it is a direct application of the BPO. The underlying idea is to split the complete problem into a finite number of small problems that can be easily solved. Thus, the time span of the problem is divided into n_t discrete time instants t_i where the following sub-problem is to be addressed:

$$\min_{\boldsymbol{u}} \left\{ \int_{t_i}^{t_{i+1}} L(\boldsymbol{x},\boldsymbol{u},t)\,\mathrm{d}t + \mathcal{J}(\boldsymbol{x},t_{i+1}) \right\} \quad (3.4)$$

subject to the particular constraints of the OCP of interest. This sub-problem may be approached in numerous ways–other numerical optimization algorithms, brute force, etc. A common method is to explore the complete $(\boldsymbol{x},\boldsymbol{u})$ space

and choose the $\boldsymbol{u}$ vector that minimizes the above quantity. Anyhow, these sub-problems are generally affordable to solve regardless of the method.

Once it is solved, nearly any OCP of interest may be addressed by repeating this step from $i = n_t - 2$ to $i = 0$ and accumulating $\mathcal{J}$–cost-to-go–for the whole $\boldsymbol{x}$ space. The resulting $\mathcal{J}(\boldsymbol{x}, 0)$ is a space of costs-to-go for the optimal solution of the OCP from 0 to $\mathcal{T}$ as a function of the initial vector of states $\boldsymbol{x}$. Choosing $\mathcal{J}(\boldsymbol{x}_0, 0)$ will deliver the optimal cost-to-go to the problem satisfying the constraints–and consequently the corresponding optimal trajectories. Therefore, the OCP will be solved.

The BPO is inherently discrete and so the DP method is. Although any numerical method demands to approximate time as a finite set of discrete intervals, DP also requires to grid, at least, the state space so the cost-to-go function $\mathcal{J}$ can be accumulated as a function of the state vector $\boldsymbol{x}$–otherwise $\mathcal{J}$ should be computed in an analytical form which is not possible in the usual case. The discretization of the state space restricts the trajectories to be within a finite set of numbers, while states are continuous functions in $\mathbb{R}$ for most of the cases. As a consequence, equality constraints may be impossible to fulfill as they might fall out of the discretized grid. In this situation equality constraints should be considered with an *acceptance threshold* or the grid density must be increased. At the end, it is a question of the tradeoff between constraints precision and computational burden.

A major drawback is what Bellman calls the *curse of dimensionality*. It refers to the superlinear increase in the dimensions of the DP problem as the number of states N_x raises. Bellman argued long ago in his work [5] that the memory capabilities of 1950s computers would limit DP to problems with $N_x \leq 3$. Despite computer technology has spectacularly evolved from those days, the *curse of dimensionality* is still the main handicap to solve an OCP with DP. The magnitude of this issue can be explained by calculating the dimensions of a general DP problem. The number of elements that must be in memory to store the cost-to-go are:

$$n_{\mathcal{J}} = {n_x}^{N_x} \tag{3.5}$$

where n_x is the number of elements each state is discretized in. The optimal controls are also stored in memory to keep track of the optimal trajectory. The number of elements that they require in the worst case scenario–when the whole problem has been covered and optimal controls are calculated for each state value as a function of time–are:

$$n_{\mathcal{U}} = n_t {n_x}^{N_x} N_u \tag{3.6}$$

where n_t is the number of elements the total time span $\mathcal{T}$ is discretized in and N_u the number of controls to optimize in the problem. Therefore, the total amount of elements that must be stored in memory at a time for a generic DP problem are:

$$n_{\mathrm{DP}} = (n_t N_u + 1){n_x}^{N_x} \tag{3.7}$$

which increases linearly with time or the number of controls but as a power of the number of states. Rising the number of states in one unit involves an increase of $\Delta N_x = (n_t N_u + 1){n_x}^{N_x}(n_x - 1)$ elements, while a rise of one unit in n_x increases the number of elements in $\Delta n_x > (n_t N_u + 1)N_x {n_x}^{(N_x - 1)}$ (derived from a Taylor expansion of (3.7) around n_x for $n_x + 1$) which are still power functions. The quotient $\Delta N_x / \Delta n_x = n_x(n_x - 1)/N_x$ denotes that ΔN_x grows faster, meaning that it is cheaper in computational terms to increase the discretization of the states than their number.

As a reference, figure 3.1 shows the minimum memory allocation requirements for a generic DP problem of 600 sample times as calculated with (3.7) in Megabyte (MB). It can be seen that in general terms a large number of states demands more memory than a dense grid as stated above. Modern computers with 64-bit architecture address memory using 48 bits [6, 7], meaning that they have a technical limitation of 2^{48} bytes, *i.e.* 256 Terabyte (TB) of total memory to address (depicted in red). However, in practice, a Random-Access Memory (RAM) overflow requires the allocation of data in a paging file dramatically penalizing the system performance, so a practical limit of a half of the available RAM capacity is much more realistic. 4 Gigabyte (GB) and 8 GB limits–representative of modern desktop computers ranging between 8 and 16 GB of RAM–are shown with a green and yellow dashed lines respectively, and denote that a problem featuring between 3 and 4 states is the limit for current machines with a moderately populated grid. In the case of discrete states with a sparse grid, the number of states that can be handled might be twice the former. Note the logarithmic scale of the figure which is a subtle detail with major implications: first, N_x is the term that makes (3.7) grow the fastest–it is the exponent–resulting in an exponential increase of memory requirements with the number of states–that is the reason why 4 and 8 GB lines are so close to each other; second, despite the capabilities of a machine to address a DP problem are based on its RAM capacity, it is somehow insensitive to the range of memory of nowadays' technology–perhaps that is why Bellman was already talking about a limitation at $N_x \leq 3$ in the 1950s [5]; and third, considering that even with an 256 TB RAM machine (thousands of times the average capacity of modern computers) a limitation of $N_x \lesssim 5$ applies, the

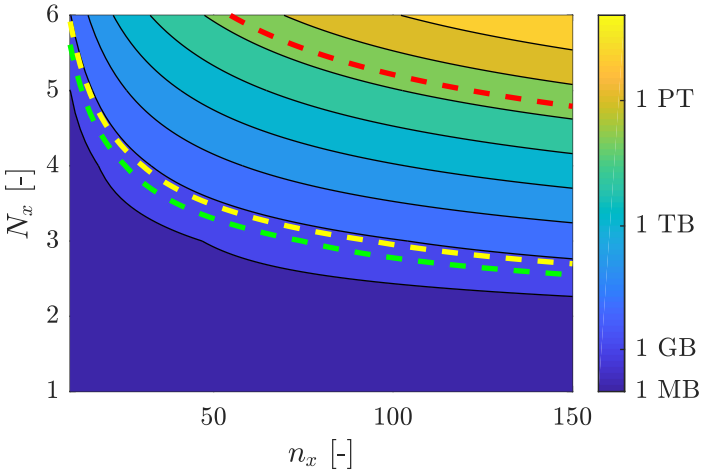

Figure 3.1: Minimum memory allocation requirements in MB of a generic DP problem with 600 time samples and $N_u = 2$ as a function of the number of states N_x and the number of elements per state n_x. 8 Byte variables (double precision) are assumed. The technical limitation of a 64-bit machine (256 TB) is depicted with a red dashed line. Also, practical limits of 4 and 8 GB–which would avoid system slowdown due to paging in most modern computers–are shown as a green and yellow dashed lines respectively. Note that despite contours are interpolated iso-memory curves, the number of states and the discretization grid must be integer values.

curse of dimensionality will continue being a major drawback of DP method during several decades.

Several workarounds have been proposed in literature to somehow circumvent the *curse of dimensionality*. Bellman himself suggested that his DP method might be combined with the classical analysis of variations [5]. He introduced the idea of adjoining N_λ states–or more precisely their dynamics–to the cost index with a vector of Lagrange multipliers. Hence, he is constructing an equivalent problem with $N_x - N_\lambda$ states and N_λ unknown Lagrange multipliers, effectively reducing the dimensions of the problem at the expense of increasing its complexity, especially with time varying Lagrange multipliers. Other authors such as Rust introduced pseudo-random techniques to break the *curse of dimensionality* in [8]. Those transform some particular subclasses of problems that are untractable with deterministic algorithms into tractable problems using Montecarlo integration schemes to estimate the cost-to-go and multigridding–an iterative re-meshing algorithm that increases grid density. Another different approach is the approximate DP followed by Powell at [9].

It is founded in approximating the cost-to-go $\mathcal{J}$ with another function $\widetilde{\mathcal{J}}$ that might be calculated with a simpler but related problem, some kind of heuristics or a prescribed suboptimal policy. Hence, the problem can be approached in a forward fashion, solving the HJB equation from 0 to $\mathcal{T}$. A part from reducing the impact of the *curse of dimensionality*, it brings the possibility of building a real-time controller as this method only requires a rough approximation of ahead conditions instead of detailed information.

The interested reader is redirected to the works [3, 10, 11] for an extensive review of DP.

3.2.2 On the algorithm implementation

The DP algorithm used throughout the works presented in the following chapters is mostly a direct application of the BPO. The procedure to address an OCP with N_x states and N_u controls begins by dividing the time span $\mathcal{T}$ of the problem[1] into n_t equidistant points, that is, $[t_0, t_1, \ldots, t_{n_t-1}]$, such that $t_{i+1} - t_i = \Delta t$. States and controls are also discretized into n_x and n_u points respectively: $\mathrm{x} = [\mathrm{x}_0, \mathrm{x}_1, \ldots, \mathrm{x}_{n_x-1}]$, $\mathrm{u} = [\mathrm{u}_0, \mathrm{u}_1, \ldots, \mathrm{u}_{n_x-1}]$. The grid distribution depends upon the particularities of each problem.

Then, the BPO–which is indeed the integral form of the HJB equation–is applied for each time instant t_i starting at $i = n_t - 2$ and proceeding backwards. The particular cost-to-go equation for a discrete state value x_j and a control u_k at time t_i is:

$$J_i(\mathrm{x}_j, \mathrm{u}_k) = L(\mathrm{x}_j, \mathrm{u}_k, t_i)\Delta t + \mathcal{J}_{i+1}(\hat{\mathrm{x}}) + \mathcal{I}(\mathrm{x}_j, \mathrm{u}_k, t_i) \tag{3.8}$$

where $\hat{\mathrm{x}}$ is the state resulting of applying the above control to the system from t_i to t_{i+1}. It can be calculated as:

$$\hat{\mathrm{x}} = \mathrm{x}_j + f(\mathrm{x}_j, \mathrm{u}_k, t_i)\Delta t \tag{3.9}$$

In the case $\hat{\mathrm{x}}$ does not fall within the state grid, the cost-to-go $\mathcal{J}_{i+1}(\hat{\mathrm{x}})$ can be calculated by interpolation of the available grid. The quantity $\mathcal{I}$ is a penalization term to take into account path constraints by assigning a near-infinity cost to the combinations that violate these constraints:

$$\mathcal{I}(\mathrm{x}_j, \mathrm{u}_k, t_i) = \begin{cases} 0, & c(\mathrm{x}_j, \mathrm{u}_k, t_i) \leq 0 \\ \epsilon, & c(\mathrm{x}_j, \mathrm{u}_k, t_i) > 0 \end{cases} \tag{3.10}$$

[1] For the sake of clarity and, in line with OC literature, in this chapter the problem is solved in time domain, while the transformation to distance or any other monotonic domain is straightforward by following the procedure introduced in appendix A

with ϵ as big as desired. Final value constraints are similarly considered at the terminal cost-to-go value:

$$\mathcal{J}_{n_t-1}(\mathrm{x}_j) = \begin{cases} 0, & \phi(\mathrm{x}_j) \leq 0 \\ \epsilon, & \phi(\mathrm{x}_j) > 0 \end{cases} \tag{3.11}$$

The above process is repeated for all the elements at the control grid $\mathbf{u}$ and the minimum cost-to-go is selected:

$$\mathcal{J}_i(\mathrm{x}_j) = \min_{\mathbf{u}} \{J_i(\mathrm{x}_j, \mathbf{u})\} \tag{3.12}$$

This minimization problem is solved by brute-force search. Hence, J_i is evaluated at each time step for the whole grid of state and control values at the implementation, resulting in a matrix with $N_x \cdot N_u$ dimensions, which can be much larger than $\mathcal{J}_i$. Therefore, the *curse of dimensionality* may be even worse than from the theoretical point of view that was shown in the figure 3.1, where only the memory requisites for the state grid were taken into account. Figure 3.2 shows the minimum memory requisites for a generic DP problem when using brute-force search for optimal u. It can be appreciated that $N_u = 5$ is hardly tractable for $N_x = 1$ while, for example, a problem with $N_x = 3$ would be intractable with $N_u \geq 3$. Fortunately, any problem with $N_u \leq 2$ will, at most, double the memory usage with brute-force search compared to any other minimization algorithm. Of course, these comments are a consequence of the chosen grid density and problem length for this example; however, as discussed in previous sections, the most influential parameter regarding memory requisites is N_x, so the above conclusions are not far from being somehow general.

The control that minimizes the above quantity is stored as $\mathcal{U}_i(\mathrm{x}_j)$. This minimization is performed for all x_j and all states to build the cost-to-go matrix $\mathcal{J}_i$ and $\mathcal{U}_i$.

The whole process described in eqs. (3.8)–(3.12) is sequentially reproduced backwards until reaching t_0. Then, choosing $\mathcal{J}_0(\boldsymbol{x}_0)$ fulfills the initial value constraints (2.4) and its corresponding $\mathcal{U}_0(\boldsymbol{x}_0)$ yields the optimal control trajectories of the OCP.

Finally, due to the discrete nature of the DP algorithm, a forward simulation of the system is performed to guarantee constraints fulfilling. If a constraint is violated, a grid re-meshing must be performed–with a different discretization distribution or increasing grid density–or tolerances should be modified for that particular constraint.

The DP algorithm cannot considerate integral constraints such as (2.7)

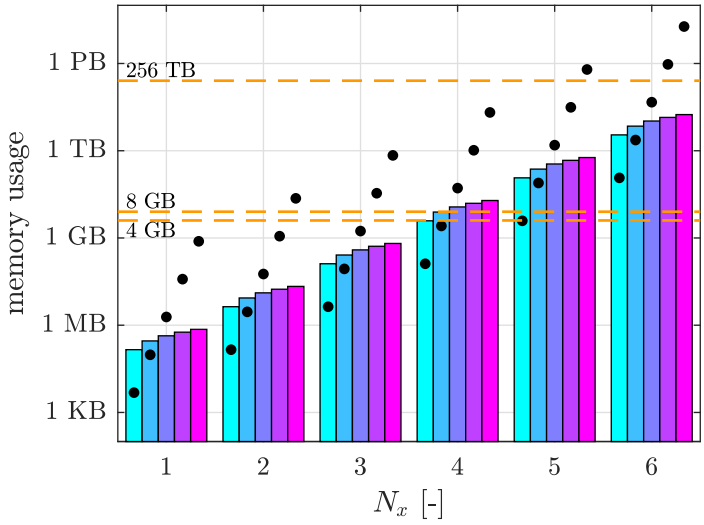

Figure 3.2: Memory requisites for a generic DP problem considering controls gridding for brute-force search of optimal u. The presented problem features $n_x = 30$, $n_u = 20$ and $n_t = 600$. Color bars represent, from light blue to purple, memory requirements to store J_0 and $\mathcal{U}$ with $N_u = 1, \ldots, 5$. The corresponding memory allocation for the brute-search algorithm is displayed with black dots. Orange dashed lines represent, from top to bottom, the technical limit of a 64-bit machine (256 TB), and two practical limits of 4 and 8 GB. Note that the memory usage of the DP implementation is the sum of the color bars and the black dots.

explicitly. However, a dummy state x_{N_x+1} may be added to the original problem with the ODE:

$$\dot{x}_{N_x+1} = q(\boldsymbol{x}, \boldsymbol{u}, t) \tag{3.13}$$

and boundary constraints:

$$\begin{aligned} x_{N_x+1}(0) &= 0 \\ x_{N_x+1}(\mathcal{T}) &\leq 0 \end{aligned} \tag{3.14}$$

Hence, this additional state is equivalent to the integral constraint. As a drawback, the original OCP has grown its number of states in one unit, aggravating the *curse of dimensionality* issues commented before.

Throughout the works developed in this thesis, two different implementations have been used. On the one hand, the generic DP function for MATLAB developed by Sundström and Guzzella has been employed in several applications as it provides out-of-the-box functionality for a user given model. It is

rather flexible, allowing up to 5 state variables, and distributed under Mozilla Public License. Despite the basic functionality follows the above algorithm, more details can be found in [12]. On the other hand, an *ad-hoc* DP solver has been implemented in MATLAB with the precise algorithm described in this section. It features a slightly faster calculation but at the expense of reduced flexibility.

3.3 Indirect method

The IM to approach an OCP was originated in the classical calculus of variations–a field of mathematical analysis concerned with the calculation of minima or maxima (extrema) of functionals (informally called *functions of functions*). During the 1950s and 1960s Pontryagin et al. developed this theory further in the field of optimal control theory to finally state the PMP [13] (originally known as Pontryagin Maximum Principle) named after the Russian mathematician, and also referenced as *minimum principle* or simply as *necessary conditions* in several works.

The IM describes the necessary optimality conditions of an OCP solution. The idea that lies behind the IM is to use these necessary conditions to transform the global OCP problem into a much simpler BVP. The term *indirect* refers to the fact that a second problem is solved–the BVP–in order to find the solution of the first, hence the solution is found in a somehow indirect manner. The main drawbacks of IM are: (i) the resulting system of differential equations might be too nonlinear and unstable (it is usually ill-conditioned) for a forward numerical simulation, and (ii) the method is founded around necessary conditions, not sufficient, and therefore optimality cannot be guaranteed beforehand. However, it also features interesting advantages. On the one hand it offers an exact and explicit form for the optimal trajectories of an OCP, and on the other hand it reduces the dimensions of the global problem to a relatively simple BVP, where there is not an explicit time dependency and, therefore, might be suitable for a real-time application.

The IM, or more particularly the PMP, has been a popular topic in many fields of engineering, from robotics to aerospace applications. It has been also the germ of the *bang-bang* control.

3.3.1 Pontryagin Minimum Principle

The PMP describes the necessary optimality conditions for an OCP solution. These conditions can be derived from the differential form of the HJB equation

stated in (3.3). The abbreviation of the *cost-to-go* gradient, $\lambda = \nabla_{\boldsymbol{x}}\mathcal{J}$, introduces the Hamiltonian:

$$H(\boldsymbol{x}, \boldsymbol{u}, \lambda) = L(\boldsymbol{x}, \boldsymbol{u}) + \lambda^T f(\boldsymbol{x}, \boldsymbol{u}) \tag{3.15}$$

where the time dependency of $\boldsymbol{x}(t)$, $\boldsymbol{u}(t)$ and $\lambda(t)$ has been deliberately obviated for the sake of clarity. The functions λ are known as costates. The optimal control trajectory can then be expressed as:

$$\boldsymbol{u}^*(\boldsymbol{x}, \lambda) = \arg\min_{\boldsymbol{u}} H(\boldsymbol{x}, \boldsymbol{u}, \lambda) \tag{3.16}$$

This particular equation is sometimes referred to as the *minimum principle*. It is remarkable that the optimal solution depends on λ (the gradient of the cost-to-go) and not on $\mathcal{J}$ itself. Using the Hamiltonian, the HJB equation results as:

$$\dot{\mathcal{J}}(\boldsymbol{x}(t), t) + H(\boldsymbol{x}, \boldsymbol{u}^*, \lambda) = 0 \tag{3.17}$$

It is clear that for a given pair of states and costates, the optimal controls are explicitly defined with (3.16). However, costate trajectories remain unknown. To extract their governing equations it is necessary to differentiate the above HJB equation with respect to $\boldsymbol{x}$ assuming that states and controls trajectories are optimal:

$$\frac{\partial^2 \mathcal{J}}{\partial \boldsymbol{x} \partial t}(\boldsymbol{x}^*, t) + \frac{\partial H}{\partial \boldsymbol{x}}(\boldsymbol{x}^*, \boldsymbol{u}^*, \lambda^*) + \frac{\partial H}{\partial \lambda}(\boldsymbol{x}^*, \boldsymbol{u}^*, \lambda^*)\frac{\partial \lambda}{\partial \boldsymbol{x}} + \frac{\partial H}{\partial \boldsymbol{u}}(\boldsymbol{x}^*, \boldsymbol{u}^*, \lambda^*)\frac{\partial \boldsymbol{u}}{\partial \boldsymbol{x}} = 0 \tag{3.18}$$

According to (3.16) it is known that $\frac{\partial H}{\partial \boldsymbol{u}}(\boldsymbol{x}^*, \boldsymbol{u}^*, \lambda^*) = 0$ to be the optimal trajectory, so that the last term vanishes. From the definition of the costates, $\frac{\partial \lambda}{\partial \boldsymbol{x}} = \nabla^2_{\boldsymbol{x}}\mathcal{J}$. Also, $\frac{\partial H}{\partial \lambda}(\boldsymbol{x}^*, \boldsymbol{u}^*, \lambda^*) = f(\boldsymbol{x}^*, \boldsymbol{u}^*)$ according to the definition of the Hamiltonian. In addition, $\frac{\partial^2 \mathcal{J}}{\partial \boldsymbol{x} \partial t}(\boldsymbol{x}^*, t)$ might be rewritten as $\frac{\partial}{\partial t}\nabla_{\boldsymbol{x}}\mathcal{J}(\boldsymbol{x}^*, t)$. Then the above equation results:

$$\frac{\partial}{\partial t}\nabla_{\boldsymbol{x}}\mathcal{J}(\boldsymbol{x}^*, t) + f(\boldsymbol{x}^*, \boldsymbol{u}^*)\nabla^2_{\boldsymbol{x}}\mathcal{J}(\boldsymbol{x}^*, t) + \frac{\partial H}{\partial \boldsymbol{x}}(\boldsymbol{x}^*, \boldsymbol{u}^*, \lambda^*) = 0 \tag{3.19}$$

Taking into account that $\dot{\boldsymbol{x}}^* = f(\boldsymbol{x}^*, \boldsymbol{u}^*)$, the first two terms of the above equation can be substituted with $\frac{\mathrm{d}}{\mathrm{d}t}\nabla_{\boldsymbol{x}}\mathcal{J}(\boldsymbol{x}^*, t) = \dot{\lambda}^*$. The expression finally results:

$$\dot{\lambda}^* = -\frac{\partial H}{\partial \boldsymbol{x}}(\boldsymbol{x}^*, \boldsymbol{u}^*, \lambda^*) \tag{3.20}$$

This ODE governs the dynamics of the costates. In the case of a final constraint such as (2.5), the corresponding terminal condition can be obtained differentiating $\mathcal{J}(\boldsymbol{x}, \mathcal{T}) = \phi(\boldsymbol{x})$:

$$\lambda(\mathcal{T}) = \nabla_{\boldsymbol{x}} \phi(\boldsymbol{x}^*(\mathcal{T})) \tag{3.21}$$

Note that the absence of final constraints is equivalent to a null gradient, yielding the condition $\lambda(\mathcal{T}) = 0$.

Expressions (3.16), (3.20) and (3.21) gathers the necessary conditions for the optimality of an OCP solution that, in combination with the OCP constraints, can be summarized as:

$$\begin{array}{rcl} \boldsymbol{x}^*(0) & = & \boldsymbol{x}_0 \\ \dot{\boldsymbol{x}}^*(t) & = & f(\boldsymbol{x}^*(t), \boldsymbol{u}^*(t)) \\ \lambda^*(\mathcal{T}) & = & \nabla_{\boldsymbol{x}} \phi(\boldsymbol{x}^*(\mathcal{T})) \\ \dot{\lambda}^*(t) & = & -\nabla_{\boldsymbol{x}} H(\boldsymbol{x}^*(t), \boldsymbol{u}^*(t), \lambda^*(t)) \\ \boldsymbol{u}^*(t) & = & \arg\min_{\boldsymbol{u}} H(\boldsymbol{x}^*(t), \boldsymbol{u}, \lambda^*(t)) \end{array} \tag{3.22}$$

These conditions formulate a two-point BVP as long as they are given at the beginning and at the end of the time span. The solutions of this equivalent problem are candidates to the solution of the original OCP, but the PMP does not give any clue about which is the optimal solution since it is constructed around necessary conditions.

3.3.2 Additional constraints

The PMP has been introduced as a methodology to transform a complicated OCP into a much simpler BVP making use of necessary conditions. However, only final constraints have been introduced in the formulation so far.

Path constraints on the control variables are pretty straightforward to include. These simply reduce the seeking space for the control to the permitted range $\boldsymbol{U}$ when applying the *minimum principle*:

$$\boldsymbol{u}^*(t) = \arg\min_{\boldsymbol{u} \in \boldsymbol{U}} H(\boldsymbol{x}^*(t), \boldsymbol{u}, \lambda^*(t)) \tag{3.23}$$

The introduction of path constraints on the state variables of the form $c(\boldsymbol{x}, \boldsymbol{u}) \leq 0$ is a much more difficult job as the derivation of costates becomes more complicated. The main idea is that the ODE results in:

$$\dot{\lambda}^*(t) = -\nabla_{\boldsymbol{x}} H(\boldsymbol{x}^*(t), \boldsymbol{u}^*(t), \lambda^*(t)) - \nabla_{\boldsymbol{x}} c(\boldsymbol{x}^*(t), \boldsymbol{u}^*(t)) \mu^* \tag{3.24}$$

where μ^* is a constant multiplier. The complication lies on the fact that there is no straightforward way to calculate the appropriate value of this multiplier, which usually jumps from one value to another when the state trajectory touches the boundary [3, 4]. In practice this makes the state constraints very difficult if not impossible to include in many OCPs. The formalism to reach the above expression is complex and falls out of the scope of this dissertation, so the interested reader is redirected to one of the numerous works that discuss this particular case for a complete development, such as [3, 10, 11].

Finally, integral constraints of the form $\int_0^{\mathcal{T}} q(\boldsymbol{x}, \boldsymbol{u})\,\mathrm{d}t \leq 0$ can be easily included in the formulation with an additional state

$$\dot{x}_{N_x+1} = q(\boldsymbol{x}, \boldsymbol{u}) \tag{3.25}$$

with conditions

$$\begin{array}{rcl} x_{N_x+1}(0) & = & 0 \\ x_{N_x+1}(\mathcal{T}) & \leq & 0 \end{array} \tag{3.26}$$

which is the same philosophy followed to include integral constraints in DP (see section 3.2). Applying necessary conditions yields to:

$$\dot{\lambda}^*_{N_x+1} = \frac{\partial H}{\partial x_{N_x+1}}(\boldsymbol{x}^*, \boldsymbol{u}^*, \lambda^*) \tag{3.27}$$

Since Hamiltonian does not explicitly depend on x_{N_x+1} but at the corresponding λ_{N_x+1} term, the above differential vanishes:

$$\dot{\lambda}^*_{N_x+1} = 0 \tag{3.28}$$

Therefore the costate is a constant multiplier μ:

$$H(\boldsymbol{x}, \boldsymbol{u}, \lambda) = L(\boldsymbol{x}, \boldsymbol{u}) + \lambda^T f(\boldsymbol{x}, \boldsymbol{u}) + \mu q(\boldsymbol{x}, \boldsymbol{u}) \tag{3.29}$$

defined by the costate terminal condition as described previously:

$$\mu = \nabla_{\boldsymbol{x}} x^*_{N_x+1}(\mathcal{T}) \tag{3.30}$$

3.3.3 Bang-bang and singular control

An interesting yet complex situation is when the Hamiltonian depends linearly on the control, *e.g.*:

$$H(\boldsymbol{x}, u, \lambda) = \varphi(\boldsymbol{x}, \lambda)u + C \tag{3.31}$$

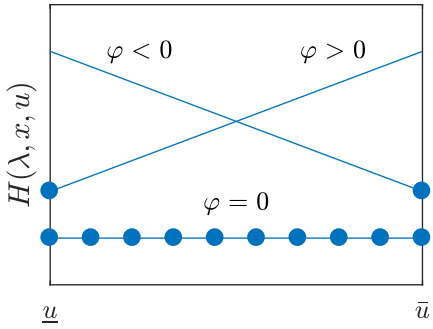

Figure 3.3: Illustration of a Hamiltonian for a *bang-bang* control situation. Note that for $\varphi < 0$ or $\varphi > 0$ the control that minimizes the Hamiltonian–represented with a dot–is trivial. However, if $\varphi = 0$, any value between $\underline{u}$ and $\bar{u}$ might be the optimal control. PMP theory does not give any additional information to find which is the correct solution.

The application of PMP yields to:

$$\dot{\lambda}^* = -u \nabla_{\boldsymbol{x}} \varphi(\boldsymbol{x}, \lambda) \tag{3.32}$$

and to the following *minimum principle*:

$$u^* = \arg\min_u \{\varphi(\boldsymbol{x}^*, \lambda^*) u\} \tag{3.33}$$

which is trivial for both $\varphi(\boldsymbol{x}^*, \lambda^*) < 0$ or $\varphi(\boldsymbol{x}^*, \lambda^*) > 0$, but not in the case of $\varphi(\boldsymbol{x}^*, \lambda^*) = 0$. In particular, if $\underline{u} \leq u \leq \bar{u}$:

$$u^* = \begin{cases} \bar{u}, & \varphi(\boldsymbol{x}^*, \lambda^*) < 0 \\ ?, & \varphi(\boldsymbol{x}^*, \lambda^*) = 0 \\ \underline{u}, & \varphi(\boldsymbol{x}^*, \lambda^*) > 0 \end{cases} \tag{3.34}$$

Figure 3.3 illustrates the above situation. If φ adopts a non-zero value, then the optimal control trajectory is immediate and only the switching points between $\bar{u}$ and $\underline{u}$ are to be found. This type of binary control is called *bang-bang control* because it jumps between the boundaries of the control variable [3]. It is the typical control of simple systems (or systems that have been simplified to a linear model) and can be found in many applications due to its easy implementation on real systems [4]. Several works deepen the subject such as [3, 11, 14].

The difficult part lies in determining the control trajectory when $\varphi = 0$ since the control variable vanishes from (3.33). This particular case is called

singular control as the PMP gives no clue to find the appropriate value and the control variable must be deducted from other considerations. One approach to bypass this issue is to repeatedly differentiate $\frac{\partial H}{\partial u}$ with respect to time until the control variable explicitly appears again [4] which is equivalent to state that the optimal control is such that the singular case holds for a determined period of time. Another approach is to use additional information such as the fact that the costate is constant as long as the *singular control* holds:

$$\dot{\lambda} = \frac{\partial \varphi}{\partial \boldsymbol{x}}(\boldsymbol{x}^*, \lambda^*)u = 0 \tag{3.35}$$

The term $\frac{\partial \varphi}{\partial \boldsymbol{x}}$ vanishes as long as $\frac{\partial \varphi}{\partial t} = 0$. Therefore, since the costate during the singular period must equal its value just before and after this period of time, it can be calculated and the control trajectory might be indirectly deducted.

A deeper discussion on *singular control* can be found in the works [3, 11, 14].

3.3.4 On the algorithm implementation

The numerical approach followed in this thesis is based on a shooting method to reduce the two-point BVP to a IVP which is easier to solve by forward integration.

Instead of considering the complete BVP stated in (3.22), the following IVP is stated:

$$\begin{array}{rcl} \boldsymbol{x}^*(0) & = & \boldsymbol{x}_0 \\ \dot{\boldsymbol{x}}^*(t) & = & f(\boldsymbol{x}^*(t), \boldsymbol{u}^*(t)) \\ \lambda^*(0) & = & \lambda_0 \\ \dot{\lambda}^*(t) & = & -\nabla_{\boldsymbol{x}} H(\boldsymbol{x}^*(t), \boldsymbol{u}^*(t), \lambda^*(t)) \\ \boldsymbol{u}^*(t) & = & \arg\min_{\boldsymbol{u}} H(\boldsymbol{x}^*(t), \boldsymbol{u}, \lambda^*(t)) \end{array} \tag{3.36}$$

where the final constraint $\lambda^*(\mathcal{T})$ in (3.21) has been exchanged with an initial condition $\lambda^*(0)$.

To numerically solve this IVP, the time span is discretized as $[t_0, t_1, \ldots, t_{n_t-1}]$ with $t_{i+1} - t_i = \Delta t$. The states and costates are known at the first time instant, so the optimal control can be calculated with the *minimum principle*. To do so, a brute-force search is used to find the control variable that minimizes $H(\boldsymbol{x}^*(t_i), \boldsymbol{u}, \lambda^*(t_i))$. Then, states and costates may be updated by forward integration:

$$\begin{array}{rcl} \boldsymbol{x}^*(t_{i+1}) & = & \boldsymbol{x}^*(t_i) + f(\boldsymbol{x}^*(t_i), \boldsymbol{u}^*(t_i))\Delta t \\ \lambda^*(t_{i+1}) & = & \lambda^*(t_i) - \nabla_{\boldsymbol{x}} H(\boldsymbol{x}^*(t_i), \boldsymbol{u}^*(t_i), \lambda^*(t_i))\Delta t \end{array} \tag{3.37}$$

The controls, states and costates trajectories can be calculated by repeating this sequence for all t_i from t_0 to t_{n_t-1}. These are the optimal trajectories of the IVP but does not necessarily correspond to the optimal solution to the BVP. Obviously, to be a solution to the BVP it must verify the final condition of the costates that has been previously neglected in favor of an initial constraint. Therefore, if $\lambda^*(t_{n_t-1}) = \nabla_{\boldsymbol{x}}\phi(\boldsymbol{x}^*(\mathcal{T}))$, or more practical, if $\phi(\boldsymbol{x}^*(t_{n_t-1})) = 0$–note that the inequality in (2.5) has been exchanged for an equality for the sake of clarity–, it is a solution to the BVP. In any other case, the value λ_0 must be modified accordingly and the whole process should be repeated until the final condition is fulfilled.

The strategy to choose different values of λ_0 is based on a nested intervals scheme. First, two boundaries, $\underline{\lambda}_0$ and $\bar{\lambda}_0$, are selected to build a first interval Λ_0 of λ_0 candidates such that their corresponding values for $\phi = \phi(\boldsymbol{x}^*(t_{n_t-1}))$ are $\underline{\phi} < 0 < \bar{\phi}$. Then, assuming a linear relation between λ_0 and ϕ, the next λ_0 candidate can be chosen as:

$$\lambda_0 = \frac{\bar{\phi}\underline{\lambda}_0 - \underline{\phi}\bar{\lambda}_0}{\bar{\phi} - \underline{\phi}} \tag{3.38}$$

This λ_0 candidate will produce a ϕ_0 value. Then, the following nested intervals can be selected as a function of ϕ_0:

$$\Lambda_i = \begin{cases} [\lambda_0, \bar{\lambda}_0], & \phi_0 < 0 \\ \lambda_0, & \phi_0 = 0 \\ [\underline{\lambda}_0, \lambda_0], & \phi_0 > 0 \end{cases} \tag{3.39}$$

A new λ_0 is calculated for the chosen interval with (3.38) and a new nested interval will be built again. The appropriate ${\lambda_0}^*$ value can be approached as much as desired with this strategy. Of course, the required number of iterations to deliver a satisfactory accuracy depends on the particular BVP. Note that in the description of this search algorithm a single costate has been assumed. Despite the same strategy might be followed with $N_x \geq 2$, the search of ${\lambda_0}^*$ gets much more complicated as cross relations between states affect to ϕ.

An important drawback of a numerical approach to PMP is faced when integrating the costate ODEs since these are generally ill-conditioned [3, 4]. Numerical integration methods produce a divergence from the $\lambda^*(t)$ trajectory even with tight tolerances. Many interesting problems suffer from this issue when PMP is applied and, therefore, they are very difficult to solve numerically. However, there are several workarounds to avoid the numerical integration of costates. In the case of systems where bang-bang or singular control applies,

an analytical solution to the *minimum principle* is usually possible, eliminating the need of a numerical approach. Also, if costates are constant multipliers, the problem can be solved numerically regardless of costates integration. If none of the two previous cases applies and an OCP is to be solved with PMP, a last workaround is possible. Recalling that $\lambda = \nabla_{\boldsymbol{x}} \mathcal{J}$ as it was derived in (3.15), if a previous solution to the OCP is available (*e.g.* from a DP calculation), $\lambda^*(t)$ can be obtained calculating the gradient [15, 16].

It is remarkable that the application of PMP only offers a set of solution candidates as long as (3.22) form a set of necessary but not sufficient conditions. However, if the candidate is unique, it must be the optimal solution to the OCP.

3.4 Direct methods

DM are a family of mathematical algorithms to numerically solve an OCP. They all share the same philosophy consisting in discretizing the infinite dimensional control variables to a finite succession of values such that the continuous time OCP can be transformed into a finite dimensional NLP problem. For this reason, this approach is often referred to as *first discretize, then optimize* [17].

These methods became popular in the last decades among various engineering fields with the profusion of powerful NLP solvers, with special interest in aerospace applications [18–21]. DMs have even been used to move the International Space Station with large energy savings compared to other approaches [22]. Nowadays it is gaining interest in numerous topics and can be found in many recent works on the optimal control field such as [1, 23–25].

The main advantage of DM is that it takes profit of advances on state-of-the-art solvers to address the equivalent NLP. This allows to handle large scale problems featuring numerous states and actuators with reduced computation time as this method does not suffer the *curse of dimensionality*. In addition, as it will be shown in the following points, constraints of any kind are pretty straightforward to include. However, since NLP algorithms are generally a combination of a gradient seeking technique and some heuristics–to enhance convergence and/or robustness of the method–the solutions are local optima depending on the initial seed. Therefore, there is no guarantee that the global optimum will be found, and even reaching a solution might be especially difficult for highly nonlinear systems or problems with many hard constraints.

According to [1], direct methods can be classified in three subgroups: (i) Direct Single Shooting (DSS), (ii) Direct Multiple Shooting (DMS), and

(iii) Direct Collocation (DC). These methods differ in the way they transform the OCP into a NLP.

With the DSS method, the control variables are parametrized by polynomials, piecewise functions, or more generally by piecewise polynomials. The state trajectories are considered dependent variables of the controls, so they are integrated according to the system dynamics. Therefore, the infinite dimensional OCP is transformed into a NLP whose unknowns are the parametrization of the controls, such that the integrated state trajectories fulfill the path, integral and boundary constraints. The resulting NLP is dense–a control decision not only affects the present time but also the upcoming behavior of the system states–and therefore expensive to compute. Thus, this method is usually aimed to quadratic problems that are much cheaper to solve.

The DMS method proceeds somehow in the same manner than DSS. Control variables are also parametrized, but the whole time span of the problem is split in several intervals. At each interval a single shooting problem is solved with fictitious initial states. An additional *continuity constraint* such that the state values at the end of an interval must meet the initial states at the following one is included to guarantee states continuity across intervals. The unknowns of the NLP are the control parametrization plus the fictitious initial states at each interval. The main advantage of this approach compared to DSS is that the resulting NLP is sparse–in general terms, although dense within an interval–at the expense of increasing the number of unknowns with the fictitious initial states, since each interval is an independent problem. This NLP, if addressed with an sparsity exploiting solver, should be relatively cheap to solve.

DC methods address the transcription to a NLP by discretizing not only control variables but also states. An embedded ODE solver is used to transform the continuous time dynamic system into a large set of algebraic constraints which also guarantees the continuity of the solution. Following this scheme, the integration of the state trajectories is no longer necessary. The unknowns of the NLP are both control and state variables. Note that the NLP solver itself is also used to *simulate* the system as the state trajectories are unknowns to the problem. The main advantage of this method is that the resulting NLP is extremely sparse and, therefore, much cheaper to solve than the above methods. On the contrary, the number of unknowns that the solver must optimize is much larger compared to shooting methods where only controls are discretized.

Due to computational burden reasons, the DC method is chosen for the works presented in this thesis. Therefore, this method is described in depth

in the following points. For a exhaustive discussion on the DSS and DMS methods, the reader is forwarded to [26].

3.4.1 Direct collocation

This DM is based on the collocation method, which is a numerical algorithm to solve ODEs, Partial Differential Equations (PDEs) and integral equations. The idea is to parametrize the solution by a known function, usually piecewise polynomials. Then, a number of collocation points are chosen and differential equations are evaluated at these points. The evaluation of the parametrized solution results in a system of algebraic equations, one for each collocation point, whose unknowns are the parameters of the candidate solution. This is the idea behind the DC method.

Similarly to the collocation method described above, the DC method parametrizes controls and states by piecewise polynomials in general–although it is very common to find works where piecewise constant functions are used instead due to their simplicity [27]. Following the philosophy of DMS as well, the time span is split in a number of independent intervals where the system dynamics are evaluated. The continuity of the solution is guaranteed including continuity constraints between intervals, enforcing that the states at the end of an interval must meet the initial values at the next one.

Within an interval, the parametrized controls and states are evaluated at each collocation point, resulting in a large system of algebraic equations. These algebraic equations in combination with the continuity constraints form a large scale but sparse NLP. Integral equations (namely the cost index and integral constraints) are approximated with quadrature formulas at the same collocation points. Path and boundary constraints are enforced at the unknowns of the NLP, either at the controls and states or at a linear combination of both.

Thus, the original infinite dimensional OCP has been transcribed into a finite and large scale NLP where time dependency has vanished. Then, to find a solution to the OCP the following NLP has to be addressed:

$$\min_{\mathbf{x},\mathbf{u}} \sum_{i=0}^{N_t-1} L_i(\mathbf{x}_i, \mathbf{u}_i) \tag{3.40}$$

subject to the following constraints:

$$\begin{array}{rcll} \mathbf{x}_0 - \boldsymbol{x}_0 & = & 0 & \\ \phi(\mathbf{x}_{N_t-1}) & \leq & 0 & \\ f(\mathbf{x}_i, \mathbf{u}_i) - \dot{\mathbf{x}}_i & = & 0, & i = 0, \ldots, N_t - 1 \\ c(\mathbf{x}_i, \mathbf{u}_i) & \leq & 0, & i = 0, \ldots, N_t - 1 \\ \sum_{i=0}^{N_t-1} q(\mathbf{x}_i, \mathbf{u}_i) & \leq & 0 & \end{array} \tag{3.41}$$

namely initial, final, system dynamics, path and integral constraints.

The OCP is no longer a dynamic problem after the transcription, so static optimization algorithms apply here. Usually, derivatives of the NLP are recommended–or even mandatory for some algorithms–so the solver has extensive information of the gradients. There are mainly two different approaches to supply the derivatives: numerical differentiation or explicit derivation of analytical functions. The first method consists in evaluating the problem functions at the neighborhood of a given value and calculate numerical gradients with an algebraic approach. This does not require much information about the NLP and in fact it may allow to handle black-box models. However, the gradients might be affected by numerical precision and the chosen differentiation step. The calculation of gradients requires numerous evaluations of the NLP functions and must be performed at each solver iteration, jeopardizing the performance of the algorithm. On the contrary, analytical differentiation provides exact derivatives that must be evaluated only once at each solver iteration. The derivatives may be supplied by hand or, more convenient, by a symbolic computation package. The main drawback of this approach is that full knowledge of the NLP functions is required, so only white-box models are suitable. Of course, to calculate derivatives the functions must show at least C^1 continuity.

The solution to the above NLP may be addressed with a sparsity exploiting solver. Interior point methods are generally the most efficient for this kind of problems [28]. Recall that the solution to the NLP might be a local minimum different from the global optimum. The minimum that is reached by the solver may depend on the starting seed so an appropriate initial solution is highly recommended to increase the probabilities of finding the global optimum. Anyhow, a global optimum is generally hard to guarantee, especially for highly nonlinear systems.

3.4.2 On the algorithm implementation

The algorithm used in the works presented in this thesis is an implementation of DC methods. State trajectories are discretized by piecewise polynomials of degree 1 and controls by piecewise constant functions, or more precisely, by

a finite set of discrete values situated at each collocation point. Collocation points are homogeneously distributed along the time span of the OCP with a constant spacing:

$$\Delta t = \frac{\mathcal{T}}{N_t} \tag{3.42}$$

where $N_t + 1$ is the number of collocation points at the state trajectory. The collocation points are set at different locations for control and state variables due to smoothness reasons given that they are approximated with different functions. The collocation grid for states is:

$$t = k\Delta t, \quad k = 0, \ldots, N_t \tag{3.43}$$

while for controls it is shifted $\Delta t/2$:

$$t = \left(\frac{1}{2} + k\right)\Delta t, \quad k = 0, \ldots, N-1 \tag{3.44}$$

Therefore, control and state trajectories result in the following set of discrete values:

$$\begin{array}{rcll} \mathbf{x} & = & \mathbf{x}_i, & i = 0, \ldots, N_t \\ \mathbf{u} & = & \mathbf{u}_i, & i = 0, \ldots, N_t - 1 \end{array} \tag{3.45}$$

Due to the fact that at each collocation interval both state and control trajectories are polynomials of degree 1 and 0 respectively, only continuity constraints are required to guarantee smoothness between discrete values. To do so, an embedded ODE solver is necessary to break time dependency and transform the continuity requisite into an algebraic constraint. The chosen solver is Euler's method for several reasons: (i) it is the simplest method to address differential equations, (ii) it involves only two consecutive collocation points, so the resulting NLP is as sparse as possible, and (iii) its low order produce simple algebraic functions that are cheap to evaluate. Of course, as a drawback, grid spacing should be chosen tight enough to guarantee a sufficient precision, close to high order methods. The dynamics of the system are then transcribed into a large number of algebraic constraints:

$$f\left(\frac{\mathbf{x}_{i+1} + \mathbf{x}_i}{2}, \mathbf{u}_i\right) - \frac{\mathbf{x}_{i+1} - \mathbf{x}_i}{\Delta t} = 0, \quad i = 0, \ldots, N_t - 1 \tag{3.46}$$

Note that the average of two consecutive collocation points is used at f since a centered method–which is indeed implicit–is used to avoid stability problems present at forward Euler's method.

Boundary constraints present in the OCP, namely (2.4) and (2.5), are enforced as constraints to the NLP unknowns $\mathbf{x}_i$:

$$\begin{aligned} \mathbf{x}_0 &= \boldsymbol{x}_0 \\ \phi(\mathbf{x}_{N_t}) &\leq 0 \end{aligned} \tag{3.47}$$

Path constraints of the form (2.6) are set individually for each collocation point:

$$c\left(\frac{\mathbf{x}_{i+1}+\mathbf{x}_i}{2}, \mathbf{u}_i\right) \leq 0, \quad i = 0, \ldots, N_t - 1 \tag{3.48}$$

Note that if c is only function of one state or control, the above expression does not apply as long as that path constraint is actually a boundary for the corresponding state or control.

If integral constraints such as (2.7) are present, they are managed with a quadrature scheme, particularly the trapezoidal rule:

$$\sum_{i=0}^{N_t-1} q\left(\frac{\mathbf{x}_{i+1}+\mathbf{x}_i}{2}, \mathbf{u}_i\right) \Delta t \leq 0 \tag{3.49}$$

The choice of the trapezoidal rule attends to the type of functions used to parametrize the states.

Finally, the cost index (2.1) is transcribed with the trapezoidal rule at the same collocation points:

$$J = \sum_{i=0}^{N_t-1} L\left(\frac{\mathbf{x}_{i+1}+\mathbf{x}_i}{2}, \mathbf{u}_i\right) \Delta t \tag{3.50}$$

Therefore, the original OCP has been transcribed into the following large scale NLP where dynamic and time dependent functions have vanished in favor of algebraic constraints:

$$\min_{\mathbf{x},\mathbf{u}} \sum_{i=0}^{N_t-1} L\left(\frac{\mathbf{x}_{i+1}+\mathbf{x}_i}{2}, \mathbf{u}_i\right) \Delta t \tag{3.51}$$

subject to the algebraic constraints in eqs. (3.46)–(3.49). Note that although Δt is constant and may be removed from the above minimization problem, it is kept in the formulation so that the algorithm supplies the cost index value in the appropriate units regardless of the chosen time step since it does not penalize the computation performance.

At this point, many NLP solvers require the user to provide at least first derivatives of cost index and constraints [29]. Even if it is not mandatory,

it is highly recommended since they give a very good clue about where the gradients of the functions point to. Obviously the more information the solver handles the faster the convergence to the optimal solution is, especially if this information indicates in which direction should proceed a seeking algorithm. Particularly, the cost index L, the constraints vector C, the gradient vector of the cost index G and the Jacobian matrix J–gradient of the constraints–are given in this implementation.

As stated in previous points, there are several methods to calculate the derivatives, two of which are common: numerical and symbolic differentiation. The last is the choice for this work, particularly because of two reasons: (i) the gradients are exact, avoiding a typical source of numerical errors, and (ii) once the symbolic derivatives are computed, it is much cheaper to evaluate those differentials at each solver iteration than calculating numerical gradients *ad-hoc*. However, this choice has two drawbacks as well: (i) functions must show at least C^1 continuity, which might be troublesome for discrete systems, and (ii) symbolic differentiation may be time consuming for complex systems. These two issues are addressed in this implementation as it will be discussed in the following points.

The transcription of the OCP is performed with a custom MATLAB function created *ad-hoc* for this thesis. The function only requires the user to provide analytical expressions for cost index and constraints; transcription and optimization are performed automatically without requiring any action from the user. It makes use of the Symbolic Math Toolbox to perform the algebra and differentiation of the supplied functions. The MATLAB function accepts theoretically any number of controls and states–there is no limitation at the code–although it has been tested up to $N_x = 8$ and $N_u = 6$. The user can provide as many constraints as necessary, namely boundary, path and integral constraints. The function proceeds performing first a simplification of the functions, following it applies the described DC method and calculates first derivatives, and finally it constructs individual functions for cost index, gradient, constraints and Jacobian matrix–note that the Jacobian is declared as an sparse matrix to save memory. It also builds a function to automatically call the NLP solver and proceed with the calculation of the solution to the OCP. The time it takes to transcribe a problem depends upon the number of states, controls and constraints, and the complexity of the functions–but not on the number of collocation points. For reference, the simplest problem addressed in this thesis took < 1 second, while the toughest one–engine model with $N_x = 6$ and $N_u = 4$–took about 75 seconds.

Concerns on NLP sparsity and memory usage

This NLP is extremely sparse due to the choice of piecewise constant functions and Euler's method. As it can be appreciated in (3.46) and (3.48), algebraic constraints are only a function of states and controls at the neighbor collocation points i and $i+1$, so a diagonal NLP is to be expected. Only (3.49) and (3.50) are dense since the sum includes all collocation points. The general sparsity of the problem makes functions cheap to evaluate with a significant reduction in the computation time of the optimization task.

The number of non-zero elements of a generic OCP with N_x states, N_u controls, N_{ic} integral constraints and N_{pc} path constraints can be easily calculated assuming that all cross relations between controls and states are present. On the one hand, the cost index L is a single element so:

$$N_{\mathrm{L}} = 1 \tag{3.52}$$

The constraint vector $\mathrm{C} \in \mathbb{R}^{N_{\mathrm{C}}}$ has N_t algebraic constraints for each state dynamics and path constraint, according to (3.46) and (3.48), while a single algebraic constraint stands for each integral constraint (3.49). Therefore:

$$N_{\mathrm{C}} = N_t(N_x + N_{pc}) + N_{ic} \tag{3.53}$$

The gradient vector G has as many components as unknowns of the NLP since the cost index is differentiated with respect to these unknowns:

$$N_{\mathrm{G}} = (N_t + 1)N_x + N_t N_u \tag{3.54}$$

Finally, the Jacobian matrix $\mathrm{J} \in \mathbb{R}^{N_{\mathrm{C}} \times N_{\mathrm{G}}}$ has as many rows as constraints and one column for each unknown. Taking into account that derivatives with respect to states depend upon two consecutive collocation points while they do upon only one collocation point for controls, the number of non-zero elements of this sparse matrix is no greater than:

$$N_{\mathrm{J}} = N_t(2{N_x}^2 + N_x N_u + (2N_{pc} + N_{ic})N_x + (N_{pc} + N_{ic})N_u) \tag{3.55}$$

Therefore, the total number of non-zero elements that the NLP must handle is as high as:

$$N_{nz} = N_{\mathrm{L}} + N_{\mathrm{C}} + N_{\mathrm{G}} + N_{\mathrm{J}} \tag{3.56}$$

which represents a tiny fraction of the total size of J, as it can be appreciated in the depiction of a generic Jacobian matrix in figure 3.4 where non-zero elements are approximately an 8% of the matrix. The same NLP with an increased

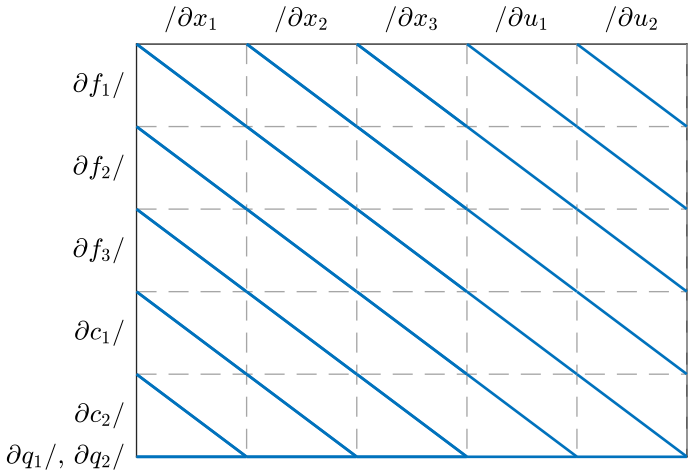

Figure 3.4: Representation of a generic Jacobian matrix for an OCP with $N_x = 3$, $N_u = 2$, $N_{pc} = 2$, $N_{ic} = 2$ and 20 collocation points, where blue dots represent non-zero values. This matrix contains the derivative of NLP problem constraints with respect to all unknowns (x and u). Each quadrant correspond to the derivative of a constraint with respect to a state or a control, from $t_i = 0$ to $t_i = \mathcal{T}$. The diagonal shape is due to the dependency of constraints on only two consecutive time instants. Constraint functions are referenced on the left side (dynamic, path and integral constraints from top to bottom), while state and controls are indicated on top. Note that integral constraints appear at the bottom of the matrix as dense rows. For reference, this matrix has 900 non-zero elements out of 10403, roughly representing an 8% of the full matrix.

number of collocation points–the example at the figure has 20 points only for a better display–such as $N_t = 600$, features a 0.3% of non-zero elements.

It is interesting that the amount of information to manage is a polynomial function of the number of states–degree 2–and control–degree 1. Contrary to the DP method, where memory requirements are an exponential function of the number of states, DMs are not affected by the *curse of dimensionality*. Functions are light and cheap to evaluate so the DC method can handle bigger problems with a reasonable computation time. According to the memory usage shown in figure 3.5, the requisites for this algorithm might lie under 1 MB, which is a very low value compared to DP requirements. To reach the 1 GB barrier, the OCP should feature about 100 states, controls, path and integral constraints, and 100000 collocation points which would be, of course, a massive system.

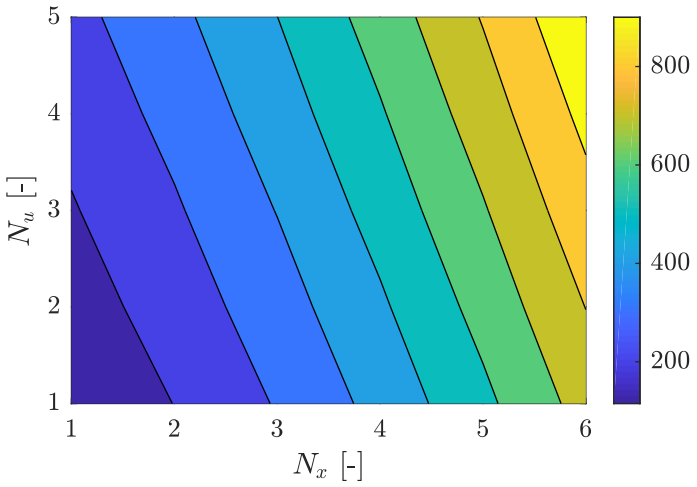

Figure 3.5: Maximum memory usage in kB for a generic OCP optimization using the proposed DC algorithm as a function of the number of states and controls. The number of collocation points for this example is $N_t + 1 = 600$. Additional constraints are $N_{pc} = 3$ and $N_{ic} = 3$.

Embedded ODE solver precision

The performance of the chosen ODE solver has been evaluated and compared to two common options: forward Euler and fourth-order Runge-Kutta. To do so, an arbitrary ODE is used as a benchmark:

$$\frac{\mathrm{d}y}{\mathrm{d}x} = 2y - x^2 \tag{3.57}$$

with initial condition $y(0) = 1$. The analytical solution to this ODE is:

$$y = \frac{1}{4}\left(5e^{2x} - 2x^2 - 2x - 1\right) \tag{3.58}$$

The ODE is addressed with the solver used for the described DC method as well as with the two additional methods mentioned above at the interval $[0, 1]$. The mean error between exact and numerical solutions is calculated as:

$$E(\tilde{y}) = \frac{1}{N_t} \sum_{i=0}^{N_t - 1} \left| \frac{y_i - \tilde{y}_i}{y_i} \right| \tag{3.59}$$

and can be found in the figure 3.6 for a number of collocation points ranging from $N_t + 1 = 10$ to $N_t + 1 = 50$. Of course, the error of a numerical method can be tightened as much as desired by increasing the grid density. However,

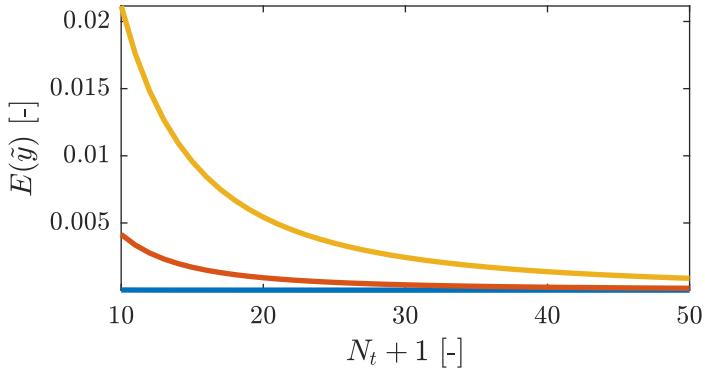

Figure 3.6: Mean error in the solution of the benchmarking ODE for various numerical methods as a function of the number of collocation points in the interval $[0, 1]$. The displayed methods are fourth-order Runge-Kutta (blue), centered Euler (red) and forward Euler (yellow).

for a given number of collocation points, it can be appreciated that a significant increase in the solution accuracy–about a factor of four–can be achieved by shifting from forward Euler to centered Euler. The Runge-Kutta method is still more accurate than centered Euler, but both methods converge to similar precision rapidly as N_t increases. Regarding computational burden, forward Euler took 32% less time than centered Euler while Runge-Kutta took 15% more for this example. Note that Runge-Kutta not only takes more time but it also would produce a denser Jacobian matrix, increasing the memory requirements. Therefore, as Euler's method produce very simple and cheap to evaluate algebraic constraints, centered Euler is the choice for the embedded ODE solver.

Symbolic differentiation

Symbolic differentiation is performed automatically in the MATLAB environment with the Symbolic Math Toolbox. In order to avoid the expensive derivation of complex functions, cost index and constraints are first partitioned in simpler expression as a composition of functions. The derivatives of these expressions are computed separately and then the chain rule is applied to rebuild the original function. This not only permits reducing the symbolic computation burden but also delivers more compact functions to the solver since expressions that take part in several constraints are only evaluated once.

NLP solver

The NLP resulting from the transcription of the OCP is addressed with a third-party solver. Due to the specific characteristics of this NLP, a sparsity exploiting solver able to handle large scale problems would be more appropriate. Among all the available options, IPOPT is the choice for its efficiency and ease of use. It is based on the interior point method and is specifically made to solve large scale problems. The cross-platform source code can be downloaded at the COIN-OR initiative website. For further information and a discussion about its internal algorithms, please check [29]. The interested reader my found a comprehensive discussion about NLP in [30].

The solver is provided with the cost index, its gradient, the constraints, the Jacobian, unknowns boundaries and an initial solution. Second derivatives–*i.e.* the Hessian–are not supplied explicitly due to the prohibitive computation time it takes to calculate all cross-derivatives with symbolic differentiation. Instead, the embedded algorithm for numerical differentiation present in IPOPT–Limited-memory Broyden-Fletcher-Goldfarb-Shanno (L-BFGS)–is used. More details about this numerical approximation can be found in [31].

In general, default options are used. Specific tweaks are left for the particular requisites of each OCP. Iterations limit and convergence tolerance are tuned individually. Warm start functionality is used in some particular problems as it will be discussed in following points.

The performance of the solver is strongly related to the quality of the provided initial solution. There is no general rule to infer which would be good guess and which would not as it is a problem-specific question. A problem with many local minima might be affected by a bad initial seed; however, it is not usually the case, and smooth problems tend to converge to the same minimum for many different initial guesses. In this last case, the suitability of a seed lies more on the number of iterations IPOPT requires to find a minimum, which is not a big issue for problems with functions that are cheap to evaluate. Given all the above, initial solutions in this dissertation are specified as constant quantities for each control and state variable–within a reasonable range according to their physical meaning. Better performance may be achieved with heuristics to derive a better initial guess, but the impact of the adopted approach is already small.

Management of discrete systems

The transcription of the OCP requires problem functions to show at least C^1 continuity, as it was introduced above. This requisite prevents the application

of DMs to systems where one or several variables–states or controls–adopt discrete values.

The straightforward way to handle this issue is to reconsider the transcription of the OCP including integer variables on its formulation. Therefore, the NLP defined above in eqs. (3.40) and (3.41) can be extended to:

$$
\begin{array}{rrcll}
\min_{\mathbf{x},\mathbf{u}} & \sum_{i=0}^{N_t-1} L_i(\mathbf{x}_i, \mathbf{u}_i) & & & \\
\text{s.t.} & \mathbf{x}_0 - \boldsymbol{x}_0 & = & 0 & \\
& \phi(\mathbf{x}_{N_t-1}) & \leq & 0 & \\
& f(\mathbf{x}_i, \mathbf{u}_i) - \dot{\mathbf{x}}_i & = & 0, & i = 0, \ldots, N_t - 1 \\
& c(\mathbf{x}_i, \mathbf{u}_i) & \leq & 0, & i = 0, \ldots, N_t - 1 \\
& \sum_{i=0}^{N_t-1} q(\mathbf{x}_i, \mathbf{u}_i) & \leq & 0 & \\
& \check{\mathbf{x}}_i & \in & \mathbb{Z}^{N_{\check{x}}}, & i = 0, \ldots, N_t \\
& \check{\mathbf{u}}_i & \in & \mathbb{Z}^{N_{\check{u}}}, & i = 0, \ldots, N_t - 1
\end{array}
\tag{3.60}
$$

where $\check{\mathbf{x}}$ and $\check{\mathbf{u}}$ are subsets of state and control vectors containing integer variables. The above program is known as a MINLP as long as it combines integer and continuous variables in a single problem.

Unfortunately, this type of problems are tough to solve. According to the computational complexity theory, MINLPs are considered NP-hard problems, *i.e.* at least as hard to solve as the hardest non-deterministic polynomial (NP) problem [32]. An NP problem is a class of computational problems that can be solved in polynomial time (in a limited amount of time given by a polynomial of the dimensions of the problem or less) with a non-deterministic Turing machine [33]; on the contrary, NP-hard problems are thought to require super-polynomial time to be solved (*e.g.* exponential) or, even worse, an algorithm different from brute-force search may not exist and only suboptimal guesses can be achieved [32]. All the above means that, in practice, finding a solution to an MINLP is a difficult task that might require large amounts of resources and time. Anyhow, MINLP solvers such as Bonmin [34] or Nomad [35] exist. They use branch-and-bound [36], branch-and-cut [37] or outer-approximation [38] techniques that usually end up solving a relaxed NLP–the original program but assuming $\check{\mathbf{x}}, \check{\mathbf{u}} \in \mathbb{R}$. These algorithms are practical for small problems–or at least featuring few integer variables. An OCP with a single integer control will involve hundreds or thousands of integer variables (as many as collocation points), making this problem untractable with the above techniques.

A simpler approach is proposed in this thesis. First, the relaxed form of the MINLP described in (3.60)–*i.e.* removing the last two constraints–is

addressed as a plain NLP. Then, the resulting continuous trajectories of $\check{\mathbf{x}}$ and $\check{\mathbf{u}}$ are rounded to fulfill the integer constraints:

$$\check{\mathbf{x}}^* = \lfloor \check{\mathbf{x}} \rceil \tag{3.61}$$

where $\lfloor \cdot \rceil$ is the nearest integer function. A second NLP is then addressed with these integer trajectories as disturbances to the problem. The aim of this last program is to guarantee that, given the integer trajectories, the optimal solution fulfills all the constraints. Thankfully, this NLP is relatively cheap to solve since it features $N_x - N_{\check{x}}$ states and $N_u - N_{\check{u}}$ controls. Warm start is also possible to improve performance as the solution to the second NLP is usually on the surroundings of the solution to the relaxed problem.

The solution achieved with the proposed workaround is of course sub-optimal but should be as close to the optimum as the integer variables are to be smooth functions and does not require significant computational resources compared to an NLP. On the contrary, this method should not be suitable for binary variables or integer quantities that are difficult to approximate to continuous functions.

References

[1] M. Diehl et al. "Fast direct multiple shooting algorithms for optimal robot control". In: *Fast motions in biomechanics and robotics*. Springer, 2006, pp. 65–93.

[2] R. Bellman. "The theory of dynamic programming". In: *Bulletin of the American Mathematical Society* 60.6 (1954), pp. 503–515.

[3] F. Lewis and V. Syrmos. *Optimal control*. Wiley-Interscience, 1995.

[4] A. E. Bryson and Y.-C. Ho. *Applied optimal control: optimization, estimation, and control*. Taylor & Francis, 1975.

[5] R. Bellman. "Dynamic programming and Lagrange multipliers". In: *Proceedings of the National Academy of Sciences* 42.10 (1956), pp. 767–769.

[6] *AMD64 architecture programmer's manual volume 2: System programming*. Advanced Micro Devices. 2006.

[7] R. Grisenthwaite. "ARMv8 technology preview". In: *IEEE Conference*. 2011.

[8] J. Rust. "Using randomization to break the curse of dimensionality". In: *Econometrica* 65.3 (1997), pp. 487–516.

[9] W. B. Powell. *Approximate dynamic programming: solving the curses of dimensionality*. Vol. 703. John Wiley & Sons, 2007.

[10] H. P. Geering. *Optimal control with engineering applications*. Springer, 2007.

[11] R. Vinter. *Optimal control*. Springer, 2010.

[12] O. Sundström and L. Guzzella. "A generic dynamic programming Matlab function". In: *IEEE Control Applications, Intelligent Control*. 2009, pp. 1625–1630.

[13] L. S. Pontryagin et al. *The mathematical theory of optimal processes*. Interscience, New York, 1962.

[14] H. Schättler and U. Ledzewicz. *Geometric optimal control: Theory, methods and examples*. Springer, 2012.

[15] C. Guardiola et al. "A new approach to optimally tune the control strategy for hybrid vehicles applications". In: *Engine and Powertrain Control, Simulation and Modeling*. Vol. 3. 1. 2012, pp. 255–261.

[16] C. Guardiola et al. "Insight into the HEV/PHEV optimal control solution based on a new tuning method". In: *Control Engineering Practice* 29 (2014), pp. 247–256.

[17] M. Hinze and A. Rösch. "Discretization of optimal control problems". In: *Constrained optimization and optimal control for partial differential equations*. Springer, 2012, pp. 391–430.

[18] P. J. Enright and B. A. Conway. "Optimal finite-thrust spacecraft trajectories using collocation and nonlinear programming". In: *Journal of Guidance, Control and Dynamics* 14.5 (1991), pp. 981–985.

[19] O. A. Yakimenko. "Direct method for rapid prototyping of near-optimal aircraft trajectories". In: *Journal of Guidance, Control, and Dynamics* 23.5 (2000), pp. 865–875.

[20] F. Fahroo and I. M. Ross. "Advances in pseudospectral methods for optimal control". In: *AIAA Guidance, Navigation and Control Conference and Exhibit*. 2008, pp. 1–23.

[21] C. L. Darby and A. V. Rao. "Minimum-fuel low-earth orbit aeroassisted orbital transfer of small spacecraft". In: *Journal of Spacecraft and Rockets* 48.4 (2011), pp. 618–628.

[22] W. Kang and N. Bedrossian. "Pseudospectral optimal control theory makes debut flight, saves NASA $1 M in under three hours". In: *SIAM news* 40.7 (2007), pp. 1–3.

[23] L. V. Pérez and E. A. Pilotta. "Optimal power split in a hybrid electric vehicle using direct transcription of an optimal control problem". In: *Mathematics and Computers in Simulation* 79.6 (2009), pp. 1959–1970.

[24] J. Asprion, O. Chinellato, and L. Guzzella. "Optimal control of diesel engines: Numerical methods, applications, and experimental validation". In: *Mathematical Problems in Engineering* 1 (2014), pp. 1–21.

[25] Y. Wang et al. "Optimal trajectory planning for trains under fixed and moving signaling systems using mixed integer linear programming". In: *Control Engineering Practice* 22 (2014), pp. 44–56.

[26] J. T. Betts. *Practical methods for optimal control and estimation using nonlinear programming*. SIAM, 2010.

[27] D. A. Benson et al. "Direct trajectory optimization and costate estimation via an orthogonal collocation method". In: *Journal of Guidance, Control, and Dynamics* 29.6 (2006), pp. 1435–1440.

[28] K. Fujisawa, M. Kojima, and K. Nakata. "Exploiting sparsity in primal-dual interior-point methods for semidefinite programming". In: *Mathematical Programming* 79.1 (1997), pp. 235–253.

[29] A. Wächter and L. T. Biegler. "On the implementation of an interior-point filter line-search algorithm for large-scale nonlinear programming". In: *Mathematical Programming* 106.1 (2006), pp. 25–57.

[30] D. P. Bertsekas. *Nonlinear programming*. Athena scientific Belmont, 1999.

[31] J. Nocedal. "Updating quasi-Newton matrices with limited storage". In: *Mathematics of Computation* 35.151 (1980), pp. 773–782.

[32] J. Van Leeuwen. *Handbook of theoretical computer science: algorithms and complexity*. Vol. A. Elsevier, 1990.

[33] D. E. Knuth. "Postscript about NP-hard problems". In: *SIGACT News* 6.2 (1974), pp. 15–16.

[34] P. Bonami et al. "An algorithmic framework for convex mixed integer nonlinear programs". In: *Discrete Optimization* 5.2 (2008), pp. 186–204.

[35] S. Le Digabel. "Algorithm 909: NOMAD: nonlinear optimization with the MADS algorithm". In: *ACM Transactions on Mathematical Software* 37.4 (2011), pp. 1–15.

[36] A. H. Land and A. G. Doig. "An automatic method of solving discrete programming problems". In: *Econometrica: Journal of the Econometric Society* 28.3 (1960), pp. 497–520.

[37] M. Padberg and G. Rinaldi. "A branch-and-cut algorithm for the resolution of large-scale symmetric traveling salesman problems". In: *SIAM Review* 33.1 (1991), pp. 60–100.

[38] M. A. Duran and I. E. Grossmann. "An outer-approximation algorithm for a class of mixed-integer nonlinear programs". In: *Mathematical programming* 36.3 (1986), pp. 307–339.

Chapter 4

Modeling

You should always bear in mind that entropy is not on your side.

— Elon Musk

Contents

Work (chapter or section)	Model
HP- and LP-EGR control (6.2)	Experimental measurements
Full engine control (6.3)	(4.5) MVEM w/ quasi-steady cylinder
Speed and engine control (7)	(4.2) Vehicle dynamics
	(4.3) Gearbox and clutch
	(4.5) MVEM w/ quasi-steady cylinder
HEV energy management (8)	(4.2) Vehicle dynamics
	(4.3) Power-split
	(4.4) Motor and battery
	(4.5) Quasi-steady engine
HRL design (9.2)	(4.5.5) Detailed in-cylinder process
HEV powertrain sizing (9.3)	(4.2) Vehicle dynamics
	(4.3) Gearbox and power-split
	(4.4) Motor and battery
	(4.5) Quasi-steady engine

Table 4.1: Summary of the models described in this chapter along with the works in which they have been used.

4.1 Introduction

The states of an OCP are driven by a dynamic model of the system. This model is usually expressed as a set of ODEs. The model might be a black-box, gray-box or any other approach if gradients are supplied. In this case, a physical model is chosen since: (i) it can extrapolate the behavior of a system with a certain confidence, (ii) it works fine with little experimental information, and (iii) the physical laws that govern the system are known.

For the works presented in this thesis, models for vehicle dynamics, transmission, electrical path and engine are required. These models are summarized in table 4.1 according to the study they are aimed to, and described in the following sections.

4.2 Vehicle dynamics

The vehicle is modeled attending to longitudinal dynamics only, since it is considered to travel in normal conditions such that transversal dynamics are negligible. Several forces act on the vehicle as it can be appreciated in figure 4.1, where direction and sign are displayed in a general case. Following this scheme, all forces are analyzed following.

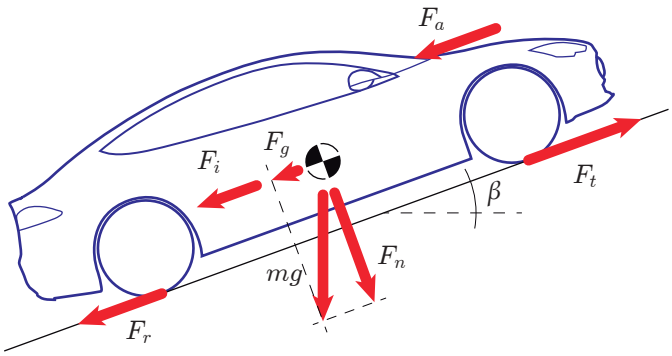

Figure 4.1: Scheme of forces acting on a vehicle. The sign of the forces displayed assumes an acceleration in the direction of movement. Note that forces are applied to different areas, namely the contact between tire and road, the center of mass and the front.

First, the vehicle is exposed to the aerodynamic drag which is a function of the vehicle's frontal area A, the external shape represented by the dimensionless drag coefficient C_d, the air density ρ and the square of the speed v [1]:

$$F_a = \frac{1}{2} A C_d \rho v^2 \tag{4.1}$$

The contact between the tire and the road induces a rolling friction [2]. This is characterized with the dimensionless rolling friction coefficient c_r which depends on the particular tire model and tarmac composition [3]. However it is commonly accepted to be in the range of 0.010 to 0.015 for passenger cars [4]. The rolling friction force can then be represented as:

$$F_r = c_r m_v g \cos\beta \tag{4.2}$$

Note the presence of the road grade β in the above equation to account for the normal component of the weight $m_v g$ if the track is not flat. Similarly, the parallel component entails a deterrent to the progress of the vehicle as it climbs up:

$$F_g = m_v g \sin\beta \tag{4.3}$$

According to Newton's Second Law, a variation on the speed of the vehicle produces a force that is proportional to the mass m_v:

$$F_i = m_v \dot{v} \tag{4.4}$$

The contribution of the traction torque at the wheels T_w can be accounted with the wheel radius r_w as:

$$F_t = \frac{T_w}{r_w} \tag{4.5}$$

Finally, if brakes are actuated, there is an additional force that can be modeled as:

$$F_b = u_b \widehat{F}_b \tag{4.6}$$

where $u_b \in [0, 1]$ is the position of the brake pedal and $\widehat{F}_b$ is the maximum braking force.

The sum of all the forces acting on the vehicle must count zero. Therefore, summing all the above and ordering terms results in the following ODE:

$$\dot{v} = \frac{F_t - F_a - F_r - F_g - F_b}{m_v} \tag{4.7}$$

which is the main equation of the vehicle longitudinal dynamics. Recall that not all forces are applied to the center of mass, producing a moment and a variation on the pitch. However, assuming the vehicle as a rigid body, these moment is canceled by the reaction to the normal F_n on the point of contact between tire and road and is negligible to longitudinal dynamics.

Most of the required parameters for the above equation have a physical meaning and, therefore, they can be easily quantified. Mass m_v, frontal area A, drag coefficient C_d and wheel radius r_w are found at manufacturer data-sheets. The road grade β can be obtained from a geographic database. The road grade profiles displayed in this thesis are gathered from the Google Maps Elevation API web service that returns the elevation for a given coordinates by issuing an HTTP request. It must be noted that torque demand is specially sensible to road grade variations, as long as a 1° deviation could make around 25% difference in engine torque. Unfortunately, within the works developed in this dissertation, there was no other elevation source to contrast the data. However, for benchmarking studies and comparisons, a reasonable source of orographic data is enough.

Rolling friction coefficient is much difficult to identify as it depends on tires, road roughness and weather, but it can be safely set to a value between 0.010 and 0.015.

Further terms might be introduced in (4.7) such as the moment of inertia of the wheels, or shafts and transmissions efficiency, but their effects on vehicle dynamics can be also included in (4.7) in its current form. For example, the introduction of the moment of inertia is equivalent to the use of the corrected

vehicle mass $\tilde{m}_v = m_v + \frac{I_\omega}{{r_w}^2}$, since the dragging force that creates the moment of inertia I_ω is $F_\omega = \frac{I_\omega}{{r_w}^2}\dot{v}$. Similarly, including an efficiency–that penalizes the tractive force–is equivalent to consider a lower T_w output. If experimental data is available, a fitting may be performed to account for these effects.

This model has been used for the different vehicles that have been used during the elaboration of this thesis. Validation is done with experimental data from a pre-production 4-door sedan with results displayed in figure 4.2. These plots show two simulations of road load accelerations in 3rd gear starting at two different speeds. The red and blue simulations are obtained after a fitting to the experimental data for a fine tune of vehicle parameters, while gray data makes use of information from manufacturer's data-sheet only. The error between simulations and experimental data is always below 1 km/h which can be considered an acceptable accuracy for most of the cases. If no fitting is performed errors may be higher, but speed trajectories are still close to experimental data. Considering that in this particular case the only differences after fitting are an increase in mass of 40 kg and a reduction of 26 mm in wheel radius, the use of vehicle's data-sheet information only may be sufficient in many situations.

4.3 Transmission

The transmission of energy to wheels is conducted throughout several devices according to the type of vehicle. The torque is transferred through a clutch, a gearbox and the final drive in a conventional vehicle with manual gearbox. In the case of a HEV the power flow gets more complicated since several architectures may be adopted with the introduction of a power-split device. The main powertrain architectures and their energy flow layout are shown in figures 4.3, 4.4 and 4.5. Models for the transmission chain are described in the following points.

4.3.1 Gearbox

The gearbox is modeled as a discrete set of gear ratios with a fixed efficiency [4, 5]. Therefore, the kinetic relations in the gearbox are:

$$\omega_{gb,ds} = \frac{\omega_{gb,us}}{R_{gb}} \tag{4.8}$$

$$T_{gb,ds} = \eta_{gb} R_{gb} T_{gb,us} \tag{4.9}$$

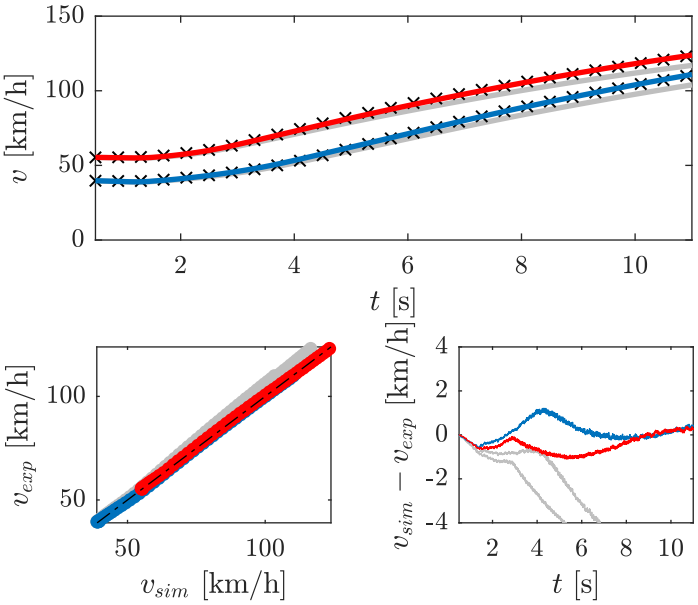

Figure 4.2: Validation of vehicle model. Two road load accelerations are shown in top plot for different initial speeds. Gray lines correspond to the model using data-sheet information, while red and blue lines are simulations after a fine tune of model parameters. Experimental data is displayed as black crosses. Bottom plots quantify model discrepancies by showing the correlation between simulated and experimental results (left) and the error in speed between both (right).

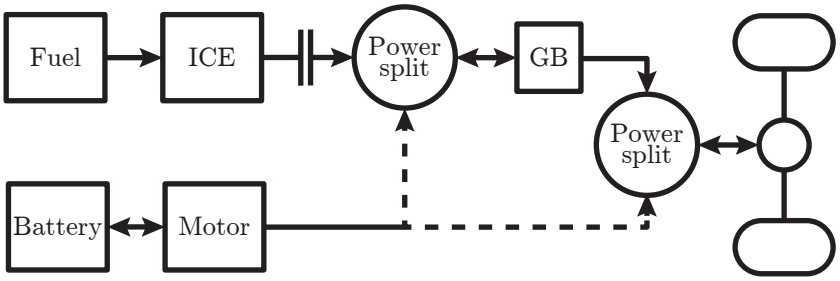

Figure 4.3: Layout scheme of a parallel HEV. Note that the power-split device might be present upstream or downstream the gearbox.

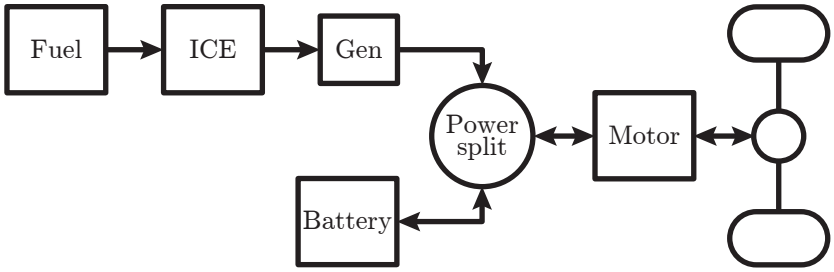

Figure 4.4: Layout scheme of a series HEV.

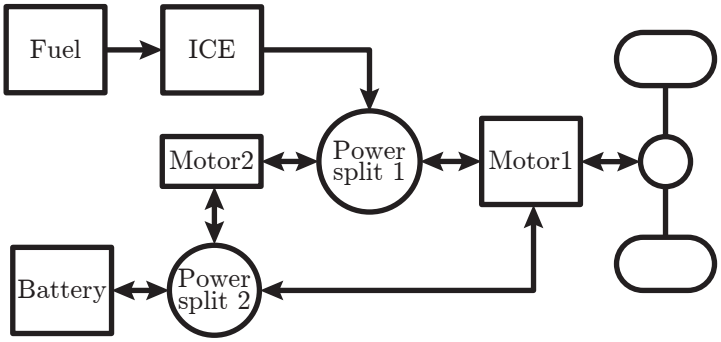

Figure 4.5: Layout scheme of a combined HEV.

where the gearbox ratio R_{gb} is a function of the selected gear number:

$$R_{gb} = R_{gb}(N_{gb}) \tag{4.10}$$

4.3.2 Clutch

The clutch is a pair of friction discs that allows the disconnection between the ICE and the gearbox with the action of a control variable u_{clt}. This element introduces a discontinuity since discs can be: (i) rigidly coupled, (ii) slipping, and (iii) separated. In the first case, the model is just a shaft so input and output variables are the same:

$$T_{clt,ds} = T_{clt,us} \tag{4.11}$$

$$\omega_{clt,ds} = \omega_{clt,us} \tag{4.12}$$

The slipping case is more complex and is represented with a friction model. The clutch consists of two annular surfaces that are in contact with a pressure

p_{clt} [5]. The transferred force in a infinitesimal annular section of radius r and width $\mathrm{d}r$ is:

$$\mathrm{d}F = 2\pi r \mu_{clt} p_{clt}\, \mathrm{d}r \tag{4.13}$$

Therefore, the torque for this slice is:

$$\mathrm{d}T = 2\pi r^2 \mu_{clt} p_{clt}\, \mathrm{d}r \tag{4.14}$$

Integrating the above expression between the inner and outer radius $r_{clt,i}$ and $r_{clt,o}$, the total transferred torque between both friction discs is:

$$T = 2\pi \mu_{clt} p_{clt} \frac{r_{clt,o}^3 - r_{clt,i}^3}{3} \tag{4.15}$$

Applying conservation of angular momentum at both upstream and downstream discs:

$$T_{clt,us} = T + I_{clt,us}\dot{\omega}_{clt,us} \tag{4.16}$$

$$T_{clt,ds} = T - I_{clt,ds}\dot{\omega}_{clt,ds} \tag{4.17}$$

Introducing (4.15) in the two above expressions and arranging terms, the equations for the slipping model result:

$$\dot{\omega}_{clt,us} = \frac{T_{clt,us}}{I_{clt,us}} - \frac{2\pi \mu_{clt} p_{clt} (r_{clt,o}^3 - r_{clt,i}^3)}{3 I_{clt,us}} \tag{4.18}$$

$$T_{clt,ds} = 2\pi \mu_{clt} p_{clt} \frac{r_{clt,o}^3 - r_{clt,i}^3}{3} - I_{clt,ds}\dot{\omega}_{clt,ds} \tag{4.19}$$

The slipping model also consider the case where both discs are separated if $p_{clt} = 0$. In that situation, the upstream rotational speed is only determined by the upstream moment of inertia $I_{clt,us}$ while the downstream torque is just a consequence of the variation of the rotational speed.

The switch between models is performed attending to the upstream torque and difference in speed between discs. In the case $T_{clt,us} > T$ the slipping model is used regardless of speed since the clutch is unable to transfer that amount of torque and it will slip. Otherwise, the coupled model is used when $\omega_{clt,us} - \omega_{clt,ds} = 0$.

4.3.3 Power-split device

Power-split devices manage the supply of energy to the wheels splitting the demand between two different energy sources. They can be devices of many different types, both mechanical and electrical. The precise internal architecture of the power-split device is not relevant for the scope of this work–only energy transfer relations are of interest. Therefore, they are modeled as black boxes with a set of input/output relations and a constant efficiency, specific for each powertrain layout [5, 6].

Parallel HEV

The power-split device in a parallel HEV is a mechanical divisor. It splits the torque requirements between the electric motor and the ICE. As shown in figure 4.3 the power-split device may be installed upstream or downstream the gearbox. Physically, the device can be a mechanical joint with any kind of gearing or, most of the times, a motor mounted coaxially in the transmission shaft. In the case of a device installed downstream the gearbox, the motor may propel an axle while the ICE propels the other, being the road the power-split device itself. In any case, the kinetic relations that a power-split device must fulfill are:

$$\omega_{ps,ds} = \frac{\omega_{ps,us1}}{R_{ps,1}} \tag{4.20}$$

$$\omega_{ps,us2} = \omega_{ps,ds} R_{ps,2} \tag{4.21}$$

$$T_{ps,ds} = \eta_{ps}(T_{ps,us1} R_{ps,1} + T_{ps,us2} R_{ps,2}) \tag{4.22}$$

where $R_{ps,1}$ and $R_{ps,2}$ are the gear ratios between inputs and output. The subindices in rotational speeds ω_{ps} and torques T_{ps} refer to one of the two input shafts (upstream, us) or the output shaft (downstream, ds). In the case of a coaxial motor, the efficiency of the device is $\eta_{ps} = 1$ since there is no kinetic chain involved in the torque transfer.

Series HEV

A series HEV is basically an EV with a gen-set–ICE coupled to a generator, see figure 4.4–that contributes to the battery charging or eventually delivering additional current peaks. The power-split device is typically an electric bus fed by both the gen-set and the batteries through their corresponding converter

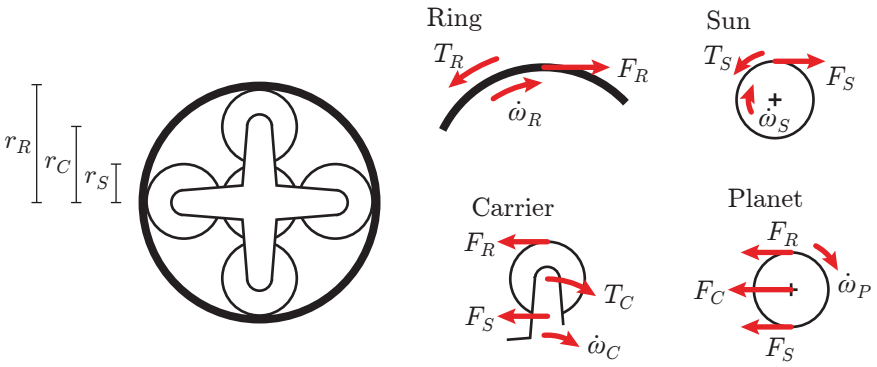

Figure 4.6: Analysis of forces acting on an epicyclic gearing.

and power electronics to deliver energy to the traction motor. The energy relations in terms of input and output power P_{ps} are:

$$P_{ps,ds} = \eta_{ps}(P_{ps,us1} + P_{ps,us2}) \tag{4.23}$$

Of course, there are no kinetic relations since the ICE and the wheels are mechanically decoupled. This offers the advantage of being able to run the engine at the most efficient speed regardless of the vehicle speed.

Combined HEV

A combined HEV is the most complex hybrid architecture as it doubles the number of power-split devices, but it is probably the most versatile as well [7, 8]. It can operate as a series HEV, as a parallel HEV or as both at the same time. To do so, there is a loop that links the engine crankshaft to a generator to operate in series mode; similarly, the ICE is also mechanically linked to the wheels together with a coaxial motor to operate in parallel mode. Both loops can be appreciated in figure 4.5. Usually, the power-split device linking ICE, motor and generator is an epicyclic gearing [7], while the one connecting battery and motors is just an electric power bus.

The equations governing the epicyclic gearing can be deducted by analyzing the forces at each part of the system. According to figure 4.6, the forces equilibrium on the planet can be written as:

$$F_S r_P - F_R r_P - I_P \dot{\omega}_P = 0 \tag{4.24}$$

Since the moment of inertia I_P of the planet is negligible compared to the rest of the components–they are linked to big machines such as the engine and

motors–the identity $F_S - F_R = 0$ stands. Therefore, let us call $F = F_S = F_R$ henceforth. Analyzing the ring, carrier and sun, leads to the following relations:

$$Fr_R + T_R - I_R\dot{\omega}_R = 0 \tag{4.25}$$

$$T_C - Fr_R - Fr_S - I_C\dot{\omega}_C = 0 \tag{4.26}$$

$$Fr_S + T_S - I_S\dot{\omega}_S = 0 \tag{4.27}$$

Solving for F, it results:

$$(T_C - I_C\dot{\omega}_C)\frac{r_R}{r_R + r_S} - T_R - I_R\dot{\omega}_R = 0 \tag{4.28}$$

$$(T_C - I_C\dot{\omega}_C)\frac{r_S}{r_R + r_S} - T_S - I_S\dot{\omega}_S = 0 \tag{4.29}$$

The kinematic relation that governs the epicyclic gearing is:

$$\omega_R = \frac{\omega_C(r_R + r_S) - \omega_S r_S}{r_R} \tag{4.30}$$

Combining eqs. (4.28)–(4.30) and introducing the substitution $n = r_R/r_S$, the equations that govern the epicyclic gearing are:

$$\dot{\omega}_S = \frac{(n+1)T_C - (n+1)^2 T_S - nI_C\dot{\omega}_R}{I_C + (n+1)^2 I_S} \tag{4.31}$$

$$\dot{\omega}_C = \frac{\dot{\omega}_S + n\dot{\omega}_R}{n+1} \tag{4.32}$$

$$T_R = \frac{T_C - I_C\dot{\omega}_C}{n+1}n - I_R\dot{\omega}_R \tag{4.33}$$

The electric power bus follows the energy conversion mechanism described in (4.23).

4.4 Electrical path

HEV powertrains include an electric loop with–at least–one motor, a battery pack, electric buses and power electronics such as converters and inverters [5]. Electric buses are considered ideal conductors so a model is not needed. Power electronics are assumed to be included in their corresponding battery and motor models and therefore no additional equations are required. These

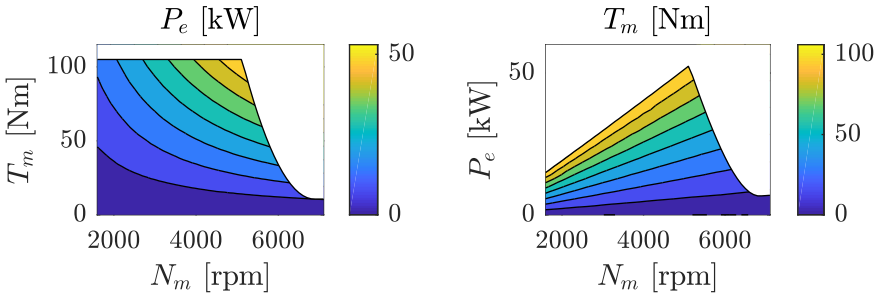

Figure 4.7: Two different approaches to represent a motor map. On the left, power consumption is listed by motor speed and torque; on the right, torque output is represented as a function of motor speed and power supply. These maps represent the continuous operation region only.

assumptions have no significant impact on the accuracy of the powertrain model since the main interest of this dissertation is the ICE. A detailed characterization of these elements may be necessary for other targets such as low level electric bus controllers.

4.4.1 Electric machines

According to the scope of this dissertation, an electric machine can be modeled with a quasi-steady approach. This simplification becomes valid as long as motor response is much faster than ICE dynamics. The torque at the motor shaft is a consequence of the supplied electrical power at a particular rotational speed. A typical motor map as supplied by a manufacturer represents electrical power consumption listed by motor speed and torque. For convenience, this map has been inverted to list torque output by motor speed and power supply, which is the causal approach.

A prototype Permanent Magnet Synchronous Machine (PMSM) to be installed in a RE has been used. Motor maps can be appreciated in figure 4.7. The electrical power supply P_e has been measured upstream the power electronics, so the maps include the behavior of both machines coupled together. These maps represent the continuous operation region of the motor; the consideration of higher torque regions require additional states and would only be interesting if performance constraints are taken into account, which is not the case of the works in this dissertation. It is remarkable that the causal map–right plot–shows a linear surface which is, therefore, easier to fit to an analytical function. Based on the observation of the available maps, the following expression is proposed to represent the output torque T_m:

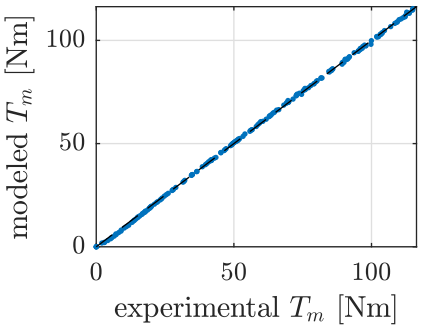

Figure 4.8: Correlation between experimental measures of the electric motor and the proposed analytical expression for motor torque.

$$T_m = P_e(c_{10}e^{c_{11}N_m} + c_{20}e^{c_{21}N_m}) \tag{4.34}$$

where N_m is the motor speed. The agreement between experimental data and the above analytical fitting can be checked in figure 4.8.

The maximum torque curve is defined by software at the motor controller and can be expressed as a piecewise function:

$$T_{m,max} = \begin{cases} c_{30} + c_{31}N_m, & N_m \leq \widehat{N}_m \\ c_{40} + c_{41}N_m + c_{42}N_m^2, & N_m > \widehat{N}_m \end{cases} \tag{4.35}$$

with $\widehat{N}_m$ the motor speed where the controller switches from maximum torque to temperature limitation, which is $\widehat{N}_m = 5100$ rpm for the motor shown in this section.

Similarly, additional variables can also be mapped. Motor efficiency η_m and supplied current i_m are shown in figure 4.9. Note that the voltage is kept roughly constant at the battery, resulting in a current map mostly dependent on the supplied power.

4.4.2 Batteries

The battery pack in a HEV is composed of a number of cells connected both in parallel and series to deliver the desired voltage and capacity [5, 9]. The output performance of the assembly is identical to a single cell following the Thevenin equivalent circuit of the battery pack. According to the Thevenin theorem [10], the equivalent circuit is composed of an ideal voltage source V_{oc} and a resistor R_b in series, as displayed in figure 4.10. With this approach, the battery voltage at terminals is:

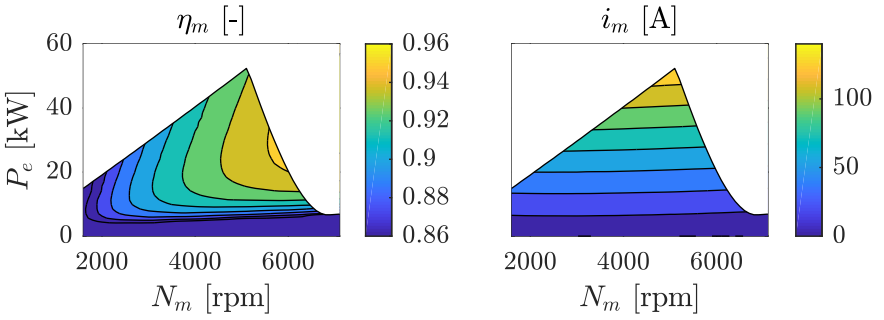

Figure 4.9: Representation of motor efficiency η_m and current i_m drawn by the motor, listed by motor speed and electric power consumption. Note that as long as the supply voltage remains somehow constant thanks to the power electronics, the current is only a function of the power consumption.

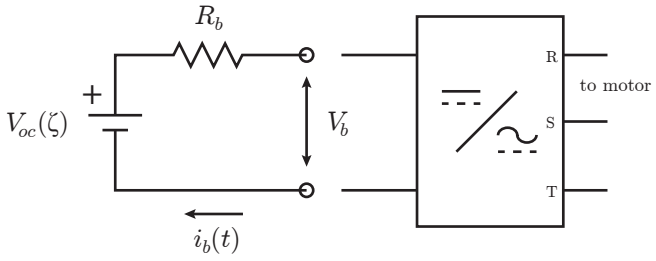

Figure 4.10: Scheme of the battery model using its Thevenin equivalent circuit. On the right, the battery pack power electronics whose efficiency is included in the resistance R_b quantification.

$$V_b = V_{oc} - i_b R_b \tag{4.36}$$

where i_b is the current drawn from the battery and R_b its internal resistance. The current is the variation of the battery charge Q_b:

$$\dot{Q}_b = -i_b(t) \tag{4.37}$$

Consequently, the actual charge stored in the battery can be accounted as:

$$Q_b(t) = Q_{b,0} - \int_0^t i_b(\tau)\,\mathrm{d}\tau \tag{4.38}$$

The charge level may be also measured as a fraction of the nominal charge of the battery $Q_{b,0}$ with the so-call SoC ζ [11]:

$$\zeta(t) = 1 - \frac{\int_0^t i_b(\tau)\,\mathrm{d}\tau}{Q_{b,0}} \tag{4.39}$$

which is generally expressed as a fraction with $\zeta = 1$ the maximum charge of the battery. Similarly, a State of Energy (SoE) might be defined as a measure of the energy level in terms of remaining energy relative to the total energy content of a fully charged battery. The nominal energy stored within the battery is:

$$E_{b,0} = Q_{b,0} V_{oc,0} \tag{4.40}$$

with $V_{oc,0}$ the open circuit voltage of the battery in a fully charged situation. The actual energy content is:

$$E_b = Q_b V_{oc} \tag{4.41}$$

Therefore, the SoE ξ can be calculated as:

$$\xi = \frac{E_b}{E_{b,0}} = \zeta \frac{V_{oc}}{V_{oc,0}} \tag{4.42}$$

Note that nominal and actual open circuit voltages may differ, otherwise SoE and SoC would take the same values. Open circuit voltage in a battery is SoC-dependent, decreasing with the charge. A typical voltage vs. SoC curve for a lithium-ion battery is shown in figure 4.11.

More accurate models may be built by introducing several RC sets (resistor and capacitor) in series with the voltage source in order to capture nonlinear dynamics. However, the increase in model complexity and the introduction of additional states to the problem–voltage at each capacitor involves an additional differential equation–are considered major drawbacks in this work for a control-oriented model.

4.5 Internal combustion engine

Two different ICE models have been used for the works performed in this thesis. The most simple one is based on a quasi-steady approach with an engine map, and it is used for vehicular purposes where no engine control is performed, such as in HEV energy management. The most detailed model is aimed for engine controls optimization where no predefined calibration is used and an engine map may be inappropriate. It is a 0-D MVEM [12] combining

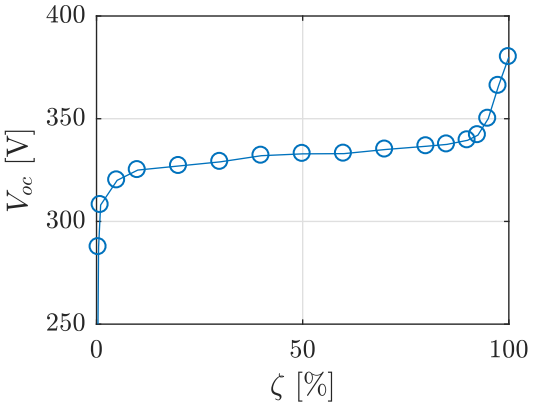

Figure 4.11: Typical open circuit voltage relative to the SoC ζ for a lithium ion battery composed of 100 individual cells. The shown curve is an average of the charge and discharge curves.

physical and empirical models for the different subsystems. An effort has been made to produce a continuous and smooth engine model for control purposes, avoiding any sharpness that might compromise the optimization procedure. This particularity is the main contribution of this model and the main difference to other approaches [13, 14].

Models correspond to a light-duty Euro 5 diesel turbocharged ICE with VGT, LP- and HP-EGR. Model parameters are fitted to experimental data consisting on two types of tests: (i) a set of 980 steady state experiments that explore different combinations of operating conditions and controls, and (ii) a dynamic cycle providing transient information. These tests are described in deep in section 5.3. The model is validated with an additional cycle featuring different dynamics in order to provide a fair benchmarking.

Following, the ICE subsystems are described and validated according to the engine layout shown in figure 4.12. Subsections 4.5.1 to 4.5.6 correspond to the detailed engine model while subsection 4.5.7 describes the quasi-steady approach model.

4.5.1 Intake manifold

Intake manifold is modeled as a reservoir [13] where gases coming from the compressor–through the intercooler–and recirculation gases from the HP-EGR loop are mixed together. Figure 4.13 depicts this scheme. Cylinders breathe gases from this reservoir. The equilibrium between the incoming and outgoing

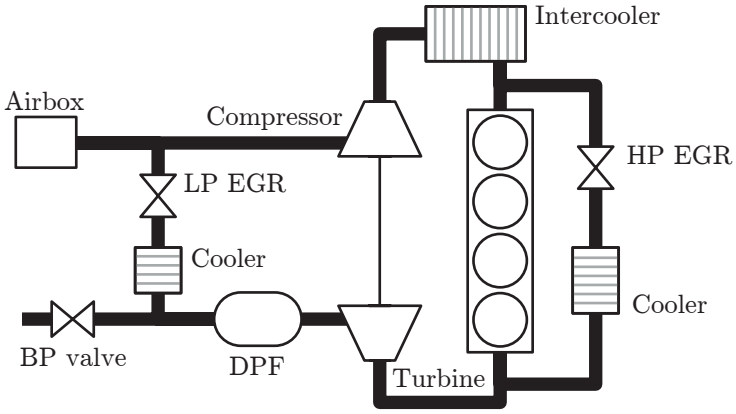

Figure 4.12: Layout of the modeled engine and its subsystems.

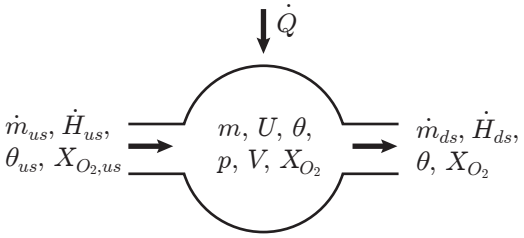

Figure 4.13: Representation of the reservoir that serves as manifold model and the incoming and outgoing flows.

gases produces a variation on the reservoir pressure, energy and composition. These quantities are solved using the mass and energy conservation principles:

$$\dot{m}(t) = \dot{m}_{us}(t) - \dot{m}_{ds}(t) \tag{4.43}$$

$$\dot{U}(t) = \dot{H}_{us}(t) - \dot{H}_{ds}(t) + \dot{Q}(t) \tag{4.44}$$

with m the mass of gas in the reservoir, U the internal energy of that gas, H the enthalpy of incoming and outgoing flows, and $\dot{Q}$ the heat flow exchanged

with the environment. Note that the energy conservation principle can be deducted from the definition of the internal energy stored in a control volume:

$$\begin{aligned}\dot{U} = \dot{Q} - \dot{W} + \dot{m}_{us}\left(u_{us} + pv_{us} + \frac{1}{2}\mathrm{c}_{us}^2 + \rho_{us}z_{us}\right) \\ -\dot{m}_{ds}\left(\dot{m}_{ds} + pv_{ds} + \frac{1}{2}\mathrm{c}_{ds}^2 + \rho_{ds}z_{ds}\right)\end{aligned} \tag{4.45}$$

where the kinetic energy of the fluid, its potential energy and the work W–manifolds are assumed to be rigid and fixed volumes–are neglected. Also, since the intake manifold is considered an adiabatic system due to its rapid dynamics and relatively low temperatures compared to other parts of the engine, heat flow exchange $\dot{Q}$ is neglected. The gas inside the reservoir can be modeled as an ideal gas:

$$pV = mR\theta \tag{4.46}$$

with R the specific gas constant, obtained by dividing the universal gas constant by the molar mass of the gas. Note that the explicit dependency on time has been neglected for simplicity of the nomenclature. The energy associated to the reservoir gas temperature is:

$$U = c_v m\theta \tag{4.47}$$

Introducing the ideal gas law in the above expression, the energy results:

$$U = \frac{1}{\kappa - 1}pV \tag{4.48}$$

Note that the relations $R = c_p - c_v$ and $\kappa = \frac{c_p}{c_v}$ have been used to reach the above expression. The energy of upstream and downstream flows can be calculated as:

$$\dot{H}_{us} = c_p\dot{m}_{us}\theta_{us} \tag{4.49}$$

$$\dot{H}_{ds} = c_p\dot{m}_{ds}\theta_{ds} \tag{4.50}$$

Introducing eqs. (4.48)–(4.50) in the energy conservation relation (4.44), and neglecting $\dot{Q}$–adiabatic hypothesis–the variation of the pressure in the reservoir results:

$$\dot{p} = \frac{\kappa R}{V}[\dot{m}_{us}\theta_{us} - \dot{m}_{ds}\theta_{ds}] \tag{4.51}$$

Similarly, substituting with eqs. (4.47), (4.49) and (4.50) in (4.44), the reservoir temperature follows the equation:

$$\dot{\theta} = \frac{R\theta}{pV}\left[\dot{m}_{us}(\kappa\theta_{us} - \theta) - \dot{m}_{ds}(\kappa\theta_{ds} - \theta)\right] \tag{4.52}$$

Note that the relation $\dot{U} = c_v(\dot{m}\theta + m\dot{\theta})$ has been used in the above equation.

The mass conservation principle (4.43) must be verified for every specie in the gas composition. Therefore, the oxygen mass relation is:

$$\dot{m}_{O_2} = \dot{m}_{O_2,us} - \dot{m}_{O_2,ds} \tag{4.53}$$

Oxygen mass flow can be expressed as a function of the oxygen fraction X_{O_2}:

$$\dot{m}_{O_2} = \dot{m}X_{O_2} + m\dot{X}_{O_2} \tag{4.54}$$

$$\dot{m}_{O_2,us} = \dot{m}_{us}X_{O_2,us} \tag{4.55}$$

$$\dot{m}_{O_2,ds} = \dot{m}_{ds}X_{O_2,ds} \tag{4.56}$$

The above expressions can be introduced in the oxygen mass conservation relation 4.53. Additionally, the gas mass m in the reservoir can be substituted with the ideal gas law, and $\dot{m}$ with the total mass conservation principle in 4.43 as well. Therefore, the variation of the oxygen fraction at the reservoir is:

$$\dot{X}_{O_2} = \frac{R\theta}{pV}\left[\dot{m}_{us}(X_{O_2,us} - X_{O_2}) - \dot{m}_{ds}(X_{O_2,ds} - X_{O_2})\right] \tag{4.57}$$

The eqs. (4.51), (4.52) and (4.57) can be particularized for the ICE shown in figure 4.12. Thus, the variation of pressure at the intake manifold is:

$$\dot{p}_2 = \frac{\kappa R}{V_{im}}[\dot{m}_c\theta_{ico} + \dot{m}_{hpegr}\theta_{hpegr} - \dot{m}_{ip}\theta_{im}] \tag{4.58}$$

Similarly, the variation of the intake manifold temperature follows the ODE:

$$\dot{\theta}_{im} = \frac{R\theta_{im}}{p_2V_{im}}\left[\dot{m}_c(\kappa\theta_{ico} - \theta_{im}) + \dot{m}_{hpegr}(\kappa\theta_{hpegr} - \theta_{im}) - \dot{m}_{ip}\theta_{im}(\kappa - 1)\right] \tag{4.59}$$

Finally, the variation of oxygen fraction ends up as:

$$\dot{X}_{O_2,im} = \frac{R\theta_{im}}{p_2V_{im}}\left[\dot{m}_c(X_{O_2,c} - X_{O_2,im}) + \dot{m}_{hpegr}(X_{O_2,hpegr} - X_{O_2,im})\right] \tag{4.60}$$

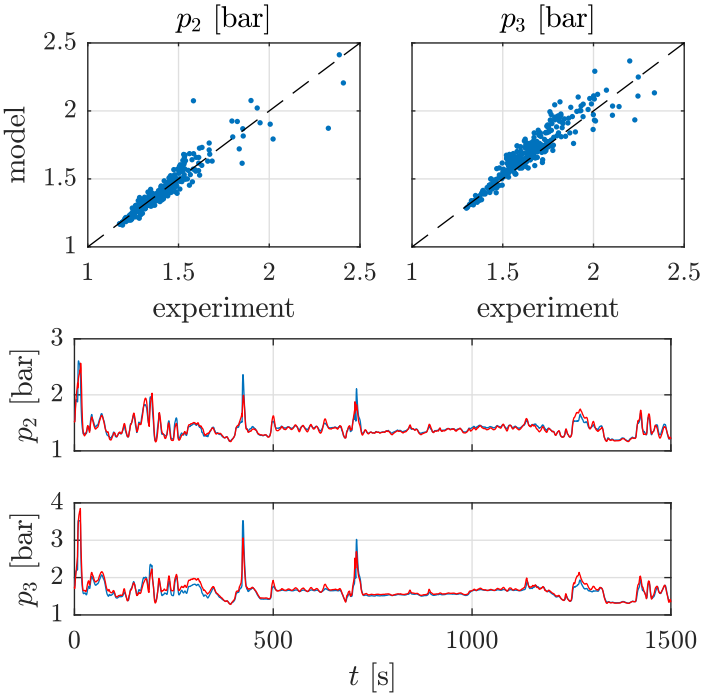

Figure 4.14: Correlation between experimental values of intake and exhaust manifolds pressure p_2 and p_3, and the results of a simulation of the complete engine model at the validation cycle. Bottom plots show the time trajectories of the experimental (blue) and modeled (red) variables.

Note that the temperature and oxygen fraction of the downstream flow is the same than at the intake manifold as perfect mixing is assumed.

The intake manifold model can be simplified considering it as an isothermal system based in the fact that it is rapidly filled of gas and depleted. In this case, the polytropic coefficient is $\kappa = 1$ and the pressure ODE is:

$$\dot{p}_2 = \frac{\kappa R \theta_{im}}{V_{im}} [\dot{m}_c + \dot{m}_{hpegr} - \dot{m}_{ip}] \tag{4.61}$$

The expression 4.60 remains the same while 4.59 vanishes since there are no temperature dynamics.

A validation of the manifold model is carried out by simulating the whole engine model at a benchmarking cycle. The correlation between experimental and simulated values are shown in the left plot of figure 4.14.

4.5.2 Exhaust manifold

The exhaust manifold is modeled as an adiabatic reservoir [13] as the intake manifold. The same mass and energy conservation equations apply here–see eqs. (4.51), (4.52) and (4.57). Assigning the appropriate quantities to these equations according to the engine layout, they result in:

$$\dot{p}_3 = \frac{\kappa R}{V_{em}}[\dot{m}_{ep}\theta_{ep} - \dot{m}_{hpegr}\theta_{em} - \dot{m}_t\theta_{em}] \tag{4.62}$$

$$\dot{\theta}_{em} = \frac{R\theta_{em}}{p_3 V_{em}}\left[\dot{m}_{ep}(\kappa\theta_{ep} - \theta_{em}) - \dot{m}_{hpegr}\theta_{em}(\kappa - 1) - \dot{m}_t\theta_{em}(\kappa - 1)\right] \tag{4.63}$$

$$\dot{X}_{O_2,em} = \frac{R\theta_{em}}{p_3 V_{em}}\dot{m}_{ep}\left[X_{O_2,ep} - X_{O_2,em}\right] \tag{4.64}$$

The same isothermal hypothesis that was considered in the intake manifold model can be applied here. In this case, the exhaust manifold pressure variation is:

$$\dot{p}_3 = \frac{\kappa R\theta_{em}}{V_{em}}[\dot{m}_{ep} - \dot{m}_{hpegr} - \dot{m}_t] \tag{4.65}$$

Again, 4.64 applies while 4.63 vanishes from the model.

Validation results of the exhaust manifold model can be checked at the right plot of figure 4.14.

4.5.3 Turbocharger

The turbocharger model is composed of two subsystems, namely a compressor and a turbine, both coupled together through a shaft. These subsystems are described in the following points.

Compressor

The compressor forces an amount of air coming from the airbox into the intake manifold at the expense of mechanical energy produced by a turbine. For a given pressure ratio Π_c, between upstream and downstream, and a corrected rotational speed, the compressor propels a known mass flow. Note that the corrected speed is defined as $\widetilde{\omega}_{tc} = \omega_{tc}\sqrt{\theta_{ci,0}/\theta_{ci}}$ [15] with $\theta_{ci,0}$ the inlet temperature at which the compressor map was measured and θ_{ci} the actual inlet temperature. Usually, turbocharger manufacturers supply compressor maps as a function of pressure ratio and turbo speed. In order to have a

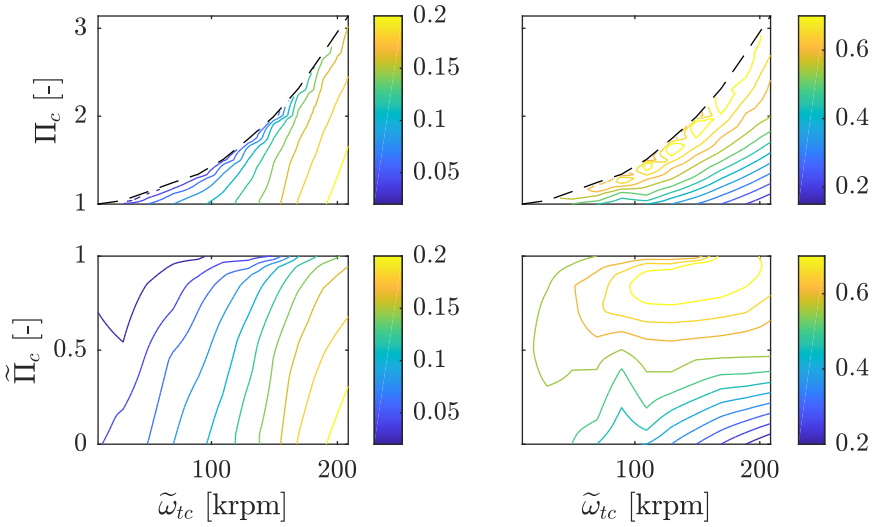

Figure 4.15: Compressor maps as measured in the turbocharger test bench. Top plots show the mass flow in kg/s (left) and efficiency (right) maps relative to the corrected speed $\widetilde{\omega}_{tc}$ and pressure ratio Π_c, with the surge limit represented with the black dashed line. The bottom plots show the same quantities but as a function of the normalized pressure ratio $\widetilde{\Pi}_c$.

proper starting point for compressor modeling, both compressor and turbine have been tested in a turbocharger test bench. The compressor maps for mass flow and efficiency are shown in figure 4.15.

Compressor surge is a phenomena that happens when the fluid-dynamics are too unstable to sustain the regular flow inside the compressor. It is generally produced by an excessive pressure ratio, causing the blades to stall, and should be avoided [13, 15]. The surge limit on the compressor plays a critical role in the model, since it represents a discontinuity on the compressor behavior. In order to take this issue into account, the experimental surge limit has been approximated with the following exponential equation:

$$\Pi_{srg} = c_{10} \exp(c_{11} \widetilde{\omega}_{tc}) + c_{20} \exp(c_{21} \widetilde{\omega}_{tc}) \tag{4.66}$$

whose fitting to the actual surge limit can be checked at figure 4.16. Then, the compressor map can be expressed as a function of a normalized pressure ratio of the form:

$$\widetilde{\Pi}_c = \frac{\Pi_c - 1}{\Pi_{srg} - 1} \tag{4.67}$$

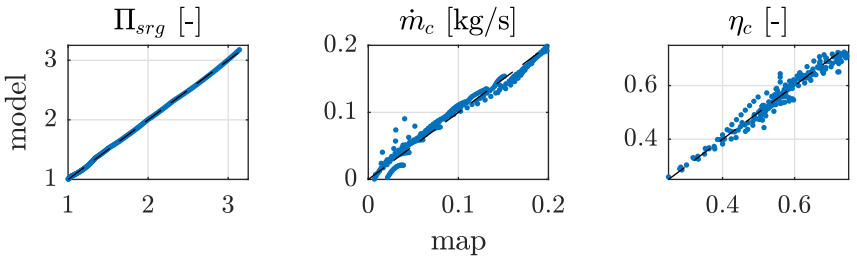

Figure 4.16: Comparison between experimental maps and the proposed analytical expressions for–from left to right–surge limit Π_{srg}, compressor mass flow $\dot{m}_c$ and compressor efficiency η_c.

with $\Pi_c = p_2/p_1$. Then, $\widetilde{\Pi}_c$ must be in the range $[0, 1]$ for the surge to be avoided.

With the above transformation, compressor maps are easier to approximate to an analytical equation. The following expressions are proposed:

$$\dot{m}_c = c_{00} + c_{10}\widetilde{\omega}_{tc} + c_{01}\widetilde{\Pi}_c + c_{11}\widetilde{\omega}_{tc}\widetilde{\Pi}_c + c_{02}\widetilde{\Pi}_c^2 \tag{4.68}$$

$$\eta_c = \left[c_{00} + c_{10}\widetilde{\omega}_{tc} + c_{01}\widetilde{\Pi}_c + c_{20}\widetilde{\omega}_{tc}^2 + c_{11}\widetilde{\omega}_{tc}\widetilde{\Pi}_c + c_{02}\widetilde{\Pi}_c^2\right]\left[1 - \exp(c_A\widetilde{\Pi}_c + c_B)\right] \tag{4.69}$$

whose agreement with the experimental maps can be checked at figure 4.16.

The compression is considered to be an adiabatic process with an isentropic efficiency η_c [14]. Therefore, the power required to produce the compression process is:

$$P_c = \frac{1}{\eta_c}\frac{\gamma R}{\gamma - 1}\dot{m}_c\theta_{ci}\left(\Pi_c^{\frac{\gamma-1}{\gamma}} - 1\right) \tag{4.70}$$

The temperature increase of the fluid after the adiabatic compression is:

$$\theta_{co} = \left(\Pi_c^{\frac{\gamma-1}{\gamma}} - 1\right)\frac{\theta_{ci}}{\eta_c} + \theta_{ci} \tag{4.71}$$

The mass flow model is first fitted to the compressor map as a starting point and, then, to the engine experimental data. The correlation between measurements and model are displayed in figure 4.17.

Turbine

The turbine is in charge of expanding exhaust gases and taking profit of their thermal energy to generate a mechanical torque. The turbine is physically

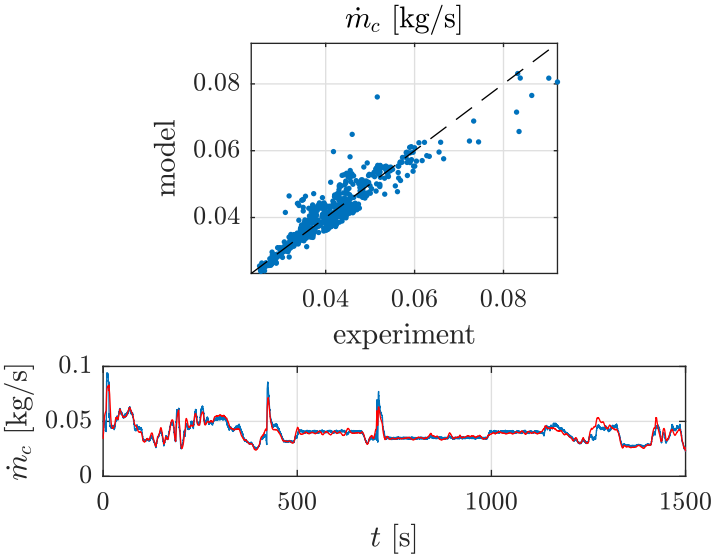

Figure 4.17: Correlation between experimental values of compressor mass flow $\dot{m}_c$ and the results of a simulation of the complete engine model at the validation cycle. Bottom plot shows the time trajectories of the experimental (blue) and modeled (red) variables.

linked to the compressor, which makes use of the mechanical energy to develop the compression process [15]. Turbines may have movable stator blades in order to produce a variable pressure drop and control the boost pressure p_2. This type of turbine is known as VGT and its use is widespread in diesel engines. The turbine modeled in this work is a VGT.

Similarly to the case of the compressor, manufacturers use to supply their information with a map which is theoretically function of the turbine speed ω_{tc}, the pressure ratio Π_t and the position of the stator blades–which is a control variable–u_{vgt}. Fortunately, turbines are not affected by the same fluid-dynamic instabilities than compressors and surge does not happen. The turbine has been tested in a turbocharger test bench to measure these maps, which are displayed in figure 4.18. As it can be appreciated, the dependency on the turbine speed is limited as curves for different speeds overlap. In order to produce a simple and robust control-oriented model, turbine maps are simplified and speed dependency is neglected.

Corrected turbine mass flow can be approximated as:

$$\dot{m}_{t,cor} = c_{00} + c_{10}\Pi_t + c_{01}u_{vgt} + c_{20}\Pi_t^2 + c_{11}\Pi_t u_{vgt} + c_{02}u_{vgt}^2 \tag{4.72}$$

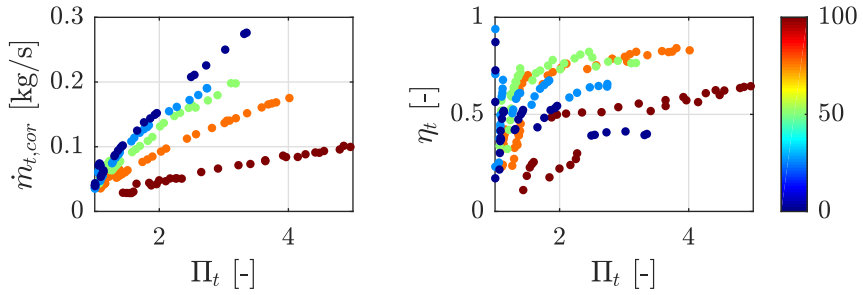

Figure 4.18: Turbine maps measured at the turbocharger test bench, representing the corrected mass flow (left) and efficiency (right) relative to the expansion ratio (x-axis) and geometry position u_{vgt} (color map). Each u_{vgt} position contain a number of turbine speeds but, as it can be appreciated, different rotational speeds collapse into a single curve.

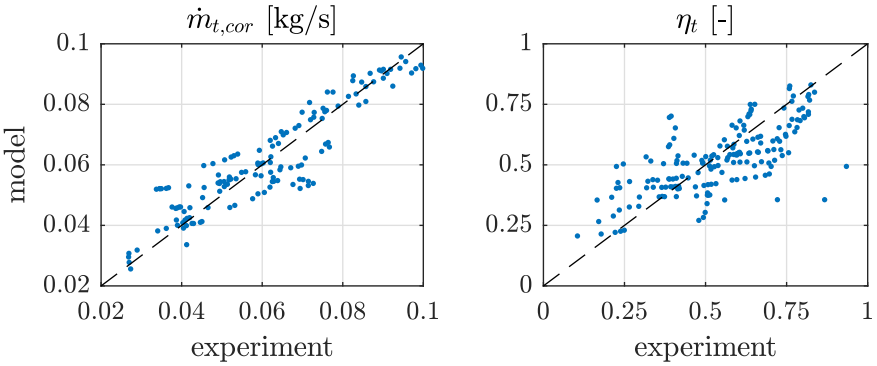

Figure 4.19: Correlation between experimental turbine maps and the proposed empirical equations for the corrected mass flow (left) and efficiency (right).

where $\Pi_t = p_3/p_4$ and $\dot{m}_{t,cor} = \dot{m}_t p_3/p_{3,0}\sqrt{\theta_{em,0}/\theta_{em}}$, with $p_{3,0}$ and $\theta_{em,0}$ the inlet pressure and temperature at which the turbine maps were measured.

The efficiency was found to be quite accurately represented with the following empirical equation:

$$\eta_t = [1 - \exp(c_A(\Pi_t - 1))]\left[c_2 u_{vgt}^2 + c_1 u_{vgt} + c_0\right] + c_B(\Pi_t - 1) \tag{4.73}$$

Correlation between experimental maps and the above expressions is shown in figure 4.19.

The thermodynamic process in the turbine is considered to be an adiabatic

expansion with an isentropic efficiency η_t [14]. The power that this process develop in the shaft is:

$$P_t = \eta_t \frac{\gamma R}{\gamma - 1} \dot{m}_t \theta_{em} \left(1 - \Pi_t^{\frac{1-\gamma}{\gamma}} \right) \tag{4.74}$$

Since the expansion is an adiabatic process, the temperature of the gas at the turbine outlet is:

$$\theta_{to} = \theta_{em} - \eta_t \theta_{em} \left(1 - \Pi_t^{\frac{1-\gamma}{\gamma}} \right) \tag{4.75}$$

Note that the turbine inlet temperature is assumed to be the same than the exhaust manifold temperature θ_{em}. It might be an unrealistic hypothesis due to the heat losses at the exhaust manifold and pipings connecting to the turbine, but this effect can be included in the turbine efficiency η_t.

The mass flow model is fitted to the measured map first as a baseline and, then, it is tuned to correlate with the engine experimental data. Figure 4.20 shows the agreement between measurements and the model. Contrary to the compressor model results, the turbine shows a higher discrepancy between modeled and experimental variables. This is due to the fact that turbine temperature measurements are generally complex and less accurate compared to the compressor due to the high temperature gradients. In addition to that, the adiabatic hypothesis is less representative of the thermodynamic process due to the high temperatures at the turbine inlet.

Mechanical coupling

Both compressor and turbine are physically linked through a shaft. There is a balance between the power developed by the turbine–which is supplied to the compressor–and the power that the compression process requires. Depending on the sign of this balance and the moment of inertia of the rotating mass I_{tc}, the turbocharger will accelerate, decelerate or hold speed. The speed of this set follows the ODE:

$$\dot{\omega}_{tc} = \frac{P_t - P_c}{I_{tc} \omega_{tc}} \tag{4.76}$$

Compressor and turbine efficiency models are fitted to the experimental maps and, then, tuned such that the modeled turbocharger speed fits the measurements. The correlation between experimental and modeled ω_{tc} is shown in figure 4.21.

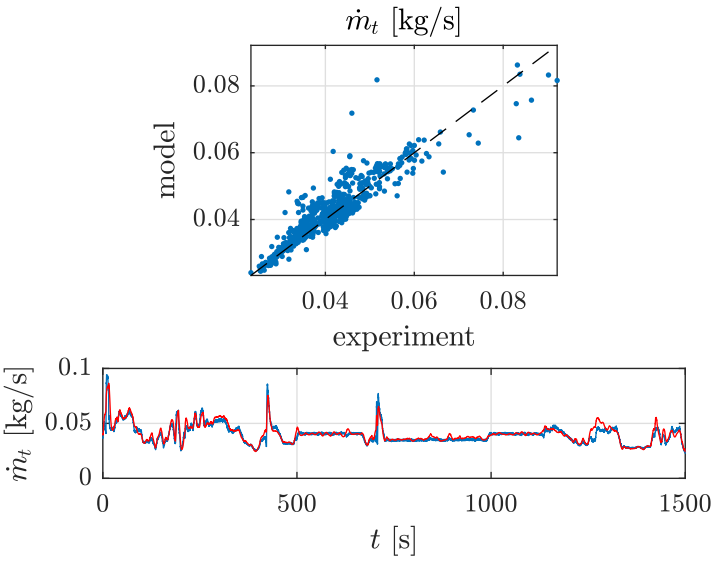

Figure 4.20: Correlation between experimental values of turbine mass flow $\dot{m}_t$ and the results of a simulation of the complete engine model at the validation cycle. Bottom plot shows the time trajectories of the experimental (blue) and modeled (red) variables.

4.5.4 EGR system

Both EGR valves–namely LP- and HP-EGR–are modeled as an isothermal orifice [13]. The flow through the valve is considered compressible with the assumptions that: (i) the flow accelerates up to the narrowest point of the orifice without losses, transferring part of the pressure into kinetic energy, and (ii) after the orifice the flow is completely turbulent and the kinetic energy is dissipated into thermal energy with no pressure recuperation. Given these hypothesis, the mass flow that goes through the valve for a known pressure drop is:

$$\dot{m}_{egr} = A_{egr} C_{d,egr} \frac{p_{us}}{\sqrt{R\theta_{us}}} \Psi_{egr} \tag{4.77}$$

where A_{egr} is the effective opening of the valve, $C_{d,egr}$ the discharge coefficient

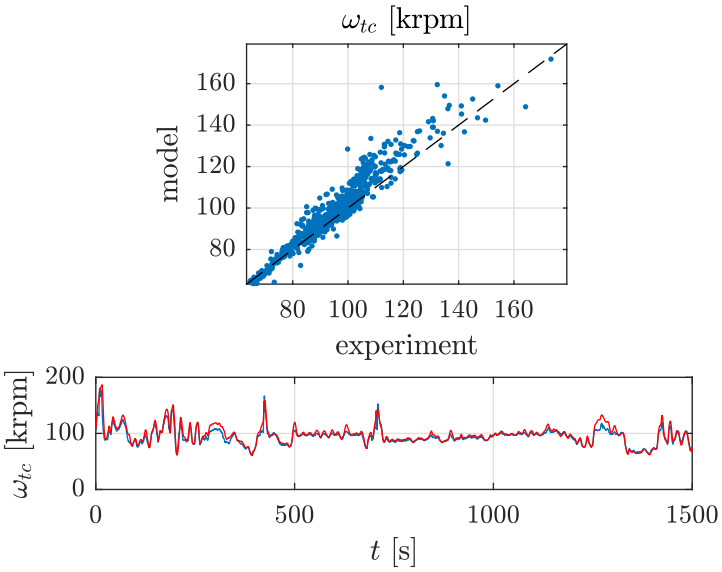

Figure 4.21: Correlation between experimental values of turbocharger rotational speed ω_{tc} and the results of a simulation of the complete engine model at the validation cycle. Bottom plot shows the time trajectories of the experimental (blue) and modeled (red) variables.

and Ψ_{egr} the expansion factor which is a function of the pressure ratio $\Pi_{egr} = p_{us}/p_{ds}$ [13]:

$$\Psi_{egr} = \begin{cases} \sqrt{\kappa \left(\frac{2}{\kappa+1}\right)^{\frac{\kappa+1}{\kappa-1}}} & \Pi_{egr} > \Pi_{cr} \\ \Pi_{egr}^{\frac{-1}{\kappa}} \sqrt{\frac{2\kappa}{\kappa-1}\left(1 - \Pi_{egr}^{\frac{1-\kappa}{\kappa}}\right)} & \Pi_{egr} \leq \Pi_{cr} \end{cases} \tag{4.78}$$

where the critical pressure ratio–when the flow reaches sonic conditions at the orifice and, therefore, it is chocked–is a function of the adiabatic factor:

$$\Pi_{cr} = \left(\frac{\kappa+1}{2}\right)^{\frac{\kappa}{\kappa-1}} \tag{4.79}$$

For the sake of simplicity, the piecewise equation (4.78) is approximated with the following continuous expression:

$$\Psi_{egr} \approx \widetilde{\Psi}_{egr} = \left(\frac{1}{2} + \frac{1}{2}\mathrm{erf}(c_1\Pi_{egr} + c_0)\right)(c_2 \exp(c_3\Pi_{egr}) + c_4) \tag{4.80}$$

The agreement between Ψ_{egr} and $\widetilde{\Psi}_{egr}$ is shown in the left plot of figure 4.22.

The effective opening of the valve as a function of the controlled position u_{egr} should be approximated with an empirical expression. The following equation is proposed based on the experimental observations:

$$A_{egr} = c_2 \left(\frac{1}{2} \mathrm{erf}(c_1 u_{egr} + c_0) - \frac{1}{2} \mathrm{erf}(c_0) \right) \tag{4.81}$$

This EGR valve model is used for both HP-EGR and LP-EGR systems, substituting the upstream and downstream variables with the corresponding flow conditions according to the layout.

The mass flow model is tuned for the experimental data. Correlation between measurements and model estimations is at the right plot of figure 4.22. EGR mass flow shows a significant level of discrepancy between the model and experiments. It must be noted that EGR mass flow measurements have a significant delay (see section 5.2) and transient readings might be unreliable, obscuring the model results. This is particularly evident in the $t = [1100, 1400]$ part of the measurements where agreement is poor. However, during most of the experiment, when dynamics are slow and measurements are reliable, the EGR model showed a quite good accuracy. Therefore, it may be concluded that the model performance is sufficient for the scope of this dissertation.

4.5.5 Cylinder

The events taking part at the cylinder are complex and highly nonlinear, involving chemical, thermodynamic and fluid-dynamic processes at every single engine cycle [15]. Instantaneous models follow all these processes throughout the duration of a cycle and can make a pretty good approximation to the cylinder dynamics. However, from a control point of view–and if no intra-cycle control is to be performed–, the cylinder is a system whose dynamics extend to few milliseconds and a mean value is generally already an adequate estimation [12].

Therefore, two different cylinder model approaches are developed: (i) a quasi-steady model to be used for high-level engine optimization works, and (ii) a detailed in-cylinder model for intra-cycle control studies.

Quasi-steady cylinder

This model avoids complex equations that would limit its control capabilities when the in-cylinder processes are not the control target. The cylinder is represented as a combination of physically meaningful expressions and black-box models whose inputs are the thermodynamic conditions of the intake

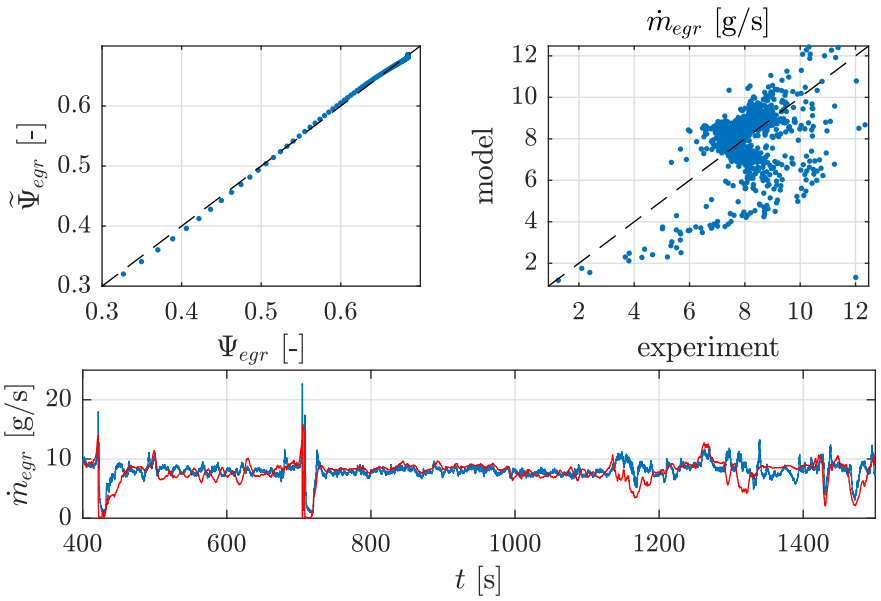

Figure 4.22: Agreement between the expansion factor Ψ_{egr} and the proposed empirical approximation $\widetilde{\Psi}_{egr}$ on the left. On the right, correlation between experimental values of EGR mass flow $\dot{m}_{egr}$ and the results of a simulation of the complete engine model at the validation cycle. Bottom plot shows the time trajectories of the experimental (blue) and modeled (red) variables.

gas and the control variables [13]. The interesting outputs are the indicated efficiency η_{ind}, the exhaust temperature θ_{ep}, NO_x emissions X_{nox} and exhaust gases opacity σ. These black-box models are approached with a second degree polynomial.

$$\begin{aligned} \eta_{ind} &= \eta_{ind}(N_{ice}, u_f, u_{\delta soi}, X_{O_2,im}, p_2) \\ \theta_{ep} &= \theta_{ep}(N_{ice}, u_f, u_{\delta soi}, X_{O_2,im}, p_2) \\ X_{nox} &= X_{nox}(N_{ice}, u_f, u_{\delta soi}, X_{O_2,im}, p_2) \\ \sigma &= \sigma(N_{ice}, u_f, u_{\delta soi}, X_{O_2,im}, p_2) \end{aligned} \tag{4.82}$$

Despite this model entails an important simplification, it is a reasonable hypothesis since the characteristic time of the airpath is several orders of magnitude higher than in-cylinder phenomena. Accordingly, a step in an airpath-related control produces a non negligible transient on intake manifold pressure and mass flow, as seen in figure 4.23. Consequently, torque output shows a similar transient since it is influenced by the intake thermodynamic conditions and admitted mass. Conversely, in figure 4.24 it can be appreciated

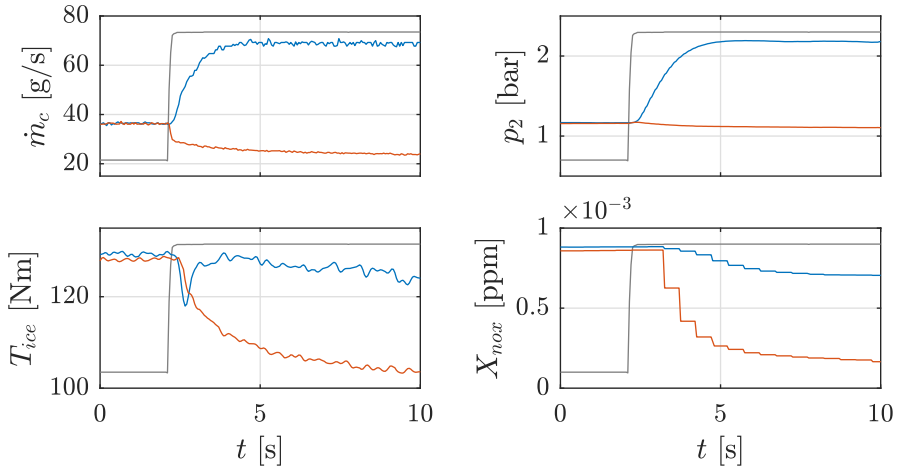

Figure 4.23: Dynamic response of airpath and cylinder variables to a VGT (blue) and EGR (red) opening step from 0% to 100%. Control variable is in gray. Remaining controls are held constant. Note that all transients, including effective torque, are affected by the characteristic time of the airpath. Note that NO_x concentration measurement is affected by the sample time and the delay of the NO_x probe.

that a step in an in-cycle control produces a sudden change in cylinder outputs such as torque, and a slow transient on airpath variables.

Torque generation is modeled as the simultaneous effect of an indicated torque and engine losses. The indicated torque is a consequence of the fuel energy liberation during the combustion process. Accordingly:

$$T_{ind} = \eta_{ind} \frac{u_f H_f n_{cyl}}{4 \cdot 10^6 \pi} \tag{4.83}$$

where H_f is the fuel heat of combustion, n_{cyl} the number of cylinders and η_{ind} accounts for both the thermodynamic and the combustion process efficiencies– $\eta_{ind} = 1$ would mean that all the fuel heat is effectively converted to an indicated torque. Engine losses are represented by a linear function of the engine speed, which can be fitted with a motoring experiment:

$$T_{loss} = c_0 + c_1 N_{ice} \tag{4.84}$$

Therefore, the effective torque at the engine crankshaft is:

$$T_{ice} = T_{ind} - T_{loss} \tag{4.85}$$

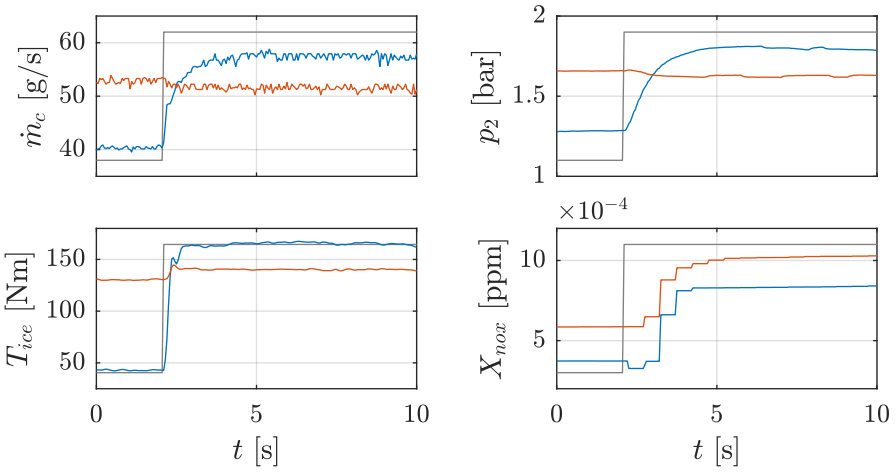

Figure 4.24: Dynamic response of airpath and cylinder variables to a fueling rate step from 8 to 28 mg/str (blue) and a SOI step from 10 to 0.75°BTCD (red). Control variable is in gray. Remaining controls are held constant. Note that airpath-related variables keep their characteristic time (approximately 3 seconds), while cylinder outputs–torque and NO_x–experiment a sudden change as a consequence of the in-cylinder change. Note that NO_x concentration measurement is affected by the sample time and the delay of the NO_x probe.

The advantage of this torque modeling approach is its ability to robustly represent motoring effects as T_{ind} becomes null when $u_f = 0$, keeping the physical relation between fuel injection and indicated torque.

In order to model the breathing process, semi-empirical expressions have been used. In particular, the total mass getting into the cylinders can be calculated by assuming the intake flow as an ideal gas. Therefore, the trapped mass can be easily calculated with the ideal gas law for the intake flow conditions and the engine displacement V_d. Taking into account that cylinders breath once per cycle–and a cycle takes place every two revolutions–the engine performs $N_{ice}/120$ cylinder fillings per second. Therefore, the mass flow getting into the cylinders is [15]:

$$\dot{m}_{ip} = \eta_v \frac{p_2 N_{ice} V_d}{120 R \theta_{im}} \tag{4.86}$$

The term η_v is the volumetric efficiency and accounts for the phenomena that jeopardizes the ideal admitted gas amount such as residuals or valve timing. This efficiency is rather variable with engine conditions and quite difficult to

model capturing the actual events taking effect in the engine. Sticking to a simple model without considering fluid-dynamic equations of the flow entering the cylinders, there still exist several approaches that can be found in the literature. Intuitively, it should be a function of the inlet and outlet conditions and engine speed, such as the expression proposed in [13] that relates η_v to pressures and engine speed:

$$\eta_v = \eta_{v,p}(p_1, p_2)\eta_{v,N}(N_{ice}) \tag{4.87}$$

with $\eta_{v,N}$ a polynomial that is function of the engine speed, and $\eta_{v,p}$:

$$\eta_{v,p} = 1 + \frac{1}{R_c} - \left(\frac{p_3}{p_2}\right)^{\frac{1}{\kappa}} \frac{1}{R_c} \tag{4.88}$$

Similarly, [16] suggests that the volumetric efficiency might be approximated with another function of the engine speed, and intake and exhaust pressures:

$$\eta_v = c_0 + c_1 N_{ice} + c_2 N_{ice}^{-1} + c_3 N_{ice}^{-1}(p_3 - p_2) \tag{4.89}$$

Another engine speed and pressure dependent approximation is that of [14]:

$$\eta_v = c_2\sqrt{N_{ice}} + c_1\sqrt{p_2} + c_0 \tag{4.90}$$

A different approach may be found in [15], where a physical expression with no parameters to calibrate is proposed:

$$\eta_v = \frac{p_2}{p_1}\frac{\theta_{atm}}{\theta_{im}}\frac{\text{AFR}}{1+\text{AFR}}\left(\frac{R_c}{R_c-1} - \frac{1}{\kappa(R_c-1)}\left[\frac{p_3}{p_2} + \kappa - 1\right]\right) \tag{4.91}$$

Results of all the above models are represented and compared in the left plot of figure 4.25. Despite these expressions work well in many situations, due to the numerous phenomena that affect the volumetric efficiency, the performance of these models may vary from engine to engine. Therefore, based on the experimental observations of the engine, an additional model for the volumetric efficiency is proposed in this thesis:

$$\eta_v = c_A \exp\left(\frac{c_2}{c_1 p_2 + c_0}\right) + c_B u_{vgt} + c_C \tag{4.92}$$

where the presence of u_{vgt} respond to purely empirical reasons and it can be argued that it is a way to take into account the effect of the backpressure in the amount of residual gases that remain in the cylinder in a simple way. The performance of this model is shown in the right plot of figure 4.25. The

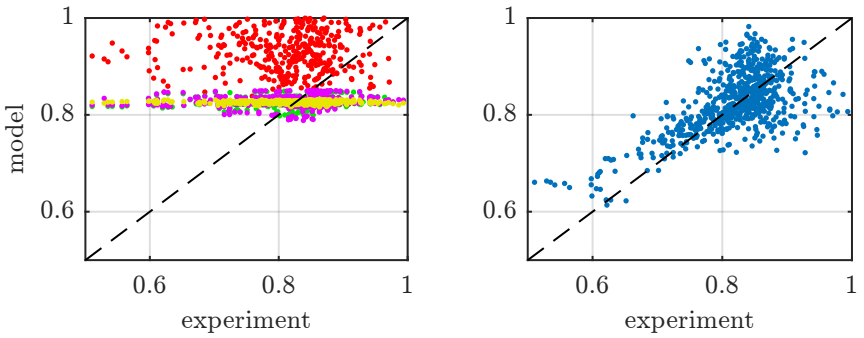

Figure 4.25: Correlation of experimental and modeled volumetric efficiency η_v. Left plot shows three models available in the literature, namely [13] in green, [16] in purple, [14] in yellow and [15] in red. Right plot displays the performance of the model proposed in this thesis.

reasons of the dispersion shown in the results is twofold: on the one hand, intake temperature variations are neglected in this model for performance and simplicity reasons, resulting in the inability to capture the effect on the volumetric efficiency; on the other hand, volumetric efficiency measurements are subject to the accuracy of EGR measurements since the recirculated mass flow is required to calculate the mass entering the cylinders. Thus, the poor transient reliability of EGR mass flow readings is partially responsible of the dispersion.

Since no reservoirs are considered in the cylinder and mass conservation must be verified, the total exhaust mass flow is the addition of the incoming flow and the injected fuel:

$$\dot{m}_{ep} = \dot{m}_{ip} + \dot{m}_f \tag{4.93}$$

The fuel mass flow can be directly calculated from the injected rate u_f– which is typically expressed in mg/str–as:

$$\dot{m}_f = u_f \frac{n_{cyl} N_{ice}}{120 \cdot 10^6} \tag{4.94}$$

where n_{cyl} is the number of cylinders of the engine.

Assuming perfect burning of the injected fuel, the oxygen fraction at the exhaust gas is a function of the stoichiometric Air to Fuel Ratio (AFR):

$$X_{O_2,ep} = \frac{X_{O_2,im}\dot{m}_{ip} - \mathrm{AFR} X_{O_2,atm}\dot{m}_f}{\dot{m}_{ep}} \tag{4.95}$$

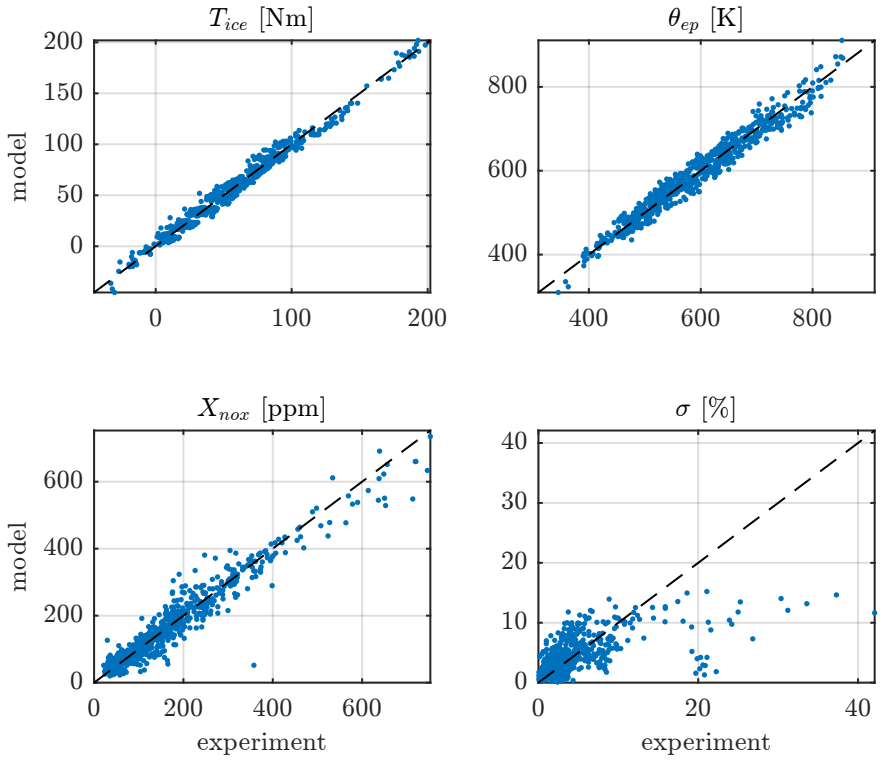

Figure 4.26: Agreement between experimental engine data and cylinder black-box models: effective torque (top left), exhaust port temperature (top right), NO_x emissions (bottom left), and exhaust opacity (bottom right).

Finally, the λ_e parameter–which measures the quotient between the available oxygen at the combustion chamber and the stoichiometric oxygen necessary to burn the injected fuel–can be calculated by applying its definition:

$$\lambda_e = \frac{\dot{m}_{ip} X_{O_2,im}}{\text{AFR} \dot{m}_f X_{O_2,atm}} \tag{4.96}$$

Polynomial black-box models as well as the volumetric efficiency model are fitted to experimental data. Validation results for black-box models are shown in figure 4.26.

Detailed in-cylinder process

This cylinder model is aimed for the intra-cycle OC works as long as they require a detailed description of the in-cylinder processes (particularly, the works at section 9.2). The compression, combustion and expansion processes of a CI engine, *i.e.* between Intake Valve Closing (IVC) and Exhaust Valve Opening (EVO), can be modeled as a process in a closed system with a single substance whose properties change with the thermodynamic conditions according to the correlations from [17].

The combustion process is modeled as a heat addition to the system. The heat transferred to the cylinder walls is represented as a function of the temperature difference between the gas and the cylinder walls with a version of the so called Woschni approach [18]. This system is modeled as a one-component (gas whose properties are a weighted average of the air, fuel and exhaust gas properties) homogeneous (gas phase) system. Then, its thermodynamic state is fully defined by two variables: volume V_{ic} and pressure p_{ic}. This selection is arbitrary but sustained by the fact that V_{ic} depends on the slider-crank mechanism, so its evolution, for a given engine geometry and operating speed, is independent of the system variables and can be considered as a disturbance in the control sense. For a particular operating point the mass of the system can be considered *a priori* known, so V_{ic} can be replaced by the specific volume v_{ic}. Regarding the selection of p_{ic} as a secondary state variable instead of the more usual selection of the temperature θ_{ic} in thermodynamic problems, the reason is that maximum pressure constraints can be directly considered. Accordingly, provided the volume during the thermodynamic cycle, the cylinder pressure evolution can be obtained by integration of the first law of thermodynamics applied to the closed system between the IVC and EVO:

$$\frac{\mathrm{d}p_{ic}}{\mathrm{d}\alpha} = \frac{\gamma - 1}{v_{ic}} \left(\frac{\partial q_b}{\partial \alpha} + \frac{\partial q_{wall}}{\partial \alpha} \right) - \frac{\gamma p_{ic}}{v_{ic}} \frac{\mathrm{d}v_{ic}}{\mathrm{d}\alpha} \tag{4.97}$$

where the dependence of the variables on the crank angle α has been omitted for the sake of clarity, v_{ic} is the specific volume in the cylinder, γ is the heat capacity ratio, q_b and q_{wall} represent the heat released during the combustion process and the heat transfer to the cylinder walls respectively. Note that equation (4.97) is obtained from the application of the first law of thermodynamics to a closed system, which involves that there is not mass exchange between the system and its surroundings. In the case at hand it means that since the injection process involves some mass exchange, the fuel mass injected should be neglected compared to the total mass admitted in the cylinder. As far as the stoichiometric fuel to air ratio for the considered fuel is 1/14.5 and

taking into account the lean operation of diesel engines–below 0.7–the fuel only represents around a 4% of the total mass admitted by the cylinder, so this assumption can be done without introducing a significant error. The heat released during the combustion is calculated as:

$$\partial_\alpha q_b = m_f H_f u_{fbr} \tag{4.98}$$

where m_f is the fuel injected during the cycle, H_f stands for the lower heating value of the fuel and u_{fbr} represents the fuel burning rate, *i.e.* the derivative of the fuel mass fraction burnt respect to the crank angle. Note that ∂_α represents the partial derivative with respect to α.

The heat transfer to the cylinder walls is modeled as:

$$\dot{q}_{wall} = h_{wall} A_{wall} (\theta_{ic} - \theta_{wall}) \tag{4.99}$$

where h_{wall} the heat transfer coefficient, A_{wall} is the heat exchange area and θ_{wall} the temperature of the walls. The heat transfer coefficient is modeled with a Nusselt like correlation, particularly a variation of the Woschni's correlation proposed in [19] and [20]:

$$h_{wall} = k_1 b^{-0.2} p_{ic}^{0.8} \theta_{ic}^{-0.53} \mathrm{c}_g^{0.8} \tag{4.100}$$

where k_1 is a constant (in the case at hand 0.12), b is the piston bore, p_{ic} and θ_{ic} represent the pressure and temperature evolution in the combustion chamber and c_g is the gas velocity obtained from the following correlation:

$$\mathrm{c}_g = k_{w1} \mathrm{c}_m + k_{w2} \mathrm{c}_u + k_2 \frac{V_d p_{ivc}}{V_{ivc} \theta_{ivc}} (p_{ic} - p_{mo}) \tag{4.101}$$

where c_m and c_u are the mean piston speed and the tangential flow velocity due to swirl respectively, p_{ivc}, V_{ivc} and θ_{ivc} are the cylinder pressure, volume and temperature at the intake valve closing, V_d is the cylinder displacement, p_{mo} is the pressure evolution in motoring conditions and k_{w1}, k_{w1} and k_2 are calibration constants.

The in-cylinder pressure may be calculated from the integration of (4.97) between IVC and EVO. This pressure can be used to calculate the indicated work. It is straightforward to compute the indicated efficiency or the Indicated Specific Fuel Consumption (ISFC).

There are several low computational cost models to predict $\mathrm{NO_x}$ emissions in the literature for a given HRL. Some of them rely on correlations that provide the generated $\mathrm{NO_x}$ as a function of the operating conditions [21, 22], while others, physically-based, use the evolution of the thermodynamic variables during the cycle to compute the in-cycle evolution of $\mathrm{NO_x}$ generation.

For the works in this thesis, one of the last kind proposed by [23] has been used because of its good accuracy and the easy combination with the combustion model previously described. According to the referred model, the thermal NO_x generation can be calculated as:

$$\partial_\alpha m_{nox} = k_f \partial_\alpha q_b \exp\left(-\frac{k_{act}}{\theta_{ad} - k_{\Delta\theta}}\right) \tag{4.102}$$

where k_f represents the proportionality between the heat released and the amount of reactants passing through the flame front, and k_{act} is a constant to model the NO_x reaction rate with an Arrhenius-like correlation depending on the temperature of the reactants. This temperature is estimated as the adiabatic temperature θ_{ad} with an offset given by the calibration parameter $k_{\Delta\theta}$. A deep explanation of the physical background of this expression can be found in [23]. Note that this model only takes into account NO_x formation via the thermal mechanism, so despite being the most important in diesel engines, some deviation between the model results and experimental NO_x emissions can be observed, specially when premixed combustion plays an important role [23].

4.5.6 Coolers

Intake gas coming from the compressor goes through an intercooler to increase density before going to the intake port. EGR valves also include a cooler for performance reasons and to avoid excessive exposure of the valve mechanism to high temperatures. These elements are represented with a simple model of a heat exchanger that transfers thermal energy from the gas to another fluid–engine coolant in the case of EGR valves and water for the intercooler in the testing facility custom setup–with an efficiency η_{ic}:

$$\theta_{ds} = (1 - \eta_{ic})\theta_{us} + \eta_{ic}\theta_{cf} \tag{4.103}$$

where θ_{cf} is the temperature of the cooling fluid. Note this expression is also valid for air-to-air heat exchangers.

4.5.7 Quasi-steady engine approach

Due to the high complexity of the above model, a simplified approach is performed to assess optimization problems where engine dynamics are not relevant or when control is performed acting only on the throttle. In those cases the goal is to assess an engine supervisory control consisting on the choice of the operating setpoint, neglecting the dynamic response as it would

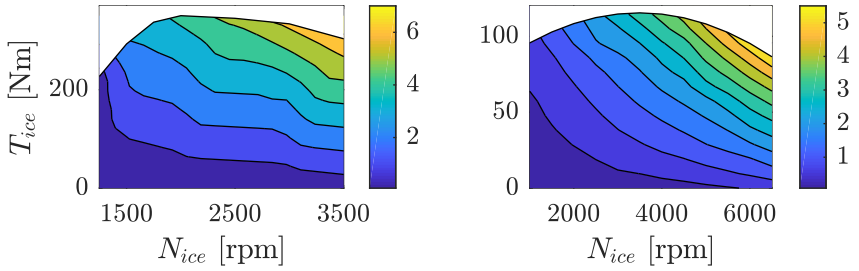

Figure 4.27: Two engine maps showing fuel consumption in g/s as a function of engine speed N_{ice} and torque T_{ice}. Left plot corresponds to a turbocharged diesel engine and right plot to a naturally aspirated gasoline engine.

be managed by an additional low level controller. Therefore, only steady state engine performance is interesting.

The classic approach is to reduce the engine to a map as a function of engine speed N_{ice} and fueling rate u_f [13]. Many quantities may be mapped, but probably the most interesting for a vehicle model is the fuel consumption– see figure 4.27 for the fuel consumption map of two different engines used in this thesis. Efficiency, if needed, may be estimated with the quotient between mechanical power and the heating energy of the fuel:

$$\eta_{ice} = \frac{N_{ice} T_{ice}}{\dot{m}_f H_f} \tag{4.104}$$

where H_f is the fuel heating value.

This engine model is not able to reproduce transient effects since only steady state values are mapped. However, it is usually enough for many control applications as it is a simple approach to an ICE.

References

[1] W. F. Milliken and D. L. Milliken. *Race car vehicle dynamics*. Vol. 400. Society of Automotive Engineers Warrendale, 1995.

[2] P. Waltermann. "Modelling and control of the longitudinal and lateral dynamics of a series hybrid vehicle". In: *Proceedings of the IEEE International Conference on Control Applications*. 1996, pp. 191–198.

[3] T. D. Gillispie. *Fundamentals of vehicle dynamics*. SAE International, 1992.

[4] R. Rajamani. *Vehicle dynamics and control*. Springer Science & Business Media, 2011.

[5] L. Guzzella and A. Sciarretta. *Vehicle propulsion systems. Introduction to modeling and optimization.* Springer-Verlag, 2005.

[6] A. Emadi et al. "Topological overview of hybrid electric and fuel cell vehicular power system architectures and configurations". In: *IEEE Transactions on Vehicular Technology* 54.3 (2005), pp. 763–770.

[7] J. Liu, H. Peng, and Z. Filipi. "Modeling and analysis of the Toyota hybrid system". In: *Proceedings of the IEEE/ASME International Conference on Advanced Intelligent Mechatronics.* Vol. 200. 2005, pp. 134–139.

[8] J. Liu and H. Peng. "Modeling and control of a power-split hybrid vehicle". In: *IEEE Transactions on Control Systems Technology* 16.6 (2008), pp. 1242–1251.

[9] T. Mesbahi et al. "Improved model of battery/supercapacitor hybrid energy storage system based on thermo-electrical and aging behaviors". In: *7th IET International Conference on Power Electronics, Machines and Drives.* 2014, pp. 1–8.

[10] D. H. Johnson. "Origins of the equivalent circuit concept: the voltage-source equivalent". In: *Proceedings of the IEEE* 91.4 (2003), pp. 636–640.

[11] H. He, R. Xiong, and J. Fan. "Evaluation of lithium-ion battery equivalent circuit models for state of charge estimation by an experimental approach". In: *Energies* 4.4 (2011), pp. 582–598.

[12] C. Guardiola et al. "Representation limits of mean value engine models". In: *Identification for Automotive Systems.* Springer, 2012, pp. 185–206.

[13] L. Guzzella and C. H. Onder. *Introduction to modeling and control of internal combustion engine systems.* Springer, 2004.

[14] J. Wahlström and L. Eriksson. "Modelling diesel engines with a variable-geometry turbocharger and exhaust gas recirculation by optimization of model parameters for capturing non-linear system dynamics". In: *Proceedings of the Institution of Mechanical Engineers, Part D: Journal of Automobile Engineering* 225.7 (2011), pp. 960–986.

[15] J. Heywood. *Internal combustion engine fundamentals.* McGraw-Hill, 1988.

[16] J. Asprion, O. Chinellato, and L. Guzzella. "Optimisation-oriented modelling of the NOx emissions of a diesel engine". In: *Energy Conversion and Management* 75 (2013), pp. 61–73.

[17] M. Lapuerta, O. Armas, and J. J. Hernández. "Diagnosis of DI diesel combustion from in-cylinder pressure signal by estimation of mean thermodynamic properties of the gas". In: *Applied Thermal Engineering* 19.5 (1999), pp. 513–529.

[18] G. Woschni. *A universally applicable equation for the instantaneous heat transfer coefficient in the internal combustion engine.* Tech. rep. SAE Technical Paper, 1967.

[19] F. Payri et al. "A new tool to perform global energy balances in DI diesel engines". In: *SAE International Journal of Engines* 7 (2014), pp. 43–59.

[20] F. Payri et al. "Experimental and theoretical analysis of the energy balance in a DI diesel engine". In: *SAE Technical Paper.* 2015.

[21] C. Guardiola et al. "ECU-oriented models for NOx prediction. Part 1: a mean value engine model for NOx prediction". In: *Proceedings of the Institution of Mechanical Engineers, Part D: Journal of Automobile Engineering* 229.8 (2015), pp. 992–1015.

[22] J. Arrégle et al. "On board NOx prediction in diesel engines: a physical approach". In: *Automotive Model Predictive Control.* Springer, 2010, pp. 25–36.

[23] C. Guardiola et al. "Semiempirical in-cylinder pressure based model for NOx prediction oriented to control applications". In: *Applied Thermal Engineering* 31.16 (2011), pp. 3275–3286.

Chapter 5

Experimental tools

I have had my results for a long time but I do not yet know how I am to arrive at them.

— Carl Friedrich Gauss

Contents

Work (chapter or section)	Setups	Experimental validation
HP- and LP-EGR switching control (6.2)	Setup A	yes
Full engine control (6.3)	Setup A	yes
Speed management with engine control (7)	Setup C	no
HEV energy management (8)	Setup D	no
HRL design (9.2)	Setup B	yes
HEV powertrain sizing (9.3)	Setup D	no

Table 5.1: Summary with the experimental facilities and setups used at the diverse works presented in this thesis.

5.1 Introduction

Optimal control is intimately related to the actual system it drives. Despite the theoretical work is somehow universal–the mathematical problem might differ from case to case, but it is ultimately an optimization problem–, the chosen method and the practical implementation is system-specific. Also, the quality of the control-oriented models is critical for the optimization results to stick to the actual capabilities of the controlled system.

Several experimental tests are performed in this thesis, mainly because of two reasons: (i) in order to provide realistic models based on the available experimental information–fitting data and validation cycles–, and (ii) to test and validate the optimization results on the actual facility.

5.2 System setup

According to the specific requisites of the studies carried out in this thesis, several experimental tools have been used. On one hand, theoretical works have been mostly developed with manufacturers' experimental data, especially those where quasi-steady models are sufficient. On the other hand, experimental facilities have been used for studies where a practical validation has been performed. A summary with the experimental setups that have been used throughout this thesis can be found in table 5.1. These setups are described in the following sections.

5.2.1 Setup A

This setup consists of an engine test bench. It is the main experimental facility used in this thesis to validate the results of optimal control applications.

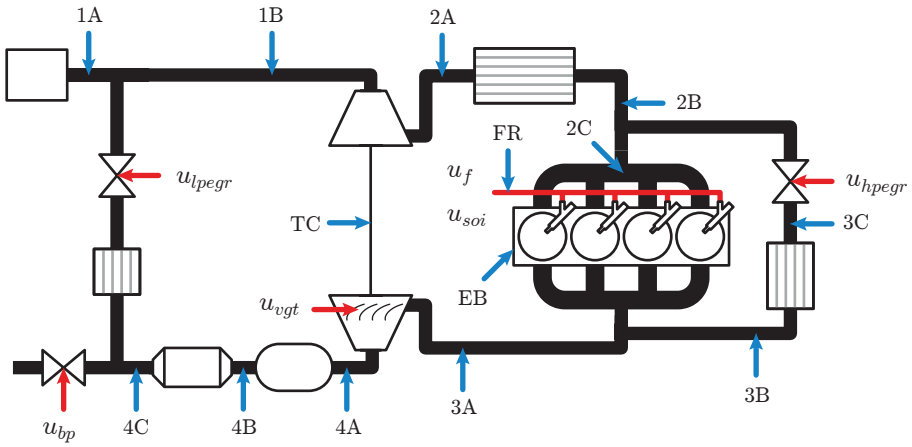

Figure 5.1: Engine A layout with location of the factory and additional instrumentations. Blue arrows denote readings while red arrows represent controls that can be actuated.

The test bench is composed of an ICE and a dyno that absorbs the engine power and drives it if necessary. A number of measuring devices and control electronics are also part of the facility.

Engine

The ICE is a production passenger vehicle 2-liter and 4-cylinder diesel engine, in compliance with Euro 5 emission standards. Its main characteristics are summarized in table 5.2 and a schematic diagram of the airpath may be found in figure 5.1. The engine features two EGR loops, namely the factory standard HP-EGR and a custom LP-EGR loop installed to explore the capabilities of this architecture in combination of optimal control. The LP-EGR system is located downstream the DPF to minimize the amount of exhaust gas particulate through the compressor and to avoid a premature damage. The system is mostly the same than the HP loop: it is composed of a water-cooled heat exchanger and a valve. The heat exchanger is located upstream to avoid excessive thermal shock in the valve, despite this phenomenon is not as critical as in the HP system. Due to the low pressure drop in the LP-EGR system–both sides of the valve are close to the atmospheric pressure–the recirculated flow amount might be insufficient even when the valve is wide-open. To overcome this issue, a backpressure valve is installed in the exhaust line, downstream the joint where the flow diverts to the LP-EGR. This valve raises the pressure upstream the LP-EGR producing an increased pressure drop.

Architecture	Diesel, inline-four
Displacement	1997 cc
Bore x stroke	85 x 88 mm
Compression ratio	16:1
Valves	16
Injection system	Common rail
Breathing system	Turbocharged, VGT, intercooled
Emissions control	HP- and LP-EGR, DOC, DPF
Emissions standard	Euro 5
Power	120 kW @ 3750 rpm
Torque	340 Nm @ 2000 rpm

Table 5.2: Main characteristics of setup A engine.

The remaining of the engine is mainly factory standard, with intercooler, VGT, DOC and DPF. There are two bypasses on the airpath, one of them avoiding the intercooler and the other bypassing the EGR cooler. In normal conditions those bypasses remain closed and gases travel throughout the coolers. However, if a higher temperature is required at the intake manifold–during warm up, to reduce CO emissions, in DPF regeneration phases, etc.–throttles are piloted to let the flow bypass the coolers. Intercooler throttle is also used to increase the amount of recirculated gas when the EGR valve is already wide-open by slightly closing it producing a pressure decrease at the intake manifold.

The engine cooling system is custom-made due to the requisites of an engine in a stationary setup. The air-to-air intercooler is replaced with an air-to-liquid heat exchanger. Coolant flow–coming from a cooling tower–is managed with a PID controller that keeps a constant temperature at the intercooler. A different circuit is used for the engine coolant with an additional PID. EGR coolers are also air-to-liquid heat exchangers with an independent circuit. Since these devices are originally cooled with engine coolant, an electric resistance in combination with a PID controller is installed to keep the liquid at the engine temperature. Despite all these changes, differences from factory cooling system are negligible for the scope of this thesis as long as all experiments are performed after engine warm up and PID controllers keep temperatures constant.

The ICE is coupled to a Horiba Dynas3 asynchronous dyno that absorbs the delivered torque and drives the engine in overrun simulations. The test-cell is controlled with a Horiba Sparc and interfaced with a Horiba Stars environment. The facility enables to perform tests with a prescribed engine

speed trajectory or a road load simulation where speed is updated according to the vehicle's parameters.

Factory control scheme

The engine control is performed by a Delphi ECU. The control scheme follows the factory structure with the manufacturer calibration. This particular ECU, however, has an additional ETK port that allows to stream data from and to the ECU memory.

With factory standards, airpath management is performed by actuating EGR valve and VGT position. Due to the coupling between systems [1], there are two different operation modes which are switched according to the engine operation point, whose limits are shown in figure 5.2. The first mode occurs at low load and low to medium engine speed, where the fresh air mass flow is controlled in closed-loop. The mass flow meter readings are monitored and the EGR valve is controlled to reach the desired air mass flow amount: the closer the valve is, the more the fresh air flows throughout the intake–for a given volumetric efficiency, less recirculated gases means that more fresh air must be supplied. The target air mass flow, and consequently an EGR fraction, is achieved with a PID controller, aiming to reduce the generation of NO_x emissions. The VGT position is set in open-loop according to ECU maps, producing an intake manifold pressure that is not controlled. The control sequence of this operating mode is represented in figure 5.3. The second mode is activated at the rest of the engine operating region. In this case, intake manifold pressure is controlled in closed-loop. The actual pressure is measured and kept at the level specified in the ECU calibration by acting on the VGT position: closing the stator accelerates the flow, spinning the turbine faster, increasing the mass flow through the compressor and consequently rising the intake pressure. During this operating mode the EGR is completely closed. This control sequence is also represented in figure 5.3.

After setting the desired position of the EGR valve and the VGT position at any of the above two modes, the actual actuator position is measured. This reading feeds a PID controller–one for each control–that tracks the current position in order to reach the target accurately. This control variable is ultimately processed into a Pulse-Width Modulation (PWM) signal to excite the solenoid that drives the valve.

The fueling rate is calculated from the current engine speed and pedal position. This injection amount is set in open-loop since there is no instrument onboard to measure the actual injection settings. An estimation is used instead, based on the fuel rail pressure and intake conditions. Then, the ECU is able to predict the necessary injection time to reach the desired fuel amount according

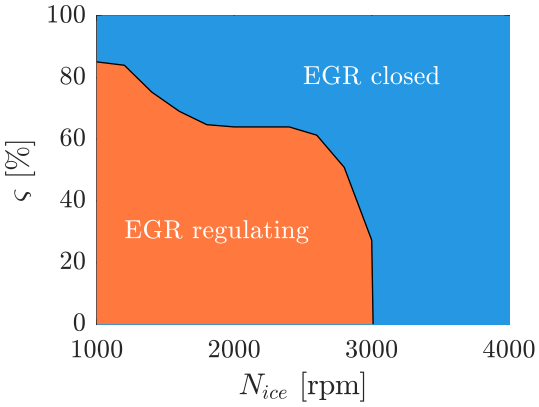

Figure 5.2: Operation zones for the two air control modes of engine A factory calibration as a function of engine speed N_{ice} and pedal position ς. The region in red is the EGR activation area where air mass flow is tracked. In the blue region the pressure is controlled in closed-loop while the EGR valve remains closed. This policy corresponds to the factory calibration.

to its calibrated values. This decision is forwarded straight to the injectors, whose plunger will lift the specified time. This ECU is capable of two pilot, a main, and two post injections. Pilot injections are scheduled to reduce engine noise and vibrations and, generally, they represent between 1 and 5% of the total injected amount. Post injections are disabled during the normal operation of the engine. SOI is set according to ECU calibrated values. The crankshaft position sensor permits to schedule all available injection events at the specified angles. The ECU has several additional safeguards to avoid potentially dangerous SOI settings that may damage the engine. The fuel rail pressure is controlled in closed-loop to match the desired value at the calibration. The pressure is measured and a valve on the rail is actuated.

LP-EGR and backpressure valves are driven with an external PID controller that monitors the actual position in closed-loop. Setpoints can be externally introduced but ECU has no real control over the valves.

Factory calibration for the main ECU controls are represented in figure 5.4. Notice that several corrections are applied to these values according to engine temperature, ambient conditions, etc. Also, additional maps exist for different operating modes such as DPF regeneration, DPF lightoff, starting or exhaust heat recovery among others.

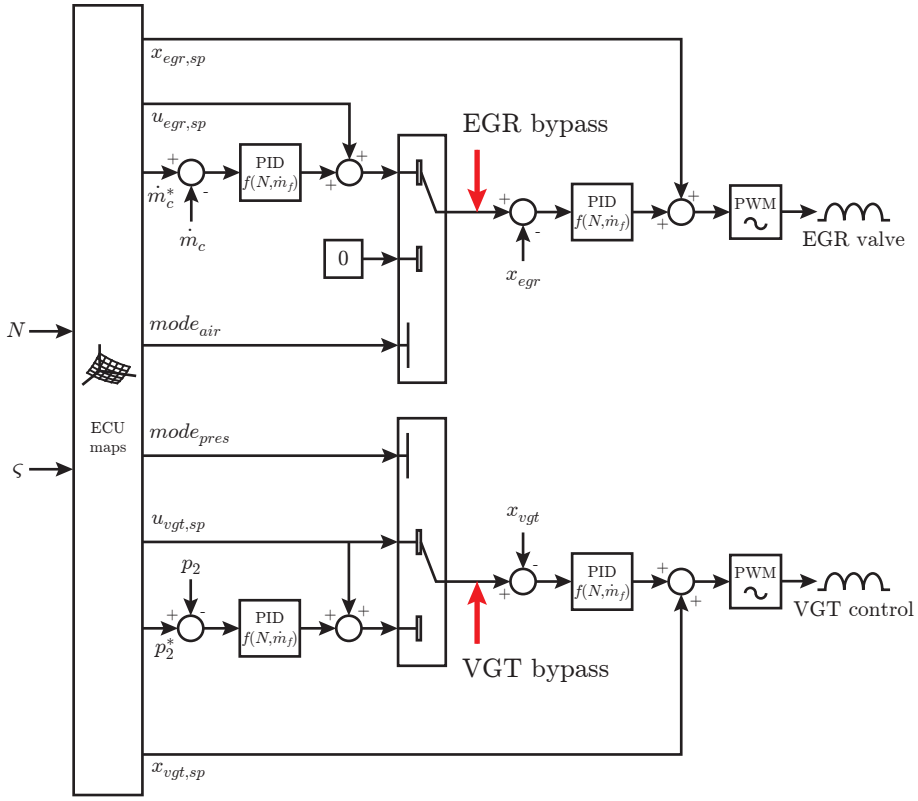

Figure 5.3: Simplified scheme of the EGR and VGT control at the factory ECU strategy (engine A). Red arrows denote the point where bypass variables are injected in the control flow.

Instrumentation

The test cell is equipped with a dynamometer, a Horiba SPARC and STARS system including numerous additional thermocouples and pressure sensors installed along the engine airpath, a turbo speed measuring sensor, a Horiba MEXA-7170DEGR exhaust gas analyzer, an AVL 439 Opacimeter, a Horiba FQ-2100DP fuel meter, an ABB Sensyflow mass flow sensor, two Continental NO_x probes and additional Negative Temperature Coefficient thermistors (NTCs). A descriptive scheme of the testing facility and these additional devices is shown in 5.5. The locations where the engine has been instrumented can be appreciated in the engine layout scheme at figure 5.1.

The dynamometer is an asynchronous machine rated to 250 kW and a maximum torque of 580 Nm. It is equipped with torque and rotational speed

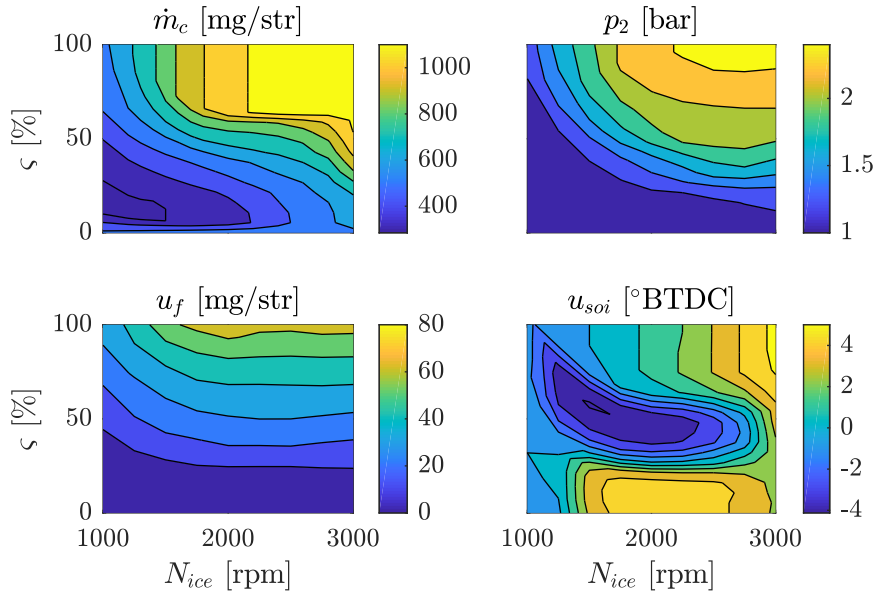

Figure 5.4: Factory calibration maps (engine A) as a function of engine speed N_{ice} and pedal position ς. These quantities (air mass flow $\dot{m}_c$, intake manifold pressure p_2, fueling rate u_f and SOI u_{soi}) represent master demands at the factory ECU calibration for the nominal operating mode. Temperature corrections, other operating modes or safeguards may apply to these setpoints during engine operation. The shown fuel injection quantity and timing correspond to the main injection.

sensors that are forwarded to the SPARC system. These measures are used to control the test bed as well.

Horiba STARS interface interacts with the testing facility. It is used to set up the experimental tests and to collect measurements from the additional engine instrumentation. Those additional sensors include numerous thermocouples and pressure sensors that are spread along the airpath, complementing the ECU sensors. Those additional measurements are useful to characterize individual components of the engine with upstream and downstream experimental data. For example, factory sensors do not include turbine inlet temperature readings, which may be pretty interesting when analyzing cylinder processes or turbine performance. In addition, an eddy current turbo speed sensor is mounted in the compressor case, detecting the pass of the blades and, therefore, accounting for the rotational speed of the turbocharger. This information is critical for turbocharging modeling purposes, which are an essential part of the optimal control.

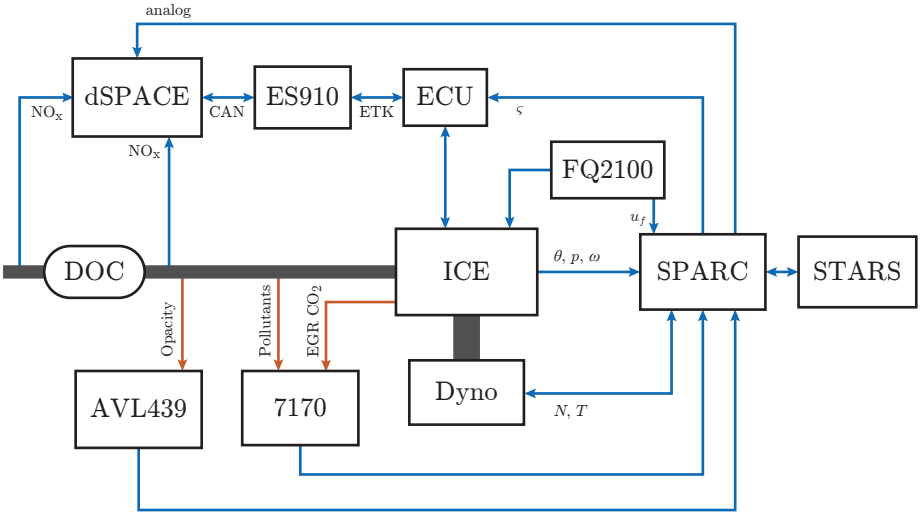

Figure 5.5: Scheme of engine A test bench facility and instrumentation. Gas bleeding is represented with orange links while electrical connections (CAN, ethernet, ETK or analogical) are represented in blue. The information flow direction and the main variables transmitted between devices are shown.

The Horiba MEXA-7170DEGR gas analyzer features two probes: one is installed at the exhaust line, upstream the DOC and other after-treatment device, and the other is placed at the intake manifold. The measured exhaust gas composition includes O_2 and pollutants such as CO_2–measured by a Non-Dispersive Infrared (NDIR) analyzer–, NO_x–using a Heated Chemiluminescent Detector (HCLD)–, HC–consisting of a Heated Flame Ionization Detector (HFID)–and CO. The EGR probe measures CO_2 concentration in order to calculate the actual fraction of EGR, which is helpful during the modeling phase. Readings have a delay due to the length of the probe line and sensor dynamics. The transport delay can be detected and corrected by performing steps in both fuel and EGR rate and comparing these steps to sensor readings response. However, sensor dynamics are neglected for the scope of this dissertation as only steady state readings are considered for pollutant measurements. Figure 5.6 shows this delay and the performed correction. For the current facility, these delays have been characterized as $\tau_{exh} = 5.1$ seconds and $\tau_{egr} = 7.2$ seconds for exhaust and EGR probes respectively.

An AVL 439 opacimeter is used to measure exhaust gases opacity. The probe is placed upstream DOC and DPF. The opacimeter uses a light source whose beam crosses the exhaust gas flow, and a photosensor detects the amount of light that reaches the other side. The measure is expressed as a percentage

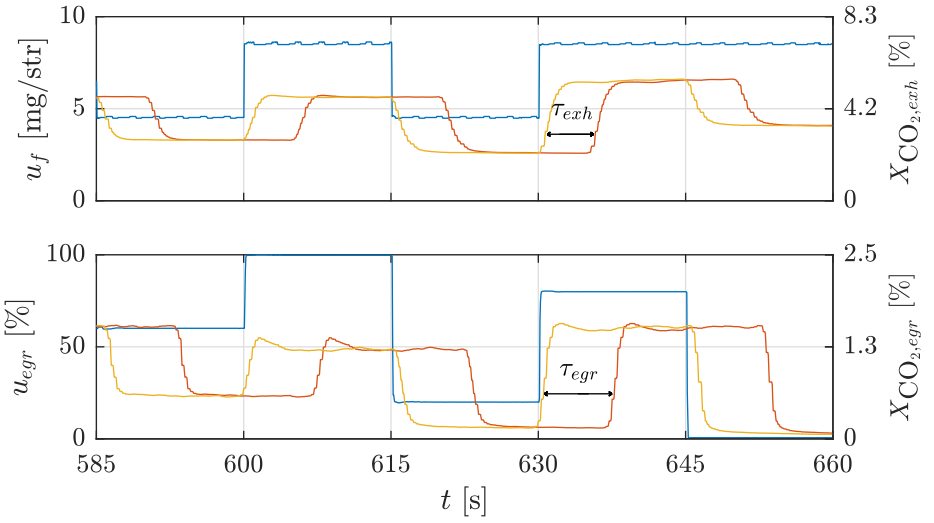

Figure 5.6: Analysis of the delay at pollutants measurement introduced by the gas analyzer. On top plot, raw CO_2 concentration at the exhaust (in red) is compared against the injected fuel amount (in blue)–CO_2 is proportional to the fuel–. Gas analyzer readings can be synchronized by shifting them a time τ_{exh} (yellow line). Similarly, on bottom plot, raw CO_2 concentration at the intake manifold (in red) is compared against EGR valve actuation (in blue). Synchronized readings can be achieved by applying a shift of τ_{egr} (in yellow).

where zero means that all light reaches the sensor, while 100% occurs when no photon is captured on the other side. This measure is correlated with the amount of smoke generated at the engine and can be translated into other units. First, according to the opacimeter manufacturer, soot in Filter Smoke Number (FSN) units can be calculated from opacimeter readings σ as:

$$\text{FSN} = \begin{cases} 0.084 + 0.18\sigma - 0.0014\sigma^2, & \sigma < 55\% \\ \frac{\sigma}{10}, & \sigma \geq 55\% \end{cases} \tag{5.1}$$

Then, according to Bosch and as defined in [2], soot mass flow can be calculated from FSN units as:

$$\dot{m}_{soot} = \left(3.97 \cdot \text{FSN} + 7.59 \cdot \text{FSN}^{1.83}\right) \dot{m}_t \tag{5.2}$$

The opacimeter readings are delayed solely due to the flow of the exhaust gas throughout the probe–sensor readings do not introduce a noticeable delay. This delay can also be easily detected and corrected as shown in figure 5.7.

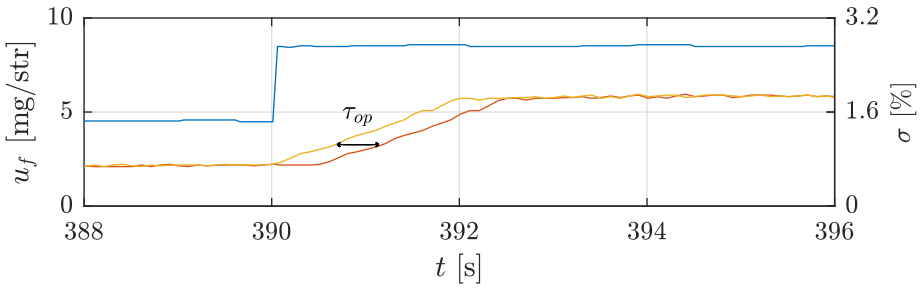

Figure 5.7: Detail of the delay introduced at the opacimeter readings. A change in fuel injection rate (blue) produces a variation on the smoke generation (red). The readings may be phased with the ECU variables by shifting them a time $\tau_\sigma = 0.5$ (yellow). This value is facility-specific.

The Horiba FQ-2100DP fuel meter consists of a balance that offers an instantaneous fuel consumption value based on the weighted fuel mass derivative. It is used to measure the actual fuel consumption with an uncertainty of 0.12% at steady state readings.

ABB Sensyflow is a hot wire sensor which is installed upstream the factory flow sensor. It is preceded and followed by straight ducts in order to achieve a laminar and cross-section-homogeneous flow through the sensor. A laminar flow improves readings quality and accuracy. Based on the Sensyflow measurements, the factory mass flow sensor curves at the ECU have been recalibrated to deliver the same readings.

The Continental NO_x probes are placed upstream and downstream the DOC. They are heated and CAN-bus ready. The sensor consists of a first chamber where oxygen is pumped out with an electrode pump, exhaust products are burned and, as a consequence, NO_2 is reduced into NO. Then, in a second chamber, NO is reduced into N_2 and O_2 and the oxygen is pumped out again and measured like in a lambda sensor. The NO_x probe measures the NO_x concentration in ppm, but it can be translated into mass flow with:

$$\dot{m}_{nox} = 10^{-6} c_{nox} X_{nox} \dot{m}_t \tag{5.3}$$

where X_{nox} is the NO_x concentration in ppm and $\dot{m}_t$ the exhaust mass flow. The coefficient c_{nox} is defined as the quotient of NO_2 and air molar masses:

$$c_{nox} = \frac{M_{\mathrm{NO_2}}}{M_{\mathrm{air}}} = 1.587 \tag{5.4}$$

The installation of two NO_x probes allows to measure raw pollutants formation at the engine as well as post-DOC NO_x concentration to evaluate the after-

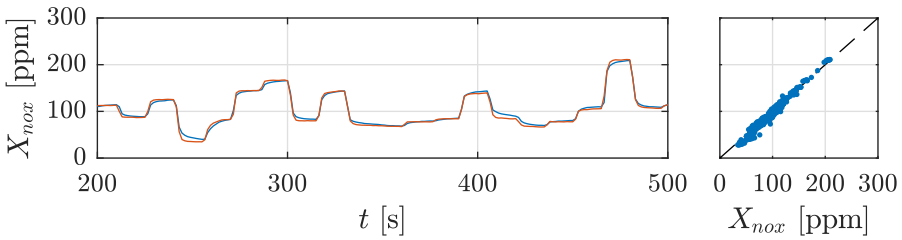

Figure 5.8: Performance analysis of the NO_x probe placed upstream the DOC. Probe readings are in blue and Horiba gas analyzer measurements are in red. The test consisted of fuel, SOI, EGR and VGT steps with 15 seconds of steady state operation. The probe sensor was calibrated with previous readings from the gas analyzer.

treatment performance. Both sensors have been calibrated to the Horiba gas analyzer readings in steady state measurements–a comparison is shown in figure 5.8. The robustness of the probes makes them a good candidate for accurate readings, avoiding the delays present at Horiba measurements–for the scope of this work, NO_x probes readings can be considered instantaneous.

All measurements are ultimately sent to a dSPACE MicroAutobox through CAN-bus (ECU variables and NO_x probes) and analog lines (Sparc/Stars, gas analyzer, turbo speed sensor, opacimeter, Sensyflow, dynamometer and NTCs). A list of all the variables measured at the engine with the different instruments is summarized at table 5.3.

Custom control scheme

In order to be able to interact with the factory engine control and to apply optimal control policies, a bypass has been set up. The ECU has an ETK port that grants access to its volatile memory on real time. Variables in the ECU can be read and overwritten with custom values that are streamed through the ETK line. An Etas ES910 device is used to interface with the ECU at the ETK port. The ES910 device can communicate with a bypass-ready ECU, gather the ECU variables of choice (60 variables in the current setup) and stream them on an additional CAN line. It can also forward CAN messages to the ETK port and inject the variables at different places in the factory control structure.

The optimal control strategies are built and implemented in a rapid prototyping dSPACE MicroAutobox device. This device streams the controls and gathers ECU variables from the ES910 CAN-bus. Additionally, it collects information from the aftermarket NO_x probes–connected to dSPACE with

Location	θ	p	Pos	$\dot{m}$	ω	T	λ_e+O_2	NO_x	Poll.	Soot
1A	●	●		●●						
1B	●●	●●								
2A	●	●								
2B	●●	●●								
2C	●								●	
3A	●	●								
3B	●	●								
3C	●	●								
4A	●●	●					●●	●	●	●
4B	●●	●					●	●		
FR	●	●		●						
EB	●●	●			●●	●				
TC					●					
HPEGR			●							
VGT			●							
LPEGR			●							
BP			●							
Pedal			●							

Table 5.3: Summary of the variables measured at the engine A test bench. Columns represent the type of measurement (temperature, pressure, position, mass flow, rotational speed, torque, lambda, NO_x concentration, pollutants and soot). Rows denote the location of that measurement at the engine according to the nomenclature in figure 5.1. Factory instrumentation is shown with blue dots and additional instrumentation in red.

an additional CAN line–, NTCs running on an analogical line, and test cell measurements (turbo speed, dyno torque, thermo couples, pressure sensors, etc.) at the additional analogical inputs. Opacimeter, Horiba gas analyzer and Sensyflow measurements are sent through analogical lines as well.

The ECU control variables that have been substituted–bypassed–for custom dSPACE variables are:

- HP-EGR valve position (0 to 100%), u_{egr}.
- Compressor air mass flow demand, $\dot{m}_{c,sp}$.
- VGT position demand (0 to 100%), u_{vgt}.
- Boost pressure demand, $p_{2,sp}$.

- Fuel amount injected in pilot injections, $u_{f,pi1}$ and $u_{f,pi2}$.
- Fuel amount injected in main injection, $u_{f,main}$.
- Fuel amount injected in post injections, $u_{f,po1}$ and $u_{f,po2}$.
- Pilot injections timing, $u_{soi,pi1}$ and $u_{soi,pi2}$.
- Main injection timing, $u_{soi,main}$.
- Post injections timing, $u_{soi,po1}$ and $u_{soi,po2}$.
- Fuel rail pressure demand, $p_{rail,sp}$.
- Throttles (intercooler and EGR cooler bypasses) position demand (0 to 100%), $u_{thr,ic}$ and $u_{thr,egr}$.
- Pedal position, ς.

During all experiments engine is kept in normal operating mode and, therefore, post injections are set to zero, intercooler throttle is closed and EGR cooler throttle is closed as well. Bypassed variables are injected in a late stage at the factory control flow to avoid additional corrections or interferences with special operating modes. Injection timing is, however, inserted before ECU safeguards in order to avoid potential damage to the engine due to a wrong setting.

5.2.2 Setup B

This setup is composed of an engine test bench with a single cylinder engine. The facility is aimed for in-cylinder pressure-related works.

Engine

The test-cell is fitted with a single cylinder DI CI engine, whose main features are shown in table 5.4. This single cylinder engine is the result of an in-house engine design process aimed to develop the minimum size DI CI engine for automotive applications (specific power around 40 KW/litre and 40% efficiency) with state-of-the -art technology [3]. The resulting engine, with 150 cm^3 displacement, is representative of a small turbocharged ICE. In order to simulate the forced induction of a multi cylinder engine, the intake line is equipped with a screw compressor. Between the compressor and the intake port, a cooler, a dryer and a heater are installed, making possible to achieve any desired thermodynamical conditions (θ,p) at the cylinder. These devices

Type	Common rail DI
Number of cylinders	1
Bore/Stroke	1.1
Displacement	150 cm^3
Compression ratio	17:1
Combustion chamber geometry	quiescent
Swirl number	0
Maximum cylinder pressure	180 bar
Number of injection nozzles	6
Nozzle diameter	92 μm

Table 5.4: Main characteristics of the setup B engine.

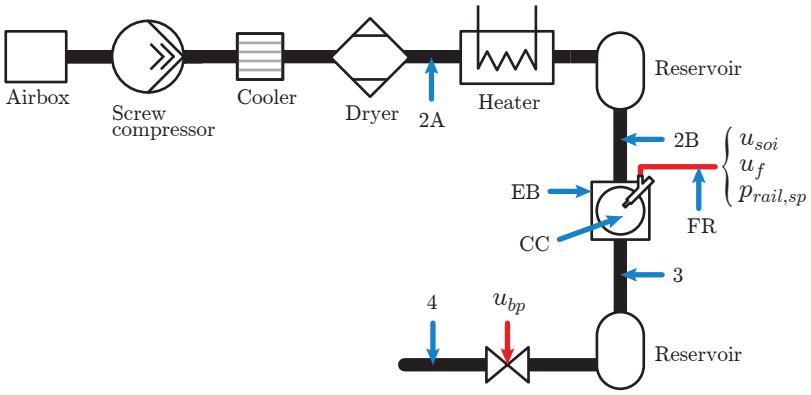

Figure 5.9: Engine B layout with measuring locations (blue arrows) and actuated controls (red arrows).

are powered with external sources and do not jeopardize engine performance. The exhaust is equipped with a backpressure valve to simulate the effect of a turbine. In order to avoid pressure pulses to reach the intake port, reservoirs are placed at the intake and exhaust manifolds that keep a constant pressure and filter wave effects. The layout of the engine is depicted at figure 5.9.

Instrumentation

The test-cell is equipped with a Horiba MEXA-7170DEGR gas analyzer and an AVL-415 opacimeter. A descriptive scheme of the facility is available at figure 5.10. The engine is fully instrumented with temperature, pressure, mass flow and concentration sensors. Table 5.5 summarizes the variables measured at the engine according to the nomenclature indicated at figure 5.9. For the

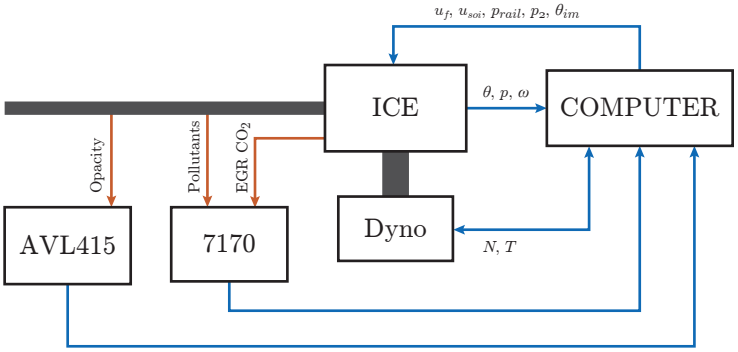

Figure 5.10: Scheme of engine B test bench facility and instrumentation. Gas bleeding is represented with orange links while electrical connections are represented in blue. The information flow direction and the main variables transmitted between devices are shown.

works in this thesis, the key signals recorded are the in-cylinder pressure signal and fuel consumption to compute the ISFC, the air mass flow and intake conditions to compute the gas conditions at the IVC and the NO_x emissions to assess the emission limits. Dyno, gas analyzer and opacimeter readings are forwarded to a computer that controls the facility. This computer is in charge of setting the controls of the engine as well. No ECU is present at this research engine and, therefore, controls are set manually. The available controls are:

- Fueling rate u_f for each injection event. The system is capable of 8 injections per cycle but only two were performed during tests since the minimum injection quantity is a significant amount for such a small engine.
- SOI u_{soi} for each injection event.
- Fuel rail pressure p_{rail}.
- Intake pressure p_2 by actuating the screw compressor.
- Intake temperature θ_{im} thanks to the heater.
- Backpressure valve position u_{bp} to simulate the presence of a turbine.

Location	θ	p	Pos	$\dot{m}$	ω	T	Poll.	Soot
2A				●				
2B	●	●						
3	●	●						
4							●	●
FR	●	●		●				
EB	●	●			●	●		
CC		●						
BP			●					

Table 5.5: Summary of the variables measured at the engine B test bench. Columns represent the type of measurement (temperature, pressure, position, mass flow, rotational speed, torque, pollutants and soot). Rows denote the location of that measurement at the engine according to the nomenclature in figure 5.9.

Mass	1285 kg
Drag coefficient	0.31
Frontal area	2.12 m^2
Rolling coefficient	0.015
Wheel radius	0.31 m
Number of gears	5
Final gear ratios	12.82, 6.81, 4.40, 3.20, 2.56

Table 5.6: Setup C vehicle parameters.

5.2.3 Setup C

This setup consists of a diesel engine and a vehicle model, representing a B-segment passenger vehicle. This setup is used for vehicle optimal control works (section 7).

The engine model corresponds to the facility from setup A. It is fitted and validated to the actual engine. This model considers the effect of HP-EGR (LP-EGR is always closed in this setup), VGT, SOI and fueling rate in the engine dynamics, according to the equations described in section 4.5. The vehicle model follows the scheme described in section 4.2 with the parameters shown in table 5.6, which are extracted from manufacturer's data sheets.

Emission standards	Euro 5
Displacement	1199 cm^3
Number of cylinders	3
Number of valves	12
Max torque	118 Nm (2750 rpm)
Max power	60 kW (5750 rpm)

Table 5.7: Main characteristics of setup D engine.

5.2.4 Setup D

This setup is a HEV consisting of an engine, a motor and a battery. These components have been experimentally characterized by the manufacturers at their facilities. The available data is a set of maps for each component. No further experimental information is available, but quasi-steady models are sufficient for the HEV energy management studies presented this thesis. No experimental validation of the optimal control strategies is performed due to the absence of the actual system. Therefore, these works are purely theoretical.

Engine

The engine is naturally aspirated and spark ignited. Table 5.7 summarizes the main characteristics of this engine. Quasi-steady maps for Specific Fuel Consumption (SFC), NVH, λ_e and pollutant emissions are provided by the manufacturer, which are shown at figure 5.11. The engine model is constructed from this experimental information.

Motor

The electrical motor is a PMSM, with a nominal output power of 50 kW. The manufacturer provided the operating maps at figure 5.12, showing motor efficiency, electrical power consumption, drawn current and voltage supply as a function of motor speed and torque output. Note that electrical variables are direct current measurements since these readings are done upstream power electronics and, therefore, converters and inverters performance is included. This machine is used both as a generator and as a traction motor.

Battery

The battery is made of individual A123 Systems ANR26650M1A lithium ion cells. The main characteristics of the cell can be found in manufacturer's

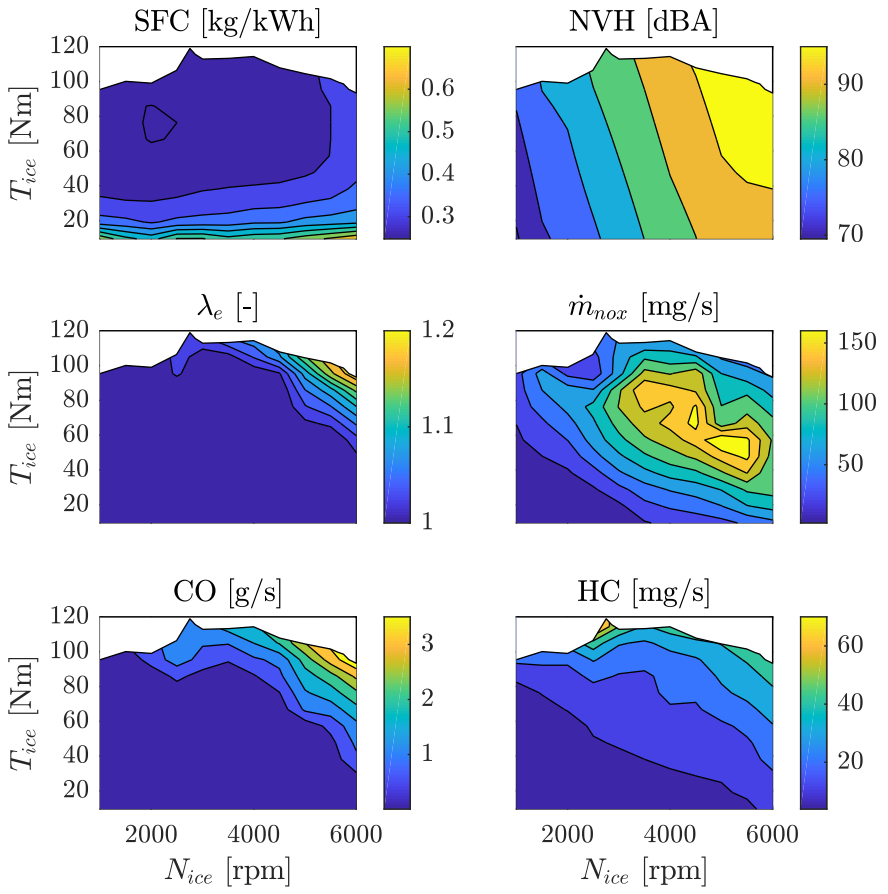

Figure 5.11: Quasi-steady maps for fuel consumption, noise, λ_e and raw pollutants (pre-catalyst), as supplied by the manufacturer. Maps correspond to a fully warmed up engine.

datasheet, which are summarized in table 5.8. Additionally, experimental performance of the cell is available at figure 5.13, where charge and discharge curves are averaged to provide a relation between open circuit voltage and SoC. A battery model is constructed with this information, following the structure described in chapter 4 and combining cells both in series and parallel.

5.3 Test description

Several tests have been performed for the different works in this thesis at the testing facilities described in the previous section. These tests respond to the

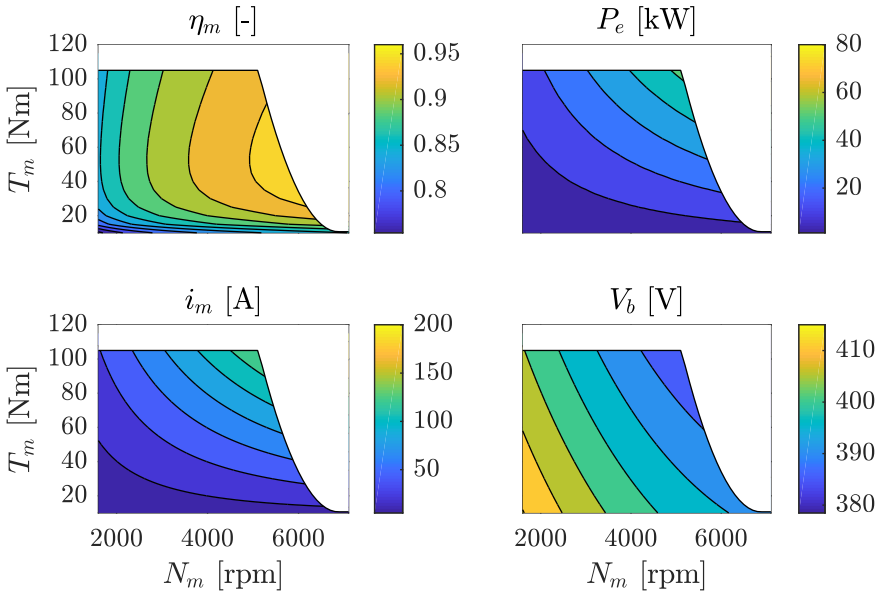

Figure 5.12: Motor (setup D) operating map as supplied by manufacturer. Efficiency η_m, electrical power consumption P_e, drawn current i_m and voltage supply V_b are shown as a function of motor speed N_m and torque output T_m.

requirements of these studies, which can be summarized as gathering data to calibrate a model first and, then, validating the results of the study in the same facility. Seven different test campaigns have been carried out. These tests are classified in the table 5.9 and are described in the following points.

5.3.1 Test 1

This test is a parametric study of engine A varying its main controls. The controls that have been actuated are: main injection fueling rate u_f and SOI

Nominal capacity Q_b	2.3 Ah
Nominal voltage V_{oc}	3.3 V
Internal resistance R_b	10 mΩ
Maximum continuous discharge $i_{b,cont}$	70 A
Maximum pulse discharge $i_{b,pulse}$	120 A
Weight m_b	70 g

Table 5.8: ANR26650M1A lithium ion cell specifications.

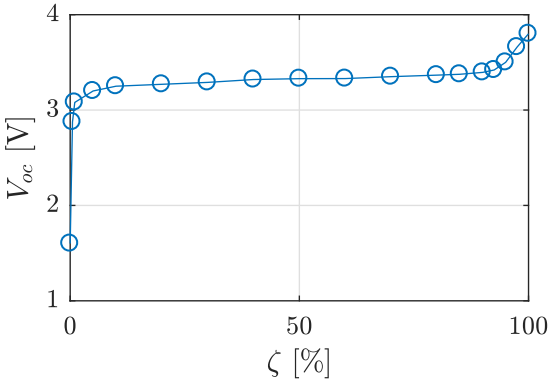

Figure 5.13: Experimental relation between open circuit voltage V_{oc} and SoC of an ANR26650M1A cell. The shown relation is the average of charge and discharge curves.

u_{soi}, HP-EGR valve position u_{egr} and VGT opening u_{vgt}. Engine speed varies from 1800 to 2700 rpm. The engine map is divided into 20 operating points, as shown in figure 5.14, according to the typical operating points of test 3 cycle. At each point, a Design of Experiments (DoE) has been set up to configure the sequence of controls at the parametric study. Table 5.10 summarizes the range of variation of the actuated controls. These sequences consists of 49 consecutive steps, randomized and with a settling time of 15 seconds, where all controls may be changed simultaneously. As an example, one of those sequences is shown in figure 5.15. Although the settling time might not be sufficient to reach a thermal steady state condition, all readings–except temperatures–show a steady behavior after few seconds. Figure 5.16 shows the evolution of different variables during this settling time.

The objective of this test is to inspect the whole operating range of the engine without restricting to the factory calibration. Although the main target of these type of test is to provide steady state measurements, the transition from one point to another can be used to capture the dynamics of the engine as well.

5.3.2 Test 2

This test is a simulation of a WLTC with engine A running factory calibration. The vehicle model used to simulate the road load is factory embedded in the testing facility with the parameters shown in table 5.11. The vehicle speed profile of this homologation cycle and the simulated engine speed and torque can be appreciated in figure 5.17.

Facility	Test no.	Description	Objective
System A	Test 1	Parametric test campaign	Model calibration
	Test 2	WLTC with factory control	Model calibration
	Test 3	Driving cycle with factory control	Model validation
	Test 4	Driving cycle with optimal control	Results validation
	Test 5	NEDC with LP- and HP-EGR	Model calibration
	Test 6	NEDC with optimal EGR switch	Results validation
System B	Test 7	Parametric test campaign	Model calibration

Table 5.9: Classification of the different tests that have been carried out at experimental facilities for the works presented in this thesis.

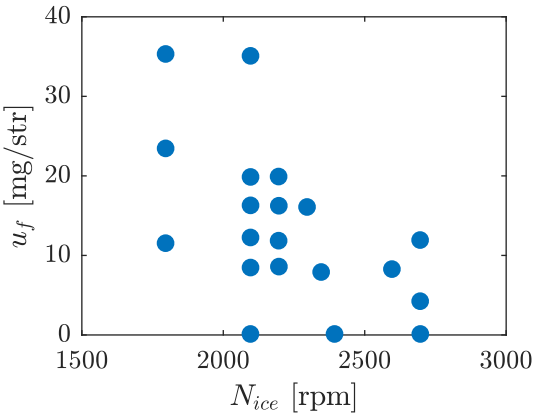

Figure 5.14: Engine test points for test 1. The distribution of these points correspond to the typical operating points of test 3 cycle.

Main injection fuel amount, u_f	[-2, 2] mg/str (around nominal)
SOI, $u_{\delta soi}$	[-5, 5]°Before Factory Calibration (BFC)
EGR valve position, u_{egr}	[0, 100]%
VGT opening, u_{vgt}	[0, 100]%

Table 5.10: Range of variation of actuated controls in test 1.

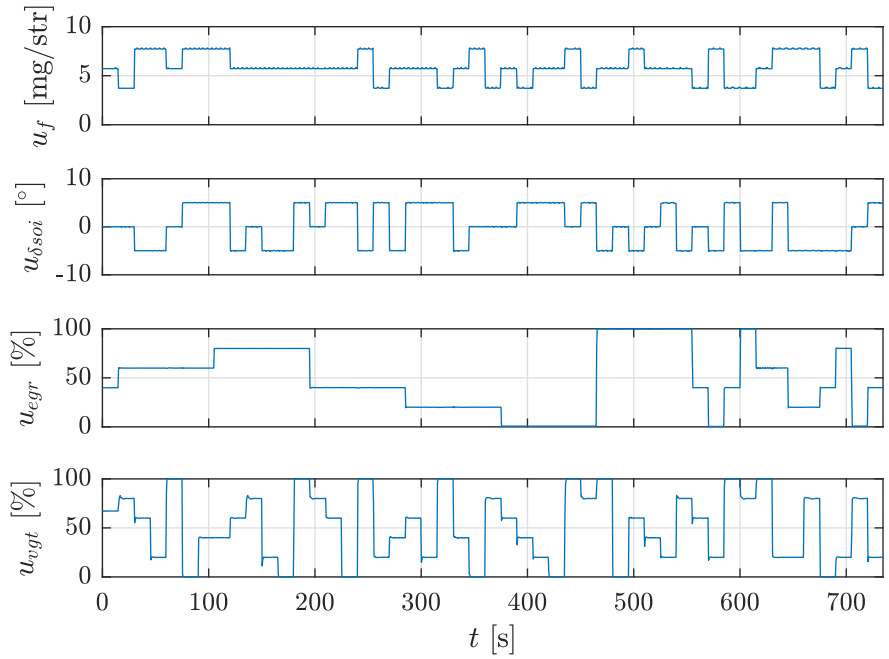

Figure 5.15: Typical controls trajectory for engine characterization at test 1.

Mass, m_v	1150 kg
Aerodynamic drag coefficient, C_d	0.31
Frontal area, A	2.1 m^2
Rolling friction coefficient, c_r	0.015

Table 5.11: Vehicle parameters used to simulate the WLTC at test 2.

The objective of this test is to provide engine measurements with a highly dynamic behavior, complementing the steady state tests for model calibration. The WLTC is chosen because it is a well-known cycle that covers a wide region of the engine operating map.

5.3.3 Test 3

This test is a simulation of a real driving cycle with engine A running factory calibration. This driving cycle corresponds to a portion of the highway driving from test 8 route–see 5.3.8–recorded with Global Positioning System (GPS) and On-Board Diagnostics (OBD)-II devices. It features both positive and negative slopes, covers approximately 40 km and lasts 25 minutes. The speed

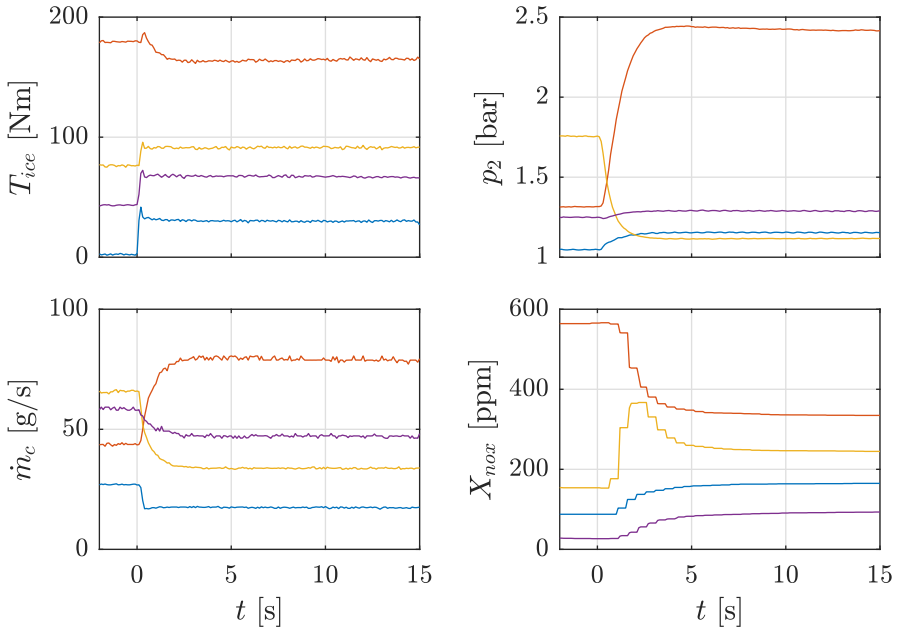

Figure 5.16: Evolution of different variables (engine torque, intake manifold pressure, air mass flow and NO_x concentration) during the 15 seconds settling time at test 1.

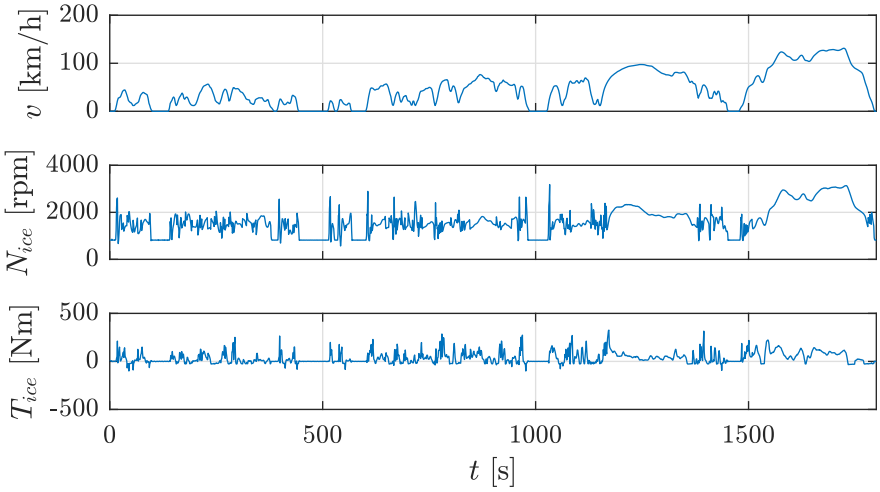

Figure 5.17: WLTC target speed (top) and experimental engine speed and torque at test 2.

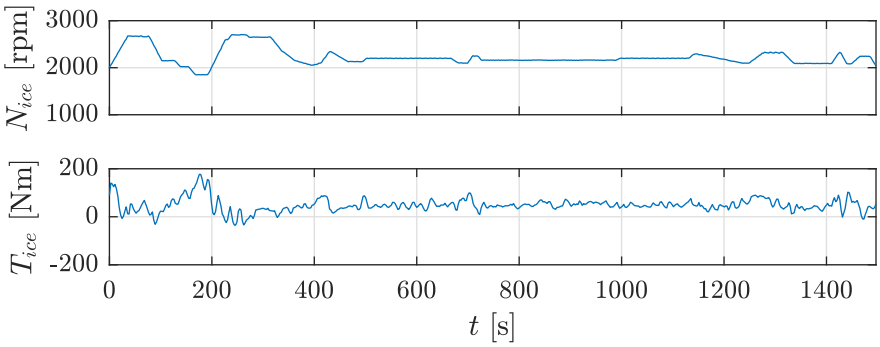

Figure 5.18: Engine speed and torque trajectories of the simulated real driving cycle from test 3.

and torque profiles are shown at figure 5.18. Note that the sharpness of engine speed is due to test bench limitations which prevented to reproduce the exact actual trajectory. Therefore, this sharp trajectory was used instead.

This test is only used as a validation to the engine A model, so simulation results are compared to these readings.

5.3.4 Test 4

This is a set of tests, each of them reproducing the same driving cycle than test 3 at engine A (figure 5.18). In this case, factory calibration is not used anymore and optimal control trajectories are applied to the engine. A total of 13 control trajectories are tested with different emission limits. EGR position, VGT opening and SOI setting may vary in the ranges shown in table 5.10. Main injection fueling rate is free. Pilot injections are scheduled with factory calibration and post injections are canceled.

The objective of these tests is to validate the simulation results of the optimal control trajectories developed in this thesis.

5.3.5 Test 5

This test campaign comprises two different tests, both simulating an NEDC with factory calibration at engine A (figure 5.19 shows the profile of this cycle). The tests are conducted according to the methodology described in [4]. One test uses the factory HP-EGR system while the other uses a custom LP-EGR loop. The use of one of the system is exclusive during the test, so both systems are not used simultaneously.

The objective of these two tests is to provide information about performance

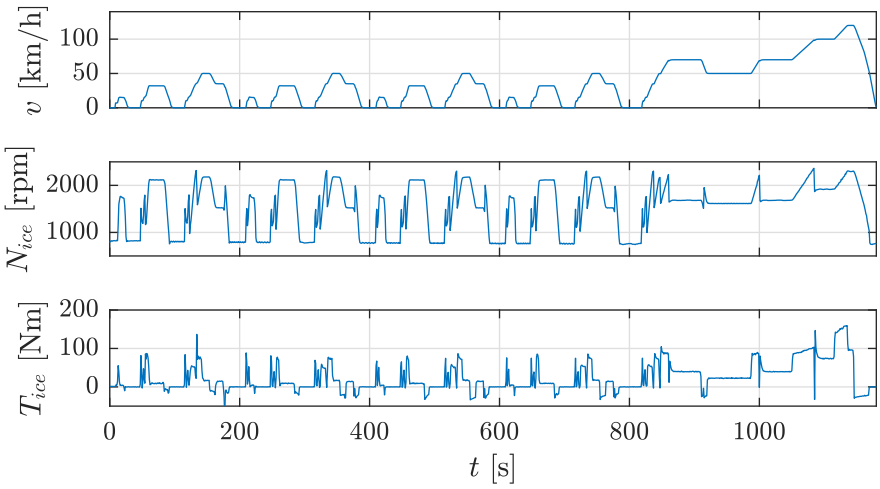

Figure 5.19: NEDC target speed (top) and experimental engine speed (middle) and torque (bottom) at test 5.

and emissions at a prescribed cycle using two different EGR systems. The choice of the European homologation cycle responds to the fact that engine emissions limit must be met with that cycle in practical situations, so the work is more attractive from an industry point of view. A simple model calibration is performed with this data.

5.3.6 Test 6

This is a set of two tests, each of them simulating a NEDC with engine A (figure 5.19). Factory calibration is used but LP- and HP-EGR systems are activated sequentially. The switching between the two systems correspond to an optimal control policy that has been previously calculated with test 5 data. This set of tests correspond to optimal strategies with different constraints. It should be underlined that different EGR systems are not used simultaneously.

The objective of this test campaign is to validate the optimal control strategies developed to manage the switching between EGR systems.

5.3.7 Test 7

This test is a parametric study of engine B varying key controls. λ_e, injection pressure p_{rail}, injection timing u_{soi} and number of injections n_{inj} are varied during this study within the ranges specified in table 5.12. Intake temperature,

Engine speed, N_{ice}	3000 rpm
Fuel amount, u_f	14.7 mg/str
λ_e	$[1.43, 2]$ mg/str
Intake temperature, θ_{im}	35°C
Injection pressure, p_{rail}	[1200, 1400] bar
Number of injections, n_{inj}	[1, 2]

Table 5.12: Operating conditions of engine B at test 7.

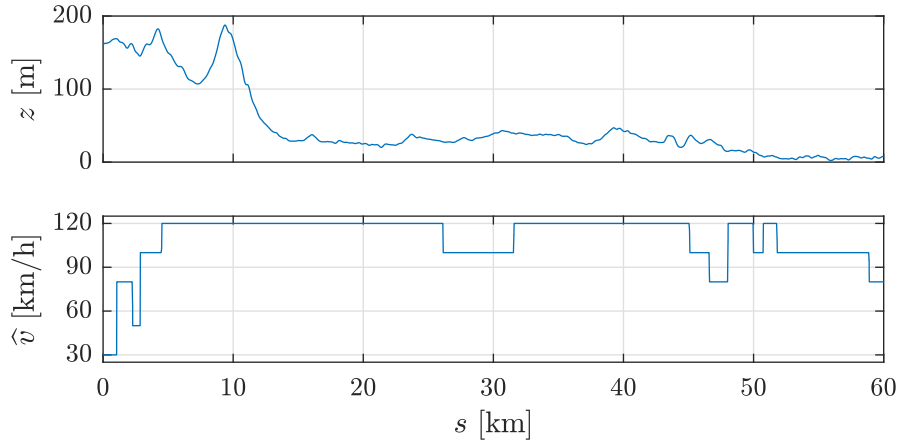

Figure 5.20: Road height z (top) and speed limit $\widehat{v}$ (bottom) profiles. Data collected from Google Maps API.

engine speed and injected fuel amount are kept constant for these tests with the values at table 5.12.

The objective of these tests is to gather information about injection system behavior with different injection settings and number of injection events. A model is calibrated with this information.

5.3.8 Test 8

This test is a daily commute between two cities, recorded from actual driving with a GPS device. The road height profile and speed limits are collected from Google Maps API and shown in figure 5.20. This route covers a total distance of 60 km. Both the beginning and the end of the route correspond to city driving where speed limits are low. The intermediate part, which comprises most of the distance, is highway cruising. This route is used in vehicle speed optimization works throughout this thesis.

References

[1] B. Pla. "Análisis del proceso de la recirculación de los gases de escape de baja presión en motores diesel sobrealimentados". PhD thesis. CMT-Motores Térmicos, Universitat Politècnica de València, 2009.

[2] *Internal combustion compression-ignition engines – Measurement apparatus for smoke from engines operating under steady-state conditions – Filter-type smokemeter.* International Organization for Standardization. Geneva, CH, 1998.

[3] F. Payri et al. "Assessing the limits of downsizing in diesel engines". In: *SAE Technical Paper.* 2014.

[4] A. Broatch et al. "Pollutants instantaneous measurement and data analysis of engine-in-the-loop tests". In: *Thiesel International Conference on Thermo and Fluid Dynamic processes in Direct Injection Engines.* 2006.

Part III

Applications to powertrain control, design and assessment

Chapter 6

Optimal engine control for predefined driving cycles

I don't sell cars; I sell engines. The cars I throw in for free since something has to hold the engines in.

— Enzo Ferrari

Contents

6.1 Introduction

A driving cycle, *i.e.* engine speed and torque profiles, is typically known for benchmarking purposes. It may be also given for predictable situations such as cruise control, overtaking maneuver, a hypothetical autonomous driving or any other case where no external disturbances are present. In those situations, where the boundary conditions of the problem are quantifiable variables, it is possible to state the control problem as an OCP. In this scenario, OC is interesting because it has the potential to offer the control strategy that minimizes a specific criterion.

Under the hypothesis of a perfectly known engine speed and torque trajectories, the application of OC is analyzed in this chapter. Two different approaches are shown below: section 6.2 addresses the management of a dual-loop EGR system, where the decision is the continuous choice of the loop to be used for a given calibration; section 6.3 applies a full OC of engine actuators, namely EGR, VGT, SOI and fueling rate settings, overriding ECU calibration. The target of both approaches is to minimize fuel consumption subject to an NO_x emissions limit.

6.2 LP- and HP-EGR splitting

An interesting approach to control the pollutant emissions of ICEs is to upgrade the EGR system with an LP loop. The traditional HP-EGR architecture guides a fraction of the exhaust gas from the exhaust manifold–upstream the turbine–to the intake manifold–downstream the compressor. The exhaust gas is redirected into the cylinders at a high temperature despite using an EGR cooler, due to the high temperatures at the turbine inlet. The introduction of recirculated gas close to the inlet ports also leads to a poor homogeneity in EGR distribution. On the contrary, LP-EGR drives a fraction of the exhaust gas from after-treatment outlet to compressor inlet. It is a suitable alternative to HP-EGR since it can provide high recirculated rates without a significant increase in intake temperature–after-treatment outlet is much colder than turbine inlet and the recirculated flow is also cooled throughout the intake line, specifically at the cooler–and minimizing cylinder-to-cylinder charge dispersion [1]. LP-EGR, however, shows other disadvantages such as compressor reliability issues, condensations, increased pumping losses and higher HC and Carbon Monoxide (CO) at low temperatures [2].

Several authors propose the dual-loop EGR system as a possible method to combine the advantages of the LP- and HP-EGR routes [3–5]. Those works are focused on controlling simultaneously both EGR circuits to reach the

intake conditions which lead to the desired fuel consumption and emissions. Considering two different EGR systems working simultaneously makes the airpath control more complex and important problems concerning the gas fraction estimation and control must be addressed [6, 7]. A simpler approach to take advantage of the benefits o both LP- and HP-EGR systems is to choose which one to use depending on the engine operating conditions but without the combination of both routes at the same time. The present study follows the second approach since the EGR loops will not operate simultaneously, *i.e.* the EGR is carried out alternatively with the LP- or the HP-EGR systems. The problem to be addressed consists in finding the optimal sequence of switches between LP- and HP-EGR circuits to minimize fuel consumption given a maximum level of NO_x emissions, following the philosophy of previous works of the author [8].

6.2.1 Problem description

The study of the effects of the LP- and HP-EGR architectures on engine performance and emissions has been issued experimentally with Setup A which is factory equipped with VGT, intercooler, DOC, DPF and a cooled HP-EGR loop. The engine is upgraded with a custom LP-EGR circuit and it is fully instrumented to measure temperatures and pressures in different locations of the intake and exhaust lines as well as pollutant emissions and smoke opacity. The engine is installed in a test cell equipped with a variable frequency fast response dynamometer able to carry out engine-in-the-loop tests. The interested reader may check section 5.2.1 for a detailed description of this experimental setup.

To address the effects of the EGR architecture on engine fuel consumption and pollutant emissions, engine behavior has been analyzed by simulating an NEDC in the engine test bench, according to Test 5 (see section 5.3.5). The reason for such selection is that on the one hand, this cycle represents the operating conditions where the emission limits should be met. On the other hand, analyzing the engine behavior with both LP- and HP-EGR architectures provides insight on the conditions where they show their best potential.

The common approach for the airpath control is to actuate EGR and VGT separately to avoid control problems due to the coupling between both systems. Therefore, at low speed and load, where EGR may be applied, the EGR valve is used to follow an air mass flow setpoint, while the turbine is controlled according to a position setpoint. On the contrary, the EGR valve is closed and the intake pressure is controlled in closed-loop with the turbine when far from the homologation region. This control scheme is described for the current experimental facility at section 5.2.1. Despite the coupling issues

in the airpath are strongly reduced when the LP-EGR loop is used–the mass flow through the turbine does not decrease when increasing the EGR amount–, the standard control strategy with two operating regions has been used with the LP-EGR configuration. Moreover, the standard engine calibration has been kept with no changes regardless of the EGR layout used. Then, the standard engine setpoints, which are optimized for the HP-EGR layout, have been also applied when the LP-EGR circuit is in use. Of course, in a final application, the engine calibration is to be adapted to the corresponding EGR architecture. However, this has been avoided in the present study because of two main reasons:

- Sharing the same calibration makes the EGR architecture the only difference between the tested configurations, in such a way that differences in engine performance can not be attributed to other reasons such as differences in the injection parameters or other control variables.
- The complexity of carrying out a complete calibration of the engine exceeds the scope of the present work.

Insight into the effects of LP- and HP-EGR

The evolution of some of the most important parameters during engine operation in the NEDC are shown in figure 6.1.

As far as the engine calibration has been kept constant with both EGR architectures, the evolution of the VGT is the same at the tests and it has important consequences in the intake pressure. In fact, the HP-EGR architecture prevents the recirculated gas from being expanded in the turbine, while with the LP-EGR loop all the exhaust gases flow through the turbine. This increase in the turbine power leads to a higher compressor mass flow and higher intake pressure as shown in the upper plot of figure 6.1.

Again, as the engine control parameters have not been modified, the setpoints for the air mass flow with both EGR configurations are roughly the same. Since the engine speed evolution is imposed by the driving cycle, only small differences in the air mass flow setpoint may appear due to differences in the fueling rate required by both systems. In this sense, the air mass flow with both EGR loops is similar as shown in the second plot of figure 6.1. To keep the actual air mass flow near the setpoint, the opening of the EGR valve is continuously modified along the cycle. However, at some parts of the cycle, the LP-EGR case shows higher air mass flows than demanded. At those conditions, even with fully open EGR valve, the air mass flow exceeds the setpoint. The reason for such a deviation from the setpoint is twofold. On

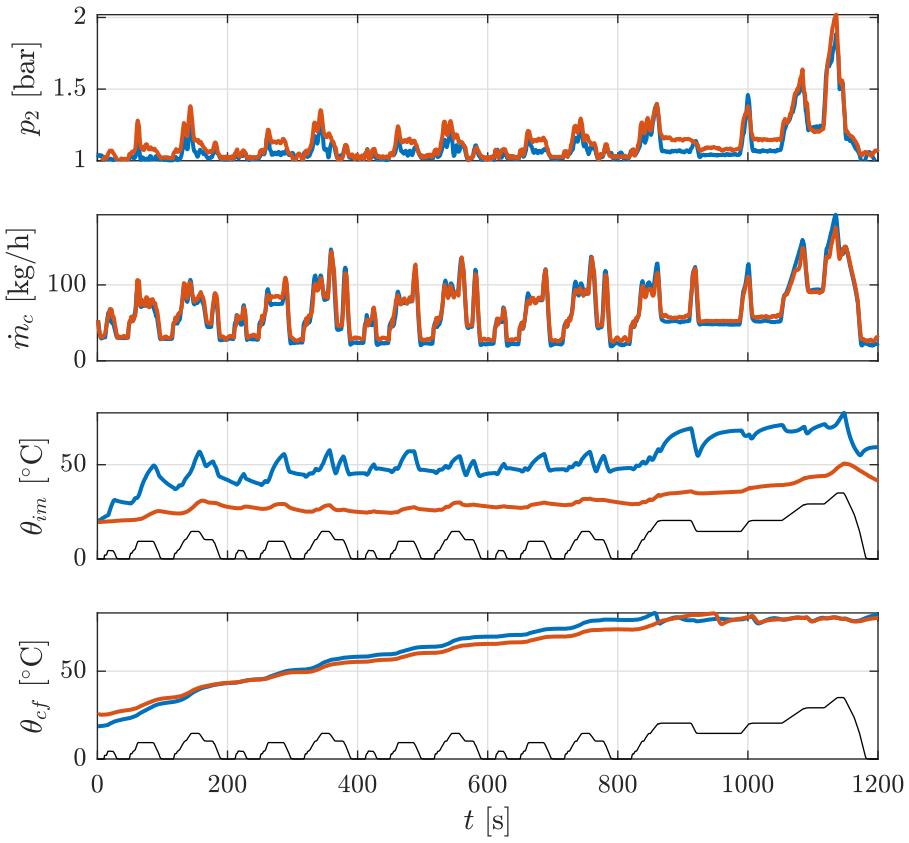

Figure 6.1: Intake pressure, air mass flow, intake temperature and coolant temperature at the NEDC using HP-EGR (blue line) and LP-EGR (red line).

the one hand, the mass admitted by the cylinders with the LP-EGR is higher due to the higher intake density, as a consequence of the higher energy in the turbine and the lower intake temperature. On the other hand, the limited pressure ratio in the LP-EGR circuit–between upstream and downstream the valve–prevents from reaching the high LP-EGR flows necessary to reduce the air mass flow to the setpoint level.

Intake temperature is also a parameter that plays a major role in the combustion process. The third plot in figure 6.1 shows an important reduction in the temperature of the intake gases when the LP-EGR architecture is used. The lower intake temperature and higher intake pressure lead to a noticeable increase in intake density, which involves an increase in the mass admitted by the engine cylinders. As far as the air mass flow is similar with both architectures, the increase in intake density involves a higher amount of

recirculated gas in the case of using the LP-EGR circuit. Changes in intake gas temperature, pressure and composition will lead to noticeable variations in the engine NO_x emissions and fuel consumption depending on the EGR architecture.

Any ICE is strongly affected by changing temperatures. Particularly, the NEDC establishes the engine start at some initial temperature between 20°C and 30°C, so the engine behavior evolves during the cycle as the temperature increases. The engine warm up impacts the fuel consumption due to changes in the heat transfer performance, affecting the engine thermal efficiency, and variations in the lubricant viscosity which may affect friction losses. A faster engine warm up is usually related to a lower fuel consumption, while its effects on emissions are not so clear to address. Generally, higher temperatures involve higher NO_x emissions, while other pollutants such as unburned HCs may be lower. The interested reader can find a deep analysis of the effects of engine temperatures on fuel consumption and emissions in [9, 10]. Regarding the effects of the EGR architecture during the engine warm up, figure 6.1 shows the evolution of the coolant temperature, as a representative temperature of the thermal state of the engine, along the test cycle with the addressed EGR loops. It may be observed that, despite a slightly lower temperature at the beginning of the cycle, the engine warm up is faster with the HP-EGR system, reaching the steady state temperature (78°C) around 100 seconds faster than using LP-EGR. This is due to the fact that the gas recirculated at the HP-EGR system, coming from the exhaust manifold at a high temperature, contributes to the engine warm up in two ways: on one hand, the gases heat the coolant in the HP-EGR heat exchanger; on the other hand, those gases allow a higher intake temperature that impacts to the heat transfer conditions at the combustion process. On the contrary, with LP-EGR, the recirculated gases are taken from the end of the exhaust line–specifically from the DPF outlet–, whose lower temperature has a minor contribution to the engine warm up.

The differences in the variables discussed in the previous paragraphs, which are exclusively due to the EGR architecture employed, lead to important variations in the engine fuel consumption and emissions level. Figure 6.2 shows the instantaneous and accumulated values for fuel consumption, NO_x emissions and unburned HC emissions. LP-EGR test shows a higher fuel consumption, excluding some peaks during accelerations that can be attributed to measuring problems due to the poor dynamic response of the fuel measuring device–a fuel balance. At the end of the complete cycle, the LP-EGR case needs a 5.2% increase in fuel compared to the corresponding test with HP-EGR. This increase in fuel consumption is due to two main causes:

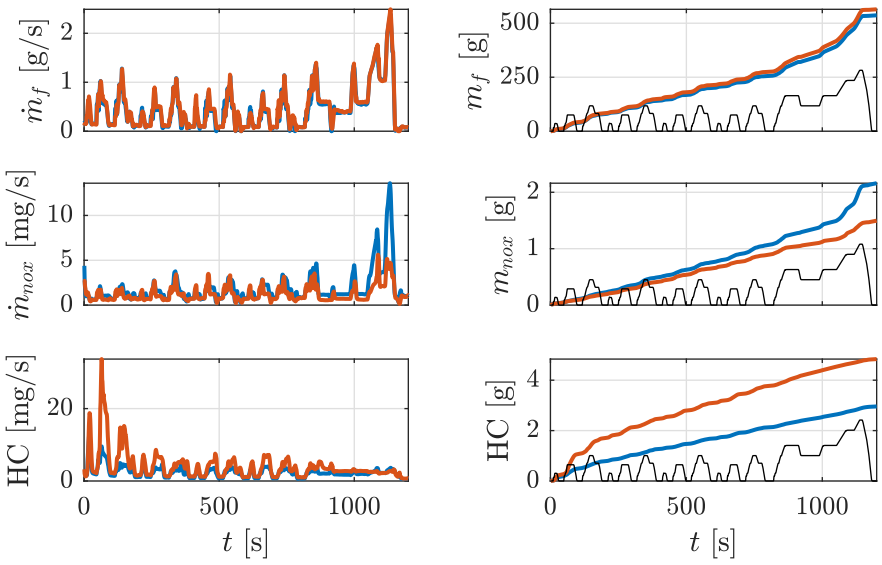

Figure 6.2: Instantaneous and accumulated fuel consumption, NO_x and HC emissions at the NEDC using HP-EGR (blue line) and LP-EGR (red line).

- The higher mass flow through intake and exhaust systems leads to higher pumping losses [1]. It should be taken into account that the recirculated flow with LP-EGR travels through elements such as the after-treatment system and the intercooler, while it is not the case at the HP-EGR system. In addition, the use of HP-EGR reduces pumping losses since intake and exhaust manifolds are connected and, consequently, pressure difference is decreased.

- The lower intake temperature and the higher amount of burnt gases recirculated both contribute to a later combustion, with lower temperatures but also with lower indicated efficiency. The effect of the EGR and the intake temperature on the engine efficiency are well-known and extensively addressed in the literature, particularly a detailed analysis of the effects of the intake temperature and composition in the combustion process may be found in [11–14].

Regarding the last point, the higher EGR rates and lower intake temperatures reached with the LP-EGR system are also responsible for the NO_x reduction and the HC increase. Figure 6.2 shows lower NO_x emissions with the LP-EGR during the whole test, regardless of the operating conditions. As a consequence, at the end of the cycle, a noticeable reduction of 30% in

the NO_x emissions level can be observed with the LP-EGR architecture. On the contrary, it also produces an increase of 60% in the HC emissions with respect to HP-EGR. Figure 6.2 shows that this increase in HC emissions is mainly produced during the first part of the cycle, after the cold start. This is consistent with the negative impact of low intake temperatures and high EGR rates on HC emissions [9]. For further discussion on the effects of the EGR layout on fuel consumption and emissions the reader is referred to [1, 2, 15].

According to figure 6.2 it is clear that HP-EGR will prevail in any EGR circuit switching strategy aimed to minimize fuel consumption, and that such strategy will impact positively in HC emissions. Conversely, the weight of LP-EGR strategies focused on the NO_x reduction is also apparent. The tradeoff obtained with both EGR architectures regarding fuel consumption and NO_x emissions shows that a proper strategy to combine LP- and HP-EGR systems is needed to obtain an equilibrium between pollutant emissions and fuel consumption.

6.2.2 Problem formulation

Consider the Test 5, where the sequence of engine speed and torque is exactly the same in both cases. Given that both tests share the same engine calibration, the only difference is the EGR architecture used and the control parameters associated to the differences in fuel injection needed to follow the engine torque profile. Therefore, for this particular cycle, the instantaneous fuel consumption $\dot{m}_f$, resulting from any arbitrary EGR switching strategy, can be represented by the following linear system:

$$\dot{m}_f\left(u_{lphp}, t\right) = c_a\left(t\right) u_{lphp}\left(t\right) + c_b\left(t\right) \tag{6.1}$$

where t represents the time spent since the start of the cycle. c_a and c_b are time-varying parameters determining the system response and the control u_{lphp} is defined as a binary variable:

$$u_{lphp} = \begin{cases} 0 & \text{then use HP-EGR} \\ 1 & \text{then use LP-EGR} \end{cases} \tag{6.2}$$

Note that the dependence of $\dot{m}_f$ on engine speed N_{ice} and torque T_{ice} is implicit since their evolution with time is predefined by the NEDC.

Regarding NO_x emission, a similar approach than that of (6.1) can be used, thus:

$$\dot{m}_{nox}\left(u_{lphp}, t\right) = c_c\left(t\right) u_{lphp}\left(t\right) + c_d\left(t\right) \tag{6.3}$$

where parameters c_c and c_d define the time-varying linear response of NO_x to the EGR architecture used. Note that neither the fuel consumption nor the NO_x emissions show a linear response with the percentage of EGR performed with LP- or HP-EGR systems. However, as long as the control is a binary variable and only extreme cases are considered (fully HP-EGR or fully LP-EGR) the linear approach becomes valid.

Regarding the parameters c_a, c_b, c_c and c_d, they can be obtained experimentally from the Test 5 by making $u_{lphp} = 0$ and $u_{lphp} = 1$ at (6.1) and (6.3):

$$\begin{aligned} c_a(t) &= \dot{m}_{f,lp}(t) - \dot{m}_{f,hp}(t) \\ c_b(t) &= \dot{m}_{f,hp}(t) \\ c_c(t) &= \dot{m}_{nox,lp}(t) - \dot{m}_{nox,hp}(t) \\ c_d(t) &= \dot{m}_{nox,hp}(t) \end{aligned} \tag{6.4}$$

where the subscript indicates the EGR loop employed.

Note the non-causality of the previous representation since the model provides the fuel consumption given the EGR architecture used and the torque and speed profiles (time evolution in the NEDC), while the physical process is exactly the opposite, *i.e.* given a certain amount of fuel injected, the engine produces some torque and the balance between the engine torque and the road load determines the resulting engine speed. However, since the model relies on experimental information on the particular cycle to study, the physical causality can be inverted to some extent in order to simplify the model.

The described linear model assumes quasi-steady behavior [16–19] and, therefore, it has no states, *i.e.* the instantaneous performance of the engine does not depend on any previous history. However, changes in the control input–the EGR architecture–may involve progressive changes in actual engine variables during transients whose duration can be not negligible, while the model proposed does not consider those transients. This simplification jeopardizes the applicability of the proposed model as will be discussed later.

In any case, assuming the model suitability, the control problem consists in finding the sequence of controls u_{lphp} along the cycle (NEDC) that minimizes the following cost index:

$$J = \int_0^{\mathcal{T}} \dot{m}_f(u_{lphp}, t)\,\mathrm{d}t \tag{6.5}$$

where the implicit engine speed N_{ice} and torque T_{ice} follow the trajectories predefined by the NEDC. The problem is constrained since there are restrictions concerning the maximum amount of pollutants emitted during the complete driving cycle. In the present study, only NO_x emissions are considered since

there is not a specific widespread after-treatment for NO_x while DOC and DPF are usually able to reduce the rest of pollutants up to regulation limits. In addition, focusing on NO_x results more interesting since a decrease in fuel consumption generally leads to a reduction of most pollutants such as HC, except NO_x. The constraint on pollutant emissions can be expressed as:

$$\int_0^{\mathcal{T}} \dot{m}_{nox}\left(u_{lphp}, t\right) \mathrm{d}t \leq \widehat{m}_{nox} \tag{6.6}$$

where $\widehat{m}_{nox}$ represents the maximum level of permissible NO_x emissions. In any case, constraints on the emissions of other pollutants may be considered just by adding the corresponding equations.

6.2.3 Optimization approach and implementation

The problem presented in (6.5) and (6.6) is in general difficult to solve due to the complex relation between the control u_{lphp} and the outputs–the fuel consumption and NO_x emissions. However, as far as the proposed model neglects the system dynamics by assuming quasi-steady behavior, the OCP is a static optimization problem that can be addressed by the method of Lagrange multipliers. This method is extensively described in section 3.3. Then the integral problem represented by (6.5) and (6.6) can be replaced by a set of optimization problems in which the following cost function J is to be minimized at each time step:

$$J\left(t, \lambda_1\right) = \dot{m}_f\left(u_{lphp}, t\right) + \lambda_1 \dot{m}_{nox}\left(u_{lphp}, t\right) \tag{6.7}$$

The optimization process consists in choosing, at any time step of the driving cycle, the control u_{lphp}, *i.e.* the EGR loop to be used, which minimizes the cost function (6.7). As only two discrete values are allowed for u_{lphp}, the problem is solved just considering the value providing the minimum cost at the considered time, which defines the optimal control policy $u^*_{lphp}\left(t, \lambda_1\right)$.

From (6.7) it follows that the higher the value of λ_1, the higher the weight of the NO_x emissions on the cost function value. Then, given the tradeoff between fuel consumption and NO_x, as λ_1 increases the NO_x emissions corresponding to the optimal solution decrease progressively at the expense of some fuel penalty. For that reason, the optimization problem is reduced to find the value of λ_1 which leads to:

$$\int_0^{\mathcal{T}} \dot{m}_{nox}\left(u^*_{lphp}\left(t, \lambda_1\right), t\right) \mathrm{d}t = \widehat{m}_{nox} \tag{6.8}$$

A simple cost function as (6.7) might result in a highly oscillating optimal control policy u_{lphp}, especially due to the fact that the control is a binary variable, that will not produce desirable results when applying the control to the actual engine. It should be recalled that, every time a switch between EGR configurations is issued, the actual engine experiences a transient that the model is not able to take into account. In this sense, figure 6.3 shows the evolution of key engine parameters during the switching from HP-EGR to LP-EGR at idle conditions. After a transient of 2.2 seconds the target air mass flow is reached. Note that the steady state air mass flow with both systems is exactly the same since the engine control establishes exactly the same air mass flow setpoint. Regarding the exhaust pressure, the steady state value is reached in less than 1 second. Closing the HP-EGR valve has a direct impact on exhaust pressure while the effect on intake pressure is slower (3.4 seconds) due to the turbocharger dynamics. Regarding the temperature evolution in the intake manifold, it can be observed that it slowly decreases due to the replacement of the hot HP-EGR gas by LP-EGR gas coming from the intercooler. On the contrary, the temperature at the compressor inlet smoothly increases due to the arrival of exhaust gases coming from the DPF outlet through the LP-EGR circuit. It should be noted that the slow response of temperatures is to a great extent due to the thermal inertia of the temperature sensors–k-type thermocouples–so the response time in the order of 20 to 30 seconds shown in the figure should exceed the characteristic time of the actual process. Taking into account the evolution of intake and exhaust pressures in figure 6.3–exhaust pressure ratio is much higher–, it can be noticed that the pumping losses are increased with the use of LP-EGR. This increase, in addition to the higher EGR rate, involves a penalty in fuel consumption that can be observed in the right-upper part of figure 6.3. Note that there is not an appreciable delay in the increase in fuel injection rate and, in fact, it is almost instantaneous after the LP-EGR circuit is activated. Taking into account the engine displacement (2 liters) and the volume of the intake line (less than 8 liters) the gases from the LP-EGR circuit will need around 4 engine cycles to arrive to the cylinders. Considering an engine speed of 750 rpm at idle, that means that in 2.7 ms the cooled gases from the LP-EGR circuit will arrive to the cylinders, producing the fuel consumption increase to keep holding the engine speed and torque output. Taking into account that this characteristic time of the fuel consumption response to an EGR switch is much faster than the characteristic time of the pedal evolution during the NEDC, a quasi-steady behavior for the fuel consumption can be considered. On the contrary, figure 6.3 shows that the response of the pollutant emissions to the EGR switching is not so fast. The response of the HC and NO_x emissions show important

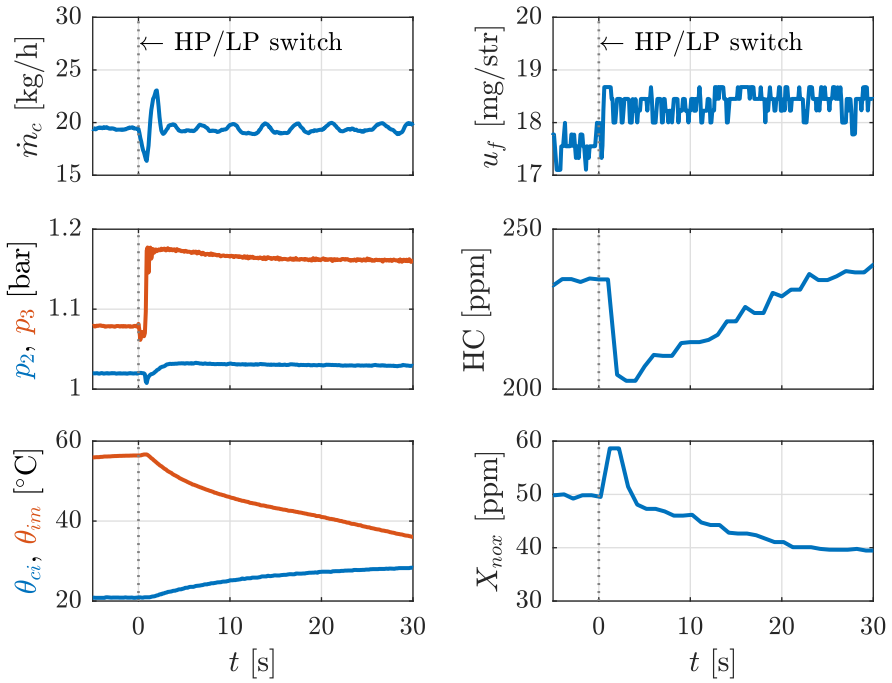

Figure 6.3: Engine operating conditions (left) and engine performance (right) at idle during an HP-EGR to LP-EGR switch.

nonlinearities such as minimum phase behavior. Despite the slow response time of the exhaust gas analyzers–which has an important impact on the time needed to achieve the steady state conditions after the EGR switch–it should be admitted that the quasi-steady hypothesis is far from the reality in the case of pollutant emissions. Consequently, the more switches between EGR systems, the stronger the impact of model uncertainties, especially emission models, on the optimization.

To deal with this issue the following cost function is proposed:

$$J\left(t, \lambda_1, \lambda_2\right) = \dot{m}_f\left(u_{lphp}, t\right) + \lambda_1 \dot{m}_{nox}\left(u_{lphp}, t\right) + \lambda_2 \left|\delta u_{lphp}(t)\right| \tag{6.9}$$

where λ_2 is a second Lagrange multiplier that penalizes the changes in the control variable u_{lphp}. The variation in u_{lphp} is denoted with δu_{lphp}, which can take the discrete values $\{-1, 0, 1\}$. Note that other constraints, *e.g.* limits on other pollutants, can be added by introducing new Lagrange multipliers.

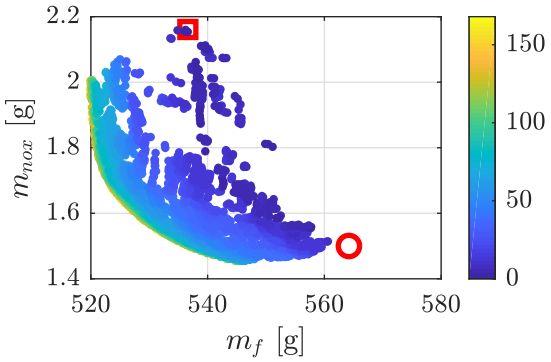

Figure 6.4: Tradeoff between fuel consumption and NO_x emissions calculated for $\lambda_1 \in [0, 1]$ and $\lambda_2 \in [0, 1]$. The color scale represents the number of switches between HP- and LP-EGR during the cycle. The red circle and square show the experimental results obtained with LP-EGR and HP-EGR respectively.

6.2.4 Results and discussion

The optimization problem described in the previous section was addressed and solved for parameters λ_1 and λ_2 ranging from 0 to 1. Figure 6.4 shows these simulation results. This figure represents the tradeoff between fuel consumption and NO_x for the optimal solution. The color scale shows the number of switches along the cycle between EGR configurations, ranging from 0 in black to 165 in white. The square and the circle show the experimental results obtained with HP-EGR and LP-EGR architectures respectively.

Several optimal solutions fall near a straight line linking both experimental points with a relatively low number of switches between EGR systems. However, the Pareto front–area where a reduction in NO_x involves an unavoidable increase in fuel consumption–is defined by points with high number of switches. Results are also clearly stratified according to the number of switches. Of course, that number of switches depends on the weight of δu_{lphp} on the cost function (6.9), and the higher the value of λ_2 the lower the number of changes in the EGR configuration.

To analyze in depth the effects of the Lagrange parameters on the optimal EGR sequence, figure 6.5 illustrates the results for different values of λ_1 and λ_2. The figure shows, for a given row, the optimal sequence of the EGR system to be used along the cycle, the total fuel consumption, the accumulated NO_x emissions and the number of switches for a range of λ_1 values. The results in the upper row correspond to $\lambda_2 = 1$, results in the lowest row are with $\lambda_2 = 0$, while rows in between contain results for intermediate values of λ_2. The gray

areas in the left plots illustrate LP-EGR usage while white areas are HP-EGR. According to these results, the following conclusions can be extracted:

- For a given value of λ_2, the increase of λ_1 involves a reduction in NO_x emissions at the expense of a penalty in fuel consumption. This is because λ_1 weights NO_x emissions at (6.9) and, therefore, low emissions become more important for higher values of λ_1. This points out the tradeoff between NO_x and fuel consumption.

- As λ_1 increases, the optimal solution tends progressively to LP-EGR because of its lower NO_x emissions. However, HP-EGR prevails in solutions where fuel consumption is the prime objective.

- Optimal trajectories with low λ_2 values show frequent changes between LP-EGR and HP-EGR architectures, which prevents the quasi-steady approach from providing good estimations of actual engine fuel consumption and NO_x emissions.

- The value of λ_1 has a negligible impact on the number of switches, that are almost exclusively affected by λ_2.

- As expected, increasing the value of λ_2 has a positive effect in the number of switches between EGR architectures. Nevertheless, increasing λ_2 involves a penalty in the theoretical minimum fuel consumption and NO_x emissions since the control policy is somehow constrained by the maximum number of switches.

- Solutions with affordable number of switches for the quasi-steady hypothesis–when λ_2 tends to 1–, show that the LP-EGR architecture has higher potential at the last part of the cycle, while the HP-EGR provides maximum benefits during the first phases of the NEDC. This is due to the fact that the benefits in fuel consumption of the HP-EGR architecture are more important during the cold start and the warm up phases, where the increase in temperature provided by it contributes to a better combustion. On the contrary, in the last phase of the cycle, where higher vehicle speeds are reached, the weight of NO_x emissions is more important. Therefore, the potential of LP-EGR system to reduce NO_x emissions should be exploited in this part. In addition, since the engine is already warmed at this phase, the penalty of LP-EGR on the fuel efficiency is not as important as during the cold start and warm up processes.

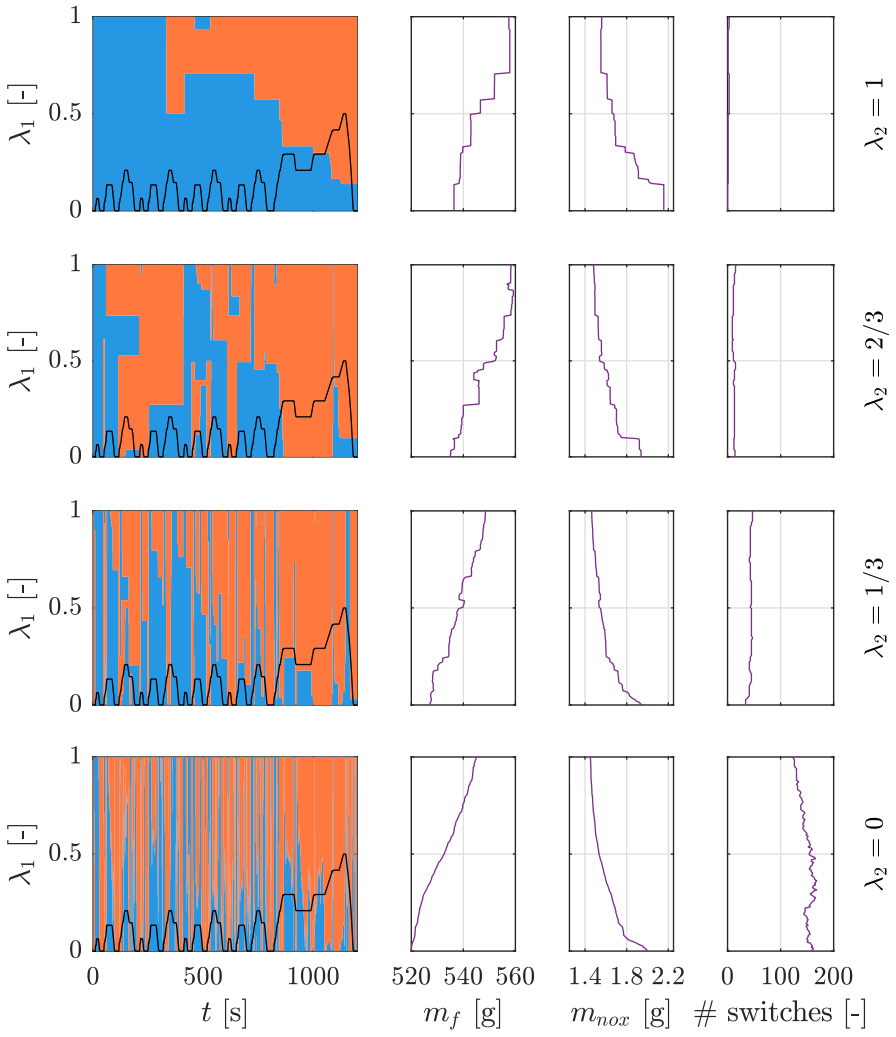

Figure 6.5: Optimal EGR architecture, total fuel consumption, emissions and number of switches between HP-EGR and LP-EGR at the NEDC cycle as a function of λ_1 (y-axis) and λ_2 (rows). Areas in blue represent HP-EGR while LP-EGR is shown in red.

According to these results shown at figure 6.5, it is clear that the optimal control strategy would be to start with HP-EGR and to keep this configuration for some time until the LP-EGR architecture should be used to meet the NO_x limit. In this sense, such a time is shown in the upper left plot of figure 6.5, where it may be found that the lower the NO_x limit is, the earlier the LP-EGR

circuit should be used. This is probably the most interesting conclusion to propose a simple yet effective control strategy based on these optimal results.

Two additional tests–Test 6 described in 5.3.5–have been carried out with different LP- and HP-EGR switching times, namely 600 and 800 seconds, to validate the conclusions from the optimization process. The results in terms of fuel consumption, NO_x and HC emissions are compared to the simulated optimization results at figure 6.6. Experimental and modeling results show a pretty good agreement, so the optimal switching times as a function of NO_x limits can be used to calibrate the proposed control strategy. In addition, it can be seen that optimizing the fuel consumption also leads to minimize HC emissions. Therefore, the quasi-steady approach of the model is suitable for the optimization when a small number of switches is allowed.

From a calibration point of view, it is more convenient to define the switch between HP-EGR and LP-EGR in terms of coolant temperature instead of time. For this engine the 600 to 800 seconds interval corresponds to 70°C to 79°C. Otherwise, in addition to regulation issues, unexpected results for driving cycles different than the NEDC may happen, *e.g.* in the case of cold conditions such as those reached in northern countries where 800 seconds may be insufficient to warm up the engine. At those conditions, a time based strategy for the EGR switching will lead to the use of LP-EGR with a cold engine, and then resulting in excessive HC emissions and fuel consumption or even promoting misfiring. Hence, EGR switching point may be specified as a function of coolant temperature as shown in figure 6.7.

6.2.5 Conclusions

This short study proposes the combination of LP- and HP-EGR systems to minimize fuel consumption with low NO_x emissions. Particularly, a methodology to find the optimal switching strategy amongst EGR architectures during the NEDC has been developed. The proposed strategy is based on OC theory so the control policy depends on the definition of a cost function, which contains three main variables to minimize–fuel consumption, NO_x emissions and number of switches between EGR architectures. Particularly, the number of switches between EGR systems is a limiting factor that should be taken into account because of the quasi-steady hypothesis used to develop the optimization model.

The analysis of the resulting control strategy shows that the optimal control policy to apply is to start with HP-EGR and to keep this configuration for some time until LP-EGR architecture should be used to meet the NO_x limit. This result is consistent with the fact that at cold conditions, the higher intake temperature and lower EGR rate produced with HP-EGR involves noticeable

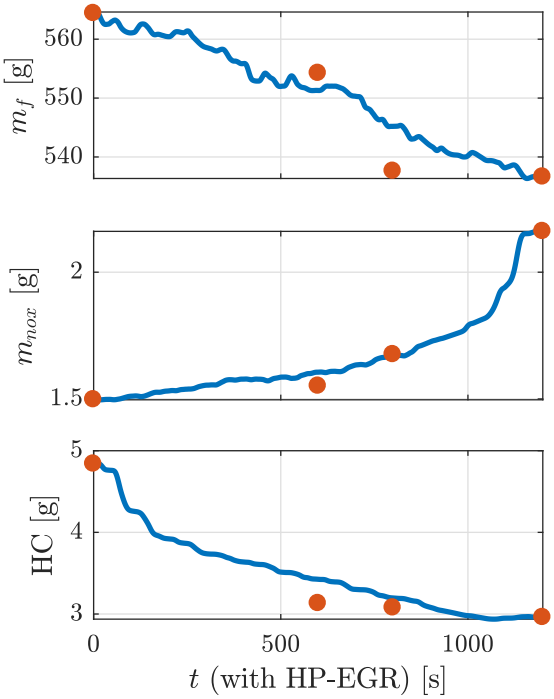

Figure 6.6: Total fuel consumption, NO_x and HC emissions as a function of the time HP-EGR is active. Red dots represent experimental measurements while blue line shows the model results.

benefits in terms of fuel consumption that are progressively diluted as the engine warms up. On the other hand, at the end of the cycle, NO_x emissions become more important, so LP-EGR becomes a suitable method to decrease NO_x emissions with a lower fuel consumption penalty.

The experimental results validate this strategy and show that combining both EGR systems sequentially along the NEDC allows to reduce noticeably the NO_x emissions of the HP-EGR system with a reduced impact on the fuel consumption.

This optimization strategy can be easily extended to take into account other constraints such as additional pollutants or drivability concerns following a similar methodology.

6.3 Full engine control

Pollutant emission regulations have pushed ICE technology to deliver cleaner yet more efficient engines, two concepts that usually take opposite directions.

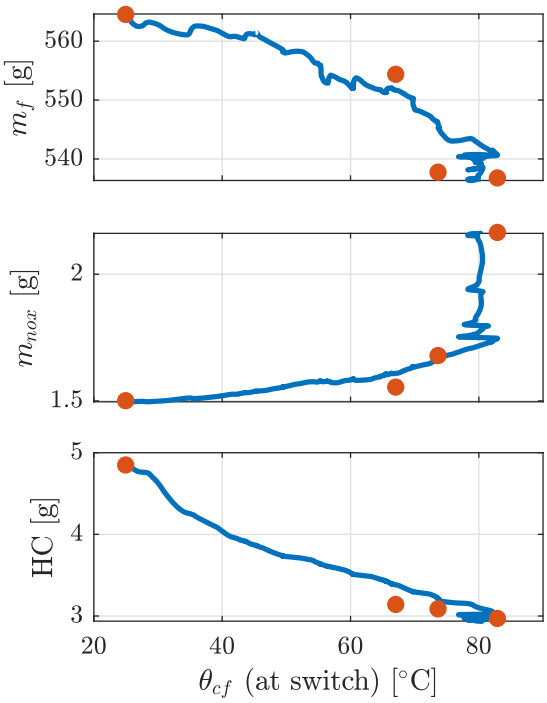

Figure 6.7: Total fuel consumption, NO_x and HC emissions as a function of the coolant temperature at the HP- to LP-EGR switch. Red dots represent experimental measurements while blue line shows the model results.

This ambitious target can be achieved at the expense of a significant increase in engine complexity, including a huge amount of peripherals, different technologies, additional systems and after-treatment devices. Engines now are much complex than those some decades ago. Systems and devices such as EGR, VGT, double forced induction, VVT, DI, DOC, DPF or SCR are common in the industry.

These powertrains are complex to manage as well. The numerous systems are mutually affected by the functioning of the others and all actuators must be managed with a common strategy. The engine is ultimately controlled by the ECU whose common approach consists of a set of prescribed maps, PID controllers and heuristics that are elaborated after many calibration tests. The increased complexity of the engine involves control issues that may be addressed by this traditional control scheme, which uses to be a difficult, expensive and time consuming task. However, the additional degrees of freedom introduced by engine systems can be seen as an opportunity to exploit those systems

in order to improve engine performance with an appropriate and innovative control strategy.

OC theory supplies tools to find out the best control strategy to achieve a particular objective. In this sense, it is an interesting methodology to–partially–replace the traditional control scheme. OC can also be used to determine the maximum level of performance that an engine may be exploited to, for a given technology. The current study follows this philosophy in order to find, both theoretical and experimentally, the OC strategy for the main engine actuators: EGR valve position u_{egr}, VGT opening u_{vgt}, SOI offset $u_{\delta soi}$ and fueling rate u_f. Note that these controls are actually setpoints for PWM actuations, but due to the slow response of the airpath compared to the controls settling time, this difference is hereinafter neglected. Optimal trajectories are calculated for an actual driving cycle with different levels of pollutant emissions and compared to the factory ECU strategy.

6.3.1 Problem description

The control of the main engine actuators, *i.e.* EGR, VGT, SOI and fueling rate, is typically performed with PID controllers and mapped setpoints. More precisely, the airpath control is founded around tabulated air mass flow and intake pressure setpoints that must be achieved by acting on the controls. At low loads the air mass flow is controlled by opening or closing the EGR valve while VGT position is set to a predefined value. At higher loads, far from the homologation region, EGR valve remains closed and the intake manifold pressure is monitored to reach the desired values by acting on the VGT position. This *divide and conquer* strategy is typically used to avoid coupling issues between both controls, so only one actuator is managed in closed-loop at a time. Fueling rate is mainly a function of the engine speed and the driver's torque request, whose response is defined at a lookup table. Meanwhile, SOI is mapped by engine speed and current fueling rate. The factory engine control is described in more detail at section 5.2.1. Therefore, this approach consists in the selection of setpoints based on current readings, namely engine speed, driver's torque request or some temperatures among others.

Of course, such a control strategy is only optimal for a set of tested conditions and optimality for any real world situation cannot be guaranteed. In fact, even assuming that mapped setpoints are optimal, PID controllers are only responsible of reaching those values, but the transient is not optimal; it can be faster or slower, smoother or sharper–depending on the calibration–, but the transition to a different operation point is completely arbitrary. Furthermore, it might happen that optimal setpoints are not a function of

current readings, but a consequence of the last history, preventing its mapping as a lookup table.

According to all these issues, OC theory has been applied to the management of the main controls of the engine: u_{egr}, u_{vgt}, $u_{\delta soi}$ and u_f. This OCP is interesting since it can be mathematically guaranteed that the obtained control strategy is the very best policy that can be applied to that engine. Of course, this strategy is cycle-specific and the results may not be applicable to a different cycle; however, the methodology is universal. Last but not least, results can be interpreted as the top performance that can be extracted from a given engine, and it is a baseline for other control strategies–such as factory control–to compare to and to have a rough idea of how optimal are those control policies.

These optimal trajectories have been calculated and experimentally tested at a light duty Euro 5 turbocharged DI diesel engine with a high pressure EGR loop, VGT and DOC. This engine is installed at an engine test bench with additional instrumentation: turbocharger speed measuring, exhaust gas analyzer, opacimeter, extended set of thermocouples and pressure sensors, NO_x probes, torque meter and engine speed measuring. The ECU is bypass-ready through an ETK port so main control variables are taken over with an external rapid prototyping dSPACE system in order to apply the optimal trajectories. This testing facility is deeply described in section 5.2.1.

In addition, a MVEM of this testing facility has been developed. It has been tried to reach a balance between fast model calculation and accuracy in simulation results. Of course, a very detailed model can reproduce engine variables pretty accurately, but a long simulation time will prevent its use as a control oriented model. Moreover, complex models tend to have a large number of states, while many OC methods are not able to deal with such huge mathematical models. Therefore, for the sake of practicality, a model following the equations described in section 4.5 has been used in this study. Its main highlights are summarized in table 6.1.

In order to fit the model to the actual engine, a set of experimental measurements has been carried out. These tests explore multiple control combinations as well as the dynamic response of the engine. To this effect, three test campaigns have been performed:

- Test 1: parametric tests at 20 different engine operating points (see 5.3.1). EGR, VGT, SOI and fueling rate are explored at each operating point. This provides steady state information at a wide range of engine conditions (980 different combinations of controls and operating points, with an approximate total duration of 4 hours).

Control inputs	EGR valve position, u_{egr} VGT opening, u_{vgt} SOI offset setpoint, $u_{\delta soi}$ Fueling rate, u_f
Model states	Intake manifold pressure, p_2 Intake manifold oxygen fraction, $X_{O_2,im}$ Exhaust manifold pressure, p_3 Exhaust manifold oxygen fraction, $X_{O_2,em}$ Turbocharger speed, ω_{tc}
Disturbances	Engine speed, N_{ice}
Main simplifications	Isothermal intake manifold No thermal transients Quasi-steady cylinder model Map-based turbocharger model

Table 6.1: Main characteristics of MVEM used for optimal airpath control.

- Test 2: dynamic cycle (WLTC) with factory calibration (see 5.3.2). This test provides transient information at a quite dynamic and well known cycle (30 minutes).

- Test 3: actual driving cycle with factory calibration (see 5.3.3). This test is used as a validation for the model to check that it has an acceptable accuracy. It is not used during the fitting process to provide a fair validation (25 minutes).

The performance of the resulting model is shown in figure 6.8. Top plots show the correlation between experiments and simulations for the main outputs of the model, namely the torque and NO_x emissions. The accuracy of these outputs are critical since they are part of the OCP constraints. It may be appreciated that both are well correlated to experiments, especially the total NO_x emissions. Note that this data corresponds to the validation cycle which the model is not fitted to. On bottom plots, the dynamic response of p_2 and ω_{tc} states is shown. Despite a minor offset at $t = [245, 255]$ s, settling time is quite similar in both simulations (red) and experiments (blue). Regarding the computational resources required by the model, a complete simulation of a 25 minutes long driving cycle takes approximately 650 ms with an i5-4440 CPU.

In addition to the model fitting tests, a set of experiments have also been later executed in order to validate the proposed OC strategy (see 5.3.4).

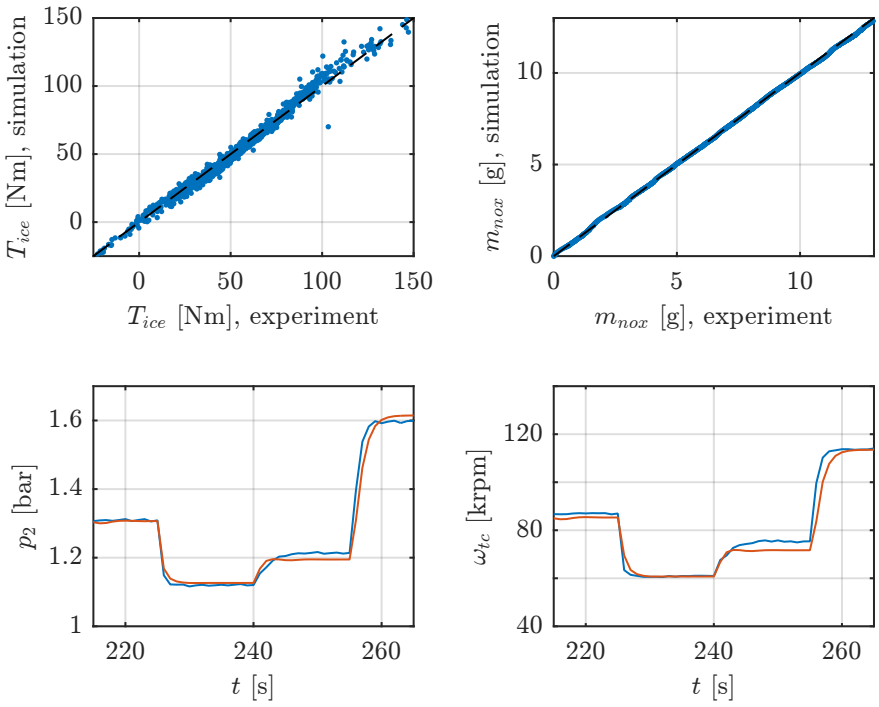

Figure 6.8: Model performance analysis. At top plots, correlation between experiments and simulations are shown for the main outputs of the OCP: engine torque and accumulated NO_x emissions. These results correspond to the validation cycle (model is not fitted to this cycle, see 5.3.3). On the bottom plots, dynamics of the model are represented for two model states, intake manifold pressure p_2 and turbocharger speed ω_{tc}. Blue corresponds to experiments and red to simulations.

These experiments consist of 12 optimal trajectories applied to the engine controls, following the same engine speed and torque profiles at all tests, and an additional experiment with factory calibration.

6.3.2 Problem formulation

The aim of this work is to find an OC strategy that minimizes fuel consumption with a specific limit on NO_x emissions for a real driving cycle. This can be synthesized as an OCP to minimize the following cost index:

$$J = \int_0^{\mathcal{T}} \dot{m}_f(\boldsymbol{x}, \boldsymbol{u}, t)\, \mathrm{d}t \tag{6.10}$$

with NO_x emission limit expressed as an integral constraint:

$$\int_0^{\mathcal{T}} \dot{m}_{nox}(\boldsymbol{x}, \boldsymbol{u}, t)\, \mathrm{d}t - \widehat{m}_{nox} \leq 0 \tag{6.11}$$

where $\widehat{m}_{nox}$ is the specified total NO_x emission limit. State vector $\boldsymbol{x}$ and control vector $\boldsymbol{u}$ components are the same as previously specified for the MVEM in table 6.1.

In order to guarantee that the same driving cycle is always followed by the engine, speed and torque profiles must be specified (see figure 5.18). On the one hand, engine speed is a disturbance to the problem and, therefore, it is directly introduced in model equations. On the other hand, engine torque is a consequence of the controls, so an additional constraint must force the torque output to deliver the required trajectory $\widetilde{T}_{ice}$:

$$\widetilde{T}_{ice} - T_{ice}(\boldsymbol{x}, \boldsymbol{u}, t) = 0 \tag{6.12}$$

An additional constraint may be included to avoid excessive smoke generation. Despite an opacity model is included in the MVEM (see model equations at section 4.5), a quasi-steady approach seems too limited for an accurate estimation of such a complex process. It may be appreciated in figure 4.26 that correlation between experimental and modeled opacity values is poor. However, a workaround is still possible to limit soot emissions. First of all, it can be appreciated that there exists a clear relation between opacity and λ_e values according to the measurements shown in figure 6.9. It looks obvious that the less fresh air that takes part in the combustion process the worse it will be, so the chances to generate more smoke increase. The red line overlaid in this same figure is the Pareto front, which can be used as a rough relation between those two variables. Thereby, an opacity limit can be translated into a λ_e limit. Of course, this is just a qualitative question, as long as a stronger limitation in λ_e values does not guarantee any particular opacity level, but will surely limit the smoke generation at some point.

Based on the above reasoning, a λ_e limit has been forced in the OCP:

$$\widehat{\lambda}_e(t) - \lambda(\boldsymbol{x}, \boldsymbol{u}, t) \leq 0 \tag{6.13}$$

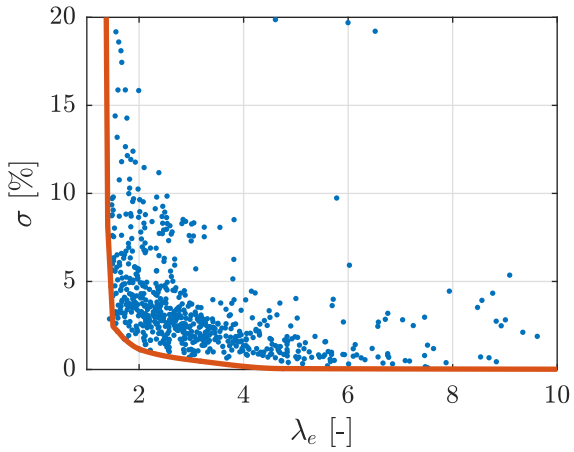

Figure 6.9: Relation between λ_e and opacity. Blue dots correspond to steady state measurements from Test 1. The red line is the Pareto front for this tradeoff.

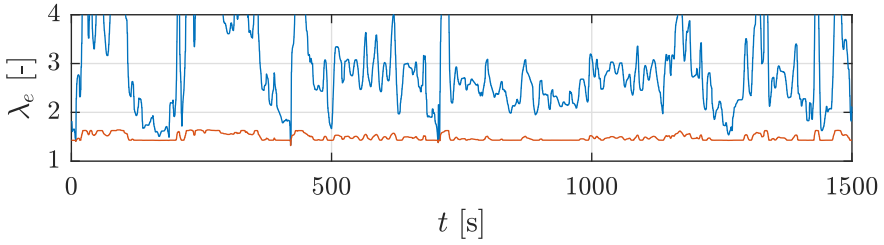

Figure 6.10: $\widehat{\lambda}_e$ lower limit imposed at the OCP to avoid excessive smoke generation (red line). This value is around $\lambda_e = 1.5$. Blue trajectory corresponds to factory calibration λ_e readings.

$\widehat{\lambda}_e$ is a lower bound calculated according to the relation from figure 6.9 with an arbitrary 2% higher opacity level than factory calibration in order to allow some room for improvement. This limit is shown in figure 6.10 together with factory calibration λ measurements.

States are initialized to those from the factory calibration in order to start all experiments with the same engine conditions, providing a fair comparison between strategies. These initial values are specified at table 6.2.

6.3.3 Optimization approach and implementation

The OCP at hand is complex and heavy. It features 5 states and 4 controls which is generally considered as a hard problem. The model from section 4.5 is

Intake manifold pressure, p_2	1.53 bar
Intake manifold oxygen concentration, $X_{O_2,im}$	9.9%
Exhaust manifold pressure, p_3	1.75 bar
Exhaust manifold oxygen concentration, $X_{O_2,em}$	7.2%
Turbocharger speed, ω_{tc}	107050 rpm

Table 6.2: Initial values of state variables.

large and nonlinear. The main idea here is to calculate the OC trajectories–one for each control–that satisfy the problem and constraints defined in eqs. (6.10)–(6.13). A time step of $\Delta t = 0.05$ seconds is to be used–ECU calculations at the current facility are scheduled at 10 to 100 ms, so it was considered that 50 ms might be enough for this study–for a driving cycle that lasts 25 minutes. Those are about 120000 unknowns.

According to the discussion carried out at chapter 3, where the three main families of OC methods were described and analyzed, it is not difficult to realize that only one of them is able to deal with such a complex problem. On the one hand, HJB equation and its well known DP implementation will definitely fail mainly because of computer memory concerns. Figure 3.2 shows an estimation of the necessary memory to address a short OCP using the DP method with different number of controls and states. Not only a problem with 5 states and 4 controls exceeds the 8 TB limit of a 64-bit machine, but also the OCP at this study is 50 times longer than the one at that example. Therefore this OCP is not affordable with DP. On the other hand, IMs, and more particularly the PMP method, may not experience memory nor computational burden issues. This method is based on the construction of an equivalent OCP–an IVP–which doubles the original number of ODEs with additional costates. Unfortunately, the additional ODEs use to be ill-conditioned, preventing the calculation of a valid solution to the problem. Also, initial values for all five costates must be found, but for complex models, such as the one at hand, it is not possible to calculate them analytically. An iterative search algorithm should be used instead, which is time consuming especially for $N_x \geq 2$.

DMs do not experience any particular issue when facing OCPs with complex nonlinear models and many states and controls. The main drawback is that the solution is a local optimum which may differ from the global one. There is no way to guarantee that the solution is a global optimum. However, a proper initial solution increases the chances to find it and, in fact, it may happen that the problem is convex so only one local optimum exists, or that it is sufficiently smooth for the solver to reach the global optimum regardless of the initial solution. Anyhow, most of the times, in practice, this is a minor

issue. Last but not least, model differentiability–C^1 continuity–is mandatory for this method. The MVEM is completely continuous so DM can be applied.

Among all DMs, DC is the choice for this work (see section 3.4.1 for a detailed description of DC method) due to computational burden reasons. According to this method, the original OCP is transcribed into a large and sparse NLP. States and controls are discretized into $N_t + 1$ time steps such that $\Delta t = \mathcal{T}/N_t$. The transcription using a centered Euler's method ends up with the following NLP:

$$\min_{\mathbf{x},\mathbf{u}} \left\{ \sum_{i=0}^{N_t-1} \dot{m}_f \left(\frac{\mathbf{x}_i + \mathbf{x}_{i+1}}{2}, \mathbf{u}_i \right) \right\} \tag{6.14}$$

where $\mathbf{x}_i$ and $\mathbf{u}_i$ are vectors containing all the five states and four controls respectively at time t_i. The NLP is subject to nearly the same constraints that applied to the original OCP:

$$\begin{array}{rcll} \mathbf{x}_0 - \boldsymbol{x}_0 & = & 0 & \\ f\left(\frac{\mathbf{x}_i+\mathbf{x}_{i+1}}{2}, \mathbf{u}_i\right) - \frac{\mathbf{x}_{i+1}-\mathbf{x}_i}{\Delta t} & = & 0, & i = 0, \ldots, N_t - 1 \\ \sum_{i=0}^{N_t-1} \dot{m}_{nox}\left(\frac{\mathbf{x}_i+\mathbf{x}_{i+1}}{2}, \mathbf{u}_i\right) \Delta t - \widehat{m}_{nox} & \leq & 0 & \\ \widetilde{T}_{ice,i} - T_{ice}\left(\frac{\mathbf{x}_i+\mathbf{x}_{i+1}}{2}, \mathbf{u}_i\right) & \leq & 0, & i = 0, \ldots, N_t - 1 \\ \widehat{\lambda}_{e,i} - \lambda_e\left(\frac{\mathbf{x}_i+\mathbf{x}_{i+1}}{2}, \mathbf{u}_i\right) & \leq & 0, & i = 0, \ldots, N_t - 1 \end{array} \tag{6.15}$$

From top to bottom, these constraints are: initial state values, set of N_t algebraic constraints to guarantee the continuity of the solution–such that original ODEs are satisfied–, NO_x emission limit from (6.11), torque path constraint from (6.12) and λ_e path constraint from (6.13). Note that continuity constraints are needed due to the fact that states are treated as free unknowns–exactly as controls are. These constraints force the states to adopt the values that correspond to the chosen controls. Although this may seem unnecessary since states are just a consequence of controls and not free variables, it allows to use an implicit ODE solver such as the centered Euler's method. Implicit numerical methods are possible as long as the simulation is not calculated forwards or backwards but iteratively. For this reason, the NLP solver not only finds an optimal solution but also simulates the system.

This NLP is extremely sparse due to the fact that only two consecutive time steps are related at most of the algebraic constraints (times t_i and t_{i+1}). Integral equations are dense, but they are only a few. Therefore, the Jacobian of this problem–derivative of constraints with respect to all unknowns, *i.e.* discretized states and controls–is made of diagonal submatrices as it can be

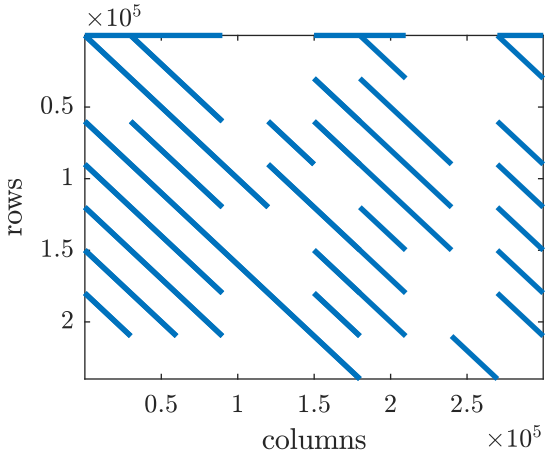

Figure 6.11: Jacobian matrix of the transcribed NLP. Blue dots are non-zero elements, whose number is 2488433, a 0.0035% of the total number of matrix elements.

appreciated in figure 6.11. Note that despite the resulting matrix is pretty big (239855×299816), only few elements are non-zero–a 0.0035% in this case. This makes possible that, even after exploiting problem dimensions by discretizing states, controls and constraints, the computational time required to compute a complete NLP iteration is 1.04 seconds with a total memory stamp of 23.1 MB.

The NLP is approached with IPOPT, a software package for large-scale nonlinear optimization that is specially efficient with sparse problems [20]. IPOPT is provided with analytical functions for objective and constraint functions as well as with their exact first derivatives. Second derivatives may be also provided explicitly, however they are numerically approximated with the quasi-Newton L-BFGS algorithm [21] for computational efficiency reasons. The provided initial solution–starting point for the solver–is a constant value trajectory for each state and control. Those constant quantities are arbitrary but on a reasonable order of magnitude. A more sophisticated initial solution, such as ECU control trajectories, may reduce the number of iterations needed to reach the optimal solution and increase the algorithm robustness. However, as long as computational time is still short with such a simple initial solution, it has been considered sufficient for this study. The NLP is scaled in order to normalize all output variables–objective function value, constraints violation and unknowns. This is a recommended procedure for any NLP solver in order to facilitate algorithm convergence.

The current NLP does not impose limits to the rate of change of controls.

It may happen that the OC strategy, according to the model, has an oscillating behavior. This is not an issue for the SOI scheduling as long as its influence only comprises the current engine cycle and torque generation, showing low interaction with other variables. It is neither a problem for the fueling rate since it has a strong impact on the torque output. The requisite to follow the driving cycle implicitly constrains the fueling rate to a smooth trajectory as fluctuating values would deliver an undesired torque curve. However, EGR and VGT controls are free to show a switching policy, producing pulsating flows along the airpath and an unstable behavior. This situation is specially harmful for the turbocharger as it would be spun with too many accelerations and decelerations. Also, it promotes unrealistic conditions and a highly dynamic transient operation which, for sure, exceeds the model capabilities to reproduce the engine behavior accurately.

In order to avoid oscillating situations, a rate of change limitation has been imposed in the VGT control. As long as this is a constraint on the derivative of a control, it is necessary to introduce an auxiliary state:

$$x_{vgt} = u_{vgt} \tag{6.16}$$

which replaces the original VGT control variable. A new control must be defined instead:

$$u_{\delta vgt} = \frac{\partial u_{vgt}}{\partial t} \tag{6.17}$$

The dynamics of the additional state are driven by the ODE:

$$\dot{x}_{vgt} = u_{\delta vgt} \tag{6.18}$$

Therefore, it is now possible to specify a limit on the rate of change by specifying upper and lower bounds to the control $u_{\delta vgt}$. Figure 6.12 shows the rate of change of VGT and EGR controls with (right) and without (left) the constraint on the control derivative. It may be appreciated that the rate of change is effectively reduced from a highly oscillating situation to a control policy that falls within the $\pm 60\%/\mathrm{s}$ range. Note that EGR oscillation is indirectly reduced as well, as a consequence of the coupling between both controls in the airpath management. For this reason, an additional state to limit the EGR control derivative was considered unnecessary.

The final OCP implementation features six states–five model states together with the auxiliary VGT control state–and four controls plus an integral constraint (6.11) and the two path constraints in eqs. (6.12) and (6.13). A summary of these variables and their boundaries is available at table 6.3. The problem has been solved with 11 different levels of emissions.

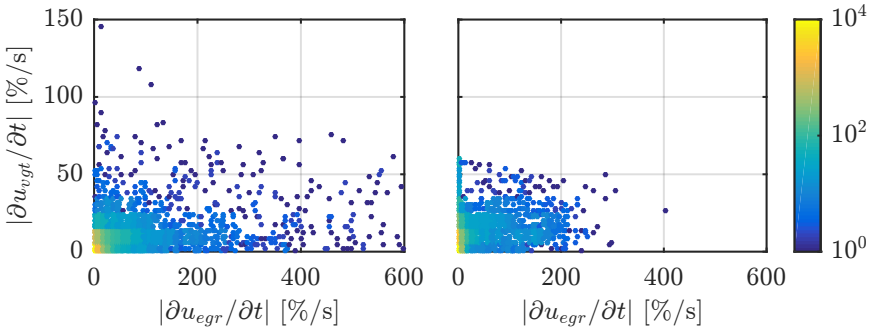

Figure 6.12: Derivative of the EGR and VGT optimal controls for an OCP with (right) and without (left) a constraint on the VGT rate of change. The colors represent the number of occurrences of the points in these diagrams. Note that not only the VGT derivative is limited but also EGR behaves smoother as a consequence of the coupling between these two controls in the airpath management.

		Boundaries	Initial solution	
States	p_2	$[p_1, 4p_1]$	1.1	bar
	$X_{O_2,im}$	$[0, 21]$	15	%
	p_3	$[p_1, 4p_1]$	1.3	bar
	$X_{O_2,em}$	$[0, 21]$	8	%
	ω_{tc}	$[5, 180]$	95	krpm
	u_{vgt}	$[0, 100]$	1	%
Controls	u_f	$[0, 80]$	10	mg/str
	u_{egr}	$[0, 100]$	0	%
	$u_{\delta vgt}$	$[-60, 60]$	0	%/s
	$u_{\delta soi}$	$[-5, 5]$	0	°BTDC

Table 6.3: Summary of states and actuators present at the final OCP implementation. The allowed boundaries for the variables and their initial solution are shown as used at the NLP solver.

Despite all control strategies deliver the same exact torque in simulation, due to the model uncertainties–such a simplified engine model cannot completely represent the actual engine at any situation–experimental tests may not follow the same results. Torque deviations might happen, resulting in an unfair comparison between different strategies. In order to approach this issue, a PID controller monitors the actual torque output during the test in closed-loop and slightly modifies the fueling rate to deliver the required torque trajectory. Only the injected fuel amount is corrected, leaving the other three controls (EGR, VGT and SOI) unmodified. Of course this simple solution somehow spoils the optimality of the control strategy, but provides a fair and clear comparison among strategies while keeping a pretty similar control policy (fueling rate corrections are bounded by ± 0.85 mg/str).

6.3.4 Results and discussion

This OCP is solved for a set of different NO_x emission levels. Two additional problems were also issued, one for minimum fuel consumption (constraint (6.11) is ignored), and another for minimum NO_x emission–$\dot{m}_f$ is replaced for $\dot{m}_{nox}$ at the optimization objective (6.10). The resulting OC trajectories are validated in the experimental setup A (see 5.2.1). NO_x limits and the corresponding experimental results are summarized in table 6.4. An additional experiment is issued with factory calibration as a reference, which is also included in the aforementioned table.

The main variables that take part in the OCP are fuel consumption–a control–, NO_x emissions–a constraint–and torque output–another constraint. Fuel consumption is only a function of the optimal trajectory, so it gives no clue regarding how close are simulations to the actual engine performance. However, NO_x and torque are outputs of the engine and, therefore, are good indicators about the agreement between simulated OC and experimental results. It is interesting that accumulated NO_x emissions are pretty well correlated to the model estimations as shown in figure 6.13. It can be found that differences are generally less than a gram, so model accuracy is more than acceptable. Regarding torque output, remember that a PID controller performs online fuel corrections to guarantee that the driving cycle is followed regardless of model inaccuracies. The tracking error histogram is shown in the left plot of figure 6.14. This histogram is quite close to a normal variable, with an average of -0.1 Nm and a standard deviation of 3.3 Nm. Torque error is, in practice, centered in zero with 80% of the time within the ± 3.4 Nm range. The right plot shows the delivered mechanical energy E_{ice} along the experiments as a percentage of the required energy $\widetilde{E}_{ice}$ to follow the driving cycle. These quotients are nearly the reference with the three cases on the left–lowest NO_x

Case	OCP		Experimental results		
	J	$\widehat{m}_{nox}$ [g]	m_f [kg]	m_{nox} [g]	m_{soot} [g]
#1	m_f	3	1.395	3.6	1.846
#2	m_f	4	1.344	5.2	0.892
#3	m_f	5	1.291	6.1	1.001
#4	m_f	6.4	1.268	6.8	0.847
#5	m_f	7.5	1.262	7.9	0.477
#6	m_f	9	1.254	10.5	0.382
#7	m_f	11	1.252	12.1	0.282
#8	m_f	13.3	1.252	13.9	0.304
#9	m_f	17	1.253	17.3	0.218
#10	m_f	20	1.257	22.5	0.208
#11	m_f	21	1.247	20.5	0.229
#12	m_{nox}	–	1.369	3.8	0.936
Factory	–	–	1.306	11.4	0.340

Table 6.4: Summary of all OCPs that have been issued and their main experimental results. The information shown is, from left to right, the case number, the minimization objective, NO_x emission limit, experimental fuel consumption, actual NO_x emission and total soot generation.

emissions–in the 99% to 100% range and the rest over 100%. These results confirm that the different control strategies are comparable since the driving cycle is followed up to a sufficient threshold.

The key results of the experiments are the total fuel consumption and accumulated NO_x emissions. These results are shown in figure 6.15. Soot generation is also included in this figure as a reference of how different control strategies and constraint limits affect to it. Note that soot is just an output since smoke level is not directly taken into account in the optimization problem but through a varying λ_e limit as it was discussed with figure 6.9. It can be appreciated that all optimal strategies define a Pareto front with different levels of fuel consumption and emissions. This frontier is the set of points that minimize fuel consumption for a given level of NO_x emissions–or alternatively the curve that minimizes the emission level for a given fuel consumption. In this sense, the Pareto front defines the limit where a system operates in the most efficient way; an OC falls within it, any suboptimal control remains over the frontier, and operation below is not possible. Factory calibration (red square) falls over of the Pareto front since this control is not optimal. In fact,

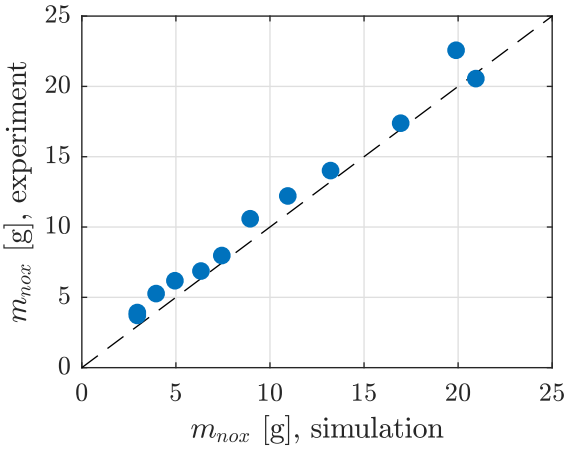

Figure 6.13: Correlation in accumulated NO_x emissions m_{nox} between OCP solving process simulations and experiments. The average error is -0.86 g and the standard deviation is 0.75 g.

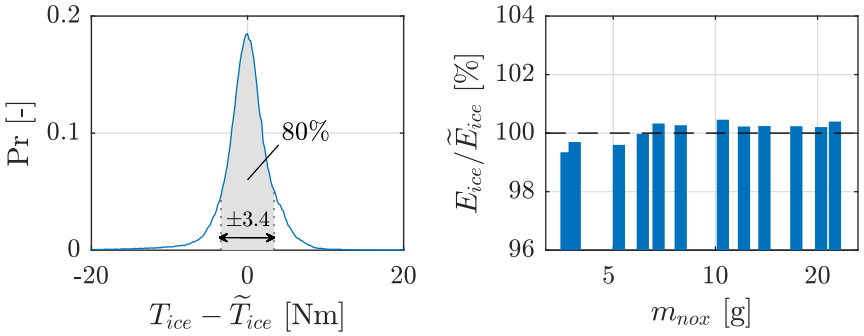

Figure 6.14: Analysis of the driving cycle tracking. On the left, the histogram of the error between experimental and reference engine torque for all experiments is shown. The gray area denotes the region where 80% of the measurements lie in (± 3.4 Nm range). On the right, the bars represent the quotient between the delivered energy along each single experiment and the reference mechanical energy. The experiments are sorted, from left to right, according to the NO_x emissions.

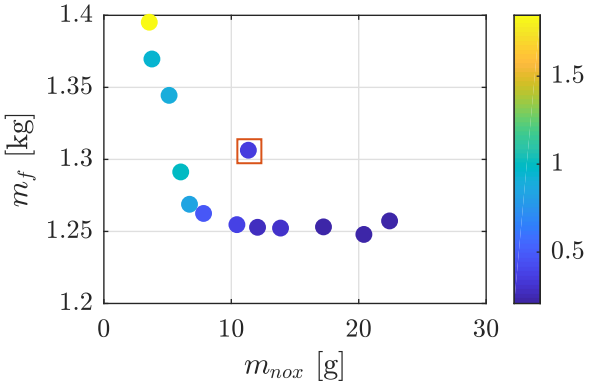

Figure 6.15: Pareto frontier analysis of experimental results for OC strategies calculated with a variety of NO_x limits. Factory calibration is surrounded by the red square. Total soot generation in grams is shown with the color scale.

several experimental tests show lower fuel consumption and NO_x emission levels. Several conclusions may be drawn from this figure:

- It is possible to decrease fuel consumption with an OC strategy without any significant impact on both NO_x emissions and soot generation levels. Savings about 4% in fuel are shown in the Pareto frontier analysis for strategies with factory NO_x emissions.

- There are possibilities to reduce both fuel consumption and NO_x emissions together. However, there is not too much room for further fuel efficiency improvements. While NO_x can be decreased to less than half, fuel savings do not exceed 4%. The reason for this is that torque is mostly a function of the injected fuel amount and, since torque is fixed for all tests, fuel consumption should be in the same order regardless of the strategy. Conversely, NO_x generation is affected by many other variables and, therefore, leaves much more room for improvement.

- Optimal solutions with lower NO_x emissions show not only a higher fuel consumption but also an increased soot generation. This may limit the minimum level of NO_x emissions that can be achieved with this engine. However, these emission levels are raw measurements–before after-treatments–and a DPF may equate the soot emissions level of all these control strategies.

The Pareto front is useful to benchmark other control strategies. For example, the performance of the ECU strategy can be compared to the

optimal frontier in a quite objective way. According to the results, ECU control shows about twice NO_x emissions than minimum emission solutions and a 5% increase in fuel consumption compared to minimum consumption solutions. Comparing ECU control to OC strategies with similar soot emission level (cases #6 and #7 from table 6.4), NO_x reduction is not so clear–OC shows between 8% reduction to 6% increase–but fuel consumption is improved by 4%. Therefore, it may be possible to define an *optimality coefficient* η_{oc} to synthesize how far is a given control strategy to completely exploit all the potential of the engine at a given cycle. The following index is proposed in this thesis:

$$\eta_{oc} = \frac{1}{1 + d_{oc}} \tag{6.19}$$

with d_{oc} the expression:

$$d_{oc} = \sqrt{\left(\frac{\widetilde{m}_{nox} - m^*_{nox}}{m^*_{nox}}\right)^2 + \left(\frac{\widetilde{m}_f - m^*_f}{m^*_f}\right)^2} \tag{6.20}$$

where $\widetilde{m}_{nox}$ and $\widetilde{m}_f$ are the NO_x emissions and fuel consumption level of the control strategy to benchmark, while variables with an asterisk correspond to the OC strategy that minimizes the quantity d_{oc}. This index will show 100% efficiency for an optimal strategy, 50% for a strategy whose weighted sum of NO_x and fuel is double the OC solution, 33% if that sum is three times the optimum, etc. According to this definition, the optimality of the ECU control strategy is $\eta_{oc} = 93\%$.

The Pareto front shows an asymptotic behavior when reaching the lower fuel and NO_x levels. This happens because of two main reasons. On the one hand, there is a technical limit on the minimum level that can be achieved in both fuel and NO_x emissions. OC cannot exploit the engine further than its technology allows to. On the other hand, at extrema the engine operates on the limits of the model where less information is available. The model accuracy is penalized preventing the optimal solution results to be reflected in the actual engine. In this particular case, it can be appreciated that decreasing fuel consumption below 1.25 kg or NO_x emissions under 6 g is pointless.

An interesting question is how do these OC strategies improve the factory control. Contours in figure 6.16 shows the histogram of the four optimized controls for all 12 optimization cases that have been issued. Each plot represents a different control with its range of operation in the x-axis. Y-axis lists the total NO_x emissions of the OC strategy, so each row belongs to a different case. ECU control is shown at its corresponding row–according to

its NO_x emissions level–and rounded with white lines. The first thing that can be appreciated is that factory control is quite different from OC. These differences are analyzed in the following points:

- u_{egr}: EGR valve actuation may be the control that differs the most from the factory calibration. OC generally focuses in recirculating as much flow as possible, staying at 100% almost 90% of the time. There are some exceptions when NO_x emissions are neglected (> 15 g), but these are few. On the contrary, ECU actuates the valve between 40% and 60% most of the times, but it does not stay in any particular setpoint for more than 30% of the time.

- u_{vgt}: factory control is mostly concentrated between 75% and 80%. OC tries to keep the turbine slightly more open and this effect is stronger when fuel consumption is decreased. Only when NO_x emissions are very low, VGT percentage is clearly lower (less turbine opening) than at factory control.

- u_f: both factory and OC show a similar dispersion as long as they follow the same torque profile. However, OC levels are significant lower with a slight increase when NO_x emissions are reduced.

- $u_{\delta soi}$: factory control is centered in zero since $u_{\delta soi} = 0$ is the factory calibration. OC is about 1° delayed regardless of the case. It looks like the engine has a strong optimal pole at that SOI setting that differs from factory calibration in this cycle.

The OC strategy tries to exploit two main aspects. On the one hand it tries to reduce pumping losses by opening the turbine. This VGT strategy decreases the intake manifold pressure and, therefore, there is less air available for the combustion. This might penalize λ_e values, but recall that λ_e was explicitly lower bounded at the OCP so this strategy still keeps AFR at acceptable values. The decrease of intake pressure also jeopardizes the torque reserve. Since ECU has no information in advance, it must keep a sufficiently high level of pressure in order to satisfy a strong load step whenever the driver requests it with a reduced lag. On the contrary, OC knows the complete cycle so does not require that torque reserve and avoids an unnecessary pumping effort. On the other hand, OC tries to decrease NO_x emissions by recirculating as much flow as possible and by delaying the combustion–a later combustion has a lower temperature–at the expense of jeopardizing the combustion efficiency. In the case of tighter NO_x constraints, VGT is also used to create a backpressure

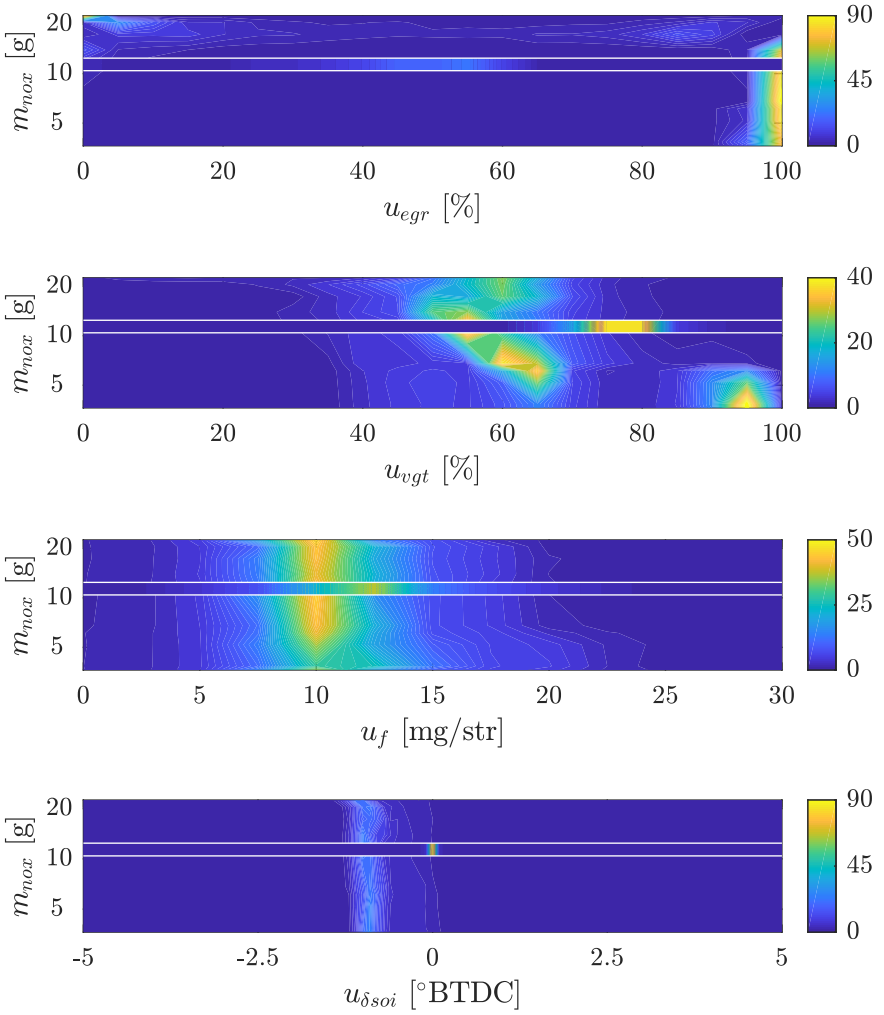

Figure 6.16: Histogram of controls (u_{egr}, u_{vgt}, u_f and $u_{\delta soi}$) for all 12 optimization cases that have been issued. Each plot represents a different control, the x-axis is its range of operation and the y-axis lists the total NO_x emissions of the OC strategy. Each row belongs to a different case. ECU control is shown at its corresponding row–according to its NO_x emission level–and rounded in white lines. The color scale shows the level of occurrence of a control as a percentage.

upstream the turbine that raises the pressure ratio at the EGR valve and promotes the increase of recirculated flow.

The OC strategy is, at the end, a question of balance between the efficiency gain avoiding pumping losses and the penalization of a reduced NO_x emission. According to the results there are many situations where the efficiency gain is greater than the penalization–several OC strategies improve both fuel consumption and emissions level as shown in figure 6.15. And, in fact, it is pretty easy to reformulate the constraints in the OCP to move the equilibrium to lower NO_x emissions or fuel consumption, getting a completely new control strategy, which is the tradeoff shown in the Pareto front at figure 6.15. However, the torque reserve is always gone.

Many of the things that have been discussed above can be also appreciated in the OC trajectories shown in figures 6.17 and 6.18. These trajectories show the whole driving cycle with factory calibration (dotted black) and three of the OC strategies:

- Low NO_x emissions (blue, case #12): high EGR rates are issued most of the time. It is interesting that despite VGT is almost closed, intake manifold pressure is still lower than factory. This happens because VGT backpressure increases EGR flow and exhaust gases through the turbine are decreased for that reason. It can be appreciated that fresh air is some times half of the factory level.

- Low fuel consumption (red, case #11): since fuel consumption is the priority in this case, EGR rates are much lower. As a consequence, fresh air and λ are higher. Note that even in this case, u_{vgt} is lower than factory to reduce pumping losses.

- Factory NO_x with lower fuel consumption (yellow, case #6): this is an intermediate case between the blue and the red. It features an opened VGT to benefit from a low pumping effort, but it also recirculates a high rate of exhaust gases. λ_e is lower than factory but still within the OCP constraints.

It can be appreciated that intake manifold pressure is lower than factory in all these trajectories. This means that reducing pumping losses is a must for the OC strategies regardless of the NO_x emissions limit. It is also significant that sometimes an oscillating behavior happens. This is specially evident in the red trajectory. It is produced because small variations on the requested torque and engine speed produces a very different OC in the model. However, it is not an important issue as long as high frequency oscillations are forbidden at the OCP with the additional state (6.16).

It is interesting that factory calibration is operating at similar setpoints for VGT and EGR valves most of the cycle. This is because of the lack of future information and, as a consequence, ECU makes a commitment solution that offers both a low fuel consumption and a reduced NO_x emission at any situation. Conversely, OC can decide which is the most appropriate part of the cycle where low NO_x strategies benefit the most, and where fuel consumption should be a priority. This is manifest in figure 6.17, where $t = [200, 300]$ s seems specially attractive for reducing NO_x. All OC strategies do recirculate exhaust gases in this phase regardless of their emission target. On the contrary, factory control EGR rate is low. Therefore, instead of operating with both low emissions and fuel consumption along the complete cycle, OC alternates NO_x reduction with low fuel consumption phases based on which is the most attractive at each part of the cycle.

The discriminating ability that shows the OC strategy may suggest that, in order to find those NO_x reduction and fuel minimization-attractive phases at the driving cycle, the OCP must account for the whole cycle at once. In that situation, control strategies addressing short control horizons would not be able to find the proper balance between fuel consumption and NO_x emissions. In fact, it would be difficult for a short horizon control to deliver the NO_x results shown in the yellow trajectory from figure 6.18: NO_x rapidly increase around $t = 200$ s since it is more efficient to reduce emissions later but, as long as a short horizon control is not aware of the characteristics of the rest of the cycle, it cannot take that kind of decisions. Anyhow, this particular aspect of OC deserves a further study, which is out of the scope of this dissertation.

6.3.5 Conclusions

OC theory has been applied to the full engine control of a Euro 5 diesel engine in a real driving cycle. To do so, a methodology to calculate the optimal trajectories for EGR position, VGT opening, fueling rate and SOI offset using DC has been presented and described above. These trajectories have been experimentally validated on a testing facility showing that OC can effectively improve fuel efficiency and NO_x emissions compared to factory calibration. Several OC strategies can be calculated just by modifying the NO_x limit at the OCP, resulting pretty straightforward to adapt the strategy to specific emissions requisites. In fact, 12 different strategies have been calculated in order to get a complete tradeoff between NO_x emissions and fuel consumption. According to the experimental results, a 45% NO_x reduction is possible keeping the factory fuel efficiency, while a 4% fuel consumption reduction can be achieved with the factory NO_x and soot emissions. These results show that an OC strategy may improve the specifications of an engine

compared to a fixed calibration, and that there is still room for improvement in both fuel consumption and NO_x emissions with an adequate control strategy in a real driving cycle.

OC trajectories follow two strategies to achieve lower NO_x emissions and fuel consumption. On the one hand they show a higher VGT opening that allows to decrease pumping losses improving fuel efficiency. This spoils the torque reserve but, since cycle is known in advance, it is no longer necessary to keep a high intake manifold pressure. Simultaneously, EGR rate is increased to reduce NO_x generation jeopardizing combustion efficiency but still taking some advantage from the reduced pumping losses. On the other hand, OC applies NO_x reduction strategies specifically on the parts of the cycle where it is more beneficial for the global efficiency. For the rest, the optimal strategy looks for the best fuel efficiency. ECU has no chance to find out that cycle-specific balance and, therefore, it has to keep a reasonable tradeoff between NO_x and fuel at any condition which is by far not the best option.

References

[1] J. M. Luján et al. "Effect of low pressure EGR on gas exchange processes and turbocharging of a HSDI engine". In: *Thiesel International Conference on Thermo and Fluid Dynamic processes in Direct Injection Engines*. 2008, pp. 429–442.

[2] J. M. Desantes et al. "On the combination of high-pressure and low-pressure exhaust gas recirculation loops for improved fuel economy and reduced emissions in high-speed direct-injection engines". In: *International Journal of Engine Research* 14.1 (2013), pp. 3–11.

[3] F. Yan and J. Wang. "Control of diesel engine dual-loop EGR air-path systems by a singular perturbation method". In: *Control Engineering Practice* 21.7 (2013), pp. 981–988.

[4] J. V. Shutty et al. "Air system control for advanced diesel engines". In: *SAE World Congress and Exhibition*. 2007.

[5] A. Suresh et al. "Thermodynamic systems for Tier 2 Bin 2 diesel engines". In: *SAE International Journal of Engines* 6.1 (2013), pp. 167–183.

[6] F. Castillo et al. "Simultaneous air fraction and low-pressure EGR mass flow rate estimation for diesel engines". In: *IFAC Proceedings Volumes* 46.2 (2013), pp. 731–736.

[7] O. Grondin, P. Moulin, and J. Chauvin. "Control of a turbocharged diesel engine fitted with high pressure and low pressure exhaust gas recirculation systems". In: *Joint 48th IEEE Conference on Decision and Control and 28th Chinese Control Conference*. 2009, pp. 6582–6589.

[8] J. M. Luján et al. "Switching strategy between HP (high pressure)- and LPEGR (low pressure exhaust gas recirculation) systems for reduced fuel consumption and emissions". In: *Energy* 90, Part 2 (2015), pp. 1790–1798.

[9] A. J. Torregrosa et al. "Experiments on the influence of inlet charge and coolant temperature on performance and emissions of a DI diesel engine". In: *Experimental Thermal and Fluid Science* 30.7 (2006), pp. 633–641.

[10] A. Broatch et al. "A procedure to reduce pollutant gases from diesel combustion during European MVEG-A cycle by using electrical intake air-heaters". In: *Fuel* 87.12 (2008), pp. 2760–2778.

[11] A. Maiboom, X. Tauzia, and J.-F. Hétet. "Experimental study of various effects of exhaust gas recirculation (EGR) on combustion and emissions of an automotive direct injection diesel engine". In: *Energy* 33.1 (2008), pp. 22–34.

[12] K. Akihama et al. *Mechanism of the smokeless rich diesel combustion by reducing temperature*. Tech. rep. SAE Technical Paper, 2001.

[13] N. Ladommatos, S. M. Abdelhalim, and H. Zhao. "Effects of exhaust gas recirculation temperature on diesel engine combustion and emissions". In: *Proceedings of the Institution of Mechanical Engineers, Part D: Journal of Automobile Engineering* 212.6 (1998), pp. 479–500.

[14] D. T. Hountalas, G. C. Mavropoulos, and K. B. Binder. "Effect of exhaust gas recirculation (EGR) temperature for various EGR rates on heavy duty DI diesel engine performance and emissions". In: *Energy* 33.2 (2008), pp. 272–283.

[15] V. Bermúdez et al. "Effects of low pressure exhaust gas recirculation on regulated and unregulated gaseous emissions during NEDC in a light-duty diesel engine". In: *Energy* 36.9 (2011), pp. 5655–5665.

[16] G. Rizzoni, L. Guzzella, and B. M. Baumann. "Unified modeling of hybrid electric vehicle drivetrains". In: *IEEE/ASME Transactions on Mechatronics* 4.3 (1999), pp. 246–257.

[17] C. Guardiola et al. "Representation limits of mean value engine models". In: *Identification for Automotive Systems*. Springer, 2012, pp. 185–206.

[18] C. Musardo et al. "Supervisory control for NOx reduction of an HEV with a mixed-mode HCCI/CIDI engine". In: *Proceedings of the American Control Conference*. Vol. 6. 2005, pp. 3877–3881.

[19] T. Nuesch et al. "Optimal energy management and sizing for hybrid electric vehicles considering transient emissions". In: *Engine and Powertrain Control, Simulation and Modeling*. Vol. 3. 1. 2012, pp. 278–285.

[20] A. Wächter and L. T. Biegler. "On the implementation of an interior-point filter line-search algorithm for large-scale nonlinear programming". In: *Mathematical Programming* 106.1 (2006), pp. 25–57.

[21] J. Nocedal. "Updating quasi-Newton matrices with limited storage". In: *Mathematics of Computation* 35.151 (1980), pp. 773–782.

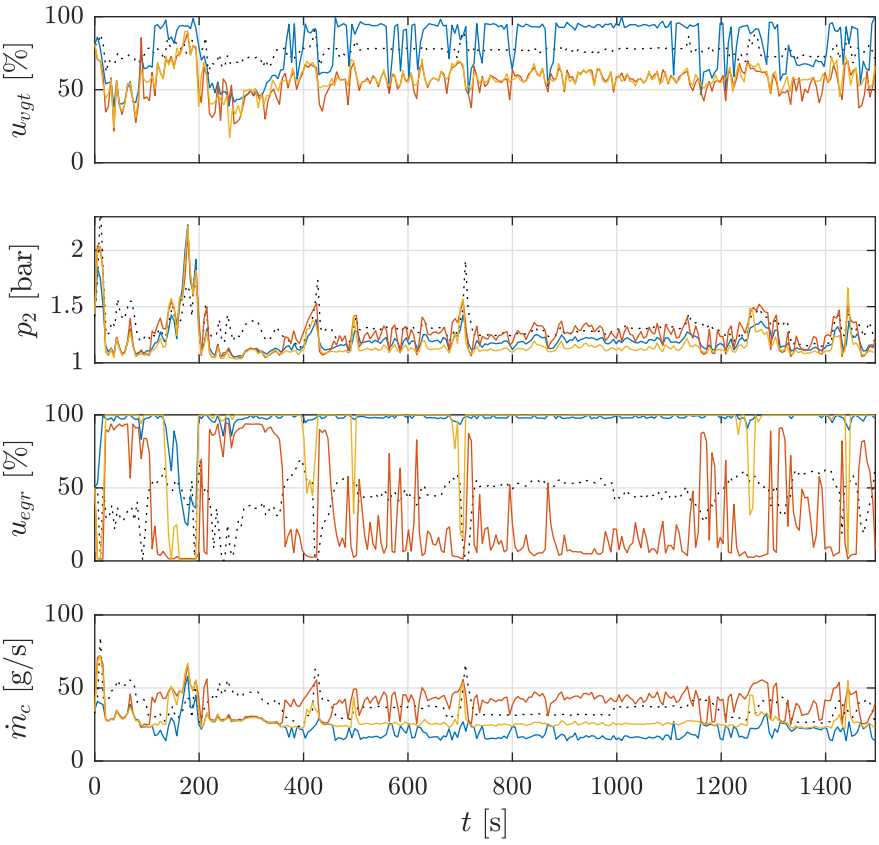

Figure 6.17: OC trajectories for the whole driving cycle. From top to bottom, VGT position, intake manifold pressure, EGR position and fresh air mass flow are shown. The cases depicted in this figure and their corresponding case number at table 6.4 are: factory calibration (dotted black), low NO_x emissions (blue, case #12), low fuel consumption (red, case #11) and factory NO_x with lower fuel consumption (yellow, case #6).

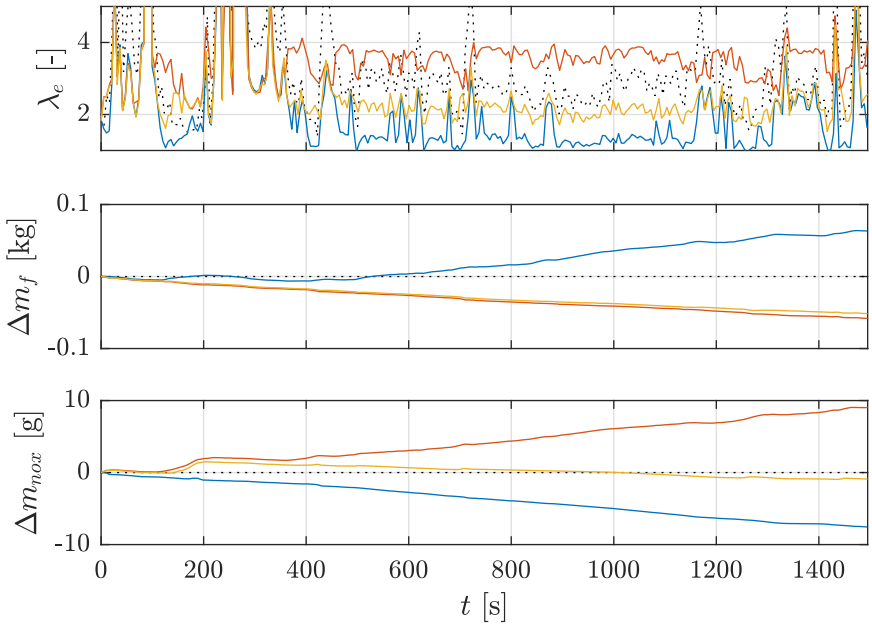

Figure 6.18: OC trajectories for the whole driving cycle. From top to bottom, λ_e value, fuel consumption difference with respect to factory and NO_x emissions compared to factory are shown (values greater than zero mean higher mass than factory). The cases depicted in this figure and their corresponding case number at table 6.4 are: factory calibration (dotted black), low NO_x emissions (blue, case #12), low fuel consumption (red, case #11) and factory NO_x with lower fuel consumption (yellow, case #6).

Chapter 7

Optimal engine control with embedded speed management

To travel is to discover that everyone is wrong about other countries.

— Aldous Huxley

Contents

7.1 Introduction

The replacement of the ECU control with an OC approach has been addressed in section 6.3, finding that an appropriate cycle-specific OC may improve the factory control performance, both in terms of fuel and emissions. Another interesting approach is to include the management of the vehicle speed in that optimal control strategy. The conversion from mechanical energy to traveled distance is a quite interesting topic that several authors have already addressed [1–5]. Engine technology is generally well exploited and a new development usually involves only a little additional efficiency. On the contrary, an efficient

use of the available mechanical energy is generally affected by many factors and delegated to the driver criterion. Therefore, there is much more room for improvement on this side.

A joined control of vehicle speed and engine management might take the advantage of an efficient use of the available energy and the exploiting of the engine technology adapted to that particular utilization. Despite this problem might be separated into two independent subproblems–a speed management and an engine control–the aim of this work is to study the coupling of both systems and the joined optimal solution.

The proposed approach is purely theoretical. It is based on an offline solution to the OCP with accurate engine and vehicle models. Optimization is performed with a DM due to the complexity of the problem. Results are shown from a simulated environment.

7.2 Problem description

The minimization of the mechanical energy required to complete a trip is an interesting question with lots of room for improvement. This problem has been already addressed in several works such as [1–5], but always from the point of view of a speed optimization problem. The engine operation is conditioned by the driving cycle and, therefore, a change in the speed profile may impact on engine performance, as demonstrated in section 6.3. According to this, engine management and speed optimization are not uncoupled problems and it might be interesting to address the joined OCP. The particular operation of the engine that may result from a speed optimization could be profitable as well for a specific engine control.

The complete vehicle optimization problem is addressed in this work. A route is given between two cities with a specific road grade profile, speed limits and a time constraint to reach the destination. To do so, the control is free to decide vehicle speed and engine controls at any time. The particular route used in this study corresponds to test 8, which comprises a total distance of 60 km to be covered in less than 41 minutes–an average of 88 km/h is required. Road grade and speed limits are shown in the test description at section 5.3.8.

This OCP is applied to the setup C vehicle (setup A engine and a B-segment chassis, see section 5.2.3). This engine model is exactly the same used in section 6.3, which is validated at the engine test bench. Some examples of the performance of this model were shown in figure 6.8. Vehicle dynamics are modeled following the approach shown in section 4.2. These equations were validated with experimental data. Despite this vehicle model is experimentally validated, this work is purely theoretical due to the inability to dispose of an

States $\boldsymbol{x}$	Intake pressure p_2 Intake oxygen fraction $X_{O_2,im}$ Exhaust pressure p_3 Exhaust oxygen fraction $X_{O_2,em}$ Turbocharger speed ω_{tc} Vehicle speed v
Controls $\boldsymbol{u}$	Fueling rate u_f EGR position u_{egr} VGT opening u_{vgt} SOI offset setting $u_{\delta soi}$ Gear number u_{gb} Brakes actuation u_b

Table 7.1: Problem states and controls.

experimental facility that allows to modify engine parameters while running in a vehicle.

7.3 Problem formulation

The task is to control the main vehicle actuators for a specific route in order to minimize the total fuel consumption. The formulation regarding the engine is, to a extent, pretty similar to that in 6.3. The following cost index to be minimized may be defined:

$$J = \int_0^{\mathcal{T}} \dot{m}_f(\boldsymbol{x}, \boldsymbol{u}, t)\, \mathrm{d}t \tag{7.1}$$

where states $\boldsymbol{x}$ and controls $\boldsymbol{u}$ are shown in table 7.3 according to the model and the OCP requisites.

The specification of a specific route, aside from disturbing the problem equations with road grade, introduces several constraints. In particular, vehicle speed must be kept below legal limits:

$$v(t) - \widehat{v}(t) \leq 0 \tag{7.2}$$

where $\widehat{v}$ is the speed limit. In addition to that, the vehicle is required to reach

the destination before a certain time limit–otherwise the optimal solution may take too much time resulting in an unrealistic control. Therefore:

$$\mathcal{S} - \frac{\widehat{\mathcal{T}}}{\mathcal{T}} \int_0^{\mathcal{T}} v(t)\,\mathrm{d}t \leq 0 \tag{7.3}$$

with $\mathcal{S}$ the total trip distance and $\widehat{\mathcal{T}}$ the time limit.

In order to provide a more accurate and realistic control, additional engine-related constraints might be considered. First of all, the turbocharger speed may be limited to preserve its health:

$$\omega_{tc}(t) - \widehat{\omega}_{tc} \leq 0 \tag{7.4}$$

Similarly to the approach shown in section 6.3.2 where a variable λ_e limit was considered to avoid excessive smoke generation, a λ_e constraint is also included in this problem:

$$\widehat{\lambda}_e - \lambda_e(t) \leq 0 \tag{7.5}$$

Note that in this case a constant limit of $\widehat{\lambda}_e = 1.3$ is considered in order to simplify the formulation. Finally, a tradeoff between fuel consumption and NO_x emissions may be specify by limiting the NO_x generation to a total mass $\widehat{m}_{nox}$:

$$\int_0^{\mathcal{T}} \dot{m}_{nox}(\boldsymbol{x}, \boldsymbol{u}, t)\,\mathrm{d}t - \widehat{m}_{nox} \leq 0 \tag{7.6}$$

7.4 Optimization approach and implementation

The driving mission consists in covering a fixed distance in a prescribed time. As long as the route is known in advance, disturbances are location-based; depending on the vehicle speed–which is a state and, accordingly, unknown in the problem definition–a hill will be reached at different times but it is always at the same location. Therefore, it is much more convenient to reformulate the OCP in distance domain s. Following the procedure described in appendix A, the OCP stated in eqs. (7.1)–(7.6) can be rewritten as the minimization of the new cost index:

$$J = \int_0^{\mathcal{S}} \frac{\dot{m}_f}{v(s)}\,\mathrm{d}s \tag{7.7}$$

subject to the same constraints, but in space domain:

$$\begin{aligned} v(s) - \widehat{v}(s) &\leq 0 \\ \int_0^{\mathcal{S}} \frac{1}{v(s)}\,\mathrm{d}s - \widehat{\mathcal{T}} &\leq 0 \\ \omega_{tc}(s) - \widehat{\omega}_{tc} &\leq 0 \\ \widehat{\lambda}_e - \lambda_e(s) &\leq 0 \\ \int_0^{\mathcal{S}} \frac{\dot{m}_{nox}}{v(s)}\,\mathrm{d}s - \widehat{m}_{nox} &\leq 0 \end{aligned} \tag{7.8}$$

The model equations keep the same formulation. However, in order to adapt to the space domain, ODEs must be rewritten as:

$$\frac{\partial x}{\partial s} = \frac{1}{v}\dot{x} \tag{7.9}$$

In principle, a solution to the above problem has the chance to move controls $\boldsymbol{u}$ with an oscillating strategy. Despite this might not be an issue for a simulated environment, high frequency switches push the model out of the fitted region and may cause an unrealistic behavior compared to the actual engine. Also, abrupt changes in controls could result in a unsafe operation of the engine and an uncomfortable situation for the driver. Therefore, a constraint on the derivative of the VGT control is introduced to this OCP. An auxiliary state is required:

$$x_{vgt} = u_{vgt} \tag{7.10}$$

replacing the VGT control variable which is no longer needed. The following system equation drives this auxiliary state:

$$\dot{x}_{vgt} = u_{\delta vgt} \tag{7.11}$$

where $u_{\delta vgt}$ is an additional control variable defined as:

$$u_{\delta vgt} = \frac{\partial u_{vgt}}{\partial t} \tag{7.12}$$

This philosophy was followed in section 6.3.3 to limit the oscillating behavior of both EGR and VGT controls in the optimal solution with successful results. This workaround eliminates the possibility of an oscillating engine control. However, there are still chances that gear shifting is managed in an abrupt way. In order to avoid this situation, a similar procedure is followed limiting the derivative of the fueling rate. The constraint is set on u_f instead of the gear

shift control because they are equivalent–a gear shift results in a change of the engine operating point and, consequently, the fueling rate–and the fueling rate derivative has a more evident physical meaning. Therefore, another additional state is included in the problem formulation:

$$x_f = u_f \tag{7.13}$$

with state equation:

$$\dot{x}_f = u_{\delta f} \tag{7.14}$$

The new control is formulated as:

$$u_{\delta f} = \frac{\partial u_f}{\partial t} \tag{7.15}$$

Note that both x_{vgt} and x_f state equations must be transcribed into space domain applying (7.9).

This OCP is obviously a huge problem comprising a total of 8 states–$\boldsymbol{x} = \{p_2,\ X_{O_2,im},\ p_3,\ X_{O_2,em},\ \omega_{tc},\ v,\ x_{vgt},\ x_f\}$–, 6 controls–$\boldsymbol{u} = \{u_{\delta f},\ u_{egr},\ u_{\delta vgt},\ u_{\delta soi},\ u_{gb},\ u_b\}$–and a large set of constraints. According to the discussion carried out in section 3.4, only DMs are capable to deal with such a complex nonlinear problem.

The applicability of a DM requires the continuity of all state equations, constraints and the cost index. Despite model equations are continuous, gear setting can only take discrete integer values. This would result in an MINLP which is, as discussed in section 3.4.2, extremely expensive to solve. In order to overcome this issue, the workaround proposed in that discussion is followed, splitting the solution process into two sequential steps:

1. The gear setting is assumed as a continuous variable that can take any finite value between its boundaries. This fully continuous OCP is solved and the resulting gear setting trajectory $u_{gb}(s)$ is rounded to integer values producing a quasi-optimal control trajectory $\breve{u}_{gb}(s)$.

2. The gear setting control u_{gb} is removed from the original OCP and the integer trajectory $\breve{u}_{gb}(s)$ is passed as a disturbance. The number of actuators of this new OCP is reduced in one unit compared to the original one.

Of course, it is not guaranteed that the rounding of a continuous trajectory is an optimal solution to the original OCP. However, as long as the gear setting has a sufficient number of integer values to be approximated to a continuous

variable–the vehicle features six gear ratios–the rounded trajectory should not be too far from the optimal solution while keeping a reasonable computational effort. In fact, after solving the OCP at the second step, the other five controls are optimal for the given integer gear shifting trajectory. This methodology is similar to addressing the OCP with a given–not optimal–gear shifting rule, with the difference that in this case this rule is based on an optimal trajectory.

The OCP described in eqs. (7.7) and (7.8) is addressed with DC, using a centered Euler's method. The reasons of this choice are discussed in sections 3.4.1 and 3.4.2. Accordingly, cost index, state equations and constraints are transcribed into a large and sparse NLP, similarly to the formulation shown in (6.15). The resulting NLP is solved with IPOPT [6]. The problem is initialized to constant values, so the initial solution is not necessarily feasible. A better initialization may be provided with some heuristics reducing the necessary number of iterations, but this is an arbitrary question whose effort is not worth. The main aim of this theoretical study is to produce an analyze the optimal solution to the OCP, so improving the calculation efficiency is out of the scope of this work.

The Jacobian matrix to this OCP is shown in figure 7.1. This Jacobian corresponds to the first step problem, which is by far the most difficult one, not only due to the additional control variable, but also because the second problem is initialized to the first solution, being much cheaper to address. The total amount of non-zero elements is 3768890–a 0.003% of the matrix elements–so it is extremely sparse. Because of this sparsity, the complete computation of an NLP iteration takes an average of 2.3 seconds. Taking into account that the solver converges to an optimal solution in 150 to 200 iterations, the OCP can be solved in approximately 7 minutes, which is considered a fast and efficient mark to solve such a complex problem.

7.5 Results and discussion

The OCP described in the above section is implemented and successfully solved with a custom DC method. The baseline case results and constraints fulfilling are summarized in table 7.2. Figure 7.2 shows the optimal speed profile for this case in red, overlaid with the road altitude profile in gray and the speed limits in black. During the first part of the cycle, the speed is constrained by low speed limits with the solution trying to accelerate as fast as possible to reach those limits. During highway operation in the flat section of the road the speed is mostly constant and is only affected by the speed limit between kilometers 26 and 32.

This optimal speed profile is also compared to the speed trajectory that

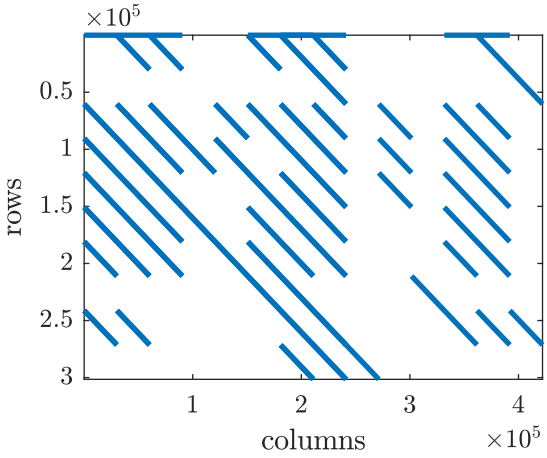

Figure 7.1: Jacobian matrix of the transcribed NLP (corresponding to the first step OCP). Blue dots are non-zero elements, whose number is 3768890, a 0.003% of the total number of matrix elements.

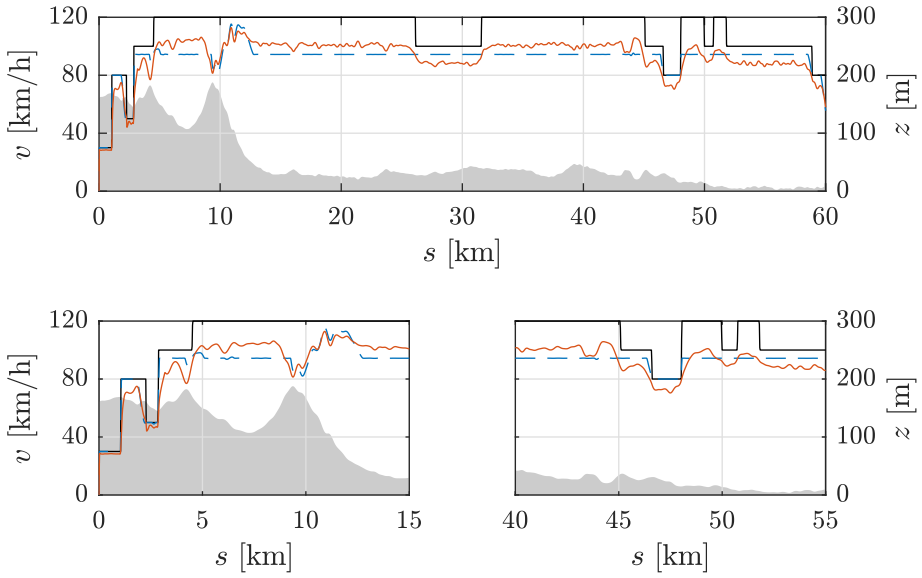

Figure 7.2: Baseline case optimal speed trajectory (in red). Road speed limits are shown in black while the blue dashed trajectory corresponds to the minimum mechanical energy consumption speed. The road altitude profile is overlaid in gray. The first 15 km and the 40 to 55 km portion are zoomed in at the bottom plots for better better appreciation of road grade (left) and speed limit (right) effects.

Fuel consumption	1.91 kg
Min margin to speed limit	$0.03 > 0$ km/h
Average speed	$88.8 > 88.7$ km/h
Max turbo speed	$146 < 200$ krpm
Min λ_e	$1.31 > 1.30$
NO_x emissions	10.8 g
Optimization CPU time	88 seconds

Table 7.2: Summary of baseline case optimization results.

minimizes the mechanical energy consumption at the wheels level–shown with a blue dashed line. Briefly, this problem consists in minimizing the cost index:

$$J = \int_0^{\mathcal{T}} F_t(t)v(t)\,\mathrm{d}t \tag{7.16}$$

where F_t is the traction force. This is a simple OCP whose only state is the vehicle speed, with traction and braking forces as controls and involving just the vehicle dynamics equation. This problem is solved with a DC method as well. It is clear that the minimization of the energy consumption is not equivalent to the complete OCP as long as it does not take into consideration the effect of engine performance and the potential benefit of driving at efficient engine points–which do not necessarily correspond to minimum mechanical energy.

The steep road grades in the first 15 kilometers have a strong impact on the optimal speed profile as it may be appreciated at the zoomed detail in the bottom plot of figure 7.2. Compared to the minimum energy speed, the vehicle prepares to the uphill with an increased initial speed at $s = 8$ km. Then, the speed decreases uphill to avoid a high load operation that may spoil engine efficiency, reaching the minimum at the very top. During the downhill the vehicle gains speed, transferring potential to kinetic energy in such a way that speed approaches the limits but does not violate the constraints.

The corresponding optimal control trajectories from the OCP can be represented in an engine map as shown in figure 7.3. Note that actually the optimal controls u_{egr} and u_{vgt} are not displayed on this figure but the two main quantities that are affected by the control, *i.e.* the fresh air mass flow $\dot{m}_c$ and the intake manifold p_2, in order to be consistent with the traditional ECU control approach. It may be appreciated that those quantities are essentially a function of engine speed and fueling rate. In some particular regions different values are shown at the same operating point–especially at high loads–but the

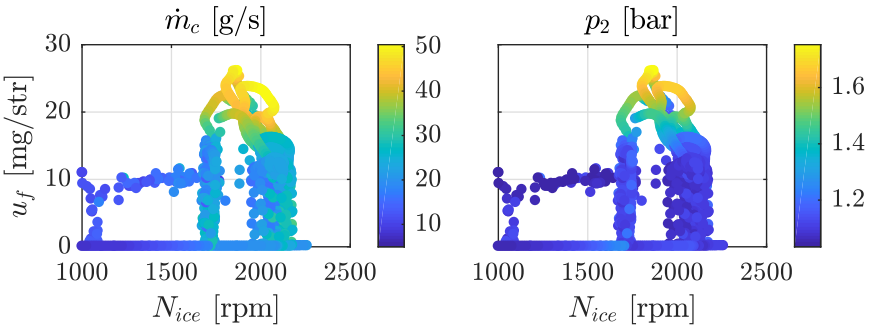

Figure 7.3: Engine fresh air mass flow $\dot{m}_c$ and intake manifold pressure p_2, corresponding to the baseline optimal solution, listed by engine speed and fueling rate. These quantities are displayed as a reference of the control trajectories. These results suggest that the optimal control strategy might be represented by a fixed calibration for this particular cycle.

optimal engine control for this cycle can be potentially mapped into a fixed calibration.

The OCP has been constrained to two different NO_x levels in order to study its effect on the vehicle control. The problem has been solved with Euro 5 and Euro 6 regulations NO_x limits–180 and 80 mg/km respectively. Figure 7.4 shows the Euro 5 speed trajectory in red and Euro 6 in blue. According to figure 7.5, both NO_x limits show no significant differences in engine control variables. Engine operating points are different–see the different speed trajectories–as long as the problem requirements change, but setpoints remain the same. This shows that engine control policy is trying to decrease NO_x emissions regardless of the limit because this reduction is almost for free compared to the effect of the speed profile (in section 6.3 it was shown that an optimal engine policy allows big NO_x reductions with low impact on fuel efficiency). On the contrary, the tightest NO_x limit strongly affects the optimal speed trajectory. High loads are avoided at the Euro 6 trajectory in order to keep low NO_x emissions. Consequently, the speed is significantly reduced when facing any positive slope. It may be appreciated that all uphills match a reduced blue speed compared to red. Therefore, the engine control does not have much impact on the vehicle efficiency and NO_x emissions but speed optimization plays a major role for a given engine technology.

The time constraint–or similarly the average cruising speed–is a key point for the speed profile optimization. Fuel consumption and average speed are strongly correlated since a higher speed produces increased losses. For example, arriving one minute before to the final destination–which is equivalent

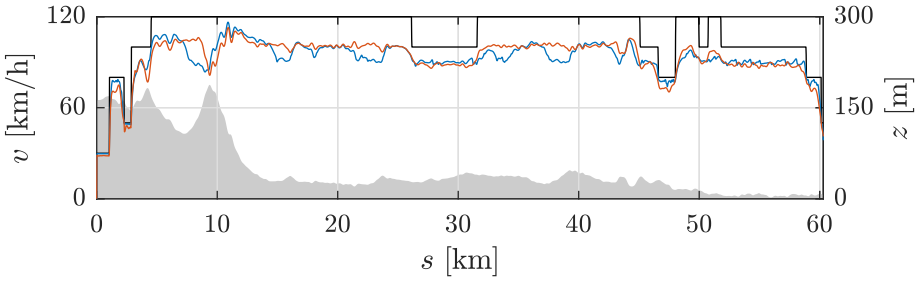

Figure 7.4: Optimal speed trajectory with Euro 5 (red) and Euro 6 (blue) NO_x constraints. Speed limits are shown in black and the road altitude profile in gray.

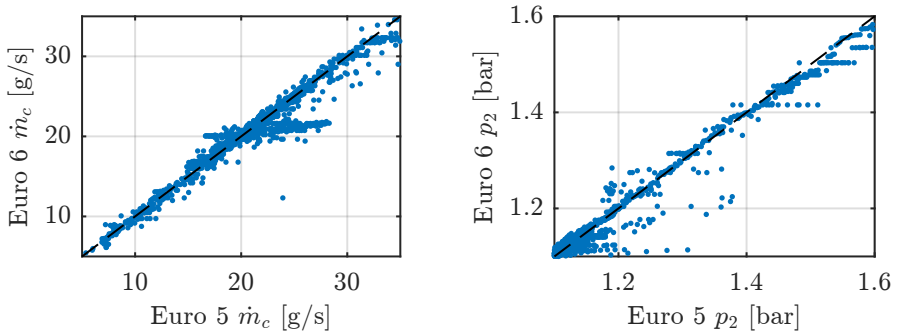

Figure 7.5: Fresh air mass flow $\dot{m}_c$ (left) and intake manifold pressure p_2 (right) correlations for optimal setpoints between Euro 5 and Euro 6 NO_x limits. The correlated setpoints correspond to actuations in the same (N_{ice}, u_f) engine operating point.

to an increase of 2 km/h on the average speed in the current cycle–carries approximately 50 grams of additional fuel consumption if NO_x emissions are held at the same level, according to the results shown in figure 7.6. In order to put this number into perspective, 50 grams is around a 3% of the total fuel consumption, *i.e.* a penalty of 0.1 liters per 100 km. In the worse case of a 4 minutes difference in this 40 minutes trip, the fuel consumption may be increased in 0.3 liters per 100 km.

The tradeoff between fuel consumption and average cruising speed from figure 7.6 has been calculated for two different NO_x levels: Euro 5 (180 mg/km) in blue and Euro 6 (80 mg/km) in red. It is interesting that, while model corresponds to a Euro 5 engine, both Euro 5 and Euro 6 regulation emission

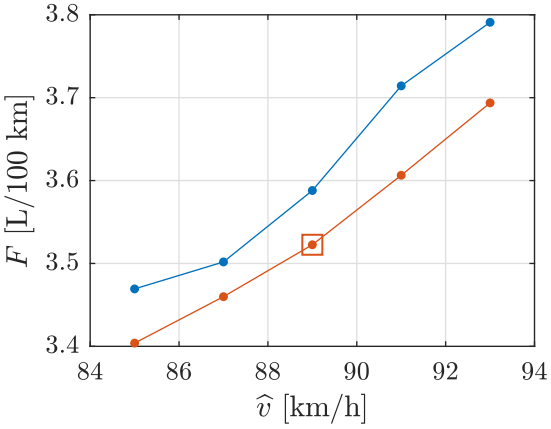

Figure 7.6: Tradeoff between average cruising speed–inversely proportional to trip duration–and fuel efficiency. Red data corresponds to simulations with Euro 5 regulation NO_x emission constraint (180 mg/km) while blue corresponds to Euro 6 values (80 mg/km). The square denotes the baseline case.

levels can be assessed with the appropriate speed control in an actual driving cycle, pointing out the importance of vehicle OC. Of course the reduction of NO_x emissions is not free and it carries a penalty in fuel consumption as shown in figure 7.6. It may be appreciated that in order to reduce emissions from Euro 5 to Euro 6 levels in this driving cycle, it is necessary to decrease the average speed in 2 km/h (with a similar fuel consumption) or to penalize fuel efficiency with additional 0.1 liters per 100 km while holding the same trip time.

Another interesting analysis can be drawn from the Pareto front shown in figure 7.7. This shows the correlation between fuel efficiency and NO_x emissions. All these results are obtained with the same problem constraints and the only difference is the NO_x limit, which ranges from nearly Euro 4 levels (250 mg/km) to Euro 6 (80 mg/km). The engine, the route and the time constraint are identical. This Pareto front is similar to that from the previous chapter (figure 6.15) where only engine control optimization was issued. In fact, results are close despite the driving cycle used in the previous work was a subset of the current route. It should be remarked that NO_x emissions are strongly affected by the speed management. This is not new, since in section 6.3 it was found experimentally that only by applying OC to the engine control, huge differences in emissions were measured. In this case, the possibilities are even wider, with NO_x emissions reduced by a factor of 3.

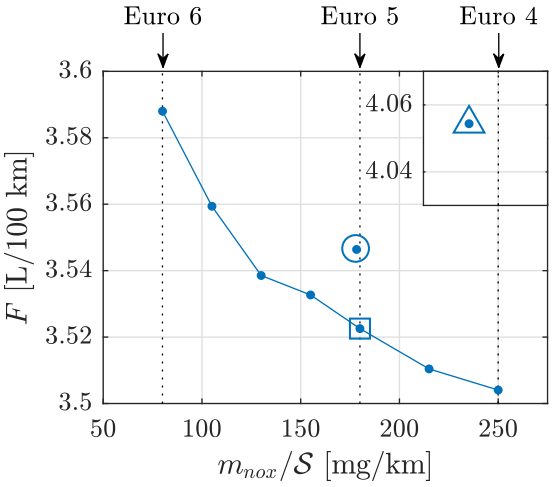

Figure 7.7: Pareto front showing the tradeoff between fuel efficiency and NO_x emissions. All cases take the same time to reach the destination. The square is the baseline case where engine control and speed management are into the OCP, the circle replaces the engine OC with a fixed calibration based on the optimal trajectories, and the triangle–which is on a different y-axis–uses the factory calibration instead. Euro 4, 5 and 6 regulations NO_x limit are shown with dotted vertical lines.

On the contrary, there is not too much room for improvement regarding fuel consumption, which is something that was also found in the previous chapter. As it can be appreciated in figure 7.7, while NO_x may be reduced to less than a half, fuel efficiency only gets penalized by an additional 0.05 liters per 100 km.

In addition to the above, figure 7.7 also shows the results with fixed calibration instead of using optimal trajectories for EGR, VGT and SOI. The square is the baseline case with OC applied to both speed management and engine actuators control, the circle exchanges the OC engine management for fixed maps specifically calibrated for this cycle (maps are obtained from the optimal control trajectories as shown in figure 7.3), and the triangle uses the factory engine calibration. The specified NO_x constraint is the same for all three cases (Euro 5) but factory calibration failed to fulfill both emissions and time limits together, so NO_x constraint was relaxed to Euro 4 levels (250 mg/km). As expected, fixing a mapped calibration–based on the optimal trajectories form the OCP–does not entail a significant penalty in fuel consumption neither NO_x emissions (less than 0.03 liters per 100 km). However, the factory calibration shows a much more inefficient operation–with

a 0.53 liters per 100 km penalty–despite the speed profile is optimal for that route and engine. This is because, on the one hand, the optimal engine control in combination with optimal speed management can be potentially mapped and, therefore, a fixed calibration constructed from the optimal trajectories may perform similarly. On the other hand, the factory calibration is not specifically designed for this route since it must perform satisfactorily in many different situations, so it cannot exploit the particularities of this cycle and benefit of a more efficient speed trajectory.

7.6 Conclusions

The control of engine actuators and the speed management of a vehicle are stated as a joined OCP. A DC method provided the solution to this problem for several levels of NO_x and average speed in an actual route.

The main conclusion of this work is the importance of an optimal speed control in order to minimize fuel consumption and emissions. The use of a joined engine and speed OC management showed that a wide range of emission levels are affordable with the appropriate controls. In this case, Euro 4 to Euro 6 levels have been reached with an experimentally validated Euro 5 engine model. This suggests that there are lots of room for improvement on the emissions side when speed is managed efficiently. Fuel consumption can also be improved but benefits are moderate.

Another remarkable conclusion is that the optimal engine control can be somehow mapped to a fixed calibration, showing a similar performance. The use of such specific engine calibration is key to benefit from an optimal speed control. Factory calibration exhibited a performance significantly worse in both emissions and fuel efficiency as long as it is not specifically designed for the route used at this study. According to this, the speed optimization problem is strongly coupled to the engine optimal control. The decoupling of vehicle dynamics and engine optimization problems may help in the proper direction but it is far from being optimum. In fact, route-specific engine calibrations are a result of the coupled problem. Therefore OC may be a valuable tool to calculate those calibrations.

References

[1] F. Mensing, R. Trigui, and E. Bideaux. “Vehicle trajectory optimization for application in ECO-driving”. In: *IEEE Vehicle Power and Propulsion Conference*. 2011, pp. 1–6.

[2] W. Dib et al. "Evaluation of the energy efficiency of a fleet of electric vehicle for eco-driving application". In: *Oil & Gas Science and Technology – Revue d'IFP Energies nouvelles* 67.4 (2012), pp. 589–599.

[3] W. Dib et al. "Optimal energy management for an electric vehicle in eco-driving applications". In: *Control Engineering Practice* 29 (2014), pp. 299–307.

[4] E. Ozatay et al. "Cloud-based velocity profile optimization for everyday driving: A dynamic-programming-based solution". In: *IEEE Transactions on Intelligent Transportation Systems* 15.6 (2014), pp. 2491–2505.

[5] A. Sciarretta, G. De Nunzio, and L. L. Ojeda. "Optimal ecodriving control: energy-efficient driving of road vehicles as an optimal control problem". In: *IEEE Control Systems* 35.5 (2015), pp. 71–90.

[6] A. Wächter and L. T. Biegler. "On the implementation of an interior-point filter line-search algorithm for large-scale nonlinear programming". In: *Mathematical Programming* 106.1 (2006), pp. 25–57.

Chapter 8

Optimal power-split of a hybrid electric vehicle under driving cycle uncertainty

Music is the silence between notes.

— Claude Debussy

Contents

8.1 Introduction

HEVs are an attractive option to reduce fuel consumption and pollutant emissions in vehicles [1]. Instead of enhancing engine technology or engine control as discussed in previous chapters, hybrids include devices to improve the way the engine is operated. Particularly, HEVs feature an additional

electric path that complements the conventional engine, showing three main ways to increase global efficiency [1]:

- Engine is off during stops and at low speeds as long as the electrical motor is sufficient to move the vehicle at those situations.
- Braking energy is recovered and stored in the battery for future use.
- Engine works at efficient operating regions avoiding low loads, which are covered with the electrical motor.

The benefit in both fuel and emissions performance comes at the expense of a more complex powertrain. A HEV features two different energy sources–fuel tank and battery–which entail a new degree of freedom. Besides the usual controls, the amount of energy that may be supplied by each source to fulfill the driver or driving cycle requirements is an additional decision to take. The split between the energy sources, known as power-split, may be controlled with heuristic rules but it is actually strongly affected by the particularities of the driving cycle [2]. For example, it might be interesting to deplete the batteries in an uphill if later there is a downhill to charge them; however, if the road becomes flat or a second uphill follows the first, it could be better to save some battery before. This is something an heuristic control cannot be aware of.

OC is a valuable tool to calculate the optimal split control that exploits the benefits of the hybrid architecture. It is specially attractive for laboratory analysis where the driving cycles are known in advance. In fact, this topic has been extensively addressed in literature [3–9]. Unfortunately, in an online application things get more difficult as long as further driving information is unknown on real time. Some authors proposed several techniques to apply OC in combination of closed-loop controllers [10–13]. These guarantee a robust operation under some kind of optimality. However, they are not true predictors of future requirements and, therefore, cannot provide an efficient operation exploiting the particularities of the current driving cycle.

This work proposes a methodology to estimate future driving conditions based on a statistical quantification of the driving style. This technique is applied to OC theory in order to provide an optimal power-split in online applications where no information is known in advance.

8.2 Problem description

Power-split control is a key point to exploit the benefits of HEVs with an efficient management of the available energy resources. The corresponding

OCP, *i.e.* the EMP, is extensively addressed in literature with many different approaches [14–18]. However, this problem is difficult to face in online applications due to the lack of future information [2]. Many approaches provide benchmarking information for offline analysis [19], or closed-loop controls at the expense of jeopardizing the optimal power-split [10–12]. Those are interesting techniques to improve HEV operation, but their efficiency in online implementations is questionable.

The aim of this work is to provide a different OC approach to the EMP with a simple methodology to estimate future driving conditions. The current driving style is characterized by means of a histogram-based statistical analysis of the energy requirements, following the scheme of [20]. This information is used to address the OCP on real time with no future knowledge. The methodology is applied to the series HEV from setup D. This vehicle is a simulation model built with manufacturer's data and, therefore, this work is a theoretical study due to the unavailability of the actual HEV. The quasi-steady models used to represent the powertrain are described at sections 4.3.3, 4.4.1, 4.4.2 and 4.5.7, and the vehicle dynamics at section 4.2. The performance analysis of the proposed methodology is carried out with city and highway real driving cycles, recorded from two non-professional drivers at the same route.

8.3 Problem formulation

The EMP consists on finding the power-split control law u_{ps} that minimizes the HEV fuel consumption. Therefore, the following cost index applies:

$$J = \int_0^{\mathcal{T}} \dot{m}_f(\boldsymbol{x}, u_{ps}, t)\,\mathrm{d}t \tag{8.1}$$

According to the quasi-steady approach of the model and assuming that the driving cycle is known so far, the only state of the problem is the battery SoC. The control may be any variable defining the power-split among the two energy sources. For convenience, the battery current is chosen as a control:

$$u_{ps}(t) = i_b \tag{8.2}$$

The dynamics of the state, *i.e.* the battery, are driven by (4.37). Applying the definition of SoC from (4.39), the state equation may be also written as:

$$\dot{\zeta} = -\frac{i_b}{Q_{b,0}} \tag{8.3}$$

The OCP is constrained to produce a solution that follows the specified driving cycle. For given speed and road profile trajectories, the total power requirements $\widetilde{P}_m(t)$ are known in advance. Therefore, the powertrain output must meet that value:

$$\widetilde{P}_m - P_m \leq 0 \tag{8.4}$$

where P_m is the power output of the traction motor. The inequality sign appears because brakes can ultimately be used if power output exceeds the requirements. Also, the power-split must verify energy conservation introducing an additional constraint as discussed in 4.3.3:

$$P_g + P_e - \frac{P_m}{\eta_m} = 0 \tag{8.5}$$

with P_g and P_e the power output of the generator and battery respectively.

Finally, the variation in battery SoC must be constrained. Otherwise, it will be depleted at the end of the cycle, compromising the efficiency of the following one. The common policy is to demand that SoC is held at the same level between the start and the end of the route. This can be represented with a state terminal constraint:

$$\zeta(\mathcal{T}) - \zeta(0) = 0 \tag{8.6}$$

This constraint is of course arbitrary and may be set to a different value with almost no changes in the formulation.

8.4 Optimization approach and implementation

The SoC describes the dynamics of the OCP from the previous section. Despite the influence of the SoC on battery performance may be significant, it is quite interesting from the formulation point of view to neglect this effect. This assumption might be excessive for a PHEV since battery depletion and full charge are part of the normal operation and battery performance is strongly variable. However, variations in charge are narrow in a charge sustaining HEV and battery performance is somehow constant [18], so this assumption may be just fine. According to this simplification, the SoC vanishes as a state of the problem and, therefore, the OCP has no states. Instead of that, there is a new integral constraint replacing the terminal state condition from (8.6):

$$\int_0^{\mathcal{T}} \zeta(u_{ps}, t)\, \mathrm{d}t = 0 \tag{8.7}$$

This integral constraint can be adjoined to the cost function as discussed in section 3.3.2. Therefore, the extended cost function L results in:

$$L = \dot{m}_f(u_{ps}) + \mu\dot{\zeta}(u_{ps}) \tag{8.8}$$

As no states are considered in this last OCP, μ is a constant multiplier (see section 3.3.2 for a detailed discussion on this) that fulfills (3.30). Note that time dependency also vanishes due to the lack of states.

This problem is specially well fitted for PMP since there are no states and only one Lagrangian multiplier μ that, in fact, is constant. The Hamiltonian, defined in (3.15), is exactly the above cost index due to the lack of states. The application of PMP to this particular problem with the above battery simplification is known as ECMS [5, 21]. The reason for this name is that (8.8) may be interpreted as the minimization of not only fuel consumption but a weighted sum of the fuel and the battery contribution–under this hypothesis $\dot{\zeta}$ is the instantaneous battery consumption. Battery energy does not actually come for free but from the recovery of mechanical energy that ultimately came from fuel. Due to this, the OCP consists in minimizing the contribution of both energy sources. The multiplier μ weights for the different costs of both sources: if μ decreases, battery becomes cheaper at (8.8) and the control will deplete it faster; otherwise, if μ value raises, electrical energy is more expensive for the cost index so battery use will be reduced.

PMP is also the method of choice because it is the only optimization algorithm that solves the problem in a forwards step-by-step fashion; both DP and DMs require the complete problem to be considered for an optimal solution. From an online application point of view, PMP is interesting as long as the solution is calculated sequentially from $t = 0$ to $t = \mathcal{T}$, and therefore the problem can be solved on real time. In addition to that, μ is the only unknown to the problem with PMP, and once it is found the solution is straightforward. Then finally, the original OCP consisting on calculating the optimal power-split control has been translated into an equivalent problem where the unknown is just a constant parameter. The solution of this problem is trivial if the cycle is known in advance; μ may be found by shooting or any other optimization algorithm in order to fulfill the integral constraint (8.7), or even analytically by solving (3.30) whenever is possible. However, in an online application the cycle is unknown and the choice of the appropriate μ value gets complicated, so it should be estimated in some manner.

The key point of this work is to propose a methodology to obtain an optimal μ value based on cycle requirement estimations. This value should guarantee charge sustainability (or any other level of battery charge/depletion) within a limited time. For the estimated μ value, PMP is used to solve (8.8) and

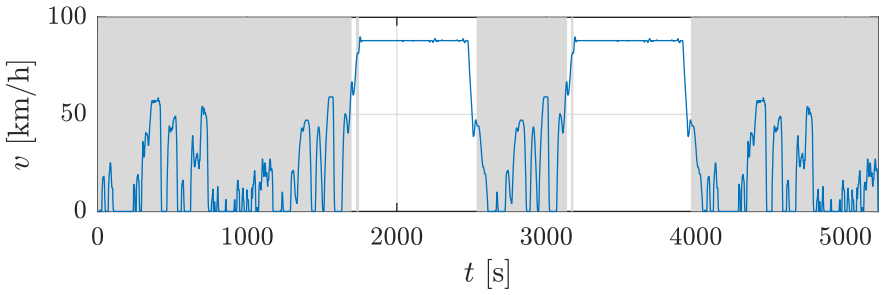

Figure 8.1: Driving style and cycle parameters recognition via histogram comparison. Gray areas correspond to city driving.

the optimal control trajectory that minimizes fuel consumption is calculated. The constrain (8.7) might look too restrictive or arbitrary, specially because in an online application it is difficult to say where the end of the cycle is. Due to this fact, the integral condition is managed somehow differently as long as $t = \mathcal{T}$ is unknown. The constraint is relaxed and the charge sustaining is not specified at any particular moment but at the end of a forwards horizon. Therefore, the control does not force a terminal battery level but constantly keeps track of it.

8.4.1 Histogram-based μ estimation

The optimal power-splitting policy in the current EMP is only determined by the instantaneous power demand. This requirement together with the cost balance that draws from (8.8) define unequivocally the optimal control for a given μ. Therefore, driving pattern may be characterized attending only to the power demand. To do so, a probability distribution is built from the history of power demands, *i.e.* a histogram.

This probability distribution contains information dealing not only with driving style but also with traffic and road related information. In [22, 23] probability distributions have demonstrated their potential to recognize driving patterns as well as different types of roads. In fact, just comparing similarities between previously trained histograms $\Pr(P_m)$ different driving styles can be detected. In figure 8.1 a cycle was built with the sequence urban/highway/urban/highway/urban and driving cycle parameters recognition via histograms was applied to identify both urban and highway parts. A further discussion on this topic is available in [23].

The OCP at hand–the EMP–consists on minimizing the cost index (8.8).

PMP reduces this problem to the instantaneous minimization of the Hamiltonian which, in this case, is the cost index itself:

$$\min_{u_{ps}} \left\{ \dot{m}_f(u_{ps}, P_m) + \mu \dot{\zeta}(u_{ps}, P_m) \right\} \tag{8.9}$$

Note that the dependency on the power requirements P_m–a disturbance to the problem–is denoted explicitly to clarify the formulation, while it was implicit on previous instances of the cost index. The absence of a time reference due to the lack of states allows to replace the power requirement time trajectory P_m for its unique values from the probability distribution $\Pr(P_m)$. P_m becomes, then, the independent variable of the OCP. This approach yields to the minimization of the Hamiltonian for different levels of power requirements P_m, also fulfilling the integral constraint (8.7) which turns into:

$$\int_{-\infty}^{\infty} \Pr(P_m) \cdot \dot{\zeta}(u_{ps}, P_m) \, \mathrm{d}P_m = \nabla\zeta \tag{8.10}$$

where the constraint is weighted with $\Pr(P_m)$ to account for the number of occurrences of different P_m levels as power requirements that occur the most have a stronger impact on the SoC variation. Note that this philosophy is equivalent to the change of the problem domain from time to P_m. The quantity $\nabla\zeta$ should be zero as deducted from (8.7), but in an online application there are no clues about where the final destination is. Instead of that, the integral constraint might be specified for a forwards horizon Γ_f of arbitrary length such that $\zeta(t + \Gamma_f) - \zeta(0) = 0$. Therefore, $\nabla\zeta$ ends up as:

$$\nabla\zeta(t) = \frac{\zeta(0) - \zeta(t)}{\Gamma_f} \tag{8.11}$$

The only thing still to be found is the appropriate value of μ such that $\nabla\zeta$ is satisfied. Figure 8.2 illustrates $\nabla\zeta$ values at different levels of μ for a given histogram. Then, the optimal control may be calculated for a given power requirements histogram by applying PMP at every single time instant. This calculation is continuously updated throughout the cycle as illustrated in figure 8.3: power requirements histogram is constructed with data form a receding horizon Γ_r, μ is found such that the current $\nabla\zeta$ is fulfilled, and PMP–or the mapped solution at figure 8.4–is applied to calculate the optimal power-split.

It is remarkable that for a given μ, the control is only a function of instantaneous P_m values since time vanished from the problem. This gives the opportunity to map it for online applications as done for figure 8.4. On the contrary, μ depends on the battery drift and histogram–which is a function–so it should be calculated online applying eqs. (8.9) and (8.10).

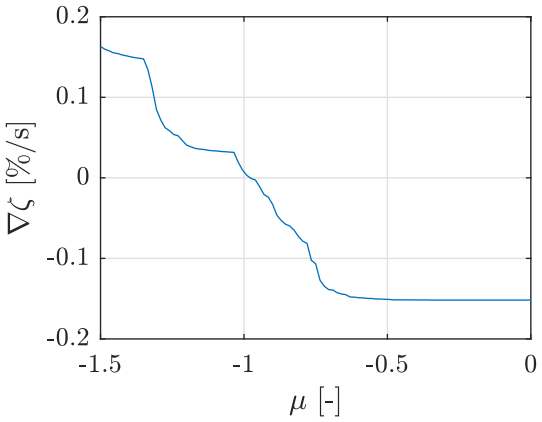

Figure 8.2: $\nabla\zeta$ levels that can be achieved at the integral constraint (8.10) for different values of μ. This curve is calculated for a given power requirements histogram. Note that $\mu = -0.98$ holds the level of charge along any cycle with this same histogram; values to the left charge the battery up to 0.15%/s while values to the right produce a battery depletion of the same order.

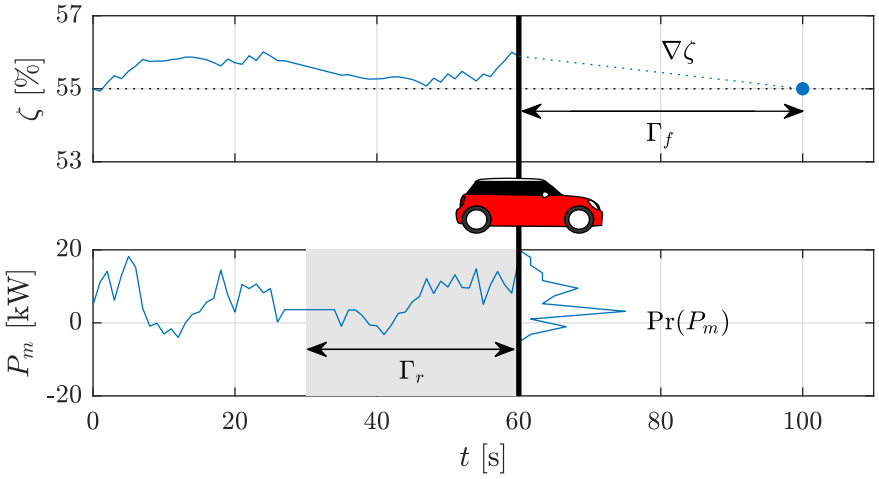

Figure 8.3: Solving sequence of histogram-based control approach. The SoC (top plot) is continuously monitored and the gradient $\nabla\zeta$ to reach the terminal value (dotted horizontal line) is controlled at a forwards horizon Γ_f. The power requirements (bottom plot) from a receding horizon Γ_r (shadowed in gray) are used to compute an histogram (on the right side). This histogram and the optimal control from map in figure 8.4 enables the calculation of the μ tradeoff shown in figure 8.2. Then, the choice of the appropriate μ value is trivial and the optimal control can be calculated for the next time step.

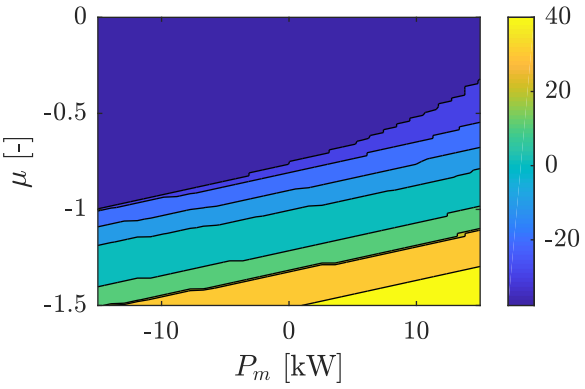

Figure 8.4: Optimal battery current as a function of power requirements P_m and the constant Lagrangian multiplier μ. This map is a result from the application of (8.9). The color scale is shown in amperes.

8.4.2 Histogram geotagging

A power requirement histogram contains information regarding driving style and road type, but it can only store one pattern–or several mixed together. However, very different styles may be found in just one trip. As an example, in figure 8.5 power demand histograms have been calculated along the route each 150 meters and, following the philosophy of [22], they are grouped attending to their similarities (how much area they share); some examples of these histograms can be found in the right plot of this same figure. Several contrasts may be appreciated in different parts of the same trip. Driving through main avenues show histograms with significant peaks for medium power demands while lower power requirements and more regeneration potential is appreciated in small streets. Attending to this, it might be interesting to apply the histogram-based PMP approach with a set of histograms corresponding to different locations instead of just one single driving pattern. This is a similar approach to that used to characterize and predict traffic conditions on Google Maps [24].

A set of geographically located power demand histograms can be easily built by means of in-car sensors and a GPS receiver. For this purpose, the relevant geographic area is discretized into individual clusters. The proposed approach works as follows: as the vehicle drives through a cluster, power requirements are stored on it; later, when the clusters are trained, the current location-based histogram is calculated weighting the four closest clusters according to their distance to the vehicle. This technique is depicted in figure 8.6. The route may be known in advance with ease just by requesting it to the driver in a

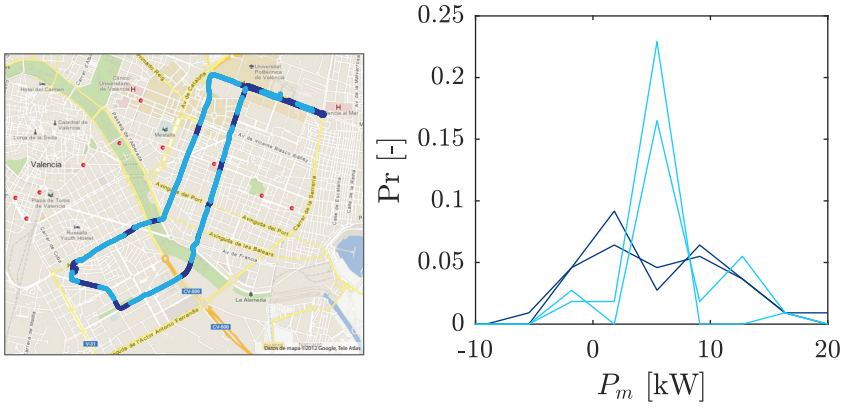

Figure 8.5: Different histograms–driving styles–that can be found in a single trip. Dark blue corresponds to an average of 2 kW and light blue to 5 kW. Their geographic distribution is displayed in the left plot, and some examples of these histograms are shown in the right plot.

navigation system, so a set of histograms for that particular trip might be known in advance.

The histogram-based approach can be applied to this methodology in a quite straightforward way. Assuming that a set of location-based histograms $\Pr(P_m, s)$ are available with the already described technique, those can be summarized into a single histogram that accounts for the patterns in a forwards horizon Γ_f:

$$\Pr(P_m) = \frac{1}{\Gamma_f} \int_t^{t+\Gamma_f} \Pr(P_m, s(t))\, \mathrm{d}t \tag{8.12}$$

The resulting histogram, weighted according to location, can be introduced seamlessly into eqs. (8.9) and (8.10) and EMP may be solved analogously to the previous approach.

8.5 Results and discussion

The histogram-based PMP approach and its location-based variation are applied to an actual driving cycle. The histograms have been trained before with four driving cycles covering the same route than the simulated cycle. No lookahead information different from the histogram is available during simulation to be representative of on an online application. In addition to that, the EMP is also addressed with DP–in this case with full knowledge of

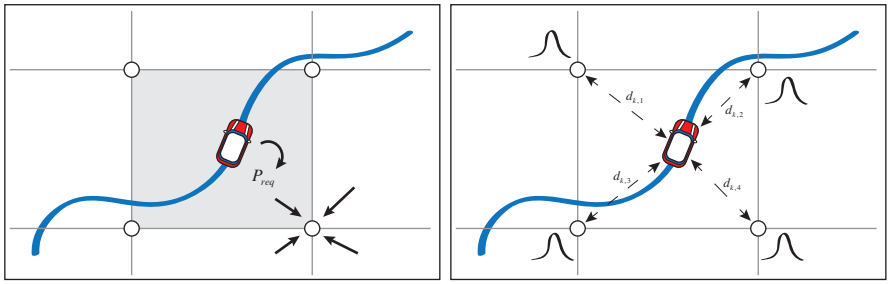

Figure 8.6: Methodology to gather and retrieve location-based histograms. Power requirements are stored in clusters during normal driving (left), and then the information from the four closest clusters is weighted with vehicle distance to construct a location-based histogram (right).

the cycle to optimize–in order to provide a benchmarking solution to compare to. Results for key variables are shown in figure 8.7.

The proposed methods show a near-optimal solution. Compared to DP solution, histogram-based approaches result in an almost identical fuel consumption despite some differences in the SoC management. Note that the OCP addressed with these approaches feature a slightly different SoC constraint because the terminal value is tracked to be permanently fulfilled within a forwards horizon. Due to this fact, the SoC trajectory is kept on the surroundings of this terminal value. It might be appreciated in the top plot at figure 8.7 that the histogram-based approach (red) is always close to $\zeta(\mathcal{T}) = 55\%$, falling in the $\pm 3\%$ band. The location-based method (yellow) shows a similar behavior although its greater knowledge of the cycle (destination and more accurate power requirements estimation) allows a looser–and potentially better–management. On the contrary, DP approach (blue) does not show that *anxiety* to hold the terminal value as long as it is fulfilled at $t = \mathcal{T}$, resulting in a wider SoC variation. Of course, the results shown here are just an example since horizon length might be tuned to modify the effect of this *anxious* behavior.

A very tight fulfilling of the integral constraint–terminal SoC value–can be appreciated as well. The continuous evaluation of $\nabla\zeta$–see eqs. (8.10) and (8.11)–works as a closed-loop controller that tracks the desired SoC level with an optimality criterion. It allows to correct misestimations in real time, even without lookahead information, providing a robust and stable operation.

The use of geographical information to geotag different driving requirements showed no significant advantages in this example, offering near the same solution with similar performance. This negligible improvement is due to three

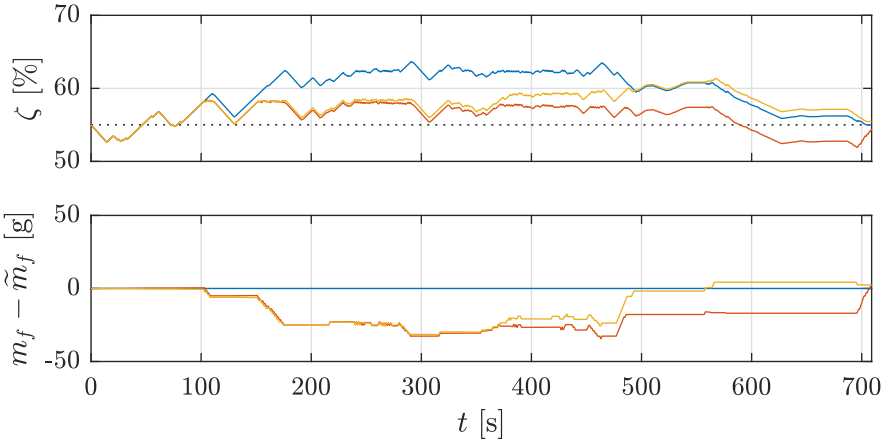

Figure 8.7: Application of the histogram-based (red) and location-based (yellow) approaches to the EMP. DP results (blue) are included as benchmark trajectories. The top plot shows the SoC evolution throughout the cycle. Integral constraint must fulfill the final SoC value denoted with a dotted line. Bottom plot shows the accumulated fuel consumption compared to DP results. Negative values correspond to a fuel consumption lower than DP solution.

factors: first, the homogeneity of the benchmarking cycle makes that specific histograms for diverse locations does not represent a great improvement; second, the availability of four additional driving cycles to train the location-based histograms might not be sufficient to capture individual particularities; and third, both histogram-based approaches and the benchmarking DP solution are so close that performance differences are insignificant. Nevertheless, the additional cycle information gathered with geotagging enables to a better SoC management that may improve the global results in other situations.

8.6 Conclusions

The use of power demand histograms permitted to characterize and estimate the driving requirements when no lookahead information is available. This information can be used to provide an optimal power-split control for HEV based on a simplified approach of the EMP. On the one hand, the proposed methodology to address this OCP shows several implementation advantages that provide a simple and compact formulation to implement an optimal power-split controller:

- The OCP is transformed into a single parameter (μ) optimization problem

under several assumptions, so only μ must be found to provide an optimal control trajectory.

- The parameter μ is only a function of power requirements histogram and current battery SoC drift.
- For a given μ, control is only a function of instantaneous power requirements, so it can be mapped.

On the other hand, this histogram-based approach shows some performance benefits in online applications:

- The integral constraint (8.10) is updated with the continuous evaluation of the battery drift from the desired terminal level. This provides an stable behavior with an optimality criterion.
- Charge sustainability can be fulfilled relaxing the terminal constraint over a forwards horizon.
- Fuel efficiency shows no significant penalty compared to optimal control trajectories where full knowledge of the cycle is used.

References

[1] A. Sciarretta and L. Guzzella. "Control of hybrid electric vehicles". In: *IEEE Control System Magazine* 27.2 (2007), pp. 60–70.

[2] C. Zhang et al. "Role of terrain preview in energy management of hybrid electric vehicles". In: *IEEE Transactions on Vehicular Technology* 59.3 (2010), pp. 1139–1147.

[3] H. Mosbech. "Optimal control of a hybrid vehicle". In: *Proceedings of the International Symposium on Automotive Technology & Automation.* 1980, pp. 303–320.

[4] J. R. Bumby and I. Forster. "Optimisation and control of a hybrid electric car". In: *IEE Proceedings D-Control Theory and Applications.* Vol. 134. 6. 1987, pp. 373–387.

[5] G. Paganelli et al. "Simulation and assessment of power control strategies for a parallel hybrid car". In: *Proceedings of the Institution of Mechanical Engineers, Part D: Journal of Automobile Engineering* 214.7 (2000), pp. 705–717.

[6] S. Delprat et al. “Control strategy optimization for an hybrid parallel powertrain”. In: *Proceedings of the American Control Conference*. Vol. 2. 2001, pp. 1315–1320.

[7] C.-C. Lin et al. “Energy management strategy for a parallel hybrid electric truck”. In: *Proceedings of the American Control Conference*. Vol. 4. 2001, pp. 2878–2883.

[8] G. Paganelli et al. “General supervisory control policy for the energy optimization of charge-sustaining hybrid electric vehicles”. In: *JSAE Review* 22.4 (2001), pp. 511–518.

[9] S. Delprat, T. M. Guerra, and J. Rimaux. “Optimal control of a parallel powertrain: from global optimization to real time control strategy”. In: *IEEE 55th Vehicular Technology Conference*. Vol. 4. 2002, pp. 2082–2088.

[10] A. Sciarretta, M. Back, and L. Guzzella. “Optimal control of parallel hybrid electric vehicles”. In: *IEEE Transactions on Control Systems Technology* 12.3 (2004), pp. 352–363.

[11] C. Musardo et al. “A-ECMS: an adaptive algorithm for hybrid electric vehicle energy management”. In: *European Journal of Control, Fundamental Issues in Control, special issue* 11 (2005), pp. 1816–1823.

[12] S. Onori, L. Serrao, and G. Rizzoni. “Adaptive equivalent consumption minimization strategy for hybrid electric vehicles”. In: *Proceedings of the ASME Dynamic Systems and Control Conference*. Vol. 1. 2010, pp. 499–505.

[13] T. van Keulen et al. “Design, implementation, and experimental validation of optimal power split control for hybrid electric trucks”. In: *Control Engineering Practice* 20.5 (2012), pp. 547–558.

[14] C.-C. Lin, H. Peng, and J. W. Grizzle. “A stochastic control strategy for hybrid electric vehicles”. In: *Proceedings of the American Control Conference*. Vol. 5. 2004, pp. 4710–4715.

[15] L. V. Pérez et al. “Optimization of power management in an hybrid electric vehicle using dynamic programming”. In: *Mathematics and Computers in Simulation* 73.1?4 (2006), pp. 244–254.

[16] L. Johannesson and B. Egardt. “Approximate dynamic programming applied to parallel hybrid powertrains”. In: *IFAC Proceedings Volumes* 41.2 (2008), pp. 3374–3379.

[17] A. Chasse, A. Sciarretta, and J. Chauvin. "Online optimal control of a parallel hybrid with costate adaptation rule". In: *Proceedings of the 6th IFAC Symposium: Advances in Automotive Control*. 2010, pp. 99–104.

[18] L. Serrao, S. Onori, and G. Rizzoni. "A comparative analysis of energy management strategies for hybrid electric vehicles". In: *Journal of Dynamic Systems, Measurement, and Control* 133 (2011), pp. 1–9.

[19] R. Cipollone and A. Sciarretta. "Analysis of the potential performance of a combined hybrid vehicle with optimal supervisory control". In: *Proceedings of the IEEE International Conference on Control Applications*. 2006, pp. 2802–2807.

[20] C. Guardiola et al. "Modelling driving behaviour and its impact on the energy management problem in hybrid electric vehicles". In: *International Journal of Computer Mathematics* 91.1 (2014), pp. 147–156.

[21] L. Serrao, S. Onori, and G. Rizzoni. "ECMS as realization of Pontryagin's minumum principle for HEV control". In: *American Control Conference*. 2009, pp. 3964–3969.

[22] F. Payri et al. "On a stochastic approach of the ECMS method for energy management in hybrid electric vehicles". In: *Engine and Powertrain Control, Simulation and Modeling*. Vol. 3. 1. 2012, pp. 341–348.

[23] F. Payri et al. "A stochastic method for the energy management in hybrid electric vehicles". In: *Control Engineering Practice* 29 (2014), pp. 257–265.

[24] D. Barth. *The bright side of sitting in traffic: Crowdsourcing road congestion data*. Google Official Blog. 2009.

Chapter 9

Applications to powertrain design and assessment

If one does not fail at times, then one has not challenged himself.

— Ferdinand Porsche

Contents

9.1 Introduction

OC is a useful methodology to address designing questions and assess control decisions. Those are immediate applications of OC theory since the OCP

boundary conditions can be accurately identified in laboratory conditions. This methodology enables to approach the development of vehicular systems from an objective perspective, according to the definition of a criteria–a cost function–and a set of requisites–constraints–that is strictly minimized (or maximized) with the application of OC.

The OC-aided designing process can be approached in many different ways. In the context of this dissertation, two methodologies are presented: (i) in section 9.2, OC is used to calculate the HRL optimal trajectory, which is a problem that can be accurately bounded and defined within a cycle, in order to design the injection schedule and to serve as a boundary for the maximum combustion efficiency, and (ii) in section 9.3, OC is employed as a tool for an objective comparison and evaluation of several HEV powertrain scales, exploiting their particularities and showing individual benefits.

9.2 Optimal heat release law

The tradeoff between fuel consumption and emissions is inherently linked to the thermodynamic process that occurs in the cylinder. Energy release and pollutants formation happen during the combustion process, and they are affected by two main factors: the design and characteristics of the engine (injector nozzle, combustion chamber configuration, etc.), and the control law that governs the heat release. Traditionally, simplified thermodynamic processes such as constant volume, constant pressure and limited pressure combustions [1] or more sophisticated Wiebe functions [2] were considered. However, from the OC point of view, it might be much more attractive to calculate optimal combustion processes instead of constraining to predefined laws. OC has already been employed in this topic by [3–5]. The aim of the present work is to find the HRL in an ICE that minimizes fuel consumption with pressure and NO_x constraints, constructing and solving an OCP.

9.2.1 Problem description

The purpose of this work is to obtain by means of OC, the HRL that minimizes the fuel consumption at some given operating conditions, taking into account different mechanical and performance constraints, particularly: the maximum cylinder pressure should be bounded to avoid engine damage; the maximum pressure derivative in the combustion chamber should be also limited to avoid both mechanical issues and noise generation; finally, provided the tradeoff between NO_x and fuel in current Diesel engines, some boundary in the maximum NO_x is to be included to fulfill with emission regulations. The proposed

approach provides both a realistic minimum fuel consumption to compare how optimal is a given engine calibration and also a HRL pattern to follow in order to minimize the engine fuel consumption fulfilling the constraints.

Accordingly, the advantages of the OC approach are twofold:

1. Constraints related to non-energy-based parameters can be taken into account. In this sense, the main advantage of this approach is that it provides a higher bound for the engine efficiency taking into account constraints on maximum cylinder pressure, maximum cylinder pressure derivative and NO_x emissions. Moreover, the framework presented in the following points is completely general and other pollutant emissions (or criteria) can be also included if a suitable model exists.

2. As far as it is optimal, it provides the best possible combustion scenario for comparison. Instead of using arbitrary combustion laws such as constant volume, or Wiebe functions, the OC shows the HRL that minimizes a cost function while strictly fulfilling the problem constraints.

This work is performed on the setup B single cylinder DI CI engine (see 5.2.2). The experimental facility is used to validate the in-cylinder model described in section 4.5.5 and to evaluate the engine performance in comparison with the optimal results provided by the OC approach. The model calibration is performed according to test 7 procedure (see 5.3.7). For this particular study, the key signals recorded are the in-cylinder pressure signal and fuel consumption to compute the ISFC, the air mass flow and intake conditions to compute the gas conditions at the IVC, and the NO_x emissions to assess the emission limits.

Figure 9.1 shows a comparison between measured and modeled ISFC and NO_x emissions. The agreement between these two quantities for the set of tested conditions is in the $\pm 2.5\%$ range, and it increases to $\pm 10\%$ in the case of NO_x emissions. While the model uncertainty in terms of ISFC seems adequate, the error in NO_x may appear excessive. Nevertheless, [6] points out that a variation of $\pm 1\%$ in the estimation of each of the parameters that affect NO_x translates into an error up to $\pm 33\%$ in final NO_x prediction. This extremely high sensitivity is a direct consequence of the involved physic-chemical mechanisms, and it is independent of the type of model used to describe these mechanisms. Therefore, it can be concluded that the accuracy of the presented model is reasonably good.

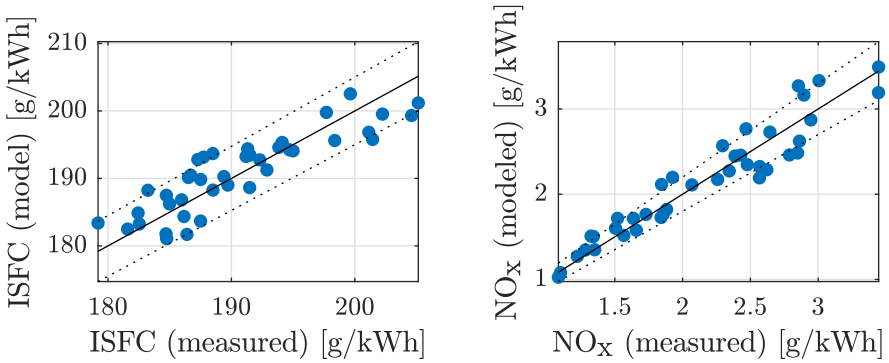

Figure 9.1: Comparison between modeled and experimental ISFC and NO_x emissions. Dotted lines correspond to 2.5% differences in the ISFC and 10% differences in NO_x.

9.2.2 Problem formulation

This OCP consists in finding the sequence of burning rates that minimizes the ISFC over the engine thermodynamic cycle between the IVC and EVO for a given operating point–engine speed, fuel injected and cylinder gas conditions at the IVC (temperature, pressure, composition). Given that:

$$\text{ISFC} = \frac{m_f}{W_i} \tag{9.1}$$

as the fuel injection m_f is included in the operating point definition, minimizing the ISFC is equivalent to maximizing the indicated work W_i. For the sake of formulation simplicity, the last option has been chosen. In addition to that, the optimal burning rate policy should also fulfill the following constraints:

- The maximum cylinder pressure should be below certain limit ($p_{ic} < \widehat{p}_{ic}$) to avoid engine damage.
- The maximum cylinder pressure derivative should be below certain limit ($\mathrm{d}p_{ic}/\,\mathrm{d}\alpha < \widehat{\delta p}_{ic}$) to avoid engine damage and excessive noise generation.
- The amount of NO_x emitted should be below certain limit ($m_{nox} < \widehat{m}_{nox}$). If this constraint is not included, provided the tradeoff between emissions and efficiency, the optimal solution may tend to a combustion with excessive NO_x that would make impossible to fulfill with current emission regulations.

To deal with the previous objective, consider the following general dynamic equation of the system:

$$\frac{\mathrm{d}x}{\mathrm{d}\alpha} = f(x, u, \alpha) \tag{9.2}$$

where the state x is the in-cylinder pressure p_{ic}. The generic function f contains the model from 4.97. The control u is the fuel burning rate u_{fbr} as introduced in (4.98). Note that the usual time reference has been replaced by a crank angle α dependency provided that the engine speed is considered constant. This modification allows to easily deal with the integration limits of the problem (IVC and EVO) for different operating points without any loss of generality.

Consider the OCP consisting in finding the optimal control policy $u^*_{fbr}(\alpha)$ that maximizes the following cost index between IVC (α_i) and EVO (α_e):

$$J = \int_{\alpha_i}^{\alpha_e} L(p_{ic}, u_{fbr}, \alpha)\,\mathrm{d}\alpha \tag{9.3}$$

The function J represents the work developed along the cycle and, therefore, the function L is:

$$L(p_{ic}, u_{fbr}, \alpha) = W_i = p_{ic}\frac{\mathrm{d}V_{ic}}{\mathrm{d}\alpha} \tag{9.4}$$

where the variation of volume with angle is known *a priori* since piston deformations are neglected.

Regarding the problem constraints, the heat released should be limited in order to assure that the fuel burnt during the cycle does not exceed the fuel injected:

$$\int_{\alpha_i}^{\alpha_e} \partial_\alpha q_b(u_{fbr})\,\mathrm{d}\alpha \leq m_f H_f \tag{9.5}$$

The above expression may be reformulated using (4.98) in terms of the control variable:

$$\int_{\alpha_i}^{\alpha_e} u_{fbr}(\alpha)\,\mathrm{d}\alpha \leq 1 \tag{9.6}$$

where obviously, to maximize the indicated work all the fuel injected should be burnt, so the equal sign prevails.

Analogously maximum $\mathrm{NO_x}$ emissions must be accounted with the integral constraint:

$$\int_{\alpha_i}^{\alpha_e} \partial_\alpha m_{nox}(p_{ic}, u_{fbr}, \alpha)\,\mathrm{d}\alpha \leq \widehat{m}_{nox} \tag{9.7}$$

where $\partial_\alpha m_{nox}$ follows the model expression from (4.102).

9.2.3 Optimization approach and implementation

The optimization problem consists of one control variable–fuel burning rate u_{fbr}–and one state–in-cylinder pressure p_{ic}–, with two additional integral constraints that may lead to significant complexity in the solution. According to (3.25), integral constraints can be adjoined to the cost function, vanishing from an explicit formulation. System dynamics can also be adjoined with the introduction of the Hamiltonian function (3.15). Therefore, dynamics from (9.2), and integral constraints in eqs. (9.6) and (9.7) can be summarized in an augmented cost function:

$$H(\boldsymbol{x}, u_{fbr}, \alpha) = L(p_{ic}, u_{fbr}, \alpha) + \lambda^T f(\boldsymbol{x}, u_{fbr}, \alpha) \tag{9.8}$$

This new OCP has three states $\boldsymbol{x} = \{p_{ic}, q_b, m_{nox}\}$, where the two last members follow the dynamics from eqs. (9.6) and (9.7). λ is the costate vector $\lambda = \{\lambda_p, \lambda_q, \lambda_m\}$ whose elements are related to the three states of this problem. According to the discussion carried out in section 3.3.2 and specially to (3.29), costates introduced with an integral constraint are constant. Therefore λ turns to be $\lambda = \{\lambda_p, \mu_q, \mu_m\}$ with μ representing constant parameters.

The advantage of adjoining states to the cost function is that their dynamics are no longer computed separately but through their corresponding costates, alleviating the computational burden of a system with many states. However, the complexity of dealing with three different Lagrange multipliers, even if some of them are constant, usually exceeds the affordability of an OCP with several states. Typically, only problems with a single costate are interesting. Therefore, costates are removed from the Hamiltonian and only μ_m is kept for practical reasons:

$$H(\boldsymbol{x}', u_{fbr}, \alpha) = L(p_{ic}, u_{fbr}, \alpha) - \mu_m \partial_\alpha m_{nox}(\boldsymbol{x}', u_{fbr}, \alpha) \tag{9.9}$$

where $\boldsymbol{x}'$ is the new state vector $\boldsymbol{x}' = \{p_{ic}, q_b\}$ that includes the state relative to the constraint (9.5). Replacing the cost function (9.4) by (9.9) allows to remove one integral constraint from the problem simplifying its solution. However, a proper μ_m value should be selected in order to fulfill the NO_x constraint. Note that the Lagrangian parameter weights the tradeoff between W_i and NO_x emissions in the cost function. If $\mu_m = 0$, the optimization only considers the W_i term, and the solution will tend to a control policy minimizing the ISFC regardless of NO_x emissions. Conversely, at the limit of μ_m tending to ∞, the NO_x emissions will be minimized at any cost. Sweeping μ_m from 0 to arbitrarily high values allows to obtain the Pareto front of the

OCP, *i.e.* the curve where fuel consumption is minimum for a given limit of NO_x emissions.

The small number of states and controls of the problem (2 and 1 respectively) makes it specially well suited for the application of DP (see 3.2.1 for a description of the method and its implementation). The solver used in this work is a MATLAB-based code presented in [7]. The same code has been used previously in [3]. Discretization in both control and states can be checked in table 9.1.

9.2.4 Results and discussion

In this section, the results obtained in the optimization problem are discussed. The problem constraints are progressively introduced, starting from the HRL optimization without constraints, then introducing the constraints on the cylinder pressure evolution (maximum pressure and maximum pressure derivative), and finally adding the constraint on the NO_x emissions.

Optimal HRL without constraints

Consider the OCP presented in section 9.2.1 without NO_x nor pressure restrictions. If the system is considered adiabatic, then the solution is the well known constant volume combustion that essentially consists of an instantaneous combustion (heat release) at the Top Dead Center (TDC). From the control policy perspective, the solution of such OCP is an impulse-like control action, *i.e.* releasing all the available heat instantaneously (with an infinite rate of heat release) at the TDC. Figure 9.2 shows the evolution of the problem states p_{ic} and q_b, the last normalized with the total heat released. The light blue line in figure 9.2 represents the solution provided by the optimization algorithm without constraints and considering the adiabatic system previously mentioned.

This solution clearly matches the constant volume combustion validating the optimization algorithm used. Note the high values of the in-cylinder pressure (280 bar) and pressure derivative (740 bar/°) of the optimal solution that would surely damage the engine in a real application. Figure 9.2 also shows the effect of the heat transfer on the optimal HRL and pressure evolution of the OCP without constraints. A constant factor ϱ has been applied to the heat transfer coefficient from (4.100). It is observed that the higher the heat transfer, the later the optimal combustion appears in order not to reach too high pressures, which, as far as they involve high gas temperatures, lead to important heat losses that jeopardize the engine efficiency. Finally, it can

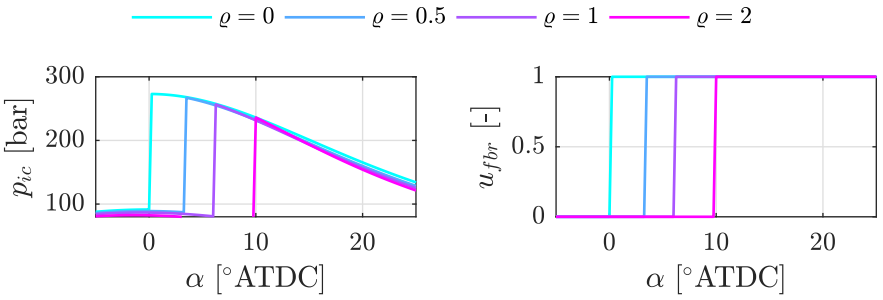

Figure 9.2: Effect of the heat transfer on the evolution of the in-cylinder pressure (left plot) and heat release (right plot) without constraints on maximum pressure nor maximum pressure derivative. The color scale represent the heat transfer coefficient.

be observed that independently of the considered heat transfer, the optimal control policy involves an instantaneous heat release.

The effect of the heat transfer on the minimum ISFC–recall that this case includes no constraints–is described in figure 9.3, resulting in an almost linear relation. The coefficients for the Woschni heat transfer correlations validated by the experimental results in figure 9.1 lead to a fuel consumption of 148 g/kWh (circle in figure 9.3), that sets a boundary for the minimum ISFC of the actual engine that can be achieved if no constraints are considered. The minimum achievable ISFC if the engine were completely adiabatic at the studied operating conditions is 131 g/kWh. Accordingly, the heat transfer involves a penalty of 17 g/kWh. Therefore, despite heat transfer wastes around 30% of the total energy released during the combustion, the improvement of a completely adiabatic engine will be limited to 11.5%, even in the case of not considering pressure restrictions. The remaining 18.5% leaves as exhaust gas energy.

Optimal Heat Release Law with pressure constraints

Figure 9.4 shows the effect of the maximum pressure derivative $\widehat{\delta p}_{ic}$ and the maximum cylinder pressure $\widehat{p}_{ic}$ on the minimum ISFC for different heat transfer hypothesis. It can be observed how, for a given level of heat transfer and cylinder pressure limit, the ISFC is progressively reduced as the pressure derivative limit increases. Particularly, the ISFC tends to a minimum that becomes lower as higher maximum cylinder pressures are considered. Increasing the maximum cylinder pressure typically leads to an increase in the area of the p–V diagram, which naturally drives to higher indicated work and consequently

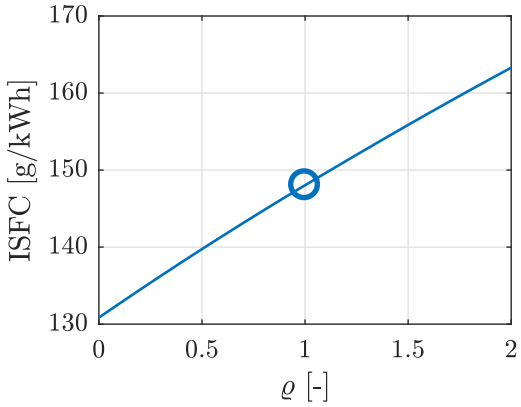

Figure 9.3: Effect of the heat transfer coefficient ϱ on the minimum ISFC without pressure constraints. The circle represents the result for the actual engine parameters.

to lower ISFC. Also, an asymptotic behavior is observed since there is a $\widehat{\delta p}_{ic}$ from which the ISFC is not reduced anymore. The minimum ISFC is reached at lower derivative levels as the maximum pressure is lower as well, since the lower the maximum in-cylinder pressure the sooner it can be achieved.

The effect of the heat transfer on the engine efficiency is shown in figure 9.4. These results are in line with those presented in section 9.2.4 and figure 9.3: the higher the heat transfer the higher the ISFC. However, figure 9.4 also shows that the potential of increasing the maximum cylinder pressure as a method to reduce the ISFC is limited by heat transfer effects. In this sense, increasing the maximum cylinder pressure limit from 140 to 180 bar involves a 3.3% rise in the efficiency of the adiabatic engine, while the same pressure limit increase only leads to a 0.6% improvement in efficiency with the nominal heat transfer ($\varrho = 1$).

The impact of the heat transfer on the optimal HRL and in-cylinder pressure evolution for the constrained OCP is represented in figure 9.5. It can be appreciated that the higher the heat transfer the later the optimal combustion takes place, which is in line with the results obtained in the OCP without constraints. Again, the reason for such behavior is that the earlier the combustion, the higher the pressure and temperature in the combustion chamber, so the higher the heat losses. In fact, provided a maximum in-cylinder pressure of 160 bar and a maximum pressure derivative of 10 bar/°, the optimal solution is to burn the available fuel following the maximum allowed pressure derivative. Then, when $\widehat{p}_{ic}$ is reached the fuel burning rate should be reduced to keep constant the cylinder pressure until all the fuel is burnt. No matter

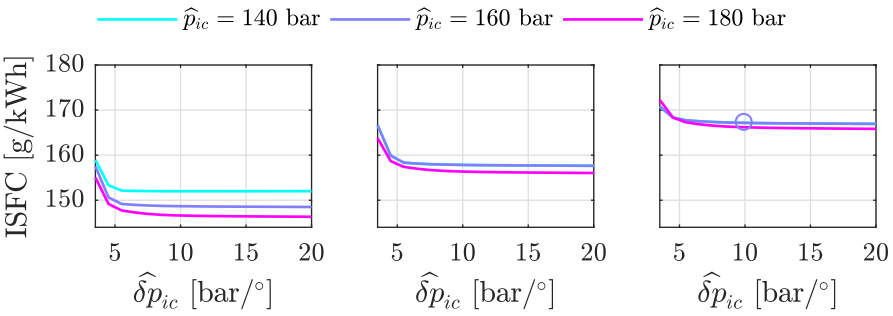

Figure 9.4: Effect of the maximum pressure derivative $\widehat{\delta p}_{ic}$ and maximum in-cylinder pressure $\widehat{p}_{ic}$ on the minimum ISFC. Left: adiabatic engine. Center: engine with half the heat transfer of the nominal engine. Right: Nominal engine (the circle represents the nominal engine with its actual constraints on maximum pressure and maximum pressure derivative).

the importance of heat transfer (between the limits considered in this study), the optimal policy in the evolution of the pressure and heat release remains the same. The only difference is the start of combustion, which, as previously stated, should be delayed as the heat transfer increases.

Concerning the effect of the pressure derivative on the optimal HRL and in-cylinder pressure evolution, figure 9.6 shows that the conditions at the end of the combustion remain independent of the pressure derivative limit imposed–in this case the combustion always finishes at 18°ATDC. Reducing the pressure derivative limit involves an earlier start of combustion. In short, figure 9.6 shows that the optimal combustion process is divided in two main phases. In the first one, the heat release rate is limited by the maximum allowed pressure derivative. The second phase starts once the maximum pressure limit is reached, where the pressure derivative constraint is not active anymore and the maximum heat release rate is limited by the maximum cylinder pressure constraint.

Finally, figure 9.7 shows the effect of the maximum pressure limit on the optimal HRL and cylinder pressure evolutions, for the same heat transfer and pressure derivative limit. In this case, the first stages of the combustion process are not sensitive to the maximum pressure constraint, and the pressure derivative limit governs the optimal heat release law. Given a constant pressure derivative, the lower the maximum pressure limit, the sooner it is reached. Then, once the pressure achieves its limit, the rate of heat release is reduced to keep the maximum pressure until the end of the combustion process, which is delayed as pressure limit decreases.

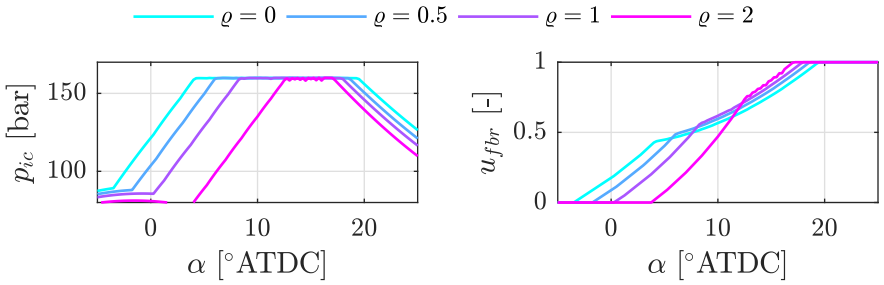

Figure 9.5: Effect of the heat transfer on the evolution of the in-cylinder pressure (left plot) and heat release (right plot). The actual constraints of the nominal engine in terms of maximum pressure and maximum pressure derivative (160 bar & 10 bar/°) have been chosen as reference conditions.

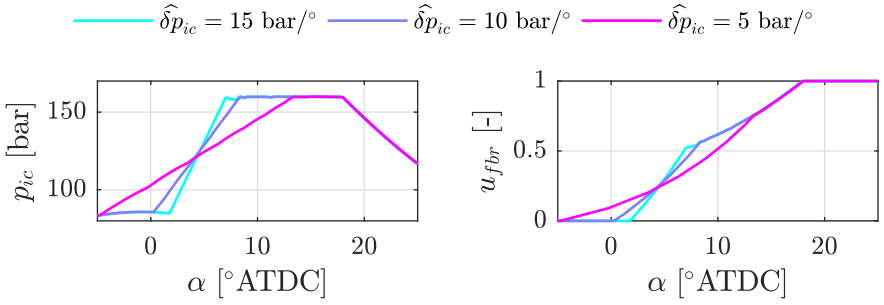

Figure 9.6: Effect of the pressure derivative limit $\widehat{\delta p}_{ic}$ on the evolution of the in-cylinder pressure (left plot) and heat release (right plot). The actual constraints of the nominal engine in terms of maximum pressure and heat transfer (160 bar & $\varrho = 1$) have been chosen as reference conditions.

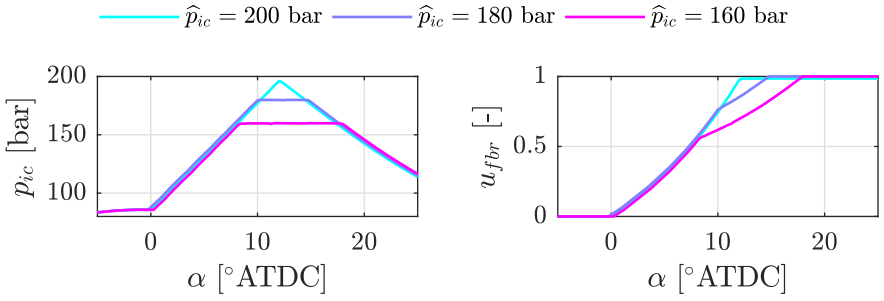

Figure 9.7: Effect of the cylinder pressure limit $\widehat{p}_{ic}$ on the evolution of the in-cylinder pressure (left plot) and heat release (right plot). The actual constraints of the nominal engine in terms of heat transfer and maximum pressure derivative ($\varrho = 1$ & 10 bar/°) have been chosen as reference conditions.

Explicit optimal HRL policy

From previous results, it can be appreciated that regardless of the heat transfer, maximum pressure or pressure derivative limits, there is a general rule that is always followed: the optimal policy consists of a fast and early HRL limited by the pressure constraints. In particular, the optimal HRL rate is initially limited by the maximum pressure derivative until the maximum in-cylinder pressure is reached. Then, the optimal HRL rate keeps a constant in-cylinder pressure until the fuel is completely burnt. In this sense, the following rule can be identified:

$$u_{fbr}(\alpha) = \begin{cases} 0, & \alpha \leq \alpha_{soc} \\ \arg\min_u \left\{ p_{ic}(u_p), p_{ic}(u_{\delta p}), p_{ic}(1 - \int_{\alpha_i}^{\alpha} u_{fbr}\, \mathrm{d}\alpha) \right\}, & \alpha > \alpha_{soc} \end{cases} \tag{9.10}$$

where $u_{\delta p}$ and u_p are the controls leading to the maximum pressure derivative and maximum in-cylinder pressure allowed at the current angle α respectively. The term $1 - \int_{\alpha_i}^{\alpha} u_{fbr}\, \mathrm{d}\alpha$ ensures that the maximum released heat does not exceed the fuel energy. The constant α_{soc} is a calibration parameter representing the optimal start of combustion, which can be obtained by shooting or any other optimization method. The use of DP can be replaced for this rule with a sweep in the variable α_{soc} to choose the value α^*_{soc} that minimizes the ISFC. Note that this rule can be easily implemented since $u_{\delta p}$ and u_p can be obtained solving (4.97) for $\partial_\alpha q_b$ with the proper pressure derivative.

The above control rule has been drawn intuitively but it can also be deducted from the problem formulation. Assuming that only constraint (9.6) applies in this case–NO_x emissions are neglected–, the Hamiltonian may be constructed for this situation as:

$$H = L + \mu_q u_{fbr} \tag{9.11}$$

being clearly a linear function of the control. According to section 3.3.3, this particularity results on a *bang-bang* control that may be expressed as a set of constant controls–in this case when $\alpha \leq \alpha_{soc}$–and singular arcs–when $\alpha > \alpha_{soc}$.

Figure 9.8 shows the evolution of the ISFC according to the application of (9.10) to a α_{soc} swept from -15° to 15° for the engine with nominal conditions ($\widehat{\delta p}_{ic} = 10$ bar/°, $\widehat{p}_{ic} = 160$ bar and $\varrho = 1$). The results are compared to DP optimization results in table 9.1. A perfect matching can be observed: the optimum start of combustion is 0.5° and the minimum ISFC is 167 g/kWh. Despite obtaining near the same results, the explicit optimal HRL policy

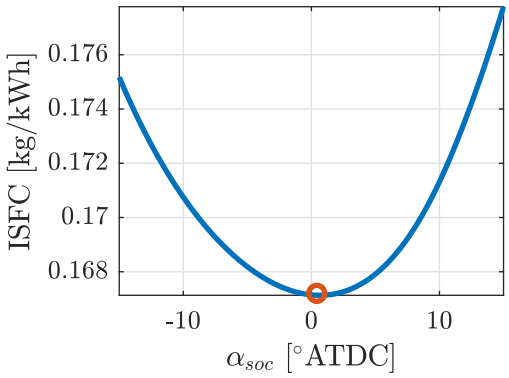

Figure 9.8: Start of combustion α_{soc} sweep at equation (9.10) compared to the optimal ISFC obtained from DP application (circle) for the engine at nominal conditions ($\widehat{\delta p}_{ic} = 10$ bar/°, $\widehat{p}_{ic} = 160$ bar and $\varrho = 1$).

	DP	Explicit policy
Angle discretization	0.25°	0.25°
u_{fbr} discretization	200 points	continuous
p_{ic} discretization	350 points	continuous
q_b discretization	200 points	continuous
Optimal start of combustion α_{soc}	0.5°	0.5°
Optimal ISFC	167.4 g/kWh	167.2 g/kWh
CPU time (standard laptop)	6120 s	64 s

Table 9.1: Discretization and performance indices of DP and explicit optimal HRL policy.

presented has some advantages compared to the DP approach. On the one hand the computation burden is highly reduced (2 orders of magnitude) despite a swept on α_{soc} has been done instead of a more efficient optimization algorithm. On the other hand discretization in states and controls are not needed, so the accuracy may be higher.

Optimal HRL with NO_x constraints

The parameter μ_m in (9.9) weights the importance of NO_x generation reduction in the optimal solution. The optimal tradeoff between NO_x and ISFC can be calculated with a swept of optimal solutions for a range of μ_m. Figure 9.9 shows this tradeoff as a Pareto front. Note that the experimental measurements shown in this figure correspond to a sweep in the injection parameters and,

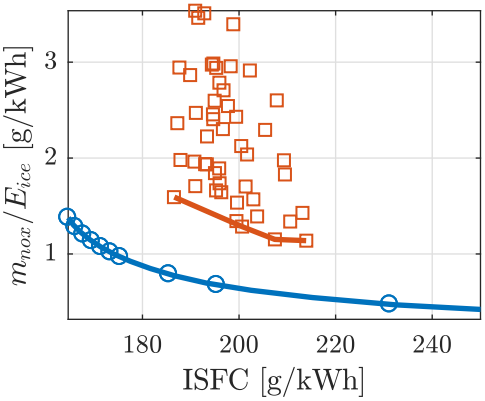

Figure 9.9: Pareto front representing the tradeoff between ISFC and NO_x emissions. The blue data points correspond to the Pareto front obtained with DP. Red squares show all experimental results with their Pareto front represented with the red line.

the theoretical Pareto front should be compared to the experimental front. According to this, ISFC increases from 167 g/kWh when NO_x constraints are neglected (μ_m=0) to more than 250 g/kWh for high values of μ_m. The Pareto front points out the negative effect of NO_x emission regulations on engine efficiency. In fact, if NO_x are not limited the ISFC could be theoretically reduced to 167 g/kWh at the expense of high NO_x emissions–around 1.4 g/kWh. If NO_x are reduced to 0.5 g/kWh, the minimum ISFC to be attained is 230 g/kWh. Therefore, a NO_x emissions reduction from 1.4 to 0.5 g/kWh has a penalty of 67 g/kWh on ISFC.

A pattern clearly exists in the relation between the NO_x emissions and the optimal evolution of the pressure and heat release rate. Figure 9.10 shows these two variables for different NO_x emission levels and may give some clues to shape the optimal combustion rate. The first mechanism to decrease NO_x is to delay the HRL. It can be appreciated that small reductions in NO_x around the case without NO_x constraints–highest NO_x generation–only produces that delay with no changes in the pressure derivative. Delaying the HRL law involves a combustion at lower temperatures with lower NO_x emissions–see the temperature effect in (4.102). If the NO_x limit is reduced even more, the combustion delay is not enough to satisfy the NO_x constraint and the rate of heat release should be reduced–see the effect of q_b in (4.98). Once an almost constant pressure combustion is reached, additional reductions in the NO_x emissions are obtained again by means of delaying the combustion process. The relation between the NO_x emissions and the maximum pressure derivative

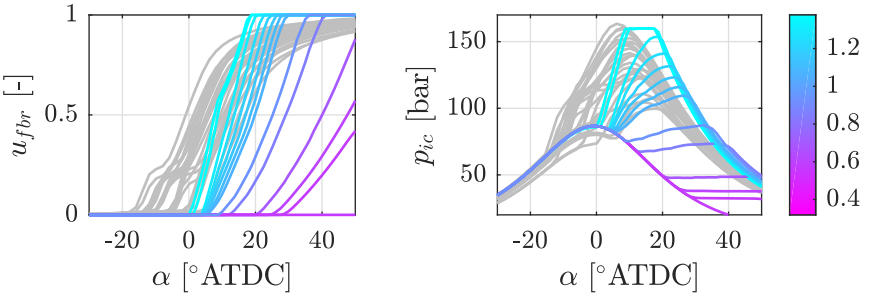

Figure 9.10: Evolution of the in-cylinder pressure (left plot) and heat release (right plot). The color scale shows the NO_x emissions of DP solution while gray results are experimental data.

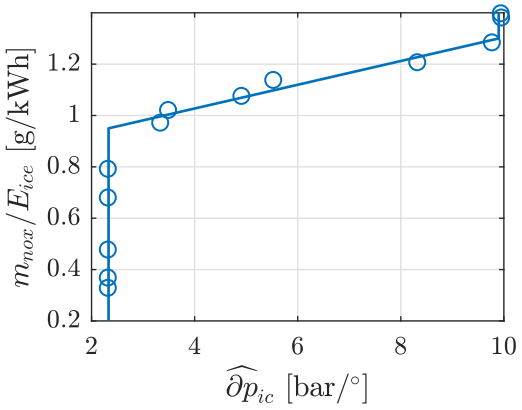

Figure 9.11: Relation between NO_x emissions and maximum pressure derivative $\widehat{\delta p_{ic}}$.

for the optimal HRL is depicted in figure 9.11. The previous three phases can be clearly identified in this figure: the NO_x emissions can be reduced from 1.4 g/kWh to 1.3 g/kWh by delaying the combustion keeping the maximum allowed pressure derivative. Then, from 1.3 g/kWh to 0.95 g/kWh the NO_x emissions can be decreased with a lower maximum pressure derivative. Finally, NO_x emissions below 0.95 g/kWh can only be reached with an almost constant pressure ($\widehat{\delta p_{ic}} = 2.3$ bar/°) evolution with increasingly later combustions.

Similarly to the explicit HRL described in the previous point, the NO_x constrained case may be also represented with a set of explicit rules. According to the integral NO_x constrain (9.7), and its analytical expression (4.102), it is clear that the corresponding Hamiltonian is again a linear function of the control. Therefore, singular control (see section 3.3.3) can be applied as well.

The experimental results from test 7 (see 5.3.7) are also included in figures 9.10 and 9.11. For a given NO_x level, the comparison between experimental and optimal ISFC allows the assessment of the HRL optimality. According to these results, the experimental tradeoff is displaced towards higher ISFC and NO_x emissions, showing some potential to optimize the combustion process. It is clear from results in figure 9.11, that the actual injection-combustion system is not able to reproduce the calculated optimal HRLs. The optimization shows that it is necessary to delay the combustion process in order to reduce the NO_x emissions, which is the general approach followed in current DI CI engines, and also in the current experimental study. In current engines this is achieved by delaying the SOI, by reducing the injection pressure to lengthen the injection process or by introducing inert gases in the combustion chamber through EGR. In the present experimental study the first two factors have been modified. Nevertheless, the actions taken to delay the combustion in the experimental facility also involve a noticeable combustion slowdown. Actually, shifting the combustion towards late phases of the expansion stroke leads to a combustion process at a lower temperature and, therefore, taking more time. The injection modulation by using different injection events introduces an additional degree of freedom that contributes to the decoupling, to some extent, of both effects. A pilot injection with different timings has been included in the experimental parametric study. However the delayed and fast combustion from optimization results has not been reproduced experimentally.

Despite the optimization results provide a lower boundary for the ISFC and NO_x emissions tradeoff of the engine, the considered model uses the HRL as an input, not being able to take into account the limitations of the injection system. The application of the OC algorithm to a more physical based model of the combustion process–considering the injection pattern as input instead of the HRL–will (at least partially) fill the gap between the model based OC and experimental results. In fact, since the injection process has not been taken into account in the performed study, the Pareto front should be taken as a lower limit for the optimal tradeoff without injection constraints. Since the optimal HRL and pressure traces are not achievable experimentally it can be concluded that the injection-combustion system has room for improvements. In particular, due to the fact that the engine is extremely small, the required injection split to shape the combustion according to the optimal HRLs will involve injection quantities below the minimum amount that can be performed with the current injection system.

In addition to the optimization potential of the current engine, the NO_x model is subject to uncertainties. Despite the NO_x model parameters were identified to reproduce the experimental measurements provided in figure 9.1,

the model only considers thermal NO_x formation, neglecting other NO_x sources such as the fuel NO_x formation, prompt NO_x formation and NO_x production via N_2O. The differences between the experimental and calculated HRLs that can be appreciated in figure 9.10 may be the consequence of non-negligible differences in the weight of the different NO_x formation mechanisms involving a model underestimation of the NO_x emissions.

9.2.5 Conclusions

OC has been shown as a valid method for shaping the HRL that minimizes the ISFC with different constraints, namely: maximum cylinder pressure, maximum cylinder pressure derivative and NO_x emissions. For that purpose, a validated model of the combustion process including the thermal NO_x formation has been employed to approach the OCP with the DP method. The main conclusions that have been drawn are:

- The use of an OC framework allows to assess the engine performance with a more representative reference than traditional thermodynamic combustion processes such as constant volume, constant pressure and limited pressure or even arbitrary Wiebe functions. Particularly, the OC approach provides the HRL showing the best efficiency subject to some predefined constraints as a basis of comparison. In the case at hand, maximum cylinder pressure, pressure derivative and NO_x emissions were constrained.

- The OCP solution provides a target HRL to define injection strategies and evaluate the systems or processes with room for improvement. This analysis has pointed out some limitations in the current injection system capabilities to shape the injection and therefore the combustion process.

- NO_x constraints are fulfilled applying two different mechanism: delaying the combustion and reducing the pressure gradient. These two strategies appear sequentially in the optimal solution as NO_x constraint becomes stricter.

- The analysis of optimal solutions allowed to define an explicit optimal HRL policy if NO_x are neglected. The computation time of this method is two orders of magnitude below DP algorithm and does not require states or controls discretization.

- Due to the physical limitations of injection systems, additional constraints should be included in further works to close the gap between

the theoretical optimal HRL and the best practically affordable injection schedule.

9.3 Optimal powertrain sizing

The adequate sizing of powertrain components, in line with the type of use of the vehicle, is a quite important question to improve the global efficiency. For example, a light urban vehicle will benefit from a small engine since a bigger one would operate at very low loads jeopardizing the efficiency. The target is to fit the powertrain performance in such a way it operates at high efficiency regions most of the time. This is not a trivial question since this sizing depends on the particular use of the vehicle. Fitting to the requisites of many different drivers may be a complex task.

In the case of HEVs, the situation gets more complicated since three devices should be sized: engine, motor and battery. It is possible to find HEVs in the same segment and aimed to similar uses with battery packs ranging from approximately 0.5 kWh to more than 15 kWh. Of course, on one hand an oversized hybrid system gives an extra performance and versatility that may not be profited, while weight and price increase; on the other hand, an extremely mild electrification would reduce the fuel saving capacity to insignificant values. This issue has motivated the proposal of more sophisticated configurations such as supercapacitors [8, 9], fuel cell [10–12] and battery-supercapacitors [13–16] powered hybrid powertrains.

Several studies have been focused on optimal powertrain sizing methodologies based on different criteria. These works consider fuel consumption, pollutant emissions, vehicle cost or performance concerns in the optimization for a particular type of use [17–22]. Besides those requisites, it is interesting to analyze two additional factors: the effect of the driving conditions and the economy of the vehicle from a user point of view. On the one hand, different driving cycles might require specific powertrain sizes according to their particular needs. On the other hand, not only vehicle cost is important for the owner but also efficiency, so a long term economic analysis could be interesting. It is important to remark that the efficiency of a HEV is strongly affected by the energy management policy. Therefore, in order to make the powertrain scale the only difference in the study, and to avoid the effect of an inefficient control policy, the works in [23, 24] implemented an optimal energy management in combination to the powertrain sizing.

An additional factor that may affect to a long term analysis is the powertrain wear. This cost could have a strong impact on the economic tradeoff of the vehicle, specially in a HEV where the battery aging directly affects

on the performance and efficiency of the powertrain. Battery aging models have been proposed in the literature [25] and several works address the OC accounting for battery wear effects [26]. In the context of this study, battery aging might have a significant impact for very long term analysis; however, the consideration of this effect is out of the scope of the work and is neglected for the sake of simplicity.

In line with the above requirements and following previous studies of the author [27], the present work presents a HEV powertrain optimal sizing methodology from the user economy point of view, addressing the total cost of ownership under different driving conditions.

9.3.1 Problem description

The aim of this methodology is to calculate the adequate powertrain component sizes of a parallel HEV and for a specific type of use. This involves the evaluation of an optimization problem that includes, not only the traditional energy management problem [28, 29], but also the selection of the appropriate engine, motor and battery sizes. The optimization target is both fuel economy [30, 31] and user initial investment in such a way that the total cost undertaken by the customer is minimized for the vehicle lifetime cycle. The parallel layout is arbitrary but the formulation is equivalent for any other topological architecture and its implementation may be almost straightforward. Different drivers and cycles are analyzed to study the effect of the use requirements in the optimal powertrain size.

Therefore, the main targets of this approach are:

- Estimate the optimum fuel economy for different types of driver.
- Propose a methodology to optimally fit a HEV powertrain to a specific type of vehicle use–*i.e.* a market niche–maximizing economy based on expected driving conditions instead of an arbitrary weighted specification.
- Calculate the proper powertrain component size in a parallel HEV for an expected type of use and mileage, minimizing the lifetime cost including purchase price.
- Analyze the optimal powertrain size sensitivity to differences in driving style and cycle, evaluating several drivers and routes.
- Find out the importance of a well sized HEV on fuel efficiency and long term economy.

This study is performed based on the setup D (see 5.2.4). It is a simulation model of a HEV based on manufacturer experimental data. Due to the unavailability of an actual facility of this kind, this work is purely theoretical. The vehicle model is kept constant throughout the study. However, engine, motor and battery must be scalable in order to analyze different sizes. A simple framework to scale these devices using setup D models and data is developed following the philosophy of [24]. The optimization procedure splits the optimum seeking task into two steps: first, OC is applied to the EMP generating a space of optimum powertrain candidates; then, the size of powertrain components is optimized attending to the total cost of ownership.

9.3.2 Problem formulation

Let us assume that the driving cycle is known in advance, so vehicle speed $v(t)$, acceleration $\dot{v}(t)$, track grade $\beta(t)$ and gear number $N_{gb}(t)$ are prescribed. Therefore, the torque trajectory at the wheels $T_w(t)$ can be calculated with the vehicle dynamics model (4.7). The splitting of this torque between engine and motor is defined by the Energy Management (EM) control policy and fulfills (4.22). Motor is modeled with (4.34) so its torque output T_m is a function of the electric power supplied by the battery:

$$T_m = T_m(P_e(x,u)) = T_m(x,u) \tag{9.12}$$

where $x = \zeta(t)$ is the state of the battery–SoC–and $u = i_b(t)$ is its control variable, specifically the current that delivers to the motor. For specific x and u trajectories, the engine torque is completely defined and, therefore, fuel consumption can be calculated from (4.34) with the corresponding efficiency map:

$$\dot{m}_f = \dot{m}_f(v,\dot{v},\beta,N_{gb},\zeta,i_b,t) = \dot{m}_f(\zeta,i_b,t) \tag{9.13}$$

If engine, motor and battery main design parameters–engine displacement V_d, motor power rating $P_{m,n}$ and battery capacity Q_b–are considered free variables, the fuel consumption increases its d.o.f. in three units:

$$\dot{m}_f = \dot{m}_f(\zeta,i_b,V_d,P_{m,n},Q_b,t) \tag{9.14}$$

The objective is to minimize the total fuel consumption at the driving cycle. Thus, the following cost index may be defined:

$$J = \int_0^{\mathcal{T}} \dot{m}_f(\zeta,i_b,V_d,P_{m,n},Q_b,t)\,\mathrm{d}t \tag{9.15}$$

Note that i_b is a control variable–consequently it is a time-varying trajectory–while the powertrain design variables are constant parameters. Therefore, the minimization of J involves two different optimization techniques: an OCP varying i_b and a parametric optimization to fit the design parameters. In order to approach this problem, it is split into two nested optimization problems:

$$\min_{V_d, P_{m,n}, Q_b} \left\{ \min_{i_b} \left\{ \int_0^{\mathcal{T}} \dot{m}_f(\zeta, i_b, V_d, P_{m,n}, Q_b, t)\, \mathrm{d}t \right\} \right\} \tag{9.16}$$

where the inner is an OCP and the outer the size optimization, which is performed over the domain of $\min_{i_b}\{:\}$. The OCP must be completely defined in order to be solved–design parameters must be known–so it is addressed for a particular powertrain size.

The state dynamic is driven by the battery SoC, $\zeta(t)$, whose state equation is drawn from eqs. (4.37) and (4.39):

$$\dot{\zeta} = -\frac{i_b}{Q_b} \tag{9.17}$$

It indicates the charge content of the battery and its variation is a measure of the net electrical energy that has been drawn. Since the vehicle at hand is not a plug-in hybrid where battery depletion is a common policy [32], the SoC variation is limited to zero in order to provide a fair comparison among different powertrain sizes. Therefore, the following constraint to the OCP applies:

$$-\frac{1}{Q_b} \int_0^{\mathcal{T}} i_b \, \mathrm{d}t = \zeta(\mathcal{T}) - \zeta(0) = 0 \tag{9.18}$$

As usual, the state ζ, the control variable i_b, as well as intermediate quantities are constrained because of the physical limits of the powertrain.

This OCP may be pretty nonlinear because of the map-based models. However, it is quite compact since it only features one state and one control variable. Due to these facts, this problem seems well fitted to be approached with DP. The generic MATLAB framework provided in [7] is used to apply this method.

Powertrain scaling

The three main powertrain elements suitable to be scaled in terms of fuel economy are: engine, electric motor and battery. For the scope of this work, models for these devices must be scalable, *i.e.* capable of representing similar machines of different sizes, both in specifications and weights as stated in [24].

The engine is scaled attending to the displacement. On the one hand, performance specifications are defined by maximum and minimum torque curves, which are given for a specific displacement. For a particular bore/stroke ratio and engine technology, Mean Effective Pressure (MEP) could be considered an invariant regardless of the displacement [33]. Then, the maximum and minimum torque may be calculated for any equivalent engine as:

$$T_{ice} = \frac{\text{MEP} \cdot V_d}{2\pi \cdot n_c} \tag{9.19}$$

where V_d is the displacement and $n_c = 2$ for a four stroke engine. On the other hand, fuel mass flow $\dot{m}_f$ is calculated from the engine efficiency according to (4.104):

$$\dot{m}_f = \frac{1}{\eta_{ice}} \frac{\omega_{ice} T_{ice}}{H_f} \tag{9.20}$$

Assuming that heat losses increase with cylinder exchange surface, the efficiency map may be estimated as follows:

$$\eta_{ice} = \frac{1}{1 + T_{loss}/T_{ice}} \tag{9.21}$$

where resized engine losses are calculated as a fraction of the reference engine losses $\widetilde{T}_{loss}$ and heat exchange surface $\widetilde{A}_{ex}$:

$$T_{loss} = \widetilde{T}_{loss} \frac{A_{ex}}{\widetilde{A}_{ex}} \tag{9.22}$$

Numbers for the reference engine can be calculated from its efficiency map with the above equations.

In order to estimate the mass of the engine a statistical analysis has been done. The correlation between homologation mass and engine displacement for several production vehicles is approached to a linear equation as shown in figure 9.12, where the slope k_{ice} is the contribution of the engine to the mass, under the assumption that different motorizations of the same vehicle do not include any extra equipment. Therefore, the engine mass is estimated as:

$$m_{ice} = k_{ice} \cdot V_d \tag{9.23}$$

The motor performance is scaled according to its power rating $P_{m,n}$. The efficiency of the reference motor is given for a pair of mechanical power P_m and rotational speed ω_m:

$$\widetilde{\eta}_m = \widetilde{\eta}_m(P_m, \omega_m) \tag{9.24}$$

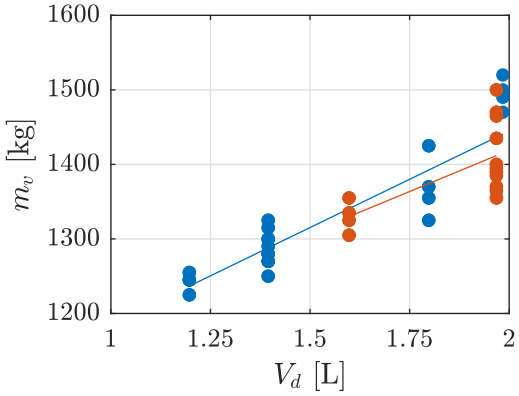

Figure 9.12: Correlation between vehicle mass and engine displacement for two vehicles equipped with different gasoline (blue) and diesel (red) engines.

Defining the scaling coefficient $\Upsilon = \widetilde{P}_{m,n}/P_{m,n}$, where asterisk refers to reference motor quantities, the efficiency of a motor of any size may be calculated from the reference motor efficiency map:

$$\eta_m(P_m, \omega_m) = \widetilde{\eta}_m(\Upsilon P_m, \omega_m) \tag{9.25}$$

Then, the electrical power consumption may be calculated as:

$$P_e = \frac{P_m}{\eta_m} \tag{9.26}$$

The motor is considered as a fully reversible machine so the operation map can be scaled to any of the four speed/torque quadrants following the same scheme.

The motor mass m_m is calculated following the approach described in [34]. It is divided into the mass of the electronics $m_{m,1}$ and the mass of the electrical machine $m_{m,2}$:

$$m_m = m_{m,1} + m_{m,2} \tag{9.27}$$

The mass $m_{m,1}$ is considered a fixed quantity regardless of the motor size. The mass $m_{m,2}$, however, can be estimated as:

$$m_{m,2} = k_m \cdot P_{m,n} \tag{9.28}$$

The battery is modeled according to the model described in 4.4.2. Scaling the battery capacity is equivalent to placing a different number of cells both in parallel–increasing maximum power supply–or in series–increasing output

voltage. The performance of the scaled battery is calculated summing up the necessary number of individual cells.

The battery mass is also estimated following the approach presented in [34]. The mass may be divided into the contribution of four terms: the battery chemicals $m_{b,1}$, the thermal management system $m_{b,2}$, the tray $m_{b,3}$ and buses, harnesses and terminals $m_{b,4}$:

$$m_b = m_{b,1} + m_{b,2} + m_{b,3} + m_{b,4} \tag{9.29}$$

The first term depends only on the type of battery since the amount of chemicals of specific energy e_{chem} required to store an amount of energy E_b weights:

$$m_{b,1} = \frac{E_b}{e_{chem}} \tag{9.30}$$

The second and third terms are expressed as a function of the battery capacity since the bigger the battery is, the heaviest the thermal system and battery tray are:

$$m_{b,2} = k_{b,2} \cdot Q_b \tag{9.31}$$

$$m_{b,3} = k_{b,3} \cdot Q_b \tag{9.32}$$

The last term is proportional to the maximum battery power output $\widehat{P}_e$ as the size of buses, harnesses and terminals depends on the maximum current that may flow instead of on the capacity of the battery:

$$m_{b,4} = k_{b,4} \cdot \widehat{P}_e \tag{9.33}$$

The total mass of the vehicle m_v is calculated as the addition of all the above components with a fixed chassis mass m_{cha}:

$$m_v = m_{cha} + m_{ice} + m_m + m_b \tag{9.34}$$

Vehicle cost

The optimal powertrain size, from an economic point of view, is influenced by two factors: the efficiency and the price. Of course, depending on the use and the mileage one term might become more important than the other. The price of the powertrain should be estimated in a scalable way as it is done for the mass and performance in previous paragraphs.

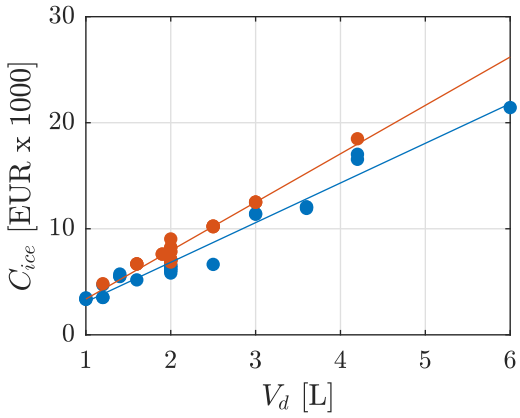

Figure 9.13: Polynomial fitting of consumer engine price as a function of displacement. Blue corresponds to naturally aspirated gasoline and red to turbocharged diesel engines.

The cost of the engine is estimated according to the displacement:

$$C_{ice} = c_{ice} \cdot V_d \tag{9.35}$$

where the coefficient c_{ice} depends only on the type of fuel; the breathing method is neglected since only turbocharged diesel and naturally aspirated engines are taking into consideration in this study. This coefficient was estimated from consumer engine prices (price for a full engine without accessories at original spare parts service) for both diesel and gasoline engines. The agreement between equation 9.35 and actual data may be advised on figure 9.13.

The cost for the motor and its electronics is calculated as stated in [34]. It proposes an empirical equation that estimates the manufacturer cost $C_{m,man}$ as:

$$C_{m,man} = c_{m,1} + c_{m,2} \cdot \ln(P_{m,n}) + c_{m,3} P_{m,n} \tag{9.36}$$

However, since engine estimated cost is at the customer level, the above motor cost must be expressed in the same way. The main differences between manufacturer and customer costs are taxes and OEM profit. Assuming that both are a fixed percentage, the final customer cost may be expressed as:

$$C_m = c_{m,4} \cdot C_{m,man} \tag{9.37}$$

The coefficient $c_{m,4}$ might be estimated with the tradeoff between prices at the original spare parts service and their corresponding manufacturing cost estimations.

		Min	Max	Points
Engine displacement	V_d [cc]	250	2500	19
Motor power rating	$P_{m,n}$ [kW]	0	100	21
Battery capacity	Q_b [Ah]	0	70	15

Table 9.2: Range of variation of the powertrain components. The combination of the above values results in a total of 5985 different cases to be considered.

The cost of the battery is also estimated following the method explained in [34]. Simplifying this algorithm, the battery cost results:

$$C_{b,man} = (c_{b,1} + c_{b,2}) \cdot m_{b,1} \tag{9.38}$$

where $c_{b,1}$ is a reference battery manufacturing cost and $c_{b,2}$ the accessories cost, both expressed per kilogram. $m_{b,1}$ is the chemicals weight, calculated in equation 9.30. Again, this cost is expressed as a manufacturing cost, so following the same philosophy, the customer cost may be estimated as:

$$C_b = c_{b,3} \cdot C_{b,man} \tag{9.39}$$

where coefficient $c_{b,3}$ is also estimated with the tradeoff between the price from the original spare parts service and the manufacturing cost estimation.

The chassis cost C_{cha}–vehicle without powertrain–is fixed for the whole work. A reference value was adopted corresponding to a 4-doors and 5-seats passenger vehicle. Then, the total cost of the vehicle is:

$$C_v = C_{cha} + C_{ice} + C_m + C_b \tag{9.40}$$

9.3.3 Optimization approach and implementation

The optimization problem is solved sequentially in two steps according to (9.16). First, the inner problem is approached. To do so, the powertrain is scaled to the set of powertrain sizes shown in table 9.2. Then, the following OCP is solved for each size individually:

$$\min_{i_b} \left\{ \int_0^{\mathcal{T}} \dot{m}_f(\zeta, i_b, t)\, \mathrm{d}t \right\} \tag{9.41}$$

subject to constraint (9.18). According to the considered griding in components size, this problem is solved for 5985 different size combinations at each driving cycle.

The dependency on the control strategy of (9.16) vanishes as the above OCP is solved. Therefore, for a given driving cycle it results in a set of optimum size candidates whose main variables are only function of the powertrain:

$$\begin{aligned} m_f &= m_f(V_d, P_{m,n}, Q_b) \\ m_v &= m_v(V_d, P_{m,n}, Q_b) \\ C_v &= C_v(V_d, P_{m,n}, Q_b) \end{aligned} \tag{9.42}$$

The above calculations were done with DP for two types of driving cycles: city and highway. However, this does not constrain calculations to two single cycles; as a matter of fact, the methodology consists of building city/highway mixed cycles from several real cycle samples with different city driving contribution, from 0 to 100%, comprising a wide variety of use conditions.

The minimum fuel consumption among all candidates in (9.42) is selected and its corresponding powertrain size is adopted as the best constructive solution that the vehicle may adopt to maximize fuel economy in that particular driving cycle.

Multi-scenario

The HEV size optimization is analyzed under diverse driving situations and for different applications. In this sense, the influence of driver style in the optimal size is studied with driving cycles corresponding to two different non-professional drivers. For every single cycle the same control strategy optimization and minimum seeking algorithm is used. The effect of the type of route is analyzed with a set of city and highway driving cycles. Those cycles not only represent a different route or type of application but also traffic conditions and time or day of the week effects, which could lead to a different vehicle selection to minimize cost.

An HEV must be aimed to a diversity of drivers with different needs, so no benchmark driving cycle is known in advance. Since the powertrain selection relies mostly on the use of the vehicle, an evaluation with an incorrect cycle could lead to a non-efficient HEV size. Therefore, a sensibility analysis is performed varying the city driving contribution to the vehicle utilization from an all-highway use to pure city driving. Thus, 11 driving cycles have been built concatenating 50 city and highway cycles in random order and weighting the amount of city mileage from 0% to 100%. The resulting cycle is expected to represent about one month of daily driving, so the constraint (9.18) has a low impact on the optimization solution.

For the sensitivity analysis, problem discretization is downgraded from values at table 9.2 to values at table 9.3 for computational reasons, narrowing

		Min	Max	Points
Engine displacement	V_d [cc]	200	2000	6
Motor power rating	$P_{m,n}$ [kW]	0	90	4
Battery capacity	Q_b [Ah]	0	100	5

Table 9.3: Range of variation of the powertrain components for the sensibility analysis.

the range closer to the former optimal solution. However, around optimum the previous discretization was kept.

Long term optimization

For homologation purposes the main indicator is the fuel economy with compliment to emission regulations. However, from the customer point of view, the key point is the long-term cost. The vehicle carries a fixed cost at the time of the purchase, and a variable cost associated to its fuel efficiency. The best solution is a good tradeoff between both costs that minimizes the outgoings throughout vehicle's lifetime. Generally, the best solution does not imply the cheapest car neither the most efficient one.

This long-term tradeoff may be estimated with a cost optimization. This consists in the minimization of the total cost per kilometer C_{km} defined as the combination of both fixed and variable costs of the vehicle:

$$C_{km} = c_f \frac{m_f}{\mathcal{S}} + \frac{C_v}{S_{year} \cdot n_{lc}} \tag{9.43}$$

where m_f is the fuel mass consumption in the optimization route of length $\mathcal{S}$, c_f is the fuel price per mass unit, S_{year} is the distance covered per year, C_v is the total vehicle cost and n_{lc} is the life cycle of the vehicle, for this example 10 years. According to this, the tradeoff between mileage and optimal HEV size may be computed selecting the cheapest operation cost per kilometer C_{km} for different mileage values.

9.3.4 Results and discussion

The simulation of the multiple HEV powertrain size combinations resulted in a 3-dimensional space of optimal fuel consumption values as stated in (9.42). Some contours of this space of solutions at different levels of battery capacity (driver A, city driving) are shown in figure 9.14. These results show that the most efficient operation points fall in the lowest engine displacement region.

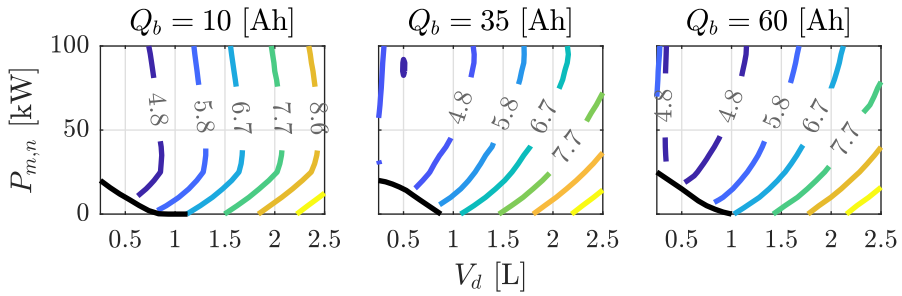

Figure 9.14: Optimal fuel economy as a function of engine displacement and motor power rating. Plots refer to different battery capacity levels. Contours correspond to fuel consumption with an OC policy at a city cycle with driver A.

Naturally, increasing the engine size spoils the fuel economy at any situation, since engine works at lower loads, *i.e.* at lower efficiency. In contrast, battery and electric motor size not always impact significantly on fuel economy.

The maximum amount of energy that can flow on one direction is limited by the battery capacity. Incorporating a bigger electric motor does not mean that the extra power can be used and, therefore, there exists a boundary profitable motor power–depending on driving cycle. Any motor above that power would not offer any advantage and, usually, will decrease fuel economy due to its greater mass and oversized specifications. In the left hand side plot of figure 9.14 it may be appreciated that, for a given engine size, above a motor power of 25 kW the fuel economy does not change too much and, in fact, it slightly decreases. Of course, increasing the battery size permits benefiting from a more powerful motor so the motor power for minimum fuel consumption moves to higher values. In the middle and right plots the turning point moved upwards out of the figure due to this effect. In addition, since the battery is mostly like an energy buffer that compensates the power peaks along the driving cycle, depending on the aggressiveness and–mostly–on the length, the maximum amount of energy that can be stored–regardless of the motor power–is limited. Therefore, above that limit no extra energy can be buffered and an increase in battery size will not improve fuel efficiency. Similarities in the middle and right plots of figure 9.14 show that the boundary battery capacity has been reached and eventually exceeded.

Based on the previous discussion it is clear that battery size is bounded by the *bufferable* driving cycle energy, while the motor size is bounded by battery size. Therefore, powertrain size is globally bounded so overcoming those values does not contribute to improve fuel economy anymore. Based on

figure 9.14 those limits can be intuited: exceeding 80 kW and 35 Ah makes no sense and, in fact, the optimum solution is 0.4 liters / 65 kW / 25 Ah (engine/motor/battery). Small engines work at higher loads, what means better efficiency, but they also have increased losses compared to their power output. Hence, there is an optimum engine size that balances both effects, which can be intuited from figure 9.14 to be about 0.3 to 0.5 liters. However, since all the vehicle energy comes ultimately from fuel, tiny engines could be unable to follow the driving cycle. This issue may be also appreciated at figure 9.14 since the bottom left region is empty due to the inability to follow the cycle.

The 3-dimensional space of solutions could be also evaluated with a Pareto frontier analysis. The optimal powertrain size and its corresponding fuel economy is depicted in figure 9.15. The optimal battery size is expressed as a function of engine displacement and electric motor power. Some of the conclusions drawn in the previous discussion may be also applied here. The minimum fuel consumption is quite similar to that from the plots in figure 9.14 that overcome the 35 Ah boundary capacity, since bigger batteries do not facilitate the energy recovery anymore. Also as the battery limits the maximum energy that can be buffered, the motor power gets limited, resulting in a strong relation between motor power and optimal battery size. This may be appreciated in the right plot from figure 9.15. However, this relation is no longer valid on the upper left region–very small engine and big motor. The engine is so small in that region that it cannot follow the driving cycle by itself–on the bottom, with no motor neither battery, the solution does not exist. The vehicle is capable of following the cycle with the help of an electric motor, but this engine inability limits the amount of energy that can be buffered along the cycle. Anyway, with the sufficient engine performance, there is a quasi-unequivocal relation between motor and battery sizes regardless of the engine.

Some size sensitivity conclusions may also be extracted from the Pareto analysis. It is obvious that engine displacement strongly affects fuel economy, however motor power (and consequently battery capacity) slightly impacts on the resulting fuel consumption. Of course, moving close to a non-hybrid powertrain (small motor and battery) increases this effect. An explicit analysis evaluating the gradient in fuel efficiency around the optimal powertrain size also results in the same conclusions. The gradients (in liters per 100 kilometers) are 0.3/100 cc, 0.003/kW and 0.007/Ah for the engine, motor and battery sizes respectively. This confirms that the engine has about two orders of magnitude more influence on the fuel efficiency than motor or battery.

The cost associated to the ownership of a vehicle may be split into two

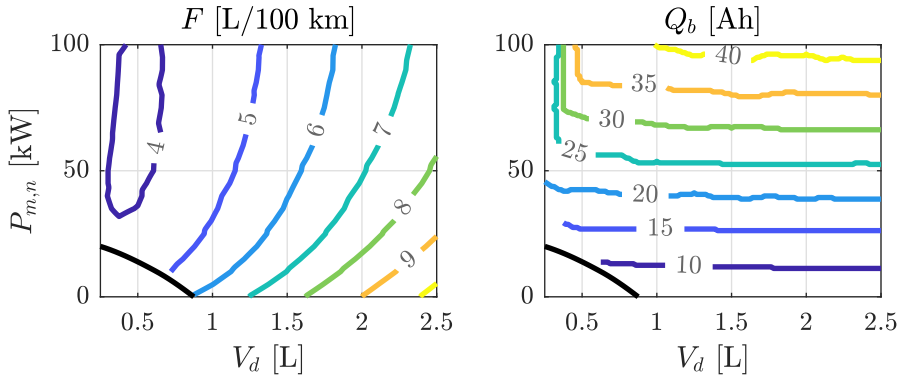

Figure 9.15: Pareto frontier analysis of powertrain size listed by engine displacement and motor power. Left plot contours show fuel consumption in liters per 100 kilometers; right plot shows the battery capacity in Ah. These results correspond to driver A and city driving.

factors: fixed costs (vehicle price) and variable costs (fuel consumption). Of course other factors may be included from an economical point of view such as service, annual taxes, etc., but since those do not explicitly depend on the powertrain size they are neglected for a long term study. The life-time cost per kilometer can be calculated for different mileages according to (9.43). The optimal cost is depicted in the upper left plot of figure 9.16 as a function of the mileage. Its corresponding powertrain size (engine, motor and battery) is shown in the right and bottom plots.

Of course, the battery lifespan and efficiency during its lifetime is an important factor on a long term analysis. Battery life-cycle could modify the theoretical optimum to, for example, a bigger battery to minimize the number of charge/discharge cycles for a given mileage. The interested reader may find an extended discussion of components sizing and battery life-cycle at [21].

Long term cost and sizes tend asymptotically to the minimum fuel consumption solution: for an infinity long distance, the fixed cost loses its weight so only variable cost matters. On the other side, for zero operation, the best option is the cheapest vehicle which, of course, consists of the smallest powertrain–no motor neither battery so basically it is not a hybrid. The transition from one powertrain to another depends on the relation between fixed and variable costs. If the most efficient powertrain is not much more expensive than the cheapest one, the best option rapidly evolves to that optimum with a little increase in mileage, which is the case of some cycles in figure 9.16.

Optimal solution for different drivers resulted in the long term tradeoff shown in figure 9.16–blue lines correspond to A-driver's cycle and red to

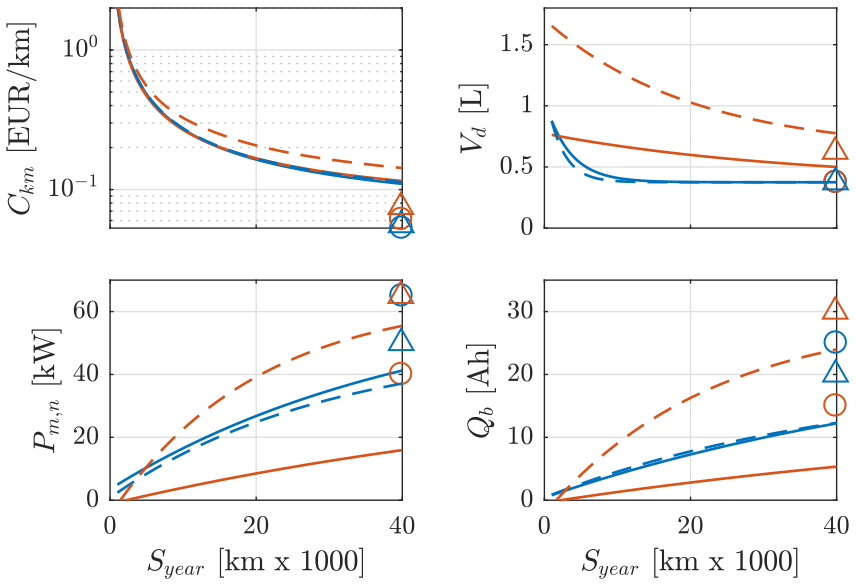

Figure 9.16: Optimal lifetime cost per kilometer (top left) and the corresponding engine displacement (top right), motor power (bottom left) and battery capacity (bottom right) as a function of mileage per year. Dashed lines and triangles are city driving while solid lines and circles are highway operation. Blue color corresponds to A-driver's cycle while red is B-driver's cycle. Circles and triangles on the right of each plot are the best fuel economy solution.

B-driver's cycle. It may be appreciated that the minimum operation cost as well as the optimal size is approximately the same for both drivers. Note that the long term tradeoff is strongly affected by the cost of the vehicle. The size of expensive components–increasing vehicle cost the most–vary less with driving cycle since a bigger unit is difficult to redeem with its corresponding improvement in fuel economy. This means that the gradient between the long-term and the fuel efficient optima defines the sensitivity of the size with respect to the driver style. In other words, battery and motor sizes are strongly driver style-dependent as those machines are slightly cheaper than the engine, offering a wider variety of long term solutions. For example, as driver B city driving style is more aggressive than A (average power requirements of 5 and 3 kW respectively), his optimal powertrain size is slightly bigger than that from driver A.

A similar study may be done for different types of driving cycle. Since driver A and B recorded their daily routes, both city and highway driving cycles were available. Another long term tradeoff is computed and depicted in

figure 9.16–dashed lines correspond to city driving and solid lines to highway. While for different drivers no significant differences were appreciated in city operation, highway driving may considerably displace the optimal powertrain size and its fuel economy. There are two reasons for this behavior: on the one hand, highway cycles were completely different from each other, since driver A drove at a constant speed–little chance to recover energy and reduced electrical path size–while driver B showed variable speed; on the other hand, intuitively, fuel efficiency may significantly vary from city to highway operation due to their different nature. Highway driving usually means higher and constant power requirements. Since energy comes ultimately from fuel, the engine must fulfill the increased average power requirement. Consequently, since requirements are more homogeneous over the time, there is less opportunity to buffer energy on the battery, so the electric path is reduced. These influences may be appreciated in figure 9.16 as motor and battery are quite reduced in highway operation. The same philosophy could be followed to evaluate any kind of driving cycle: on one hand the higher the power requirement, the bigger the engine; on the other hand the more homogeneous the demand is, the smaller the motor and battery are.

For the route type analysis the discretization of the optimization grid had to be downgraded to the values on table 9.3 for computational reasons. On a second approach the grid was restored to the values at table 9.2 in the surroundings of the optimum. The results of this analysis are presented in figure 9.17, showing the optimal size powertrain as a function of mileage and city driving fraction.

Operation costs slightly change with route type. Due to the low sensitivity of motor and battery selection, the engine is the only machine that grows with highway cycles, resulting in a worse fuel efficiency (4.59 compared to 4.13 L/100 km for 30000 km/year) but a cheaper vehicle due to the reduced motor and battery pack. Since those differences are quite small, the total operation cost in a long term evaluation is not very different as it was already appreciated in figure 9.16. The non-hybrid region (on the left-bottom area of plots in figure 9.17) gets narrow when increasing city contribution since hybridizing the vehicle is more attractive for economy. The small area at the bottom of the upper right plot where a different engine is used means that there is a displacement that fulfills highway but not city cycle. The engine size decreases as the mileage and the city driving contribution increase, reaching the smallest displacement on frequent city driving.

Battery follows a similar scheme. The size rises rapidly as the engine displacement reduces. The increased capacity with city contribution trend is quite the same. The motor size tradeoff is not so clear because it is a relatively

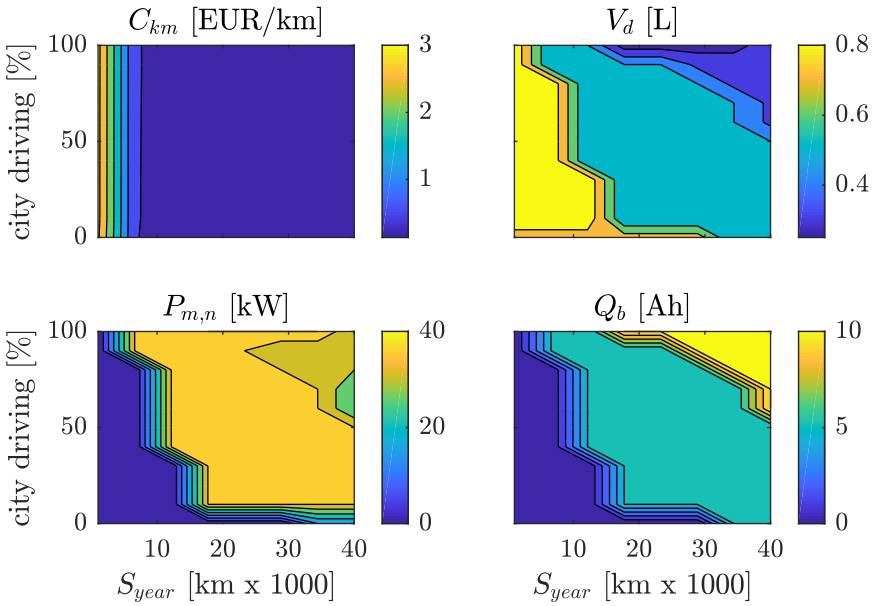

Figure 9.17: Optimum cost and size as a function of mileage and city driving contribution during vehicle lifetime. These results correspond to driver A cycles.

cheap machine that could be redeemed easily, so its selection depends mostly on its efficiency and coupling with battery. Highway driving requires a small motor, while city cycles use to have a greater chance to recover energy, so motor and battery should be bigger. On the mid area, at low mileages, the vehicle required a big motor to run a larger displacement engine at high efficiency levels, mostly during city driving. As engine displacement decreases with mileage the electric motor size is also reduced.

9.3.5 Conclusions

This study has introduced a systematic methodology to size a HEV powertrain attending to objective criteria, particularly the type of use–balance between city and highway driving–and the expected mileage. These criteria have been translated into an OCP where the power-split and size selection are optimized together. The same philosophy may be extended with additional criteria with minor changes.

Results suggests that fuel economy is strongly affected by the engine choice, while motor and battery have minor effects. In order to efficiently benefit from the regeneration possibilities of the driving cycle, the motor must be powerful

enough to recover braking energy and battery size should be somehow related to the recoverable energy along the cycle. A good choice seems to be a small engine coupled to an electrical path with sufficient motor power and battery capacity.

These optimization results are analyzed attending to vehicle cost and fuel efficiency in terms of yearly cost of operation. This has been evaluated for several driving conditions, from full city driving to full highway operation with mixed cycles at different levels. The analysis showed that HEVs are much more attractive for city driving than for highway utilization, where the payback mileage is about 40000 kilometers per year. However, even for city driving, a HEV requires a minimum mileage of 5000 kilometers per year to be interesting, otherwise fuel efficiency benefits do not compensate the increased vehicle cost.

References

[1] J. A. Caton. *A review of investigations using the second law of thermodynamics to study internal-combustion engines.* Tech. rep. SAE Technical Paper, 2000.

[2] C. D. Rakopoulos and D. C. Kyritsis. "Comparative second-law analysis of internal combustion engine operation for methane, methanol, and dodecane fuels". In: *Energy* 26.7 (2001), pp. 705–722.

[3] F. Zurbriggen et al. "Optimal control of the heat release rate of an internal combustion engine with pressure gradient, maximum pressure, and knock constraints". In: *Journal of Dynamic Systems, Measurement, and Control* 136.6 (2014), pp. 1–9.

[4] L. Eriksson and M. Sivertsson. "Computing optimal heat release rates in combustion engines". In: *SAE International Journal of Engines* 8.3 (2015), pp. 1069–1079.

[5] C. Guardiola et al. "Optimal control as a method for diesel engine efficiency assessment including pressure and NOx constraints". In: *Applied Thermal Engineering* 117 (2017), pp. 452–461.

[6] J. Arrégle et al. "On board NOx prediction in diesel engines: a physical approach". In: *Automotive Model Predictive Control.* Springer, 2010, pp. 25–36.

[7] O. Sundström and L. Guzzella. "A generic dynamic programming Matlab function". In: *IEEE Control Applications, Intelligent Control.* 2009, pp. 1625–1630.

[8] P. Rodatz et al. “Optimal power management of an experimental fuel cell / supercapacitor-powered hybrid vehicle”. In: *Control Engineering Practice* 13.1 (2005), pp. 41–53.

[9] J. Bernard et al. “Fuel efficient power management strategy for fuel cell hybrid powertrains”. In: *Control Engineering Practice* 18.4 (2010), pp. 408–417.

[10] C. C. Chan. “The state of the art of electric, hybrid, and fuel cell vehicles”. In: *Proceedings of the IEEE* 95.4 (2007), pp. 704–718.

[11] L. Xu et al. “Optimal vehicle control strategy of a fuel cell/battery hybrid city bus”. In: *International Journal of Hydrogen Energy* 34.17 (2009), pp. 7323–7333.

[12] X. Hu et al. “Optimal dimensioning and power management of a fuel cell/battery hybrid bus via convex programming”. In: *IEEE/ASME Transactions on Mechatronics* 20.1 (2015), pp. 457–468.

[13] V. Isastia and S. Meo. “Overview on automotive energy storage systems”. In: *International Review of Electrical Engineering* 4.6 (2009), pp. 1122–1144.

[14] T. Mesbahi et al. “Improved model of battery/supercapacitor hybrid energy storage system based on thermo-electrical and aging behaviors”. In: *7th IET International Conference on Power Electronics, Machines and Drives*. 2014, pp. 1–8.

[15] X. Hu et al. “Comparison of three electrochemical energy buffers applied to a hybrid bus powertrain with simultaneous optimal sizing and energy management”. In: *IEEE transactions on intelligent transportation systems* 15.3 (2014), pp. 1193–1205.

[16] X. Hu et al. “Longevity-conscious dimensioning and power management of the hybrid energy storage system in a fuel cell hybrid electric bus”. In: *Applied Energy* 137 (2015), pp. 913–924.

[17] X. Liu, Y. Wu, and J. Duan. “Optimal sizing of a series hybrid electric vehicle using a hybrid genetic algorithm”. In: *IEEE International Conference on Automation and Logistics*. 2007, pp. 1125–1129.

[18] M. Jain et al. “Optimal powertrain component sizing of a fuel cell plug-in hybrid electric vehicle using multi-objective genetic algorithm”. In: *Proceedings of the Industrial Electronics Conference*. 2009, pp. 3741–3746.

[19] X. Wu et al. "Application of particle swarm optimization for component sizes in parallel hybrid electric vehicles". In: *IEEE Congress on Evolutionary Computation*. 2008, pp. 2874–2878.

[20] T. Nuesch et al. "Cost and fuel-optimal selection of HEV topologies using particle swarm optimization and dynamic programming". In: *American Control Conference*. 2012, pp. 1302–1307.

[21] L. Johannesson et al. "Including a battery state of health model in the HEV component sizing and optimal control problem". In: *IFAC Advances in Automotive Control*. Vol. 7. 1. 2013, pp. 398–403.

[22] N. Murgovski, L. M. Johannesson, and J. Sjoberg. "Engine on/off control for dimensioning hybrid electric powertrains via convex optimization". In: *IEEE Transactions on Vehicular Technology* 62.7 (2013), pp. 2949–2962.

[23] N. Marc et al. "Sizing and fuel consumption evaluation methodology for hybrid light duty vehicles". In: *World Electric Vehicle Journal* 4.1 (2011), pp. 249–258.

[24] S. Ebbesen, P. Elbert, and L. Guzzella. "Engine downsizing and electric hybridization under consideration of cost and drivability". In: *Oil & Gas Science and Technology – Revue d'IFP Energies nouvelles* 68.1 (2013), pp. 109–116.

[25] L. Serrao et al. "An aging model of Ni-MH batteries for hybrid electric vehicles". In: *Ieee conference on vehicle power and propulsion*. IEEE. 2005, pp. 78–85.

[26] L. Serrao et al. "Optimal energy management of hybrid electric vehicles including battery aging". In: *American Control Conference*. 2011, pp. 2125–2130.

[27] J. M. Luján et al. "Cost of ownership-efficient hybrid electric vehicle powertrain sizing for multi-scenario driving cycles". In: *Proceedings of the Institution of Mechanical Engineers, Part D: Journal of Automobile Engineering* 230.3 (2016), pp. 382–394.

[28] A. Sciarretta and L. Guzzella. "Control of hybrid electric vehicles". In: *IEEE Control System Magazine* 27.2 (2007), pp. 60–70.

[29] C. Guardiola et al. "Modelling driving behaviour and its impact on the energy management problem in hybrid electric vehicles". In: *International Journal of Computer Mathematics* 91.1 (2014), pp. 147–156.

[30] S. Delprat, T. M. Guerra, and J. Rimaux. "Optimal control of a parallel powertrain: from global optimization to real time control strategy". In: *IEEE 55th Vehicular Technology Conference*. Vol. 4. 2002, pp. 2082–2088.

[31] L. Serrao, S. Onori, and G. Rizzoni. "A comparative analysis of energy management strategies for hybrid electric vehicles". In: *Journal of Dynamic Systems, Measurement, and Control* 133 (2011), pp. 1–9.

[32] C. Guardiola et al. "Insight into the HEV/PHEV optimal control solution based on a new tuning method". In: *Control Engineering Practice* 29 (2014), pp. 247–256.

[33] J. Heywood. *Internal combustion engine fundamentals*. McGraw-Hill, 1988.

[34] M. Delucchi et al. *Electric and gasoline vehicle lifecycle cost and energy-use model*. Tech. rep. Institute of Transportation Studies, 2000.

Part IV

Conclusion and future works

Chapter 10

Conclusions and future works

The true sign of intelligence is not knowledge but imagination.

— Albert Einstein

Contents

10.1 Main contributions and conclusions

This dissertation covers the use of OC to manage automotive powertrains with different applications. The unifying thread is to formulate the control of different systems as an OCP. This is conducted with the definition of an

objective function to be minimized–generally the fuel consumption–and a set of constraints that guarantee the validity of the solution. Vehicle, motor, battery, engine and transmission models are used to represent the controlled system. The OCP is addressed with the appropriate OC method according to the characteristics and requirements of the problem. Methodologies and techniques shown in this dissertation are not restricted to the examples that have been addressed. It may be extended to other powertrain applications following a similar philosophy.

The main conclusions and contributions of the applications that have been addressed in this document are detailed below.

10.1.1 Control of diesel engines

The application and performance of OC to diesel engine control has been studied for two different cases. On the one hand, the control of a dual-loop EGR system is addressed as a first approach to the OC application and advantages in terms of fuel and NO_x emissions are found. On the other hand, the more general case of the main engine actuators control with OC is addressed for an actual driving cycle. This replaces the ECU role, exploiting the capabilities of a given engine technology for a given driving cycle.

Dual-loop EGR control

The control of a dual-loop EGR system, with both LP- and HP-EGR valves, is addressed. The simultaneous operation of both systems is not allowed so they are used sequentially. This constraint simplifies the problem and removes possible EGR fraction estimation issues, and still showing significant improvements compared to HP-EGR systems. The problem is then reduced to the calculation of the switching points between both EGR loops. Therefore, the OCP can be approached with PMP which is a low cost algorithm compared to other optimization methods.

The application of OC to the NEDC has shown that the optimal control policy consists in using HP-EGR at the beginning and, after some time, switching to LP-EGR until the end of the cycle. The higher temperature that the HP system produces at the intake manifold is beneficial for the engine warm up, and its lower EGR rate shows a better fuel efficiency. However, these advantages get diluted as the engine temperature increases. Then, LP-EGR is able to perform higher EGR rates and a much lower intake temperature, promoting the reduction of NO_x production without a strong impact on engine efficiency. Different NO_x levels can be achieved by modifying the switching time between LP- and HP-EGR.

This OC strategy has been experimentally validated showing important NO_x reductions with a low impact on fuel efficiency. However, an important remark is that the quasi-steady hypothesis of the optimization model makes necessary to fix a maximum number of switches in order to avoid significant model discrepancies. This OC approach is also valid for additional optimization criteria such as other pollutants or performance concerns which may be included following a similar methodology.

10.1.2 Full engine control

The ECU setpoint and control calculations of the main engine actuators–fueling rate, SOI, EGR position and VGT opening–are replaced with an OC strategy. The corresponding OCP consists in minimizing fuel consumption and is stated with an experimentally validated MVEM, subject to several safety and pollutants constraints. The resulting OCP is a large problem that is only affordable with DMs. Particularly, a custom DC algorithm is used.

The use of OC in the lieu of a calibration shows several practical advantages. On the one hand, the number of experiments needed to build an OC strategy is determined by the requirements to construct a proper engine model. These are typically much less than those required to perform a full engine calibration as long as a physical model may be able to extrapolate most of the operating conditions with little information. On the other hand, the modification of a constraint such as emission limits might require a new complete calibration process while, with OC, it is just a question of solving the same OCP with a different constraint.

The experimental validation of OC strategies demonstrated that significant improvements in both fuel consumption and NO_x emissions can be achieved. A reduction of 4% in fuel consumption was obtained holding the factory calibration NO_x emissions; similarly, a reduction of 45% in NO_x emissions was also obtained keeping the factory fuel consumption. Higher gains can be achieved sacrificing fuel efficiency or NO_x emissions. This tradeoff between fuel and emissions suggests that there are lots of room for improvement in a ECU calibration that can be exploited with some sort of OC.

The OC policy followed two parallel strategies that allowed the above improvements. On the one hand, VGT is more open, allowing to decrease pumping losses and, consequently, raising global performance, although spoiling the torque reserve. On the other hand, EGR rate is increased to reduce NO_x production, but penalizing the combustion efficiency. The appropriate balance between those two effects produces significant NO_x and fuel consumption reductions. The torque and engine speed trajectories knowledge that is assumed with OC, allows a policy that smartly balances those two strategy

depending on the operating conditions. It promotes NO_x reductions in the parts of the cycle where it can be benefited the most, and prioritizes fuel efficiency when NO_x minimization strategy is not very attractive. This is something that a calibration cannot perform as long as it is not fed with look-ahead information.

An interesting remark is that, despite big improvements in both fuel and NO_x emissions were achieved, NO_x generation showed a much higher dependency on the control strategy. As long as pollutant emissions are highly dependent on the thermodynamic conditions within the combustion chamber, there are many chances to strongly reduce NO_x emission levels by modifying the operating conditions.

10.1.3 Engine management and speed control

Full engine control and vehicle speed management are approached with OC. This OCP has some resemblances with the above case and, in fact, the same engine actuators are controlled. However, in lieu of engine speed and torque trajectories, which are no longer fixed, a vehicle model and a distance to be covered in a fixed time are supplied. Despite the huge dimensions of this problem–8 states and 6 controls–it was successfully addressed with a custom DC algorithm.

This OCP actually involves two coupled problems that are typically split apart in literature: engine control and speed trajectory optimization. The last problem is sometimes addressed as the minimization of energy dissipation according to vehicle dynamics. In order to check the validity of this assumption, this dissertation addressed both problems together showing that the optimal speed profile is far from the minimum energy trajectory.

The main conclusion of this study is that an efficient management of vehicle speed–especially in roads with varying grade–is key for fuel and NO_x emissions minimization. Although the optimal engine control may produce some significant benefits in that direction (as concluded in the previous work), speed management is responsible of most of the fuel and emissions performance. In fact, it has been possible to assess strong NO_x reductions even with a simultaneous fuel economy improvement–Euro 6 emissions limit was reached with a Euro 5 engine in an actual driving cycle.

The resulting engine control showed clear trends. This suggested the idea of representing the optimal policy as a fixed calibration. Despite OC trajectories do not strictly fall within a map, optimal actuator positions were correlated to engine speed and fueling rate. The use of this calibration instead of OC trajectories showed a tight penalization in fuel efficiency of about 0.5% with similar NO_x emissions. On the contrary, the use of the factory calibration

entailed a grater difference: an additional fuel consumption of 15% and an NO_x increase of 25% to cover the same route. Two conclusions may be drawn from this. On the one hand, the optimal engine control, although showing an improvement compared to a fixed calibration, is responsible of minor benefits compared to the weight of an optimal speed management. On the other hand, the use of a specific engine calibration, adapted to the particular characteristics of the driving cycle, entails important benefits in fuel consumption and NO_x emissions. The use of a generic calibration that is aimed to perform well at any situation may leave lots of room for improvement.

An study on the average speed impact in fuel efficiency showed that one minute difference on the arrival time–the trip lasts approximately 40 minutes–carried a 3% difference in fuel consumption (for the same NO_x emissions), or moving from Euro 5 to Euro 6 emissions level (for the same fuel consumption). This emphasizes the importance of a proper balance between trip time, fuel efficiency and pollutant emissions.

10.1.4 Power-split of hybrid electric vehicles with no look-ahead information

The optimal power-split of HEVs is generally addressed in literature with the PMP method. Under a quasi-steady assumption, PMP can be simplified in such a way that the OCP is reduced to the selection of a single parameter, μ. The knowledge of its value is enough to obtain the optimal trajectory of the power-split. This parameter depends on the past and future operating conditions and, therefore, it must be estimated for onboard applications. The suggested approach in this work consists on a statistical analysis of past power requirements and a stochastic estimation such that battery charge is sustained in a forwards horizon.

The proposed approach showed a similar performance in terms of fuel consumption compared to other optimization algorithms that assume a full knowledge of the driving cycle. The contributions of this methodology are mainly focused to a practical implementation, and they are twofold: on the one hand, the optimal power-split can be simplified to a map which is function of current power requirements and the estimated parameter μ, so no optimization is required during onboard operation; on the other hand, μ can be estimated with simple algebraic equations based on a power requirement probability chart–extrapolated from a receding horizon–and the drift in battery SoC compared to the target value. These allow a fast computation of the optimal power-split ratio.

This approach is possible due to the quasi-steady hypothesis; a more detailed powertrain model may show discrepancies with this methodology.

Nevertheless, the proposed approach is inherently a feedback control and, despite inefficiencies may happen in a real powertrain, it should show robustness and SoC sustain following optimality concerns.

10.1.5 Design applications of optimal control

OC theory has been shown as a valid tool to facilitate design decisions from an optimal and objective point of view. The definition of a minimization objective and a set of constraints in the shape of an OCP helps to find the boundary efficiency of a system. In this dissertation, this philosophy has been applied to two different processes: the injection scheduling in a diesel engine and the sizing of a HEV powertrain.

Injection scheduling

The combustion process can be addressed as an OCP instead of sticking to arbitrary HRLs, enabling to calculate the exact HRL shape that minimizes fuel consumption. Due to engine integrity concerns, maximum pressure and maximum pressure derivative constraints are included. NO_x limit is also considered in the formulation.

A comprehensive analysis of the optimal HRL under several considerations, showed some interesting facts:

1. If pressure constraints are active, the HRL is such that the pressure trace follows the maximum pressure gradient until the maximum pressure is reached. Then, that pressure level is held until the full release of fuel is completed. These constraints penalize the fuel efficiency, with a higher ISFC as maximum pressure and gradient decrease.

2. If NO_x constraints are introduced, the optimal HRL follows two strategies to limit the thermal NO_x generation: delaying the combustion and reducing the pressure gradient. The sharpness of these mechanisms is up to the tightness of NO_x limit.

Based on the above conclusions, an explicit HRL can be shaped if NO_x constraints are neglected. This law reduces the OCP to the search of the start of combustion value that maximizes the fuel efficiency. The result of this approach is equivalent to the OCP but with much lower computation requirements.

The optimal HRL may be used to calibrate the injection schedule in order to follow the optimal shape.

Powertrain sizing

A systematic methodology to size a HEV powertrain attending to objective criteria has been presented. An OCP is stated where the optimization parameters are the power-split and the sizes of engine, motor and battery. The consideration of the power-split together with the sizing problem makes the size choice the only difference and avoids misestimations due to an inefficient control that might benefit a particular powertrain size. The inputs to this problem, *i.e.* the designing criteria, are the type of expected driving–city, highway or a combination at different levels–and the estimated mileage per year.

The impact of the engine size in the vehicle efficiency is critical. An incorrect choice might produce a significant increase in fuel consumption due to an engine operating at low load conditions. On the contrary, motor and battery sizes are more flexible and the impact on fuel efficiency of a wrong choice is moderate. A Pareto analysis of the results showed that optimal battery and motor sizes are somehow related. The motor size is determines the maximum amount of energy that can be recovered, and the battery size sets a boundary to the amount of that recovered energy that may be stored for a future use. According to that, a bigger motor allows to recover more energy during braking and coasting, but battery size should be also increased to take advantage of that opportunity. The precise choice of sizes is a question of the balance between the recoverable energy and the increased weight of the vehicle.

In the case of a lifetime cost analysis, the benefits of an efficient HEV dilute. It takes around 40000 kilometers per year to redeem it if its main use is on highway driving. The relatively low benefit in that situation compared to a conventional vehicle increases significantly the HEV payback period. In addition to that, the optimal powertrain requires a bigger engine and smaller electrical path for highway cycles. City driving may be much more interesting for a hybrid since fuel savings are high when energy recovering chances increase. However, the high price of a hybrid powertrain shows that a minimum mileage of 5000 kilometers are needed to make a HEV more attractive than a conventional powertrain.

10.2 Future works

This dissertation attempted to show the applicability and potential of OC in powertrains with some success. Despite experimental validations have demonstrated that OC can perform better than traditional control schemes,

the complexity of engines and powertrains indicate that there is still a long way to implement robust and standalone onboard optimal controllers. The necessity of look-ahead information to properly define the boundaries of the OCP is a major issue that must be taken into account as it might condition the future applicability of OC.

Weaknesses deserving a further review and interesting future works that may follow the studies presented in this dissertation, attempting to close the gap between the laboratory and the road implementation of OC, are commented below.

10.2.1 Powertrain modeling

The availability of accurate powertrain models is key for any kind of model-based control, and OC is not an exception. The quality of the control is mostly related to the model ability to represent the actual system. Unfortunately, powertrain and, especially, engines are complex systems with many states and controls that usually require sophisticated models to be represented accurately. Additional peripherals such as after-treatment devices are highly nonlinear and their modeling tend to be tedious.

Anyhow, several models presented in this dissertation might deserve an additional turn of screw in order to analyze further situations and conditions. A dynamic LP- and HP-EGR modeling–a quasi-steady approach was implemented for this dissertation–may address switching strategies that are far from a real application. In addition to that, a dynamic model might be able to properly represent the combined operation of both systems together. Similarly, a dynamic HEV model with a detailed battery model would be key to address a comprehensive validation of the proposed strategies, emphasizing on the battery sustaining robustness. The introduction of additional pollutants might be interesting in order to check control strategies performance not only for NO_x, but also regarding PM, HC or CO. Particularly, the thermal NO_x model used for the HRL calculation may be extended to other NO_x formation mechanism in order to close the gap between simulations and experimental measurements. Thermal transients might also be interesting to assess the control policy in cold or warm up conditions.

10.2.2 Additional constraints

The addressed OCPs included a set of constraints related to safety and emissions concerns as well as specific problem requirements. However, the advantages of considering additional constraints is twofold: a more realistic approach can be assessed and the impact of model uncertainties might be

reduced. Particularly, the introduction of performance constraints in the engine control problem may enable to find a more robust and practical control policy that takes into account the response smoothness or the torque reserve among other concerns, which are key for onboard applications. Additionally, a proper identification of fuel injection system constraints would significantly improve the ability to produce a feasible optimal HRL.

10.2.3 Comprehensive experimental validation

The experimental validations of the OC strategies is a necessary step to analyze real-world performance and advantages of the proposed methods. Despite some works have included a detailed set of experiments, the unavailability of testing facilities for all the studies presented so far limited some approaches to the theoretical plane. In this sense, HEV power-split control and, especially, the optimal speed management problem may deserve a further experimental validation in order to prove that the advantages found in simulation can be translated to an actual vehicle.

In addition to that, a deeper experimental work can be also carried out for those OC approaches that have been already experimentally validated. A comprehensive analysis of OC performance under a bundle of different operating conditions and driving cycles is out of the scope of this dissertation, but it might throw some interesting results.

10.2.4 Adaption to onboard applications

The ultimate goal of an OC work is to be implemented for onboard applications. Due to its mathematical complexity, the requirement of a detailed model and the dependency on future operating conditions on a rigorous sense, an online optimal algorithm has been always a difficult task. Although most of the works presented in this dissertation can be directly applied for benchmarking, powertrain analysis or control calibration, their onboard implementation in an standalone form requires an extended research.

In an attempt to close the gap between offline and onboard applications, two main philosophies can be followed. On the one hand, models and methods can be simplified in order to find a sufficiently compact control law. An interesting work in this sense might be the use of variable engine calibrations extracted from several optimization instances for different levels of pollutant emissions. This way, the tedious OCP may be simplified to a smart selection of one of those available calibrations keeping the traditional control scheme, which is something that can be implemented onboard in a straightforward form. On the other hand, methodologies to estimate future requirements may

be used together with an OC strategy in order to evaluate the performance of an standalone approach. These techniques may range from a road profile look-ahead control to any kind of sophisticated estimator feeding the OCP. Of course, other numerical or stochastic algorithm may be also used in lieu of OC for onboard applications, but the optimality concern will vanish.

10.2.5 Potential applications

The proper definition of an OCP requires accurate look-ahead information which is not available in many automotive applications. Despite this is a major drawback that will prevent OC use in some fields, there are many other vehicular control problems whose boundary conditions can be easily guessed.

In this sense, some automotive control problems that may be affordable for OC are:

- Engine control during an overtaking maneuver. If the controller detects a slower vehicle ahead and the driver activates the direction indicator, it can be assumed that an overtaking maneuver is about to be performed. In this situation, the vehicle must accelerate and place in front of the other vehicle, whose speed is known, in a given time, so the situation can be accurately defined.

- Engine control during transients. In the event of an operating engine point change, a different setpoint in engine variables must be reached. Since the transient only lasts a couple of seconds, this problem is well defined–engine speed and torque request are known, similarly to the work presented in section 6.3–and optimal trajectories for the VGT, the EGR or any other actuator can be calculated.

- Cruise control with look-ahead information. A speed controller in combination of a GPS device may have a quite good look of the road. If the driver introduces a destination, the elevation profile and traffic conditions can be known beforehand. Then, the optimal speed profile–and eventually a specific engine calibration as done in chapter 7–can be computed.

- Management of vehicle dynamics in extreme situations. The picture in the event of tire slip may be defined accurately. At that very moment, roll, yaw, pitch and accelerations can be measured, and the road friction may be estimated [1–3]. The boundaries are clear: going back to a non sliding condition in the minimum time or distance. The OCP is pretty well defined and OC might be used for Anti-lock Braking System (ABS) or Electronic Stability Program (ESP) systems.

- Control of an autonomous vehicle. In a road where all vehicles are self-driven and connected together in order to exchange information, all boundaries are perfectly known and no external disturbances exist. In this context, an OCP can be accurately defined.

The unequivocal definition of an OCP in any of the above control problems– and many other the reader might imagine–enables for a practical application of OC. The methods developed and discussed in this dissertation may be applied to any of these problems as long as the necessary models are available.

References

[1] J.-O. Hahn, R. Rajamani, and L. Alexander. "GPS-based real-time identification of tire-road friction coefficient". In: *IEEE Transactions on Control Systems Technology* 10.3 (2002), pp. 331–343.

[2] S. Muller, M. Uchanski, and K. Hedrick. "Estimation of the maximum tire-road friction coefficient". In: *Journal of dynamic systems, measurement, and control* 125.4 (2003), pp. 607–617.

[3] C. Lee, K. Hedrick, and K. Yi. "Real-time slip-based estimation of maximum tire-road friction coefficient". In: *IEEE/ASME Transactions on Mechatronics* 9.2 (2004), pp. 454–458.

Appendices

Appendix A

From time domain to distance domain

The OCP formulation has been stated in time domain so far. Despite a dynamic system is generally represented with time dependent functions, an OCP can be expressed in other domains with a simple variable change. This is especially useful when the system can be easily modeled as a function of a monotonic quantity rather than time. In fact, many transportation systems might be better defined as a function of the traveled distance–speed limits or track gradient are naturally related to a position.

A domain change from time t to distance s can be addressed as a variable change:

$$\mathrm{d}t = \frac{\mathrm{d}s}{v} \tag{A.1}$$

where speed v relates both domain variables.

Applying the above variable change the cost index stays as:

$$J = \int_0^{\mathcal{S}} \frac{L(\boldsymbol{x}, \boldsymbol{u})}{v}\, \mathrm{d}s \tag{A.2}$$

Note that states $\boldsymbol{x}$ and control variables $\boldsymbol{u}$ are no longer functions of time but of distance.

The dynamics of the system are also affected by the domain change:

$$\frac{\mathrm{d}x}{\mathrm{d}s} = \frac{f(\boldsymbol{x}, \boldsymbol{u})}{v} \tag{A.3}$$

Again $\boldsymbol{x}$ and $\boldsymbol{u}$ are functions of the distance and thus the differential is defined with respect to s.

The boundary conditions (2.4) and (2.5) are not functions of time but constraints at the bounds of the problem. Therefore, they apply to the distance-domain OCP with minor changes, referring to the bounds of the distance domain:

$$\boldsymbol{x}(0) = \boldsymbol{x}_0 \tag{A.4}$$

$$\phi(\boldsymbol{x}(\mathcal{S})) \leq 0 \tag{A.5}$$

where $0 \leq s \leq \mathcal{S}$ are the bounds of the distance domain such that $\mathcal{S} = s(\mathcal{T})$.

Regarding the path constraints it might happen one of three different scenarios. First, if there is not an explicit time dependency, *i.e.* $c(\boldsymbol{x}, \boldsymbol{u}) \leq 0$, (2.6) applies without changes. Second, if the constraint is an explicit function of time, the variable change $t = \int_0^s 1/v \, \mathrm{d}s$ must be issued. This introduces the time as an additional state due to the presence of the integral term, making the domain change unattractive. And third, if a path constraint can be easily defined in distance, but in time it requires to introduce the distance as an additional state, the constraint can be directly defined in distance as:

$$c(\boldsymbol{x}, \boldsymbol{u}, s) \leq 0 \tag{A.6}$$

This is the main advantage of the domain change.

Integral constraints can be expressed in the distance domain as:

$$\int_0^{\mathcal{S}} \frac{q(\boldsymbol{x}, \boldsymbol{u})}{v} \, \mathrm{d}s \leq 0 \tag{A.7}$$

Note that if $q \propto v$ the integrand may vanish. The constraint is then proportional to $\mathcal{S}$, which is a constant quantity for the problem. This occurs because while the integral constraint was originally defined in time domain to fix a distance limit, in the distance domain this limit is implicitly included in the boundaries of the domain, leaving this constraint unnecessary. A different definition of the integral constraint is required in this situation–usually it may be interesting to fix a terminal time of the form $\int_0^{\mathcal{S}} 1/v \, \mathrm{d}s \leq \mathcal{T}$ instead.

Therefore, the time domain OCP described in eqs. (2.1)–(2.7) can be easily transformed into the equivalent problem at eqs. (A.2)–(A.7) which is defined in distance domain to reduce the OCP complexity in the appropriate situations. Note that, despite the process has been described to write the problem in distance domain, it can be moved to any other domain whose describing variable is a monotonic function (increasing or decreasing) following the same procedure.

Bibliography

E. A. Ajav, B. Singh, and T. K. Bhattacharya. "Thermal balance of a single cylinder diesel engine operating on alternative fuels". In: *Energy Conversion and Management* 41.14 (2000), pp. 1533–1541 (cit. on p. 36).

K. Akihama et al. *Mechanism of the smokeless rich diesel combustion by reducing temperature*. Tech. rep. SAE Technical Paper, 2001 (cit. on pp. 28, 171).

S. F. Alyaqout, P. Y. Papalambros, and A. G. Ulsoy. "Coupling in design and robust control optimization". In: *European Control Conference (ECC)*. IEEE. 2007, pp. 1414–1421 (cit. on p. 38).

D. Ambühl and L. Guzzella. "Predictive reference signal generator for hybrid electric vehicles". In: *IEEE Transactions on Vehicular Technology* 58.9 (2009), pp. 4730–4740 (cit. on p. 36).

D. Ambühl et al. "Explicit optimal control policy and its practical application for hybrid electric powertrains". In: *Control Engineering Practice* 18.12 (2010), pp. 1429–1439 (cit. on p. 33).

AMD64 architecture programmer's manual volume 2: System programming. Advanced Micro Devices. 2006 (cit. on p. 63).

J. Arrégle et al. "On board NOx prediction in diesel engines: a physical approach". In: *Automotive Model Predictive Control*. Springer, 2010, pp. 25–36 (cit. on pp. 129, 243).

I. Arsie et al. "Optimization of supervisory control strategy for parallel hybrid vehicle with provisional load estimate". In: *Proceedings of the 7th International Symposium on Advanced Vehicle Control* 1 (2004), pp. 483–488 (cit. on p. 33).

U. Asad and M. Zheng. "Exhaust gas recirculation for advanced diesel combustion cycles". In: *Applied Energy* 123 (2014), pp. 242–252 (cit. on p. 28).

B. Asadi and A. Vahidi. "Predictive cruise control: Utilizing upcoming traffic signal information for improving fuel economy and reducing trip time". In: *IEEE Transactions on Control Systems Technology* 19.3 (2011), pp. 707–714 (cit. on p. 21).

J. Asprion, O. Chinellato, and L. Guzzella. "Optimal control of diesel engines: Numerical methods, applications, and experimental validation". In: *Mathematical Problems in Engineering* 1 (2014), pp. 1–21 (cit. on pp. 26, 27, 75).

J. Asprion, O. Chinellato, and L. Guzzella. "Optimisation-oriented modelling of the NOx emissions of a diesel engine". In: *Energy Conversion and Management* 75 (2013), pp. 61–73 (cit. on pp. 125, 126).

D. Assanis et al. "Optimization approach to hybrid electric propulsion system design". In: *Mechanics of Structures and Machines* 27.4 (1999), pp. 393–421 (cit. on p. 37).

M. Athans. *The role of modern control theory for automotive engine control*. Tech. rep. SAE Technical Paper, 1978 (cit. on p. 25).

B. Bachmann et al. "Parallel multiple-shooting and collocation optimization with OpenModelica". In: *Proceedings of the 9th International Modelica Conference*. 76. 2012, pp. 659–668 (cit. on p. 26).

S. Barsali, M. Ceraolo, and A. Possenti. "Techniques to control the electricity generation in a series hybrid electrical vehicle". In: *IEEE Transactions on Energy Conversion* 17.2 (2002), pp. 260–266 (cit. on p. 34).

D. Barth. *The bright side of sitting in traffic: Crowdsourcing road congestion data*. Google Official Blog. 2009 (cit. on p. 233).

R. Bellman. "Dynamic programming and Lagrange multipliers". In: *Proceedings of the National Academy of Sciences* 42.10 (1956), pp. 767–769 (cit. on pp. 20, 62–64).

R. Bellman. "The theory of dynamic programming". In: *Bulletin of the American Mathematical Society* 60.6 (1954), pp. 503–515 (cit. on pp. 18, 60).

J. Bengtssonv et al. "Model predictive control of homogeneous charge compression ignition (HCCI) engine dynamics". In: *Proceedings of the IEEE International Conference on Control Applications*. 2006, pp. 1675–1680 (cit. on p. 26).

D. A. Benson et al. "Direct trajectory optimization and costate estimation via an orthogonal collocation method". In: *Journal of Guidance, Control, and Dynamics* 29.6 (2006), pp. 1435–1440 (cit. on p. 77).

M. Benz et al. "Model-based actuator trajectories optimization for a diesel engine using a direct method". In: *Journal of Engineering for Gas Turbines and Power* 133.3 (2011), pp. 1–11 (cit. on pp. 26, 27).

V. Bermúdez et al. "Effects of low pressure exhaust gas recirculation on regulated and unregulated gaseous emissions during NEDC in a light-duty diesel engine". In: *Energy* 36.9 (2011), pp. 5655–5665 (cit. on p. 172).

J. Bernard et al. "Fuel efficient power management strategy for fuel cell hybrid powertrains". In: *Control Engineering Practice* 18.4 (2010), pp. 408–417 (cit. on pp. 33, 258).

D. P. Bertsekas. *Nonlinear programming*. Athena scientific Belmont, 1999 (cit. on p. 86).

J. T. Betts. *Practical methods for optimal control and estimation using nonlinear programming*. SIAM, 2010 (cit. on pp. 18, 77).

P. Bonami et al. "An algorithmic framework for convex mixed integer nonlinear programs". In: *Discrete Optimization* 5.2 (2008), pp. 186–204 (cit. on p. 87).

A. Brahma et al. "Modeling, performance analysis and control design of a hybrid sport-utility vehicle". In: *Proceedings of the IEEE International Conference on Control Applications*. Vol. 1. 1999, pp. 448–453 (cit. on p. 32).

A. Broatch et al. "A procedure to reduce pollutant gases from diesel combustion during European MVEG-A cycle by using electrical intake air-heaters". In: *Fuel* 87.12 (2008), pp. 2760–2778 (cit. on p. 170).

A. Broatch et al. "Pollutants instantaneous measurement and data analysis of engine-in-the-loop tests". In: *Thiesel International Conference on Thermo and Fluid Dynamic processes in Direct Injection Engines*. 2006 (cit. on p. 159).

A. E. Bryson and Y.-C. Ho. *Applied optimal control: optimization, estimation, and control*. Taylor & Francis, 1975 (cit. on pp. 18–21, 61, 71–74).

J. R. Bumby and I. Forster. "Optimisation and control of a hybrid electric car". In: *IEE Proceedings D-Control Theory and Applications*. Vol. 134. 6. 1987, pp. 373–387 (cit. on pp. 31–33, 226).

D. L. Buntin and J. W. Howze. "A switching logic controller for a hybrid electric/ICE vehicle". In: *Proceedings of the American Control Conference*. Vol. 2. 1995, pp. 1169–1175 (cit. on p. 32).

F. Castillo et al. “Simultaneous air fraction and low-pressure EGR mass flow rate estimation for diesel engines”. In: *IFAC Proceedings Volumes* 46.2 (2013), pp. 731–736 (cit. on pp. 29, 167).

J. A. Caton. *A review of investigations using the second law of thermodynamics to study internal-combustion engines*. Tech. rep. SAE Technical Paper, 2000 (cit. on pp. 36, 242).

C. C. Chan. “The state of the art of electric, hybrid, and fuel cell vehicles”. In: *Proceedings of the IEEE* 95.4 (2007), pp. 704–718 (cit. on pp. 30, 258).

C. C. Chan, Y. S. Wong, and A. Bouscayrol. “Powering sustainable mobility: Roadmaps of electric, hybrid, and fuel cell vehicles”. In: *Proceedings of the IEEE* 97.4 (2009), pp. 603–607 (cit. on p. 30).

A. Chasse and A. Sciarretta. “Supervisory control of hybrid powertrains: An experimental benchmark of offline optimization and online energy management”. In: *Control Engineering Practice* 19.11 (2011), pp. 1253–1265 (cit. on p. 33).

A. Chasse, A. Sciarretta, and J. Chauvin. “Online optimal control of a parallel hybrid with costate adaptation rule”. In: *Proceedings of the 6th IFAC Symposium: Advances in Automotive Control*. 2010, pp. 99–104 (cit. on pp. 35, 227).

R. Cipollone and A. Sciarretta. “Analysis of the potential performance of a combined hybrid vehicle with optimal supervisory control”. In: *Proceedings of the IEEE International Conference on Control Applications*. 2006, pp. 2802–2807 (cit. on pp. 33, 227).

G. Constable and B. Somerville. *A century of innovation: Twenty engineering achievements that transformed our lives*. Joseph Henry Press, 2003 (cit. on p. 4).

C. L. Darby and A. V. Rao. “Minimum-fuel low-earth orbit aeroassisted orbital transfer of small spacecraft”. In: *Journal of Spacecraft and Rockets* 48.4 (2011), pp. 618–628 (cit. on pp. 18, 75).

S. C. Davis, S. E. Williams, and R. G. Boundy. *Transportation energy data book: Edition 35*. Tech. rep. Oak Ridge National Laboratory, 2016 (cit. on p. 6).

B. De Jager, T. Van Keulen, and J. Kessels. *Optimal control of hybrid vehicles*. Springer, 2013 (cit. on p. 34).

S. Delprat, T. M. Guerra, and J. Rimaux. “Control strategies for hybrid vehicles: synthesis and evaluation”. In: *IEEE 58th Vehicular Technology Conference*. Vol. 5. 2003, pp. 3246–3250 (cit. on p. 34).

S. Delprat, T. M. Guerra, and J. Rimaux. "Optimal control of a parallel powertrain: from global optimization to real time control strategy". In: *IEEE 55th Vehicular Technology Conference*. Vol. 4. 2002, pp. 2082–2088 (cit. on pp. 33, 226, 259).

S. Delprat et al. "Control strategy optimization for an hybrid parallel powertrain". In: *Proceedings of the American Control Conference*. Vol. 2. 2001, pp. 1315–1320 (cit. on pp. 32, 33, 226).

S. Delprat et al. "Control of a parallel hybrid powertrain: optimal control". In: *IEEE Transactions on Vehicular Technology* 53.3 (2004), pp. 872–881 (cit. on p. 33).

M. Delucchi et al. *Electric and gasoline vehicle lifecycle cost and energy-use model*. Tech. rep. Institute of Transportation Studies, 2000 (cit. on pp. 38, 263–266).

J. Demuynck et al. "Recommendations for the new WLTP cycle based on an analysis of vehicle emission measurements on NEDC and CADC". In: *Energy Policy* 49 (2012), pp. 234–242 (cit. on p. 7).

S. Dermann and R. Isermann. "Nonlinear distance and cruise control for passenger cars". In: *Proceedings of the American Control Conference*. Vol. 5. 1995, pp. 3081–3085 (cit. on p. 21).

C. Desai and S. S. Williamson. "Optimal design of a parallel hybrid electric vehicle using multi-objective genetic algorithms". In: *IEEE Vehicle Power and Propulsion Conference*. 2009, pp. 871–876 (cit. on p. 37).

J. M. Desantes et al. "On the combination of high-pressure and low-pressure exhaust gas recirculation loops for improved fuel economy and reduced emissions in high-speed direct-injection engines". In: *International Journal of Engine Research* 14.1 (2013), pp. 3–11 (cit. on pp. 28, 166, 172).

W. Dib, L. Serrao, and A. Sciarretta. "Optimal control to minimize trip time and energy consumption in electric vehicles". In: *IEEE Vehicle Power and Propulsion Conference*. 2011, pp. 1–8 (cit. on p. 24).

W. Dib et al. "Optimal energy management for an electric vehicle in eco-driving applications". In: *Control Engineering Practice* 29 (2014), pp. 299–307 (cit. on pp. 24, 209, 210).

W. Dib et al. "Evaluation of the energy efficiency of a fleet of electric vehicle for eco-driving application". In: *Oil & Gas Science and Technology – Revue d'IFP Energies nouvelles* 67.4 (2012), pp. 589–599 (cit. on pp. 22, 209, 210).

M. Diehl et al. “Fast direct multiple shooting algorithms for optimal robot control”. In: *Fast motions in biomechanics and robotics*. Springer, 2006, pp. 65–93 (cit. on pp. 12, 60, 75).

M. A. Duran and I. E. Grossmann. “An outer-approximation algorithm for a class of mixed-integer nonlinear programs”. In: *Mathematical programming* 36.3 (1986), pp. 307–339 (cit. on p. 87).

S. Ebbesen, P. Elbert, and L. Guzzella. “Engine downsizing and electric hybridization under consideration of cost and drivability”. In: *Oil & Gas Science and Technology – Revue d’IFP Energies nouvelles* 68.1 (2013), pp. 109–116 (cit. on pp. 38, 258, 260, 261).

M. Ehsani, K. M. Rahman, and H. A. Toliyat. “Propulsion system design of electric and hybrid vehicles”. In: *IEEE Transactions on Industrial Electronics* 44.1 (1997), pp. 19–27 (cit. on p. 37).

A. Emadi et al. “Topological overview of hybrid electric and fuel cell vehicular power system architectures and configurations”. In: *IEEE Transactions on Vehicular Technology* 54.3 (2005), pp. 763–770 (cit. on p. 101).

Energy, transport and environment indicators, 2016 edition. Eurostat, European Union. 2016 (cit. on pp. 4–7).

P. J. Enright and B. A. Conway. “Optimal finite-thrust spacecraft trajectories using collocation and nonlinear programming”. In: *Journal of Guidance, Control and Dynamics* 14.5 (1991), pp. 981–985 (cit. on pp. 10, 75).

L. Eriksson and M. Sivertsson. “Computing optimal heat release rates in combustion engines”. In: *SAE International Journal of Engines* 8.3 (2015), pp. 1069–1079 (cit. on pp. 36, 242).

F. Fahroo and I. M. Ross. “Advances in pseudospectral methods for optimal control”. In: *AIAA Guidance, Navigation and Control Conference and Exhibit*. 2008, pp. 1–23 (cit. on p. 75).

P. Falcone et al. “Predictive active steering control for autonomous vehicle systems”. In: *IEEE Transactions on Control Systems Technology* 15.3 (2007), pp. 566–580 (cit. on p. 10).

S. D. Farrall and R. P. Jones. “Energy management in an automotive electric/heat engine hybrid powertrain using fuzzy decision making”. In: *Proceedings of the IEEE International Symposium on Intelligent Control*. 1993, pp. 463–468 (cit. on p. 32).

R. Fellini et al. “Optimal design of automotive hybrid powertrain systems”. In: *Proceedings First International Symposium on Environmentally Conscious Design and Inverse Manufacturing*. 1999, pp. 400–405 (cit. on p. 37).

A. Fröberg, E. Hellström, and L. Nielsen. "Explicit fuel optimal speed profiles for heavy trucks on a set of topographic road profiles". In: *SAE Technical Paper*. 2006 (cit. on pp. 22, 23).

K. Fujisawa, M. Kojima, and K. Nakata. "Exploiting sparsity in primal-dual interior-point methods for semidefinite programming". In: *Mathematical Programming* 79.1 (1997), pp. 235–253 (cit. on p. 78).

W. Gao and S. K. Porandla. "Design optimization of a parallel hybrid electric powertrain". In: *IEEE Vehicle Power and Propulsion Conference*. 2005, p. 6 (cit. on p. 37).

W. Gao and C. Mi. "Hybrid vehicle design using global optimisation algorithms". In: *International Journal of Electric and Hybrid Vehicles* 1.1 (2007), pp. 57–70 (cit. on p. 37).

H. P. Geering. *Optimal control with engineering applications*. Springer, 2007 (cit. on pp. 21, 65, 71).

T. D. Gillispie. *Fundamentals of vehicle dynamics*. SAE International, 1992 (cit. on p. 95).

R. Grisenthwaite. "ARMv8 technology preview". In: *IEEE Conference*. 2011 (cit. on p. 63).

O. Grondin, P. Moulin, and J. Chauvin. "Control of a turbocharged diesel engine fitted with high pressure and low pressure exhaust gas recirculation systems". In: *Joint 48th IEEE Conference on Decision and Control and 28th Chinese Control Conference*. 2009, pp. 6582–6589 (cit. on pp. 29, 167).

O. Grondin et al. "Energy management strategy for diesel hybrid electric vehicle". In: *IEEE Vehicle Power and Propulsion Conference*. 2011, pp. 1–8 (cit. on pp. 33, 34).

C. Guardiola et al. "A new approach to optimally tune the control strategy for hybrid vehicles applications". In: *Engine and Powertrain Control, Simulation and Modeling*. Vol. 3. 1. 2012, pp. 255–261 (cit. on pp. 35, 75).

C. Guardiola et al. "Adaptive calibration for reduced fuel consumption and emissions". In: *Proceedings of the Institution of Mechanical Engineers, Part D: Journal of Automobile Engineering* 230.14 (2016), pp. 2002–2014 (cit. on p. 25).

C. Guardiola et al. "ECU-oriented models for NOx prediction. Part 1: a mean value engine model for NOx prediction". In: *Proceedings of the Institution of Mechanical Engineers, Part D: Journal of Automobile Engineering* 229.8 (2015), pp. 992–1015 (cit. on p. 129).

C. Guardiola et al. "Optimal control as a method for diesel engine efficiency assessment including pressure and NOx constraints". In: *Applied Thermal Engineering* 117 (2017), pp. 452–461 (cit. on p. 242).

C. Guardiola et al. "Representation limits of mean value engine models". In: *Identification for Automotive Systems*. Springer, 2012, pp. 185–206 (cit. on pp. 107, 121, 173).

C. Guardiola et al. "Insight into the HEV/PHEV optimal control solution based on a new tuning method". In: *Control Engineering Practice* 29 (2014), pp. 247–256 (cit. on pp. 35, 75, 261).

C. Guardiola et al. "Modelling driving behaviour and its impact on the energy management problem in hybrid electric vehicles". In: *International Journal of Computer Mathematics* 91.1 (2014), pp. 147–156 (cit. on pp. 35, 227, 259).

C. Guardiola et al. "Semiempirical in-cylinder pressure based model for NOx prediction oriented to control applications". In: *Applied Thermal Engineering* 31.16 (2011), pp. 3275–3286 (cit. on p. 130).

L. Guzzella and A. Sciarretta. *Vehicle propulsion systems. Introduction to modeling and optimization*. Springer-Verlag, 2005 (cit. on pp. 30, 31, 97, 100, 101, 103, 105).

L. Guzzella and C. H. Onder. *Introduction to modeling and control of internal combustion engine systems*. Springer, 2004 (cit. on pp. 108, 113, 114, 119, 120, 122, 125, 126, 131).

P. Hagelauer and F. Mora-Camino. "A soft dynamic programming approach for on-line aircraft 4D-trajectory optimization". In: *European Journal of Operational Research* 107.1 (1998), pp. 87–95 (cit. on pp. 10, 18).

J.-O. Hahn, R. Rajamani, and L. Alexander. "GPS-based real-time identification of tire-road friction coefficient". In: *IEEE Transactions on Control Systems Technology* 10.3 (2002), pp. 331–343 (cit. on p. 290).

A. Haj-Fraj and F. Pfeiffer. "Optimal control of gear shift operations in automatic transmissions". In: *Journal of the Franklin Institute* 338.2-3 (2001), pp. 371–390 (cit. on p. 27).

H. He, R. Xiong, and J. Fan. "Evaluation of lithium-ion battery equivalent circuit models for state of charge estimation by an experimental approach". In: *Energies* 4.4 (2011), pp. 582–598 (cit. on p. 107).

E. Hellström, J. Åslund, and L. Nielsen. "Design of an efficient algorithm for fuel-optimal look-ahead control". In: *Control Engineering Practice* 18.11 (2010), pp. 1318–1327 (cit. on pp. 22, 23).

E. Hellström, A. Fröberg, and L. Nielsen. "A real-time fuel-optimal cruise controller for heavy trucks using road topography information". In: *SAE Technical Paper*. 2006 (cit. on pp. 22, 23).

E. Hellström et al. "Look-ahead control for heavy trucks to minimize trip time and fuel consumption". In: *Control Engineering Practice* 17.2 (2009), pp. 245–254 (cit. on pp. 22, 23).

E. Hellström et al. "On-board calibration of spark timing by extremum seeking for flex-fuel engines". In: *IEEE Transactions on Control Systems Technology* 21.6 (2013), pp. 2273–2279 (cit. on pp. 10, 25).

H. Hemi, J. Ghouili, and A. Cheriti. "Combination of Markov chain and optimal control solved by Pontryagin's minimum principle for a fuel cell/supercapacitor vehicle". In: *Energy Conversion and Management* 91 (2015), pp. 387–393 (cit. on p. 35).

J. Heywood. *Internal combustion engine fundamentals*. McGraw-Hill, 1988 (cit. on pp. 113, 114, 116, 121, 124–126, 262).

M. Hinze and A. Rösch. "Discretization of optimal control problems". In: *Constrained optimization and optimal control for partial differential equations*. Springer, 2012, pp. 391–430 (cit. on p. 75).

J. N. Hooker. "Optimal driving for single-vehicle fuel economy". In: *Transportation Research Part A: General* 22.3 (1988), pp. 183–201 (cit. on p. 23).

J. N. Hooker, A. B. Rose, and G. F. Roberts. "Optimal control of automobiles for fuel economy". In: *Transportation Science* 17.2 (1983), pp. 146–167 (cit. on p. 22).

D. T. Hountalas, G. C. Mavropoulos, and K. B. Binder. "Effect of exhaust gas recirculation (EGR) temperature for various EGR rates on heavy duty DI diesel engine performance and emissions". In: *Energy* 33.2 (2008), pp. 272–283 (cit. on p. 171).

D. Hrovat et al. "The development of model predictive control in automotive industry: A survey". In: *IEEE International Conference on Control Applications*. 2012, pp. 295–302 (cit. on p. 26).

X. Hu et al. "Comparison of three electrochemical energy buffers applied to a hybrid bus powertrain with simultaneous optimal sizing and energy management". In: *IEEE transactions on intelligent transportation systems* 15.3 (2014), pp. 1193–1205 (cit. on pp. 37, 258).

X. Hu et al. "Longevity-conscious dimensioning and power management of the hybrid energy storage system in a fuel cell hybrid electric bus". In: *Applied Energy* 137 (2015), pp. 913–924 (cit. on pp. 37, 258).

X. Hu et al. "Optimal dimensioning and power management of a fuel cell/battery hybrid bus via convex programming". In: *IEEE/ASME Transactions on Mechatronics* 20.1 (2015), pp. 457–468 (cit. on pp. 37, 258).

V. Isastia and S. Meo. "Overview on automotive energy storage systems". In: *International Review of Electrical Engineering* 4.6 (2009), pp. 1122–1144 (cit. on p. 258).

Internal combustion compression-ignition engines – Measurement apparatus for smoke from engines operating under steady-state conditions – Filter-type smokemeter. International Organization for Standardization. Geneva, CH, 1998 (cit. on p. 144).

M. Jain et al. "Optimal powertrain component sizing of a fuel cell plug-in hybrid electric vehicle using multi-objective genetic algorithm". In: *Proceedings of the Industrial Electronics Conference*. 2009, pp. 3741–3746 (cit. on pp. 37, 258).

N. Jalil, N. A. Kheir, and M. Salman. "A rule-based energy management strategy for a series hybrid vehicle". In: *Proceedings of the American Control Conference*. Vol. 1. 1997, pp. 689–693 (cit. on p. 32).

S. Jiang, D. Nutter, and A. Gullitti. "Implementation of model-based calibration for a gasoline engine". In: *SAE Technical Paper*. 2012 (cit. on p. 10).

L. Johannesson, M. Asbogard, and B. Egardt. "Assessing the potential of predictive control for hybrid vehicle powertrains using stochastic dynamic programming". In: *IEEE Transactions on Intelligent Transportation Systems* 8.1 (2007), pp. 71–83 (cit. on p. 36).

L. Johannesson and B. Egardt. "Approximate dynamic programming applied to parallel hybrid powertrains". In: *IFAC Proceedings Volumes* 41.2 (2008), pp. 3374–3379 (cit. on pp. 33, 227).

L. Johannesson, S. Pettersson, and B. Egardt. "Predictive energy management of a 4QT series-parallel hybrid electric bus". In: *Control Engineering Practice* 17.12 (2009), pp. 1440–1453 (cit. on p. 35).

L. Johannesson et al. "Including a battery state of health model in the HEV component sizing and optimal control problem". In: *IFAC Advances in Automotive Control*. Vol. 7. 1. 2013, pp. 398–403 (cit. on pp. 37, 258, 271).

D. H. Johnson. "Origins of the equivalent circuit concept: the voltage-source equivalent". In: *Proceedings of the IEEE* 91.4 (2003), pp. 636–640 (cit. on p. 105).

T. V. Johnson. "Vehicular emissions in review". In: *SAE International Journal of Engines* 7 (2014), pp. 1207–1227 (cit. on p. 7).

W. Kang and N. Bedrossian. "Pseudospectral optimal control theory makes debut flight, saves NASA $1 M in under three hours". In: *SIAM news* 40.7 (2007), pp. 1–3 (cit. on p. 75).

D. Karbowski, C. Haliburton, and A. Rousseau. "Impact of component size on PHEV energy consumption using global optimization". In: *The World Electric Vehicle Journal* 2.2 (2008), pp. 92–100 (cit. on pp. 37, 38).

R. Katzev. "Car sharing: A new approach to urban transportation problems". In: *Analyses of Social Issues and Public Policy* 3.1 (2003), pp. 65–86 (cit. on p. 5).

T. van Keulen et al. "Design, implementation, and experimental validation of optimal power split control for hybrid electric trucks". In: *Control Engineering Practice* 20.5 (2012), pp. 547–558 (cit. on pp. 35, 226).

M. J. Kim et al. "Testing, modeling, and control of a fuel cell hybrid vehicle". In: *Proceedings of the American Control Conference*. 2005, pp. 3859–3864 (cit. on p. 36).

M.-J. Kim and H. Peng. "Power management and design optimization of fuel cell/battery hybrid vehicles". In: *Journal of Power Sources* 165.2 (2007), pp. 819–832 (cit. on p. 38).

N. Kim, S. W. Cha, and H. Peng. "Optimal equivalent fuel consumption for hybrid electric vehicles". In: *IEEE Transactions on Control Systems Technology* 20.3 (2012), pp. 817–825 (cit. on p. 36).

N. Kim, S. Cha, and H. Peng. "Optimal control of hybrid electric vehicles based on Pontryagin's minimum principle". In: *IEEE Transactions on Control Systems Technology* 19.5 (2011), pp. 1279–1287 (cit. on p. 34).

N. Kim et al. "Optimal control of a plug-in hybrid electric vehicle (PHEV) based on driving patterns". In: *International Battery, Hybrid and Fuel Cell Electric Vehicle Symposium*. 2009, pp. 1–9 (cit. on p. 36).

A. Kleimaier and D. Schroder. "Optimization strategy for design and control of a hybrid vehicle". In: *Proceedings of the 6th International Workshop on Advanced Motion Control*. 2000, pp. 459–464 (cit. on p. 37).

D. E. Knuth. "Postscript about NP-hard problems". In: *SIGACT News* 6.2 (1974), pp. 15–16 (cit. on p. 87).

N. Ladommatos, S. M. Abdelhalim, and H. Zhao. "Effects of exhaust gas recirculation temperature on diesel engine combustion and emissions". In: *Proceedings of the Institution of Mechanical Engineers, Part D: Journal of Automobile Engineering* 212.6 (1998), pp. 479–500 (cit. on p. 171).

A. H. Land and A. G. Doig. "An automatic method of solving discrete programming problems". In: *Econometrica: Journal of the Econometric Society* 28.3 (1960), pp. 497–520 (cit. on p. 87).

M. Lapuerta, O. Armas, and J. J. Hernández. "Diagnosis of DI diesel combustion from in-cylinder pressure signal by estimation of mean thermodynamic properties of the gas". In: *Applied Thermal Engineering* 19.5 (1999), pp. 513–529 (cit. on p. 128).

S. Le Digabel. "Algorithm 909: NOMAD: nonlinear optimization with the MADS algorithm". In: *ACM Transactions on Mathematical Software* 37.4 (2011), pp. 1–15 (cit. on p. 87).

C. Lee, K. Hedrick, and K. Yi. "Real-time slip-based estimation of maximum tire-road friction coefficient". In: *IEEE/ASME Transactions on Mechatronics* 9.2 (2004), pp. 454–458 (cit. on p. 290).

J. Lescot et al. "On the integration of optimal energy management and thermal management of hybrid electric vehicles". In: *IEEE Vehicle Power and Propulsion Conference*. 2010, pp. 1–6 (cit. on p. 34).

F. Lewis and V. Syrmos. *Optimal control*. Wiley-Interscience, 1995 (cit. on pp. 18, 21, 61, 65, 71–74).

S. Li et al. "Model predictive multi-objective vehicular adaptive cruise control". In: *IEEE Transactions on Control Systems Technology* 19.3 (2011), pp. 556–566 (cit. on p. 21).

C.-C. Lin, H. Peng, and J. W. Grizzle. "A stochastic control strategy for hybrid electric vehicles". In: *Proceedings of the American Control Conference*. Vol. 5. 2004, pp. 4710–4715 (cit. on pp. 36, 227).

C.-C. Lin et al. "Energy management strategy for a parallel hybrid electric truck". In: *Proceedings of the American Control Conference*. Vol. 4. 2001, pp. 2878–2883 (cit. on pp. 33, 226).

C.-C. Lin et al. "Power management strategy for a parallel hybrid electric truck". In: *IEEE Transactions on Control Systems Technology* 11.6 (2003), pp. 839–849 (cit. on pp. 33, 35).

A. Lindgren and F. Chen. "State of the art analysis: An overview of advanced driver assistance systems (ADAS) and possible human factors issues". In: *Human Factors and Economic Aspects on Safety* 1 (2006), pp. 38–50 (cit. on p. 21).

T. E. Lipman and M. A. Delucchi. *Hybrid-electric vehicle design: Retail and life cycle cost analysis.* Institute of Transportation Studies, University of California at Davis, 2003 (cit. on p. 38).

J. Liu and H. Peng. "Control optimization for a power-split hybrid vehicle". In: *American Control Conference.* 2006, pp. 466–471 (cit. on p. 33).

J. Liu and H. Peng. "Modeling and control of a power-split hybrid vehicle". In: *IEEE Transactions on Control Systems Technology* 16.6 (2008), pp. 1242–1251 (cit. on pp. 33, 102).

J. Liu, H. Peng, and Z. Filipi. "Modeling and analysis of the Toyota hybrid system". In: *Proceedings of the IEEE/ASME International Conference on Advanced Intelligent Mechatronics.* Vol. 200. 2005, pp. 134–139 (cit. on p. 102).

R. R. Liu and I. M. Golovitcher. "Energy-efficient operation of rail vehicles". In: *Transportation Research Part A: Policy and Practice* 37.10 (2003), pp. 917–932 (cit. on p. 18).

X. Liu, Y. Wu, and J. Duan. "Optimal sizing of a series hybrid electric vehicle using a hybrid genetic algorithm". In: *IEEE International Conference on Automation and Logistics.* 2007, pp. 1125–1129 (cit. on pp. 34, 37, 258).

J. M. Luján et al. "A methodology to identify the intake charge cylinder-to-cylinder distribution in turbocharged direct injection diesel engines". In: *Measurement Science & Technology* 1 (2008), pp. 1–11 (cit. on p. 28).

J. M. Luján et al. "Considerations on the low-pressure exhaust gas recirculation system control in turbocharged diesel engines". In: *International Journal of Engine Research* 15.2 (2014), pp. 250–260 (cit. on p. 28).

J. M. Luján et al. "Effect of low pressure EGR on gas exchange processes and turbocharging of a HSDI engine". In: *Thiesel International Conference on Thermo and Fluid Dynamic processes in Direct Injection Engines.* 2008, pp. 429–442 (cit. on pp. 28, 166, 171, 172).

J. M. Luján et al. "Cost of ownership-efficient hybrid electric vehicle powertrain sizing for multi-scenario driving cycles". In: *Proceedings of the Institution of Mechanical Engineers, Part D: Journal of Automobile Engineering* 230.3 (2016), pp. 382–394 (cit. on p. 259).

J. M. Luján et al. "Switching strategy between HP (high pressure)- and LPEGR (low pressure exhaust gas recirculation) systems for reduced fuel consumption and emissions". In: *Energy* 90, Part 2 (2015), pp. 1790–1798 (cit. on p. 167).

A. Maiboom, X. Tauzia, and J. F. Hétet. "Influence of EGR unequal distribution from cylinder to cylinder on NOx–PM trade-off of a HSDI automotive diesel engine". In: *Energy* 29.10 (2009), pp. 2043–2050 (cit. on p. 28).

A. Maiboom, X. Tauzia, and J.-F. Hétet. "Experimental study of various effects of exhaust gas recirculation (EGR) on combustion and emissions of an automotive direct injection diesel engine". In: *Energy* 33.1 (2008), pp. 22–34 (cit. on pp. 28, 171).

A. A. Malikopoulos, D. N. Assanis, and P. Y. Papalambros. "Real-time self-learning optimization of diesel engine calibration". In: *Journal of Engineering for Gas Turbines and Power* 131.2 (2009), pp. 1–7 (cit. on p. 25).

A. A. Malikopoulos, P. Y. Papalambros, and D. N. Assanis. "A learning algorithm for optimal internal combustion engine calibration in real time". In: *ASME International Design Engineering Technical Conferences and Computers and Information in Engineering Conference*. 2007, pp. 91–100 (cit. on p. 25).

C. Manzie, W. Palaniswami, and H. Watson. "Model predictive control of a fuel injection system with a radial basis function network observer". In: *Proceedings of the IEEE-INNS-ENNS International Joint Conference on Neural Networks*. Vol. 4. 2000, pp. 359–364 (cit. on p. 26).

C. Manzie et al. "Robustness of ECMS-based optimal control in parallel hybrid vehicles". In: *Advances in Automotive Control*. Vol. 7. 1. 2013, pp. 127–132 (cit. on p. 34).

N. Marc et al. "Sizing and fuel consumption evaluation methodology for hybrid light duty vehicles". In: *World Electric Vehicle Journal* 4.1 (2011), pp. 249–258 (cit. on pp. 37, 38, 258).

K. McDonough et al. "Modeling of vehicle driving conditions using transition probability models". In: *IEEE International Conference on Control Applications*. 2011, pp. 544–549 (cit. on p. 35).

K. McDonough et al. "Stochastic dynamic programming control policies for fuel efficient in-traffic driving". In: *American Control Conference*. 2012, pp. 3986–3991 (cit. on p. 21).

F. Mensing, R. Trigui, and E. Bideaux. "Vehicle trajectory optimization for application in ECO-driving". In: *IEEE Vehicle Power and Propulsion Conference*. 2011, pp. 1–6 (cit. on pp. 22, 209, 210).

F. Merz et al. "On the optimal thermal management of hybrid-electric vehicles with heat recovery systems". In: *Oil & Gas Science and Technology – Revue d'IFP Energies nouvelles* 67.4 (2012), pp. 601–612 (cit. on p. 34).

T. Mesbahi et al. "Improved model of battery/supercapacitor hybrid energy storage system based on thermo-electrical and aging behaviors". In: *7th IET International Conference on Power Electronics, Machines and Drives*. 2014, pp. 1–8 (cit. on pp. 105, 258).

P. Michel et al. "3WCC temperature integration in a gasoline-HEV optimal energy management strategy". In: *Advances in Mechanical Engineering* 6 (2014), pp. 281–288 (cit. on p. 34).

W. F. Milliken and D. L. Milliken. *Race car vehicle dynamics*. Vol. 400. Society of Automotive Engineers Warrendale, 1995 (cit. on p. 95).

F. Millo, P. F. Giacominetto, and M. G. Bernardi. "Analysis of different exhaust gas recirculation architectures for passenger car diesel engines". In: *Applied Energy* 98 (2012), pp. 79–91 (cit. on p. 28).

F. Millo et al. "Development of an optimal strategy for the energy management of a range-extended electric vehicle with additional noise, vibration and harshness constraints". In: *Proceedings of the Institution of Mechanical Engineers, Part D: Journal of Automobile Engineering* 227.1 (2013), pp. 4–16 (cit. on p. 34).

P. Mock et al. *Discrepancies between type-approval and "real-world" fuel-consumption and CO*. Tech. rep. International Council on Clean Transportation, 2012 (cit. on p. 7).

P. Mock et al. *From laboratory to road*. Tech. rep. 30. International Council on Clean Transportation, 2013 (cit. on p. 7).

V. V. Monastyrsky and I. M. Golownykh. "Rapid computation of optimal control for vehicles". In: *Transportation Research Part B: Methodological* 27.3 (1993), pp. 219–227 (cit. on p. 23).

M. Montazeri-Gh, A. Poursamad, and B. Ghalichi. "Application of genetic algorithm for optimization of control strategy in parallel hybrid electric vehicles". In: *Journal of the Franklin Institute* 343.4 (2006), pp. 420–435 (cit. on p. 34).

J. Moreno, M. E. Ortuzar, and J. W. Dixon. "Energy-management system for a hybrid electric vehicle, using ultracapacitors and neural networks". In: *IEEE Transactions on Industrial Electronics* 53.2 (2006), pp. 614–623 (cit. on p. 34).

J. Morimoto, G. Zeglin, and C. G. Atkeson. "Minimax differential dynamic programming: Application to a biped walking robot". In: *Proceedings of the IEEE/RSJ International Conference on Intelligent Robots and Systems*. Vol. 2. 2003, pp. 1927–1932 (cit. on p. 18).

H. Mosbech. "Optimal control of a hybrid vehicle". In: *Proceedings of the International Symposium on Automotive Technology & Automation*. 1980, pp. 303–320 (cit. on pp. 31, 34, 226).

S. J. Moura et al. "A stochastic optimal control approach for power management in plug-in hybrid electric vehicles". In: *IEEE Transactions on Control Systems Technology* 19.3 (2011), pp. 545–555 (cit. on p. 36).

R. Muller and G. Nocker. "Intelligent cruise control with fuzzy logic". In: *Proceedings of the Intelligent Vehicles Symposium*. 1992, pp. 173–178 (cit. on p. 21).

S. Muller, M. Uchanski, and K. Hedrick. "Estimation of the maximum tire-road friction coefficient". In: *Journal of dynamic systems, measurement, and control* 125.4 (2003), pp. 607–617 (cit. on p. 290).

N. Murgovski, L. M. Johannesson, and J. Sjoberg. "Engine on/off control for dimensioning hybrid electric powertrains via convex optimization". In: *IEEE Transactions on Vehicular Technology* 62.7 (2013), pp. 2949–2962 (cit. on pp. 38, 258).

C. Musardo et al. "A-ECMS: an adaptive algorithm for hybrid electric vehicle energy management". In: *European Journal of Control, Fundamental Issues in Control, special issue* 11 (2005), pp. 1816–1823 (cit. on pp. 35, 226, 227).

C. Musardo et al. "Supervisory control for NOx reduction of an HEV with a mixed-mode HCCI/CIDI engine". In: *Proceedings of the American Control Conference*. Vol. 6. 2005, pp. 3877–3881 (cit. on pp. 35, 173).

J. E. Naranjo et al. "Adaptive fuzzy control for inter-vehicle gap keeping". In: *IEEE Transactions on Intelligent Transportation Systems* 4.3 (2003), pp. 132–142 (cit. on p. 21).

T. Nilsson, A. Froberg, and J. Aslund. "Optimal operation of a turbocharged diesel engine during transients". In: *SAE International Journal of Engines* 5 (2012), pp. 571–578 (cit. on pp. 26–28).

J. Nocedal. "Updating quasi-Newton matrices with limited storage". In: *Mathematics of Computation* 35.151 (1980), pp. 773–782 (cit. on pp. 86, 191).

T. Nuesch et al. "Optimal energy management and sizing for hybrid electric vehicles considering transient emissions". In: *Engine and Powertrain Control, Simulation and Modeling*. Vol. 3. 1. 2012, pp. 278–285 (cit. on pp. 33, 34, 173).

T. Nuesch et al. "Cost and fuel-optimal selection of HEV topologies using particle swarm optimization and dynamic programming". In: *American Control Conference*. 2012, pp. 1302–1307 (cit. on pp. 37, 38, 258).

R. Omran, R. Younes, and J. C. Champoussin. "Optimal control of a variable geometry turbocharged diesel engine using neural networks: applications on the ETC test cycle". In: *IEEE Transactions on Control Systems Technology* 17.2 (2009), pp. 380–393 (cit. on pp. 26, 27).

S. Onori, L. Serrao, and G. Rizzoni. "Adaptive equivalent consumption minimization strategy for hybrid electric vehicles". In: *Proceedings of the ASME Dynamic Systems and Control Conference*. Vol. 1. 2010, pp. 499–505 (cit. on pp. 35, 226, 227).

D. F. Opila et al. "An energy management controller to optimally trade off fuel economy and drivability for hybrid vehicles". In: *IEEE Transactions on Control Systems Technology* 20.6 (2012), pp. 1490–1505 (cit. on p. 36).

P. Ortner and L. del Re. "Predictive control of a diesel engine air path". In: *IEEE Transactions on Control Systems Technology* 15.3 (2007), pp. 449–456 (cit. on p. 26).

E. Ozatay et al. "Cloud-based velocity profile optimization for everyday driving: A dynamic-programming-based solution". In: *IEEE Transactions on Intelligent Transportation Systems* 15.6 (2014), pp. 2491–2505 (cit. on pp. 24, 209, 210).

M. Padberg and G. Rinaldi. "A branch-and-cut algorithm for the resolution of large-scale symmetric traveling salesman problems". In: *SIAM Review* 33.1 (1991), pp. 60–100 (cit. on p. 87).

G. Paganelli et al. "Simulation and assessment of power control strategies for a parallel hybrid car". In: *Proceedings of the Institution of Mechanical Engineers, Part D: Journal of Automobile Engineering* 214.7 (2000), pp. 705–717 (cit. on pp. 32, 33, 226, 229).

G. Paganelli et al. "General supervisory control policy for the energy optimization of charge-sustaining hybrid electric vehicles". In: *JSAE Review* 22.4 (2001), pp. 511–518 (cit. on pp. 32, 226).

B. Passenberg, P. Kock, and O. Stursberg. "Combined time and fuel optimal driving of trucks based on a hybrid model". In: *European Control Conference*. 2009, pp. 4955–4960 (cit. on pp. 22, 23).

F. Payri et al. "A new tool to perform global energy balances in DI diesel engines". In: *SAE International Journal of Engines* 7 (2014), pp. 43–59 (cit. on pp. 36, 129).

F. Payri et al. "Assessing the limits of downsizing in diesel engines". In: *SAE Technical Paper*. 2014 (cit. on p. 148).

F. Payri et al. "Experimental and theoretical analysis of the energy balance in a DI diesel engine". In: *SAE Technical Paper*. 2015 (cit. on pp. 36, 129).

F. Payri et al. "On a stochastic approach of the ECMS method for energy management in hybrid electric vehicles". In: *Engine and Powertrain Control, Simulation and Modeling*. Vol. 3. 1. 2012, pp. 341–348 (cit. on pp. 35, 230, 233).

F. Payri et al. "A challenging future for the IC engine: New technologies and the control role". In: *Oil & Gas Science and Technology – Revue d'IFP Energies nouvelles* 70.1 (2015), pp. 15–30 (cit. on p. 9).

F. Payri et al. "A stochastic method for the energy management in hybrid electric vehicles". In: *Control Engineering Practice* 29 (2014), pp. 257–265 (cit. on pp. 35, 230).

F. Payri et al. "Effects of the intake charge distribution in HSDI engines". In: *SAE World Congress and Exhibition. SAE Technical paper*. 2010 (cit. on p. 28).

L. V. Pérez and E. A. Pilotta. "Optimal power split in a hybrid electric vehicle using direct transcription of an optimal control problem". In: *Mathematics and Computers in Simulation* 79.6 (2009), pp. 1959–1970 (cit. on pp. 34, 75).

L. V. Pérez et al. "Optimization of power management in an hybrid electric vehicle using dynamic programming". In: *Mathematics and Computers in Simulation* 73.1?4 (2006), pp. 244–254 (cit. on pp. 33, 227).

N. Petit, A. Sciarretta, et al. "Optimal drive of electric vehicles using an inversion-based trajectory generation approach". In: *Proceedings of the 18th IFAC World Congress*. 2011, pp. 14519–14526 (cit. on p. 24).

B. Pla. "Análisis del proceso de la recirculación de los gases de escape de baja presión en motores diesel sobrealimentados". PhD thesis. CMT-Motores Térmicos, Universitat Politècnica de València, 2009 (cit. on p. 139).

B. Pla et al. *Fuel and immission potential of context aware engine control.* Tech. rep. SAE Technical Paper, 2013 (cit. on p. 25).

L. S. Pontryagin et al. *The mathematical theory of optimal processes.* Interscience, New York, 1962 (cit. on pp. 18, 21, 32, 68).

D. Popovic et al. "Extremum seeking methods for optimization of variable cam timing engine operation". In: *IEEE Transactions on Control Systems Technology* 14.3 (2006), pp. 398–407 (cit. on p. 25).

W. B. Powell. *Approximate dynamic programming: solving the curses of dimensionality.* Vol. 703. John Wiley & Sons, 2007 (cit. on pp. 35, 64).

R. Rajamani. *Vehicle dynamics and control.* Springer Science & Business Media, 2011 (cit. on pp. 95, 97).

C. D. Rakopoulos and D. C. Kyritsis. "Comparative second-law analysis of internal combustion engine operation for methane, methanol, and dodecane fuels". In: *Energy* 26.7 (2001), pp. 705–722 (cit. on pp. 36, 242).

A. Ravey et al. "Combined optimal sizing and energy management of hybrid electric vehicles". In: *IEEE Transportation Electrification Conference and Expo.* 2012, pp. 1–6 (cit. on pp. 37, 38).

A. Reig and L. del Re. "Evaluation of impact on pollution of a linear HEV optimal control strategy by engine-in-the-loop simulation". In: *7th IFAC Symposium on Advances in Automotive Control.* Vol. 7. 1. 2013, pp. 29–34 (cit. on p. 34).

G. Rizzoni, L. Guzzella, and B. M. Baumann. "Unified modeling of hybrid electric vehicle drivetrains". In: *IEEE/ASME Transactions on Mechatronics* 4.3 (1999), pp. 246–257 (cit. on p. 173).

P. Rodatz et al. "Optimal power management of an experimental fuel cell / supercapacitor-powered hybrid vehicle". In: *Control Engineering Practice* 13.1 (2005), pp. 41–53 (cit. on pp. 33, 258).

S. M. Ross. *Introduction to stochastic dynamic programming.* Academic press, 1983 (cit. on p. 36).

J. Rust. "Using randomization to break the curse of dimensionality". In: *Econometrica* 65.3 (1997), pp. 487–516 (cit. on p. 64).

Y. Saboohi and H. Farzaneh. "Model for developing an eco-driving strategy of a passenger vehicle based on the least fuel consumption". In: *Applied Energy* 86.10 (2009), pp. 1925–1932 (cit. on p. 23).

B. Saerens et al. "Minimization of the fuel consumption of a gasoline engine using dynamic optimization". In: *Applied Energy* 86.9 (2009), pp. 1582–1588 (cit. on pp. 26, 27).

H. Schättler and U. Ledzewicz. *Geometric optimal control: Theory, methods and examples*. Springer, 2012 (cit. on pp. 72, 73).

A. B. Schwarzkopf and R. B. Leipnik. "Control of highway vehicles for minimum fuel consumption over varying terrain". In: *Transportation Research* 11.4 (1977), pp. 279–286 (cit. on p. 22).

A. Sciarretta and L. Guzzella. "Control of hybrid electric vehicles". In: *IEEE Control System Magazine* 27.2 (2007), pp. 60–70 (cit. on pp. 30, 34, 225, 226, 259).

A. Sciarretta, M. Back, and L. Guzzella. "Optimal control of parallel hybrid electric vehicles". In: *IEEE Transactions on Control Systems Technology* 12.3 (2004), pp. 352–363 (cit. on pp. 33, 226, 227).

A. Sciarretta, G. De Nunzio, and L. L. Ojeda. "Optimal ecodriving control: energy-efficient driving of road vehicles as an optimal control problem". In: *IEEE Control Systems* 35.5 (2015), pp. 71–90 (cit. on pp. 22, 24, 209, 210).

P. G. Scotson and P. E. Wellstead. "Self-tuning optimization of spark ignition automotive engines". In: *IEEE Control Systems Magazine* 10.3 (1990), pp. 94–101 (cit. on p. 25).

L. Serrao, S. Onori, and G. Rizzoni. "A comparative analysis of energy management strategies for hybrid electric vehicles". In: *Journal of Dynamic Systems, Measurement, and Control* 133 (2011), pp. 1–9 (cit. on pp. 34, 35, 227, 228, 259).

L. Serrao, S. Onori, and G. Rizzoni. "ECMS as realization of Pontryagin's minumum principle for HEV control". In: *American Control Conference*. 2009, pp. 3964–3969 (cit. on pp. 33, 229).

L. Serrao and G. Rizzoni. "Optimal control of power split for a hybrid electric refuse vehicle". In: *American Control Conference*. 2008, pp. 4498–4503 (cit. on p. 33).

L. Serrao et al. "An aging model of Ni-MH batteries for hybrid electric vehicles". In: *Ieee conference on vehicle power and propulsion*. IEEE. 2005, pp. 78–85 (cit. on p. 259).

L. Serrao et al. "Open issues in supervisory control of hybrid electric vehicles: a unified approach using optimal control methods". In: *Oil & Gas Science and Technology – Revue d'IFP Energies nouvelles* 68.1 (2013), pp. 23–33 (cit. on p. 34).

L. Serrao et al. "Optimal energy management of hybrid electric vehicles including battery aging". In: *American Control Conference*. 2011, pp. 2125–2130 (cit. on pp. 34, 259).

A. Shaout, D. Colella, and S. Awad. "Advanced driver assistance systems - past, present and future". In: *Seventh International Computer Engineering Conference*. 2011, pp. 72–82 (cit. on p. 21).

C.-S. N. Shiau et al. "Optimal plug-in hybrid electric vehicle design and allocation for minimum life cycle cost, petroleum consumption, and greenhouse gas emissions". In: *Journal of Mechanical Design* 132.9 (2010), pp. 1–11 (cit. on p. 37).

J. V. Shutty et al. "Air system control for advanced diesel engines". In: *SAE World Congress and Exhibition*. 2007 (cit. on pp. 28, 29, 166).

D. Siano, F. Bozza, and M. Costa. "Reducing fuel consumption, noxious emissions and radiated noise by selection of the optimal control strategy of a diesel engine". In: *SAE Technical Paper*. 2011 (cit. on p. 28).

L. Sileghem et al. "Analysis of vehicle emission measurements on the new WLTC, the NEDC and the CADC". In: *Transportation Research Part D: Transport and Environment* 32 (2014), pp. 70–85 (cit. on p. 7).

D. Sinoquet, G. Rousseau, and Y. Milhau. "Design optimization and optimal control for hybrid vehicles". In: *Optimization and Engineering* 12.1 (2011), pp. 199–213 (cit. on p. 37).

M. Sivertsson and L. Eriksson. "Time and fuel optimal power response of a diesel-electric powertrain". In: *IFAC Proceedings Volumes* 45.30 (2012), pp. 262–269 (cit. on pp. 26, 27).

T. Stanger and L. del Re. "A model predictive cooperative adaptive cruise control approach". In: *American Control Conference*. 2013, pp. 1374–1379 (cit. on p. 21).

N. B. of Statistics of China. *China Statistical Yearbook 2015*. 2015 (cit. on p. 6).

G. Stewart and F. Borrelli. "A model predictive control framework for industrial turbodiesel engine control". In: *47th IEEE Conference on Decision and Control*. 2008, pp. 5704–5711 (cit. on p. 26).

S. Stockar et al. "Energy-optimal control of plug-in hybrid electric vehicles for real-world driving cycles". In: *IEEE Transactions on Vehicular Technology* 60.7 (2011), pp. 2949–2962 (cit. on p. 33).

S. Stockar et al. "Optimal control for plug-in hybrid electric vehicle applications". In: *Proceedings of the American Control Conference*. 2010, pp. 5024–5030 (cit. on p. 33).

H. Stuhler et al. "Automated model-based GDI engine calibration adaptive online DoE approach". In: *SAE Technical Paper*. 2002 (cit. on p. 10).

P. Sun, B. Powell, and D. Hrovat. "Optimal idle speed control of an automotive engine". In: *Proceedings of the American Control Conference*. Vol. 2. 2000, pp. 1018–1026 (cit. on pp. 26, 27).

O. Sundström and L. Guzzella. "A generic dynamic programming Matlab function". In: *IEEE Control Applications, Intelligent Control*. 2009, pp. 1625–1630 (cit. on pp. 67, 68, 247, 261).

A. Suresh et al. "Thermodynamic systems for Tier 2 Bin 2 diesel engines". In: *SAE International Journal of Engines* 6.1 (2013), pp. 167–183 (cit. on pp. 28, 29, 166).

I. Taymaz. "An experimental study of energy balance in low heat rejection diesel engine". In: *Energy* 31.2 (2006), pp. 364–371 (cit. on p. 36).

K.-Y. Teh and C. F. Edwards. "An optimal control approach to minimizing entropy generation in an adiabatic IC engine with fixed compression ratio". In: *ASME International Mechanical Engineering Congress and Exposition*. 2006, pp. 19–27 (cit. on p. 28).

The European Comission. *Comission regulation (EU) 2016/427 of 10 March 2016 amending regulation (EC) No 692/2008 as regards emissions from light passenger and commercial vehicles (Euro 6)*. 2016 (cit. on p. 8).

C. E. S. Thomas. "Transportation options in a carbon-constrained world: Hybrids, plug-in hybrids, biofuels, fuel cell electric vehicles, and battery electric vehicles". In: *International Journal of Hydrogen Energy* 34.23 (2009), pp. 9279–9296 (cit. on p. 5).

A. J. Torregrosa et al. "Experiments on the influence of inlet charge and coolant temperature on performance and emissions of a DI diesel engine". In: *Experimental Thermal and Fluid Science* 30.7 (2006), pp. 633–641 (cit. on pp. 170, 172).

L. Tribioli et al. "A real time energy management strategy for plug-in hybrid electric vehicles based on optimal control theory". In: *Energy Procedia* 45 (2014), pp. 949–958 (cit. on p. 35).

M. Tutuianu et al. *Development of a world-wide worldwide harmonized light duty driving test cycle (WLTC)*. Tech. rep. WLTP DHC Chair, 2013 (cit. on p. 7).

J. Van Leeuwen. *Handbook of theoretical computer science: algorithms and complexity*. Vol. A. Elsevier, 1990 (cit. on p. 87).

R. Vinter. *Optimal control*. Springer, 2010 (cit. on pp. 18, 21, 65, 71–73).

O. Vítek et al. "Comparison of different EGR solutions". In: *SAE World Congress and Exhibition. SAE Technical Paper*. 2008 (cit. on p. 28).

A. Wächter and L. T. Biegler. "On the implementation of an interior-point filter line-search algorithm for large-scale nonlinear programming". In: *Mathematical Programming* 106.1 (2006), pp. 25–57 (cit. on pp. 80, 86, 191, 215).

J. Wahlström and L. Eriksson. "Modelling diesel engines with a variable-geometry turbocharger and exhaust gas recirculation by optimization of model parameters for capturing non-linear system dynamics". In: *Proceedings of the Institution of Mechanical Engineers, Part D: Journal of Automobile Engineering* 225.7 (2011), pp. 960–986 (cit. on pp. 108, 115, 118, 125, 126).

J. Wahlström, L. Eriksson, and L. Nielsen. "Controller tuning based on transient selection and optimization for a diesel engine with EGR and VGT". In: *SAE Technical Paper*. 2008 (cit. on p. 25).

E. H. Wakefield. *History of the electric automobile-hybrid electric vehicles*. Vol. 187. Society of Automotive Engineers, 1998 (cit. on p. 4).

P. Waltermann. "Modelling and control of the longitudinal and lateral dynamics of a series hybrid vehicle". In: *Proceedings of the IEEE International Conference on Control Applications*. 1996, pp. 191–198 (cit. on pp. 32, 95).

N. Wan, A. Vahidi, and A. Luckow. "Optimal speed advisory for connected vehicles in arterial roads and the impact on mixed traffic". In: *Transportation Research Part C: Emerging Technologies* 69 (2016), pp. 548–563 (cit. on p. 22).

R. Wang and S. M. Lukic. "Review of driving conditions prediction and driving style recognition based control algorithms for hybrid electric vehicles". In: *IEEE Vehicle Power and Propulsion Conference*. 2011, pp. 1–7 (cit. on p. 35).

Y. Wang et al. "Optimal trajectory planning for trains under fixed and moving signaling systems using mixed integer linear programming". In: *Control Engineering Practice* 22 (2014), pp. 44–56 (cit. on p. 75).

H. Waschl et al. *Optimization and optimal control in automotive systems*. Springer, 2014 (cit. on p. 28).

R. A. Weinstock, P. T. Krein, and R. A. White. "Optimal sizing and selection of hybrid electric vehicle components". In: *24th Annual IEEE Power Electronics Specialists Conference*. 1993, pp. 251–256 (cit. on p. 37).

M. Weiss et al. "Will euro 6 reduce the NOx emissions of new diesel cars?– insights from on-road tests with portable emissions measurement systems (PEMS)". In: *Atmospheric Environment* 62 (2012), pp. 657–665 (cit. on p. 8).

WHO global urban ambient air pollution database, update 2011. World Health Organization. 2011 (cit. on p. 7).

WHO global urban ambient air pollution database, update 2016. World Health Organization. 2016 (cit. on p. 7).

V. Winstead and I. V. Kolmanovsky. "Estimation of road grade and vehicle mass via model predictive control". In: *Proceedings of IEEE Conference on Control Applications*. 2005, pp. 1588–1593 (cit. on p. 22).

J.-S. Won, R. Langari, and M. Ehsani. "An energy management and charge sustaining strategy for a parallel hybrid vehicle with CVT". In: *IEEE Transactions on Control Systems Technology* 13.2 (2005), pp. 313–320 (cit. on p. 34).

J.-S. Won and R. Langari. "Intelligent energy management agent for a parallel hybrid vehicle-part ii: torque distribution, charge sustenance strategies, and performance results". In: *IEEE Transactions on Vehicular Technology* 54.3 (2005), pp. 935–953 (cit. on p. 34).

G. Woschni. *A universally applicable equation for the instantaneous heat transfer coefficient in the internal combustion engine*. Tech. rep. SAE Technical Paper, 1967 (cit. on p. 128).

X. Wu et al. "Application of particle swarm optimization for component sizes in parallel hybrid electric vehicles". In: *IEEE Congress on Evolutionary Computation*. 2008, pp. 2874–2878 (cit. on pp. 37, 258).

X. Wu et al. "Component sizing optimization of plug-in hybrid electric vehicles". In: *Applied Energy* 88.3 (2011), pp. 799–804 (cit. on p. 37).

H. Xie et al. "Future engine control enabling environment friendly vehicle". In: *SAE Technical Paper*. 2011 (cit. on p. 10).

L. Xu et al. "Optimal vehicle control strategy of a fuel cell/battery hybrid city bus". In: *International Journal of Hydrogen Energy* 34.17 (2009), pp. 7323–7333 (cit. on pp. 33, 258).

O. A. Yakimenko. "Direct method for rapid prototyping of near-optimal aircraft trajectories". In: *Journal of Guidance, Control, and Dynamics* 23.5 (2000), pp. 865–875 (cit. on p. 75).

F. Yan, B. Haber, and J. Wang. "Optimal control of complex air-path systems for advanced diesel engines". In: *Proceedings of the ASME Dynamic System and Control Conference*. 2009, pp. 1–7 (cit. on p. 30).

F. Yan and J. Wang. "Control of diesel engine dual-loop EGR air-path systems by a singular perturbation method". In: *Control Engineering Practice* 21.7 (2013), pp. 981–988 (cit. on pp. 28, 29, 166).

X. Yang et al. "A survey on energy-efficient train operation for urban rail transit". In: *IEEE Transactions on Intelligent Transportation Systems* 17.1 (2016), pp. 2–13 (cit. on p. 10).

Z. Yuan et al. "Comparative study of dynamic programming and Pontryagin's minimum principle on energy management for a parallel hybrid electric vehicle". In: *Energies* 6.4 (2013), pp. 2305–2318 (cit. on p. 34).

G. Zamboni and M. Capobianco. "Influence of high and low pressure EGR and VGT control on in-cylinder pressure diagrams and rate of heat release in an automotive turbocharged diesel engine". In: *Applied Thermal Engineering* 51 (2013), pp. 586–596 (cit. on p. 28).

C. Zhang and A. Vahid. "Real-time optimal control of plug-in hybrid vehicles with trip preview". In: *Proceedings of the American Control Conference*. June 2010, pp. 6917–6922 (cit. on p. 35).

C. Zhang et al. "Role of terrain preview in energy management of hybrid electric vehicles". In: *IEEE Transactions on Vehicular Technology* 59.3 (2010), pp. 1139–1147 (cit. on pp. 35, 226, 227).

A. Ziebinski et al. "A survey of ADAS technologies for the future perspective of sensor fusion". In: *International Conference on Computational Collective IntelligenceInternational Conference on Computational Collective Intelligence*. 2016, pp. 135–146 (cit. on p. 21).

F. Zurbriggen et al. "Optimal control of the heat release rate of an internal combustion engine with pressure gradient, maximum pressure, and knock constraints". In: *Journal of Dynamic Systems, Measurement, and Control* 136.6 (2014), pp. 1–9 (cit. on pp. 36, 242, 247).